The Effects of Niobium in the Heat–Affected Zone of Microalloyed Steel

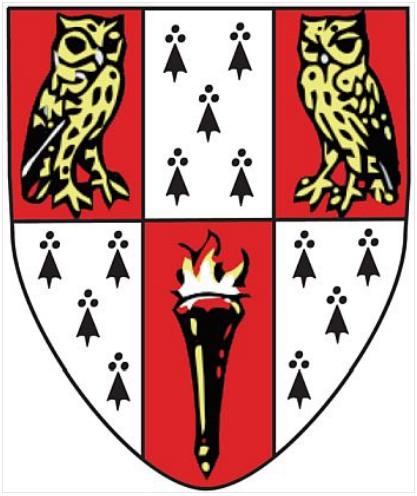

By

Neelabhro Madhav Bhattacharya

Hughes Hall

A thesis presented for the degree of Doctor of Philosophy

May 2017

Cambridge, U.K

"It is impossible to enjoy idling thoroughly unless one has plenty of work to do. There is no fun in doing nothing when you have nothing to do. Wasting time is merely an occupation then, and a most exhausting one. Idleness, like kisses, to be sweet must be stolen."

- Jerome K. Jerome, *Three Men in a Boat*

"Whence all creation had its origin,

he, whether he fashioned it or whether he did not,

he, who surveys it all from highest heaven,

he knows - or maybe even he does not know."

- Translated by A. L. Basham, *Rig Veda, Nasadiya Sukta,*

"Fè Ogou Fè, Ogou Fèray o"

'I am iron, I am covered with iron '

- Michel Lageurre, *Voodoo Heritage.*

Dedication

To my grandmothers;

Leela and Chitra

Preface

This dissertation is submitted for the degree of Doctor of Philosophy at the University of Cambridge. The work reported herein was carried out under the supervision of Professor Sir H. K. D. H. Bhadeshia in the Department of Materials Science and Metallurgy, University of Cambridge between October 2013 and October 2016. This dissertation is the result of my own work and includes nothing which is the outcome of work done in collaboration except as declared in the Preface and specified in the text. It is not substantially the same as any that I have submitted, or, is being concurrently submitted for a degree or diploma or other qualification at the University of Cambridge or any other University or similar institution except as declared in the Preface and specified in the text. I further state that no substantial part of my dissertation has already been submitted, or, is being concurrently submitted for any such degree, diploma or other qualification at the University of

Cambridge or any other University or similar institution except as declared in the Preface and specified in the text. This dissertation does not exceed 60,000 words in length.

Acknowledgements

I would like to thank Professor H.K.D.H. Bhadeshia for his patience, guidance and friendship without which this work would not have been possible. I gratefully acknowledge the generous financial support of CBMM, Brazil, and would like to express my sincere thanks to Marcos Stuart, Mariana Perez de Oliveira, Dr. Phil Kirkwood and Dr. Malcolm Gray for their efforts in supporting this project, through discussions and supplying the necessary materials on which much of this work is based. I would like to thank Professor Mark Blamire for the provision of laboratory facilities in the Department of Materials Science and Metallurgy at the University of Cambridge.

I will always be grateful to my colleagues in the Phase Transformations and Complex Properties group; Joachim, Guo Lei, Wil, Gebril, Ailsa, Tim, Shaumik, with special thanks to Steve Ooi, Arunim Ray, Chris Hulme-Smith, Ed Pickering, Di Wen, Lin Sun, and especially Dr. Mathew Peet, all of

whom offered significant help and discussions in progressing this work, and Angeline, Igor and Varun who were always ready to distract me with debates on politics and economics.

And a heartfelt thank you to my dear friends Gerson, Chris and Karolyn and my family who have been a source of constant support in all my undertakings.

Abstract

The effects of niobium in the heat-affected zone of microalloyed steel

Neelabhro Madhav Bhattacharya

The controlled, fine-grained microstructure of thermomechanically processed Nb microalloyed linepipe steels is destroyed in the vicinity of welds used in fabricating pipelines. There are conflicting views on the influence of niobium in the 'heat-affected zone', particularly in the region closest to the weld fusion line which is most dramatically impacted by the thermal cycling that occurs during welding. Consequently, there is a need to fully characterise the influence of niobium on the evolution of structures and properties in this zone.

The aim of the work presented in this thesis was to quantify and charac-

terise precipitates of niobium and dissolved niobium across sub-zones of the weld heat-affected zone, in order to develop a better understanding of the effects of niobium across the region. In order to achieve this, heat treatments were undertaken for the first time to simulate each sub-zone of the heat affected zone such that unique states of dissolved niobium and precipitated niobium were developed. A novel technique was designed and applied for the first time to measure and quantify the precipitate sizes and size distributions in bulk samples of Nb micro-alloyed steels. In addition, measurements of the dissolved niobium across the heat-affected zone were completed in order to ensure that the discrete effects of all states of niobium were subjected to analysis.

Weld simulations of the coarse-grained heat-affected zone, the region closest to the weld fusion line, were conducted and assessed against the measured states of niobium. This was followed by the manufacture of commercial welds in order to assess the variation of structures and properties across the heat-affected zone for different plate conditions generated by heat treatment prior to welding. This work established that that a wide range of niobium carbide precipitate sizes was crucial in assuring the excellent mechanical properties in the linepipe steel, coarser precipitates were found to

control the austenite grain size that evolved in the coarse-grain heat affected zone, while fine precipitates dissolved in the thermal cycles close to the weld fusion line, and produced finer microstructures.

Contents

Chapter 1

Literature Review

1.1 Overview

Increasingly demanding conditions for oil and gas transport pipelines, often with working pressures in excess of 100 MPa have stimulated research on novel steels that must satisfy a wide range of parameters, as illustrated in figure 1.1.

Niobium microalloying has been used to enhance the mechanical properties of high strength low alloy (HSLA) steels [1] used in the fabrication of these pipelines. While these engineered steels, manufactured through thermomechanical controlled processing (TMCP), are able to meet the working pressure requirements, they have to be welded to be of practical application.

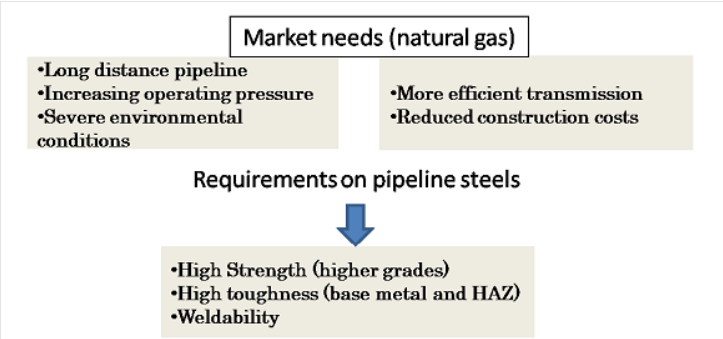

Figure 1.1: Requirements for pipeline steels [2].

The heavily controlled microstructure in the vicinity of the joint is destroyed during the welding process; there are conflicting views on the effect of niobium in the heat-affected zone of the weld, particularly in the coarse-grained heat-affected zone, closest to the weld fusion line, with some researchers reporting a decrease in toughness [3], while others claim no effects on hardenability, but increased toughness as more niobium content is increased to concentrations up to some 0.1 wt% [4]. These conflicting views likely arise from the complexity of the steel microstructure, along with the evolution of precipitates, phase transformations and micro-alloy dissolution when the steel is exposed to high temperatures during the welding process.

Therefore, it is the aim of this work to investigate the influence of niobium on the coarse-grained heat-affected zone of niobium micro-alloyed

linepipe steels. The question is considered in detail by characterising and then analysing the influence of niobium precipitates and dissolved niobium, and their effects on the evolution of structures and properties of the weld heat-affected zone.

1.2 Thermomechanical processing of steels

Hot-rolled steels traditionally depend on carbon and manganese up to 0.4 wt% and 1.5 wt% to achieve yield strengths of about 400 MPa in ferrite-pearlite microstructures. The steels do not, however, have reasonable impact toughness as illustrated in figure 1.2. Additionally, as welding began to dominate joining technology, cracking of welded joints in these steels became a limiting issue. This has led steels with reduced carbon, rolled to achieve a fine ferritic microstructure with high yield strengths in excess of 550 MPa without compromising toughness in the welded state [1].

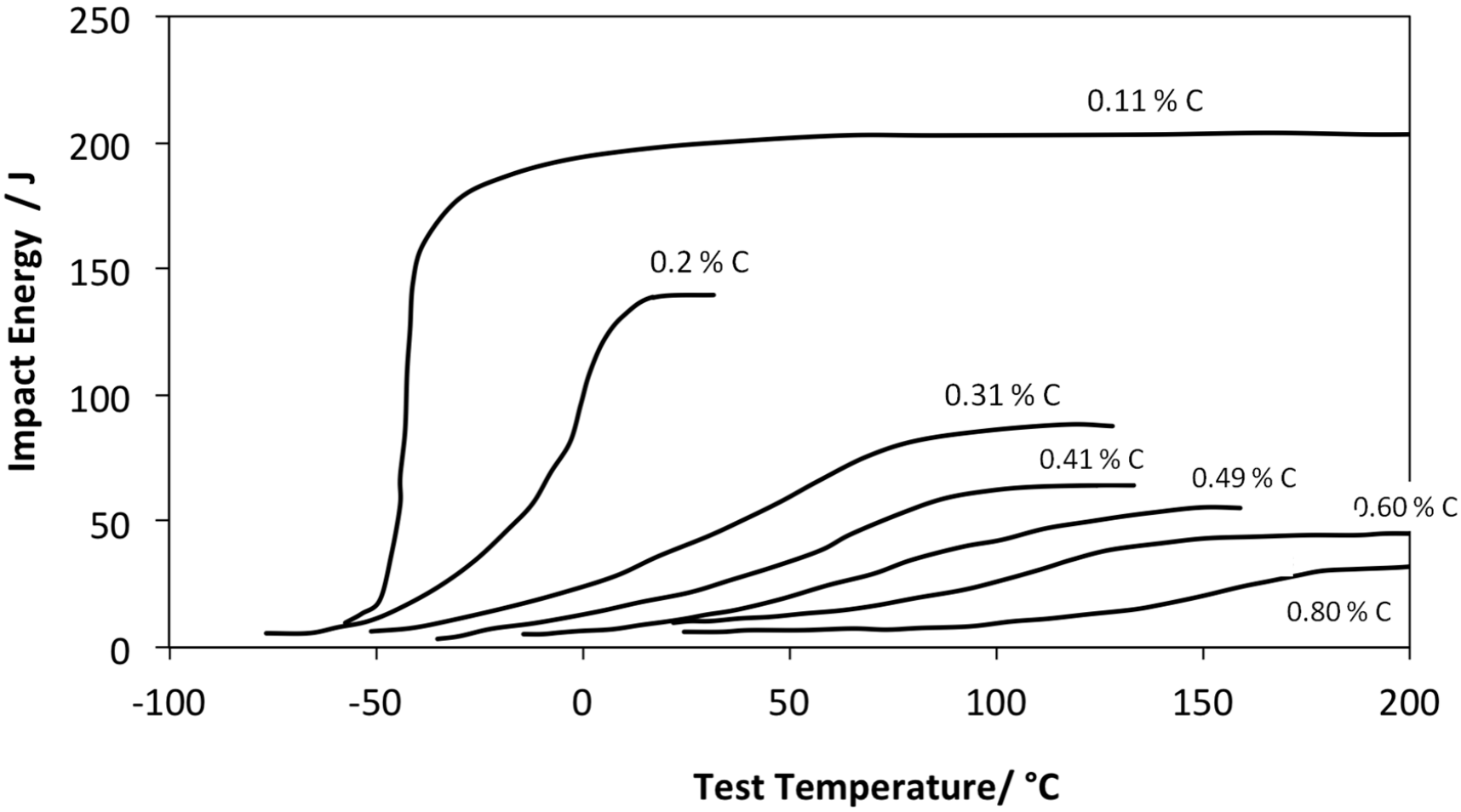

Figure 1.2: Change in absorbed energy with increasing carbon content in wt% in ferrite-pearlite steels after [5, 6].

Thermomechanically controlled processing of microalloyed steels exploits fine precipitation to control the size and shape of austenite grains, and in some cases, the micro-alloying addition that remains in solid solution can beneficially influence the development of structure [7].

Controlling grain size during rolling

The major mechanism thermomechanical processing for grain size control is the repeated recrystallisation of austenite during deformation in the presence of nanoscale precipitates that pin grain boundaries to restrict grain growth and increase the retention of strain-induced defects so that there is a large driving force for recrystallisation [8].

At high temperatures where the steel is austenitic, grain growth occurs readily in the absence of pinning particles [6, 9]. When the particle intersect the grain boundary to increase the interficial energy, in order for the boundary to migrate the local energy must be overcome, hence, a so-called 'drag' is effected on the grain boundary by the fine particles, effectivly pinning the grain boundary [6]. Gladman [10] and others have shown that for a given precipitate volume fraction there is a critical radius of particle size,

r_{crit}, beyond which grain growth dominates:

$$r_{crit} = \frac{6r_0 f}{\pi}\left(\frac{3}{2} - \frac{2}{Z}\right)^{-1} \tag{1.1}$$

Z is the ratio of radii of matrix and growing grains, f is the volume fraction of precipitates with average radius r_0 .

In the context of hot rolling, the fine grain boundary pinning precipitates, that persist at high temperature regimes (1200 ℃ - 1300 ℃). The most suitable precipitates are theramlly stable carbo-nitrides, with elements such as niobium and vanadium combining with carbon and nitrogen in the steel. The solubility of the precipitates reactive to the processing conditions is critical since fine precipitation should form at tempertaures where the γ is to be deformed [6, 11]. The advantage of niobium and titanium is in the lower solubility of the carbo-nitrides in the critical deformation temperature range (900-1300 ℃); the alloy carbides of chromium, for instance, remain in solution until the temperature is under the range for grain growth [6]. It is expected that during conventional rolling the austenite will recrystallise several times, and may even be left in a deformed state prior to the formation of ferrite; final ferrite grain sizes between 5 to 10 μm can routinely be found, with enhanced mechanical properties [12].

1.2.1 Metallurgy and microstructures of high strength low-alloy steels

Alloying elements

The role of alloying in HSLA steels is complex, with many parameters including processing, grain size and precipitation strengthening, solid solution strengthening that need to be considered. Hardenability effects also feature in determining the final structure and properties. It is therefore useful to evaluate each solute briefly.

Carbon in ferrite and in austenite occupies octahedral interstices, although the octahedron is irregular in the case of ferrite, leading to intense hardening. Its solubility is greater in austenite (where it stabilises the phase) than in ferrite, when these phases are in equilibrium. Carbon combines with many metallic solutes to form precipitates including iron carbide, molybdenum carbide, niobium carbide and titanium carbide [13]. Carbon dissolved in γ increases its hardenability; promoting the formation of martensite, α', under the appropriate conditions. An empirically determined carbon equivalent (CE) which accounts for other solutes, and is often used to assess the ability to wled the steel without forming α' in the HAZ. The goal is to avoid

cracking due to the formation of hard α' [1, 14, 15].

The Ito-Besseyo CE equation is relevant for steels with low carbon content, which are of interest to the present work [16]:

$$\text{Pcm} = \text{C} + \frac{\text{Si}}{30} + \frac{\text{Mn} + \text{Cu} + \text{Cr}}{20} + \frac{\text{Ni}}{60} + \frac{\text{Mo}}{15} + \frac{\text{V}}{10} + 5\text{B}\,\text{wt}\% \qquad (1.2)$$

In general the Pcm value should be less than 0.4 wt% in order to ensure weldability using conventional joining technology.

Nitrogen is also an interstitial solute that adds to solid solution strengthening [13]; it too has a greater solubility in austenite, in equilibrium with ferrite, and tends to form nitrides or carbonitrides sych as Nb(C,N). Dissolved nitrogen can lead to strain ageing and low toughness, so small concentrations of aluminium are often added to mitigiate its effects by forming AlN [13].

Interstitials and solution strengthening

Carbon and **nitrogen** have a stronger influence on ferrite than on austenitic iron due to the tetragonal symmetry of the intersitial sites in the former case. The strengthening effect occurs when strain fields around solutes affect dislocation motion. Substitutional solutes induce isotropic strains with dis-

location interaction limited to hydrostatic components o the strain fields of dislocations. Interstitial atoms in ferrite cause tetragonal distortions which interact with the dominant shear strain component of the dislocations [6, 17]. Figure 1.3 shows a regular octahedral interstice in austenite as compared to an irregular octahedron in ferrite, the root of the different effects of carbon in austenite versus ferrite.

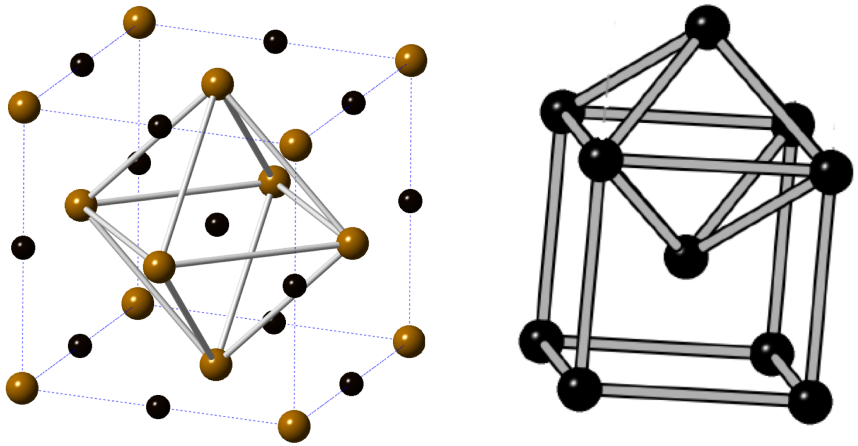

(a) **(b)**

Figure 1.3: Austenite (a) shows a regular octahedral interstice that better accommodates carbon as compared to BCC ferrite (b).

Work by Cottrell [18] showed that there was considerable interaction between dislocation strain fields and interstitial carbon and nitrogen. When atoms move into the dislocation strain fields, the total strain energy is reduced, so clouds of C atoms decorate dislocations to form *Cottrell atmospheres* [6]. The dislocations become bound to the intersitial atoms with energies of 0.5 eV [6]. The stress necessary to unpin a dislocation is substantial. A relatively small number of solute atoms are required to produce locking of long lines of dislocations, as in Figure 1.4.

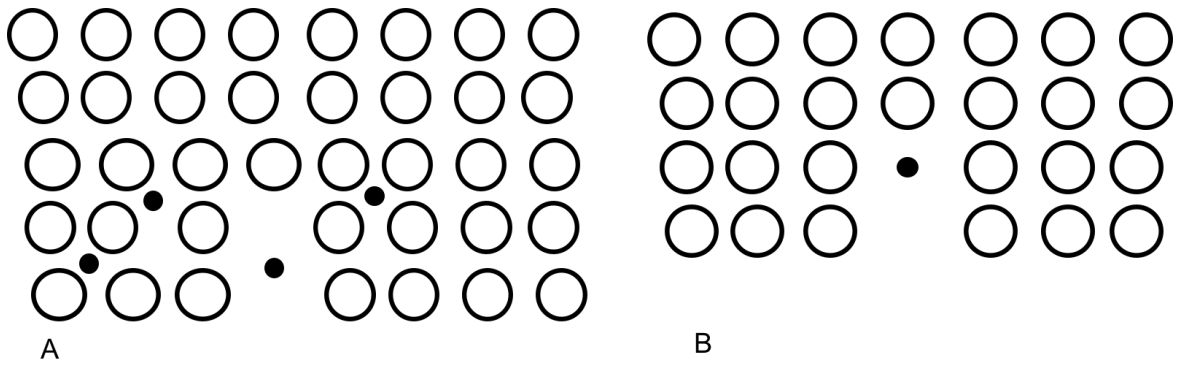

Figure 1.4: Interstials in proxomity to an edge disoclation; (A) random atmopshere (B) condensed atmosphere, after [6].

Dissolved carbon and nitrogen can influence the yield phenomenon in ferritic steel, i.e. heterogeneous deformation as dislocations initially pinned by the carbon and nitogran are suddenly unpinned at a stress that is greater than that needed to propagate them. It is possible to differentiate between an upper (A in Figure 1.5 and lower yield point (B). The section BC from Figure 1.5 describes a plastic deformation front that moves uniformly along the specimen referred to as the Lüders band [6]. The stress-strain curve rises in the normal way after the whole specimen has yielded and work hardening has commenced.

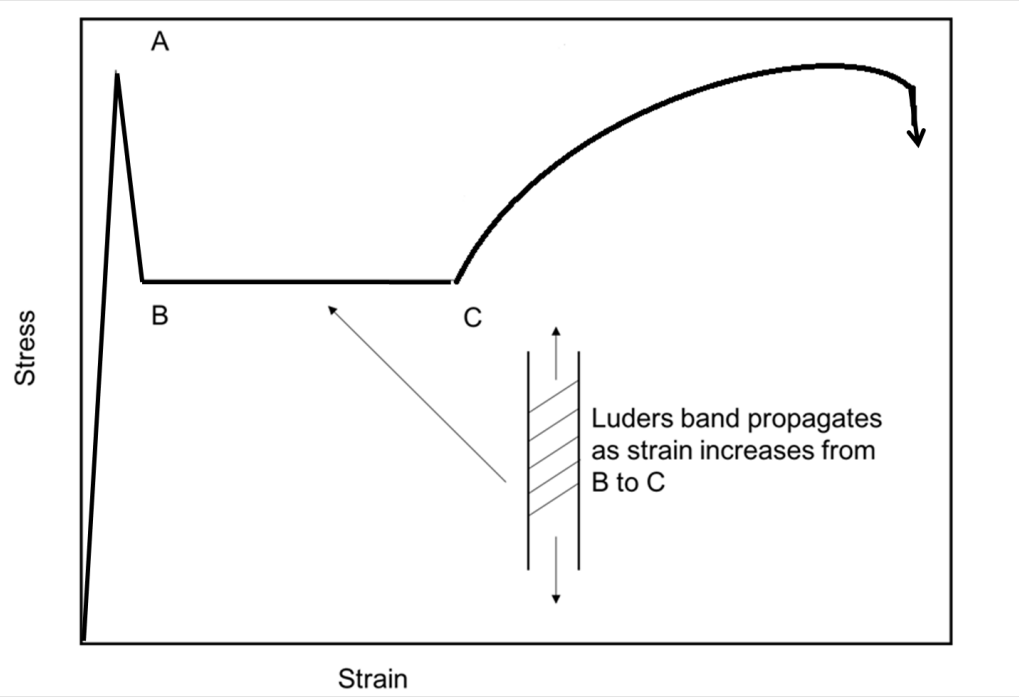

Figure 1.5: Yield phenomenon due to carbon atoms pinning dislocations, after Cottrell [6]

Other alloying elements in high strength low alloy steels

Manganese is an austenite stabiliser, dissolves in cementite and is a mild solid solution strengthener. By reducing the transfer temperature it refines the microstructure and hence helps the reduce the ductile-brittle transition temperature. Above 0.5 wt%, concentrtation gradients can lead to segregation and banding, both of which are detrimental and cause hydrogen induced cracking. Across a range of concentrations, its main benefit in steelmaking is its affinity for sulphur, with MnS formation competing with FeS inclusions that can lead to hot shortening during welding [19].

Silicon and **molybdenum** stabilise and strengthen the ferrite phase, leading to increased impact transition temperatures and tensile strength [13, 20]. Mo has a strong retarding effect on the austenite to ferrite phase transformation.

Aluminium, as noted previously, combines with nitrogen to form a fine precipitate dispersion of aluminium nitride that helps control the austenite grain size during hot deformation.

Nickel stabilizes austenite, and therefore increases hardenability. If cooling rates are controlled to avoid the formation of martensite, toughness is

improved by nickel alloying.

Chromium depresses the γ transformation temperature, while it is not an effective agent for solid solution strengthening, it offers significant corrosion resistance depending on the quanitity added to the steel [13].

Titanium, niobium, vanadium are used for grain refinement and precipitation strengthening in most HSLA steels, since they are strong carbide and nitride formers, a necessary condition for the thermomechanical processing of $\boldsymbol{\gamma}$. Titanium nitride, due to its stability even at higher temperatures limits austentite grain size at elevated temperatures but its precipitates as cuboids that can be very harmful the impact properties. Niobium carbonitrides form dispersions of precipitates that enable precipitation strengthening, as well as control austenite grain-size through pinning and the formation of heterogenous nucleation sites. Precipitation of these alloy carbides occurs between 850 ℃ and 650 ℃. The presence of dissolved niobium has been noted to retard the bainitic transformation from austentite[11]. Vanadium and its precipitates have a similar effect on HSLA steels, in addition the higher solubility of vanadium carbide (as opposed to niobium and titanium carbides) in austenite leades to greater precipitation as the austenite transforms to ferrite (during controlled rollling) at the inter-phase boundary [21].

The influence of alloying elements on the equilibrium Fe-C phase diagrams illustrate the impact on phase stabilisation [6] in figures 1.6 to1.9)[22]. The effect can therefore be summarised as to 1) expand the γ-field to stabilise austenite formation over wider compositional ranges (γ stabilisers). 2) Contract the γ-field to form ferrite over wider compositional ranges (α-stabilisers).

Important γ-stabilisers alloying elements include nickel and manganese, which at sufficient concentration suppress entirely, effectively preventing the formation of the α-phase, manufacture of austentitic steels.

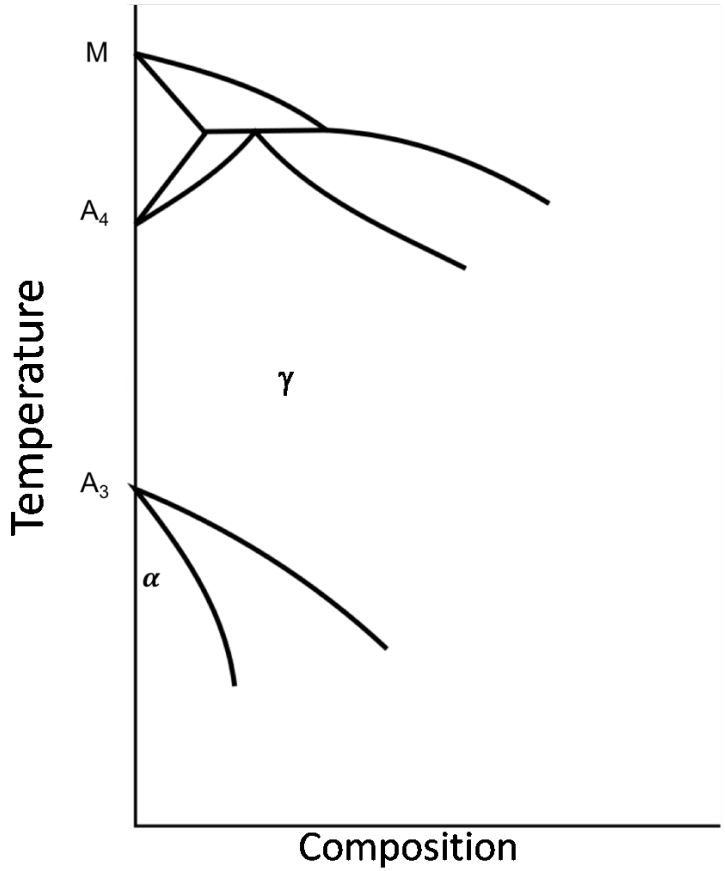

Figure 1.6: Open γ-field after Bhadeshia [6] from Wever [22]. M is the melting temperature, A_3 and A_4 are the transformation temperatures.

Carbon and **nitrogen** are the most critical alloying elements to an **expanded γ-field**. However compound formation can restrict this phenomenon. The expansion of the γ-field enables the formation of a homogenised austenitic solid solution; fundamental to modern heat treatment of steels.

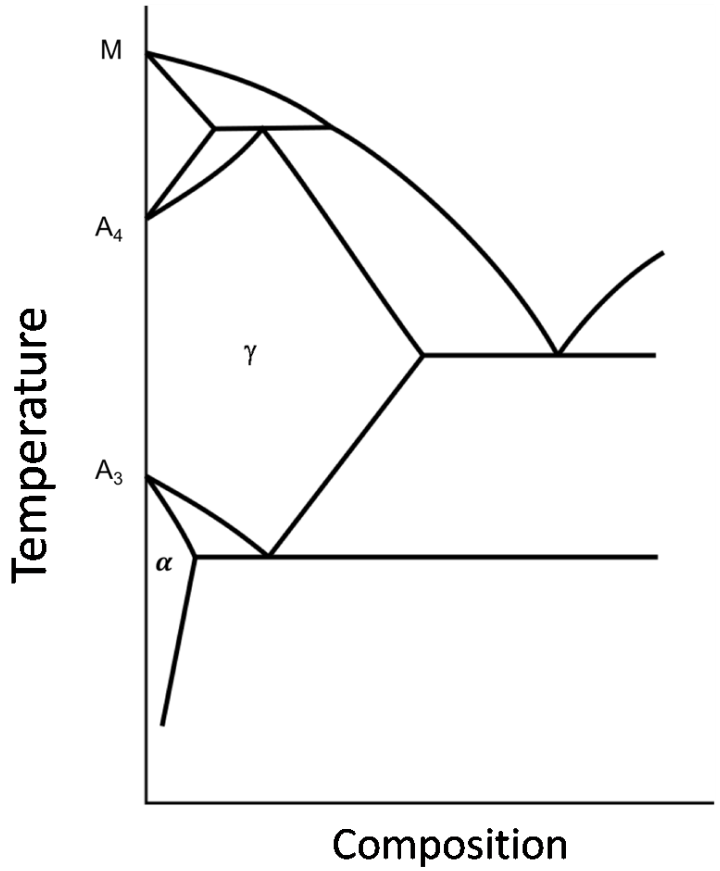

Figure 1.7: Expanded γ-field after Bhadeshia [6] from Wever [22]

Many alloying agents restrict the **γ-field**, forming the so-called gamma loop , Figure 1.8. This stabilises the ferrite phase, and the δ and α-phase fields become continuous, so conventional heat treatments cannot be applied that require cooling through the γ/α-phase transformation. This can be useful in steels that need to be magentically soft [6].

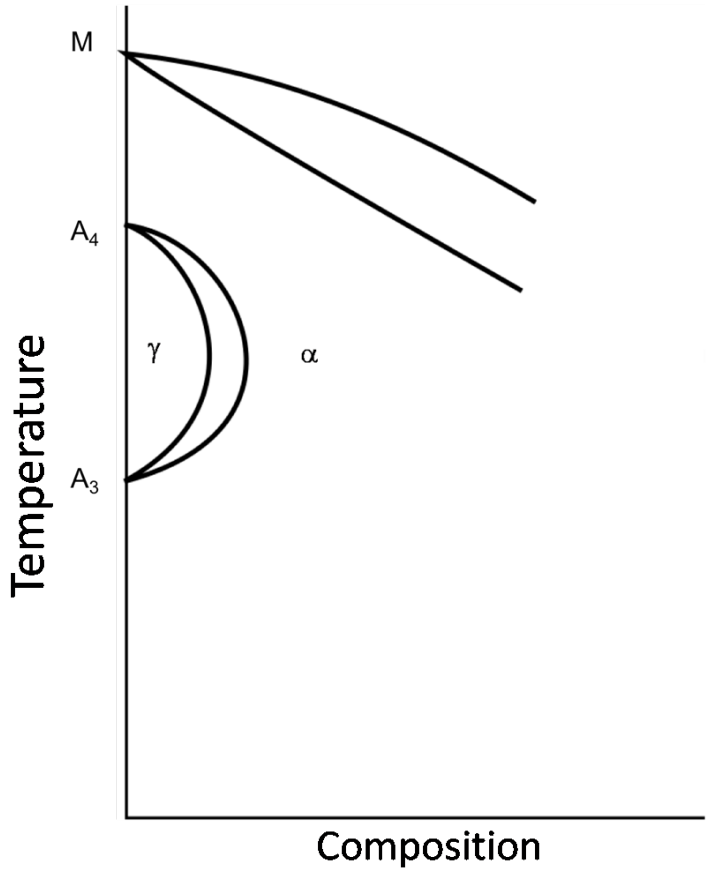

Figure 1.8: Closed γ-field after Bhadeshia [6] from Wever [22]

Carbide-forming elements, such as niobium and tantalum can cause a **contracted γ-field**, accompanied by compound formation.

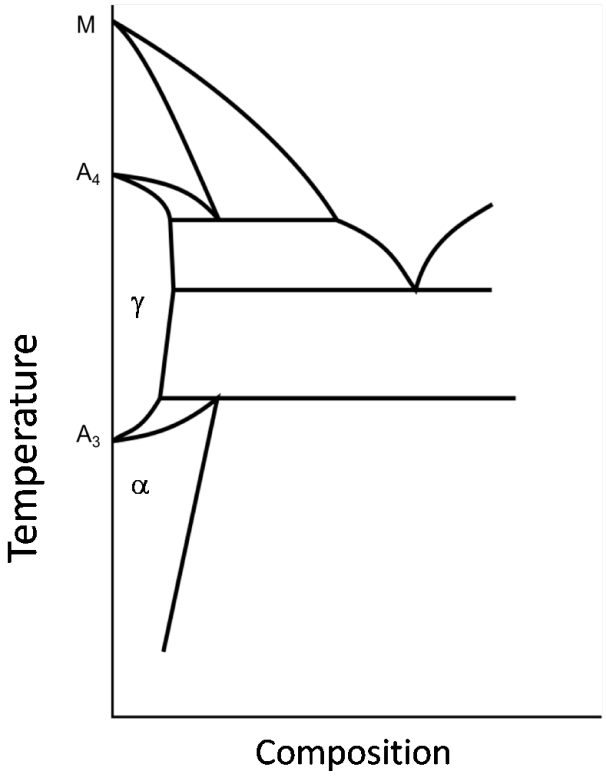

Figure 1.9: Contracted γ-field after Bhadeshia [6] from Wever [22]

Thermodynamic explanations for these phenomeon were developed by Zener and by Andrews [23]:

$$\log_e \frac{c_\alpha}{c_\gamma} = \frac{\Delta H}{RT} + \log_e \beta \tag{1.3}$$

where c_α and c_γ are the fractions of the alloying element in the respective

phase, and ΔH is the is the change between the heat of dissolution of the solute in austenite from the dissolution of the solute in ferrite. β is a constant.

In the case of alloying elements that stabilise ferrite, ΔH is positive, and those that stabilise austenite ΔH is negative. This is represented in Figure 1.10 which shows that austenite is formed when the γ-field is unlimited, while, when the reverse occurs, i.e. ΔH is positive, the γ-loop emerges, hence ferrite is formed.

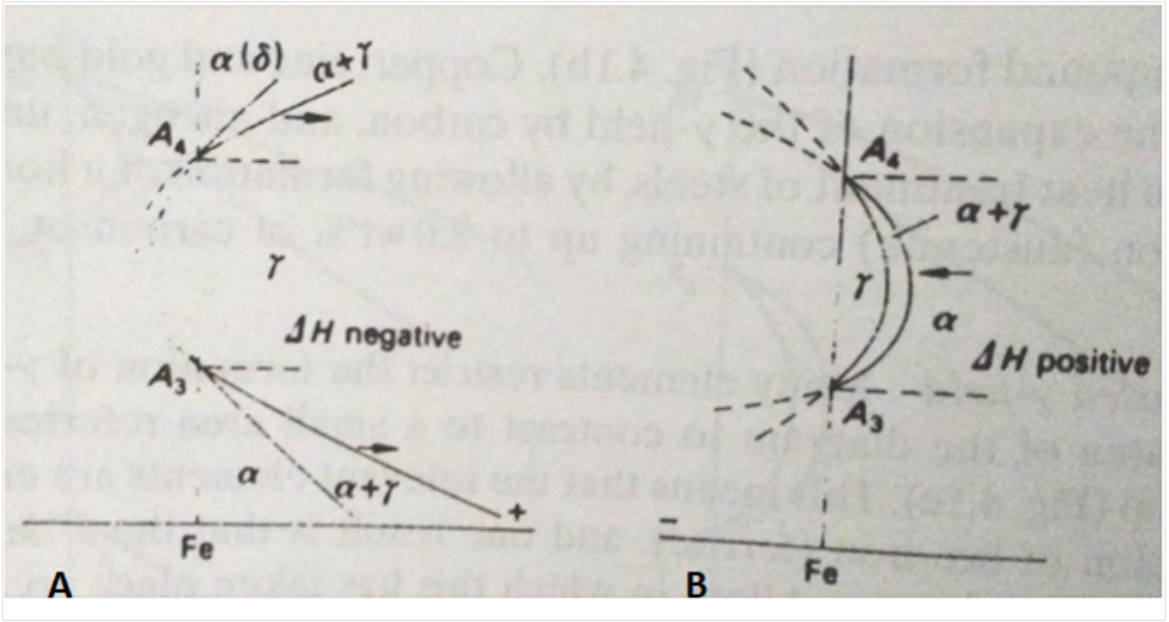

Figure 1.10: (A) ΔH negative, $H_\alpha > H_\gamma$, γ favoured. (B) ΔH negative, $H_\alpha < H_\gamma$, α favoured [23, 24].

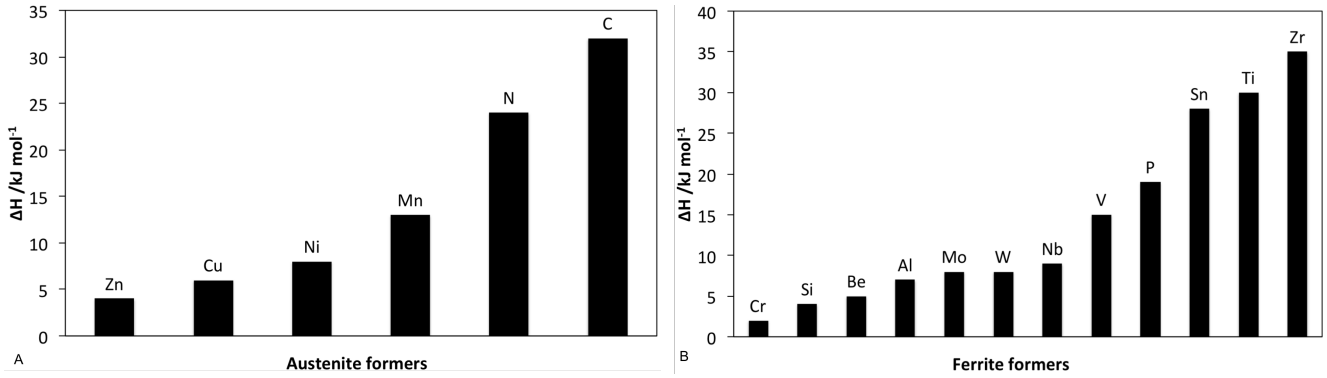

Figure 1.11: Comparative strengths of alloying agents (A) austenite forming alloys (B) ferrite forming alloys after Andrews [23]).

An analysis of the distribution of alloying elements is covered by Bhadeshia [6], however for the purposes of this review the discussion will be address the case of steels where ferrite and carbides form on equilibrium cooling. Alloying elements, under these conditions, can be considered to belong to three categories:

1. alloying elements that enter α;
2. alloying elements that form carbides, and enter α;
3. alloying elements that only form carbides

In category 1 are those elements that exist in solid solution in the ferritic phase like Ni and Si. Most alloying elements fit into category 2, i.e. they form carbides and at low concentrations enter into solid solutions in the ferritic phase and cementite. Alloy carbide formation is more stable (thermodynamically) at higher alloy concentrations [6]. The relative stability of these alloy carbides and nitrides, like vanadium, niobium and titanium, to cementite, based on the enthalpies of formation is shown in Figure 1.12.

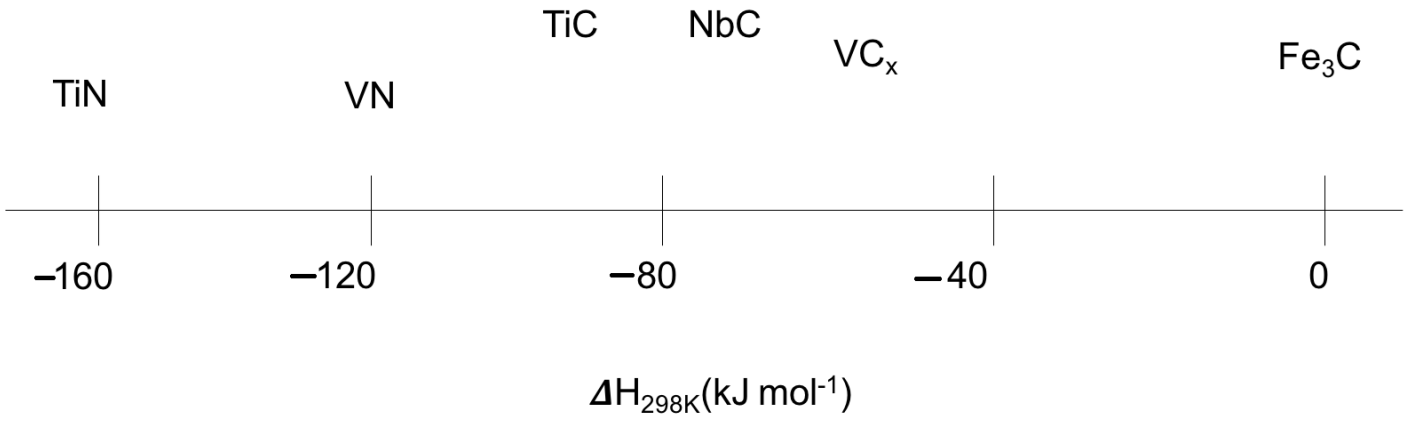

Figure 1.12: Absolute values of enthalpies of formation of some carbides and nitrides. after [25]

Typically the carbide-forming elements are added in excess of the amount required by stoichiometry with carbon content, this excess alloy enters into solid-solution along with the category 1 elements. The most important category 3 element in the context of conventional HSLA steels is nitrogen; which in the presence of strong nitride-forming elements like aluminium and titanium, forms alloy nitrides. Alloying elements have differing stabilities in ferrite and as carbides, therefore it can be anticipated that will be an effect on the kinetics and thermodynamics of decomposition of austenite, based on the concentration .

Alloying elements and changes in structure

Elements like Ni and Si do not compete with cementite for carbon. Strong carbide formers (elements in categories 1 and 2 above) in systems where carbon is less than 0.1 wt% will influence the final microstructure by removing carbon from solution to form precipitates [6]. Cottrell explains the tendency to form carbides and nitrides based on chemical bonds; the main observation is that there is decreasing carbon affinity along the rows of the periodic table, where more electrons have to fit into orbitals along each period reducing the bond order, although since maximum bond order is with Cr, Mo and W, as

illustrated in figure 1.13, and these have lower affinity for carbon, there are further implications to be considered [6, 26]. For a metal carbide (MC), the metal loses four electrons to bond with carbon, Ti has four such electrons, leaving an empty d-orbital of carbide formation. In the case of VC, V has an extra d-orbital electron which stabilises by forming a V-V bond. Hence the presence of the two bond types, V-C and V-V mutually repel, leading to instability [6, 26].

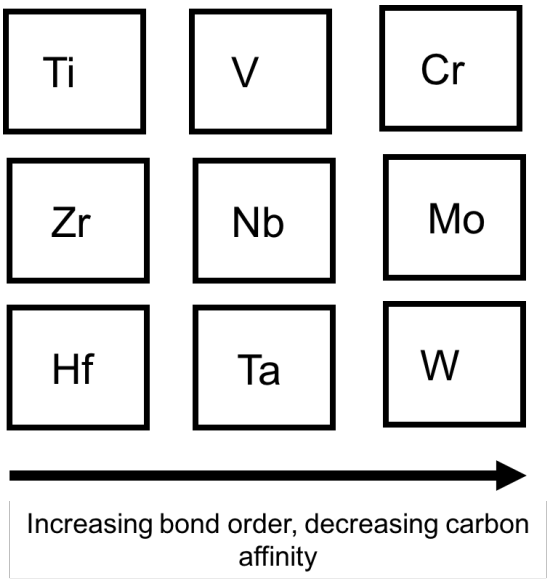

Figure 1.13: Examples of transition metal groups that form carbides. While bond order increases across the period, the stability of the carbides reduces.

The influence of carbides on ferrite formation

Carbide-forming alloys can have dramatic effects on microstructures, restricting the γ-loop, effectively lowering the carbon levels (in solution) and increasing transformation temperatures. The formation of alloy-rich carbides can completely remove pearlite from the microstructure, resulting in a microstructure that is very different to iron-carbide aggregates [6].

Microalloyed steels where carbide-forming elements are present at levels less that 0.1 wt% can often leave the ferrite supersaturated such that precipitation occurs after the γ/α phase change [6] as the steel cools. Precipitation also occurs in the ferrite grain, typically at dislocations over the duration of the transformation temperature as well as after the completion of the transformation. A range of microstructures can develop in alloy steels due to these complex interactions between alloying elements and phase transformations.

1.2.2 Transformations in low carbon steels

Allotriomorphic ferrite

Ferrite nucleates at γ grain boundaries to form allotriomorphs, when cooled to just below the Ae_3 temperature. Austenite grain boundaries are easy

diffusion paths, allowing layers of ferrite to decorate the parent boundaries [6, 27].

The thickness of the ferrite, S, can be expressed in relation to time, t;

$$S = \alpha_1 t^{1/2}, \tag{1.4}$$

where α_1 is called the parabolic rate constant, and depends on the equilibrium compositions of austentite and ferrite. Austentite stabilising elements like Mn are associated with smaller α_1 values [6]. As the amount of carbon in the steel is reduced, the growth deviates from diffusion-controlled to a mixed-mode where the rate of transfer of atoms across the interface becomes limiting [27, 28]. An important point is that the thickness of ferrite varies with the square root of time, because the distance over which the partition carbon diffuse increases with time, due to of the accumulation of carbon in front of the α/γ boundary.

Widmanstätten ferrite

Substitutional solutes and iron atoms do not diffuse in the formation of Widmanstätten ferrite, however, the carbon must partition because the low driving force available at the temperature where grows, cannot sustain. The plate shape accomodates carbon at the sides such that the plate tip grows

into fresh austentite, enabling growth at a constant rate [6]. Widmanstätten ferrite forms rapidly during welding, so it can be essentially treated as an isothermal transformation in the weld microstructures in the weld microstructures of interest in the present work, there are other phases that compete for growth as the steel cools, so Widmanstätten ferrite growth can be stifled by interference with acicular ferrite plates which nucleate intergranularly at non-metallic inclusions [6].

Acicular Ferrite

Thin, lenticular plates of acicular ferrite nucleate heterogeneously on non-metallic inclusions. Generically, the chaotic orientation of these plates is known to deflect cleavage cracks during their propagation, resulting in higher toughness. There is a range of non-metallic inclusions that are available that stimulate intragranular nucleation of acicular ferrite. Growth is diffusionless, but any excess carbon partitions into residual austenite [6].

Massive ferrite

In low-carbon steels, where partitioning between austenite and ferrite is minimal, diffusional transformation can occur to single-phase ferrite without a

change in overall composition by the growth of ferrite. This is because the average carbon concentration of the steel is close to the solubility limity of carbon in ferrite in equilbrium with austenite [29]. The resulting microstructure is composed of very coarse grains, referred to as massive ferrite. Ferrite growing by a diffusion mechanism is not limited by austenite boundaries and because the growth rate is rapid, the first nuclei to form, grow rapidly to consume several austenite grains [27, 30, 31].

Bainite

In typical steels when isothermally transfomed in the temperature range 250 ℃- 550 ℃ a fine aggregate of ferritic laths and particulate cementite forms which is generically termed bainite [6, 32].

Upper bainite forms between 550 ℃ and 400 ℃, and consists of ferritic laths or plates around 10 µm long by 0.2 µm thick [6]. The clusters of plates, which have identical crystallographic orientation are collectively called sheaves. The plates are separated by cementite particles [6]. While different theories exist on the growth mode for bainite [33–35]the evidence tends to support a displacive mechanism for the formation of bainite given the shape deformation that is observed [36, 37]. The growth of the plates

does not only affects the shape of the transformation region but also plastically deforms the adjacent austenite, illustrated in figure 1.14, causing an accumulation of dislocation debris at the trasnformation front. This limits the further movement of the interface, so the growth of the ferrite plates is terminated before impingement on the austentite grain boundaries [6]. The minimisation of the strain energy associated with the shape deformation of bainitic growth results in the thin plate morphology associated with bainite.

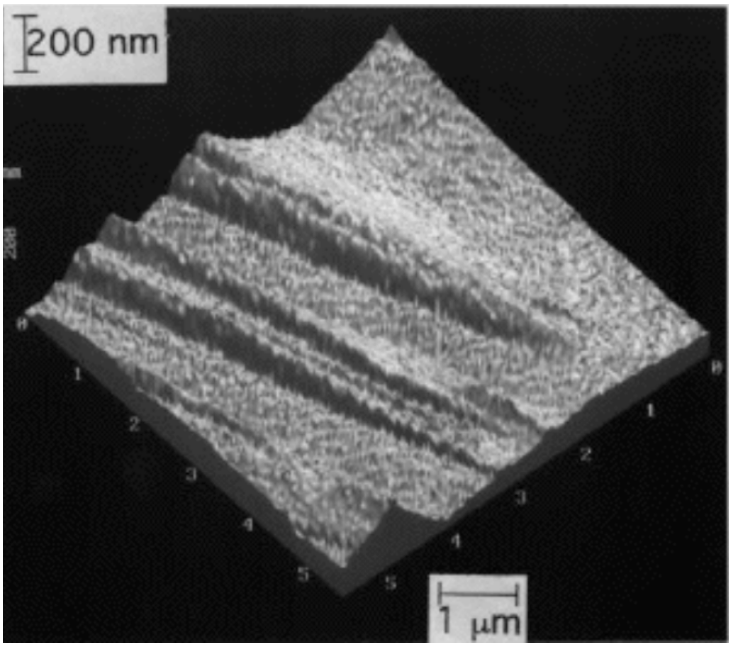

Figure 1.14: Surface relief due to bainite formation from [6].

Lower bainite typically forms between 250 ℃ and 400 ℃. The major distinction with upper bainite is that the precipitation of cementite or other

transition carbides occurs inside the ferritic plates,in addition to that between the plates as illustrated in figure 1.15. Cementite between the plates of either form of bainite grows from carbon-enriched austentite, but is finer in lower bainite because some of the carbon is precipitated from supersaturated ferrite. Therefore, lower bainite tends to be both stronger and tougher than upper bainnite [6].

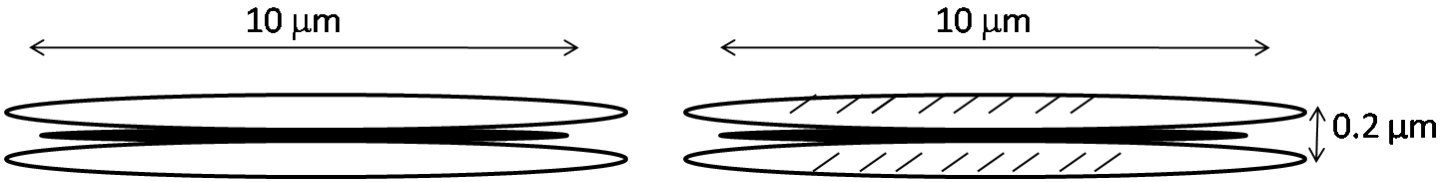

.

Figure 1.15: Schematic of upper (right)and lower bainite (left) microstructures. Particulate cementite is shown in black

Granular bainite is associated with continuous cooling transformations; it is typified by coarser packets of parallel plates, or sheaves, due to which have impinged during cooling making the structure look "granular" when using optical microscopy. Mechanistically it does not differ from conventional upper and lower bainite. However partioned carbon partly stabilizes any residual austenite, such that the microstructure of the residual austenite at the transformationam tempertaure becomes a mixture of martensite and retained austenite (at room tempertaure this is the "MA region)[6].

Alloying elements, including Nb but with the notable exceptions of Al and Co, retard the bainitic reaction depressing it to lower temperatures and leading to a greater separation of the pearlitic and bainitic reactions [6].

Martensite

The transformation is diffusionless, a process in which the structure of martensite, α', is obtained by a physical deformation of the parent austenite. It isa strain-dominated trasnformation, and when in contains carbon the martensite can be very hard [6, 38], and it usually forms at temperatures where the mobility of atoms including carbon, is limited.

Martensite/Austenite (MA) Islands

The decomposition of austenite to ferritic phases leads to the enrichment of adjacent austenitic regions by carbon, stabilising the phase. The increment in hardenability, from the carbon, affects the subsequent phase transformation, and with high cooling rates, the carbon enriched regions can form martensite, leaving residual austenite [6, 39, 40].

1.2.3 Grain size control

Alloy carbides, because of their stability at high tempertaure, have significant impact on the austentite grain size [21, 41], with a subsequent impact on hardenability [42, 43] and toughness. While niobium in solution influences the transformation temperature of austentite [44], the effects of undissolved precipitates and strain-induced precipitation remains most significant in controlling austenite grain size, by increasing the strain, at a given temperature, at which recrystallization occurs and restricting the migration of grain boundaries [20, 45].

Nucleation of precipitates

Precipitates are important in defining multipass weld microstructures via their influence on grain growth in the weld heat-affected zones that expereince temperatures in the austenite phase field [46, 47]. **Nucleation** is the formation of a second phase that should to a reduction in free energy. However, interfaces are also created so when the prticle is small, the net interfacial energy can exceed the magnitude of the volume free energy reduction due to the phase change [48]. As a consequence, the net free energy increases until the surface to volume ratio becomes small anough. The nucleus then enters a stage of continuous growth. The growth of a precipitate of critical radius is related to the interfacial energy and the driving force for transformation; which can be derived from its constituent energy terms. The free energy change for **homogenous** nucleation is based on the volume free energy change, the interfacial energy, (typically found experimentally), volumetric strain energy, and is based on thermodynamic work by Volmer and Weber [49], as well as Becker and Döring [50] and by Martin [46].

In the case of **heterogeneous nucleation** i.e. heterogeneities such as dislocations and grain boudaries are regions of higher free energy, hence when

the precipiate nucleus forms at the grain boundary or dislocation line, the associated free energy provides impetus for growth [46]. The free energy change associated with forming a particle of radius, r, in an undercooled liquid is expressed in Equation 1.5.

$$\Delta G_T = -\frac{4}{3}\pi r^3 \Delta G_V + 4\pi r^2 \gamma_{SL} \tag{1.5}$$

where ΔG_T is the total free energy, ΔG_V is the free energy change per unit volume and γ_{SL} is the surface energy.

Precipitates of alloy carbides form in a number of ways [6, 46].

1. In situ nucleation on existing precipitates or impurity particles. Niobium carbides, for example, sometimes precipitate on titanium nitride particles which form first.

2. Nucleation on dislocations occurs within the ferritic matrix.

3. Nucleation sub-boundaries or prior austentite grain boundaries as well as lath boundaries. These boundaries are also paths for solute diffusion, hence carbide nucleation is expected at these favorable sites, this is referred to as "interphase precipitation" [6].

Precipitates also occur heterogeneously at the advancing austenite to ferrite interface occur under slower cooling conditions [51, 52].

Growth of precipitates

Coarseniing or ripening is driven by an effort to minimise overall interfacial energy. Therefore, small particles dissolve preferentially due to their smaller surface to volume ratio where large particles grow although the total volume fraction is almost constant [46, 53]. There is a mass transfer from the small to the large particles driven by diffusion because the solute concentration in the matrix that is in equilibrium with a small particle is greater than with a large particle, figure 2.4.

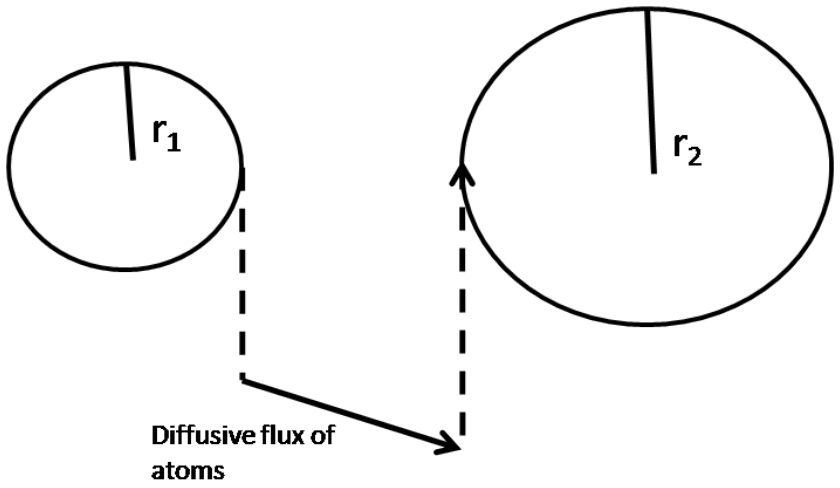

Figure 1.16: Diffusive flux results in growth of the larger precipitate at the expense of the smaller [46].

Lifshitz and Wagner developed a general theory for the bulk coarsening of a dispersion of spherical precipitates:

$$r_t^3 - r_o^3 = \frac{k}{RT} V_m^2 D\sigma t \tag{1.6}$$

where r_o is the average particle radius at $t = 0$, r_t is the average particle radius at a time, t. D is the diffusion coefficient of the solute in the matrix, σ = particle/matrix interfacial energy per unit area, V_m is the molar volume of the precipitate, and k is a constant.

Precipitation Strengthening

It has been established that an important component in thermomechanically processed HSLA steels is the dispersion of hard precipitates throughout the austenite during hot deformation. These precipiates will restrict austenite grain growth during processing, as well as contribute to strengthening due to precipiates restricting the motion of dislocations [54].The strengthening mechanisms associated with these precipitates correlates to the inter-particle spacing, λ, increases, dislocations are able to loop past the precipitate array effectively reducing the strength of the alloy, based on the relationship described by Orowan in equation 1.7.

$$\Delta\tau = \frac{2T_l}{\lambda b} \tag{1.7}$$

where $\Delta\tau$ is the increase in shear stress over a precipitate-free matrix, λ is the inter-particle spacing, b is the burgers vector and T_l is the line tension.

The effect of the precipitate size is also notable as described in

$$\tau_b = \frac{G_b}{L - 2r} \tag{1.8}$$

where τ is the shear stress, G_b is the shear modulus, $L - 2$ is the inter-particle spacing, and r is the particle radius.

Fine particles, smaller than 20 nm, and particulary smaller than 5 nm are viewed as influential in contributions to precipitation strengthening [55]. The dispersion of fine precipitates will have low inter-particle spacing, this follows from the growth of larger precipitates benefiting from the dissolution of smaller precipitates effectively increasing inter-particle distance [56, 57]

1.2.4 Niobium carbides in low alloy steels

The primary purpose of Nb in steels is to control the evolution of austenite grain size during thermo-mechanical processing, at tempertaures where the

steel is austenitic. In subsequent high-temperature processes sych as welding, NbC may tend to dissolve in the austenite that is regenerated, and precipitate during the cooling cycle. Therefore the initial distribution that forms during processing will be changed by the thermal cycles associated with welding [58]. The dispersion of NbC precipitates that form in the cooling steel, between 750℃ and 500℃, nucleate on dislocations and grain boundaries contribute to precipitation strengthening of the steel [6].

Titanium nitrides

In the presence of Ti, nitrogen that has been added to steel as a solid solution strengthener, can form TiN which is at typical concentrations more stable in austenite relative to NbC [6]. NbC precipitation generally follows that of TiN so that the latter can act as a nucleation site for the former (figure 1.17) on TiN cuboids.

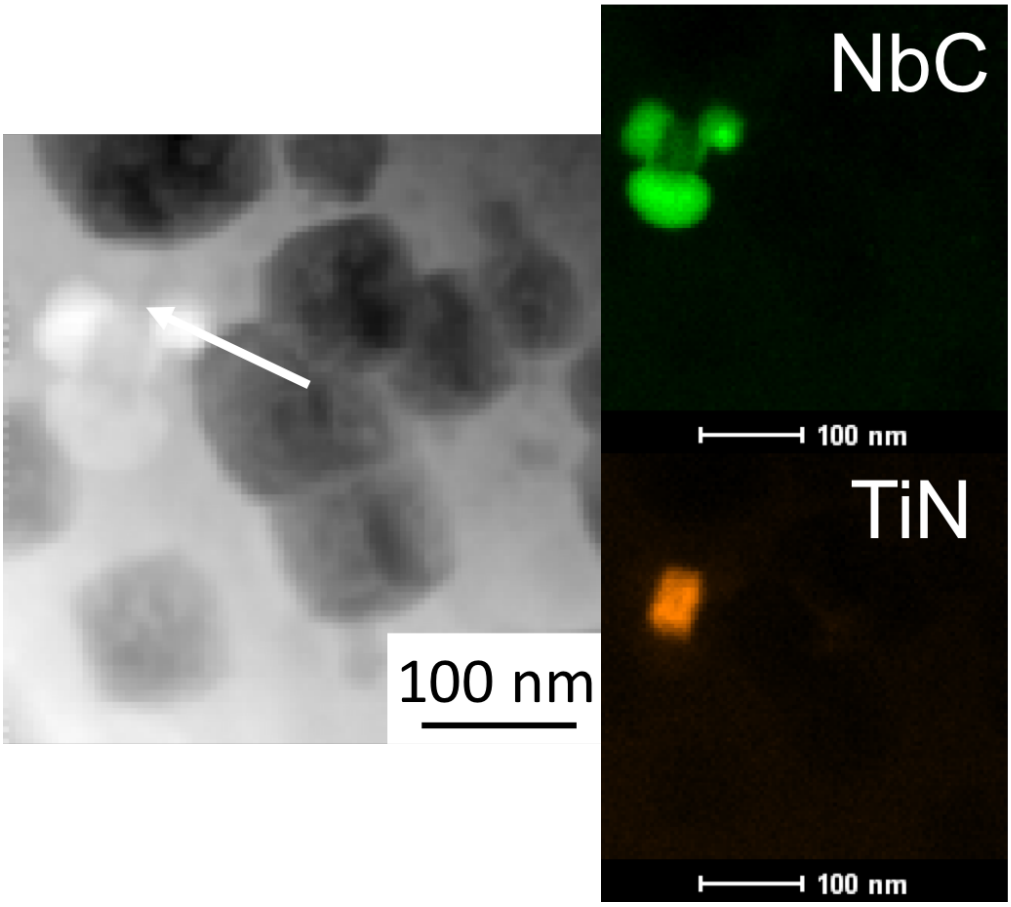

Figure 1.17: NbC precipitated on a TiN precipitate, from this work.

1.2.5 The effect of niobium in solution

While niobium precipitates are critical to austenite grain refinement, niobium in solution influences transformation start temperatures. Okaguchi reporting a reduction in the Ar_3 tempertaure with dissolved niobium concentration [59]. This effect has been used in the production of thermomechanically processed plate in older rolling mills that are incapable of exerting the loads required for hot deformation of austenite at low temperatures, with processing occurring at temperatures in excess of 1200 ℃ [60, 61]. The steel contains less than 0.05 wt% carbon at less than 0.05 wt%, and around 0.1 wt% niobium. The increased hardenability due to dissolved niobium permits a fine bainitic microstructures to be achieved over a large range of cooling rates. Dissolved niobium also retards recrystallisation and recovery of austenite during thermomechanical processing. [62, 63].

The effects of precipitated NbC and dissolved niobium on transformation temperatures are not independent of the other [64]. The primary role of nioium appears to be in retarding the nucleation rate of allotriomorphic ferrite on austenite grains, with limited effect on the bainite reaction [65, 66]. Separate work by Ouchi and Enomoto show a reduced nucleation rate due

to the segregation of niobium at the γ/γ interface, reducing the interfacial energy, and thus, the potency of these as sites for heterogeneous nucleation [67, 68]. However, since other alloying elements like Mn, Si and P also segregate to these boundaries, the influence of dissolved niobium cannot be isloated [69]. The kinetics of transformation of austenite to allotriomorphic ferrite was delayed to a greater extent than that associated with the bainitic transformation for isothermal heat treatments when comparing a Nb-containing steel as opposed to an Nb free steel of the similar composition [65, 70]. This effect is illustrated in figure 1.18.

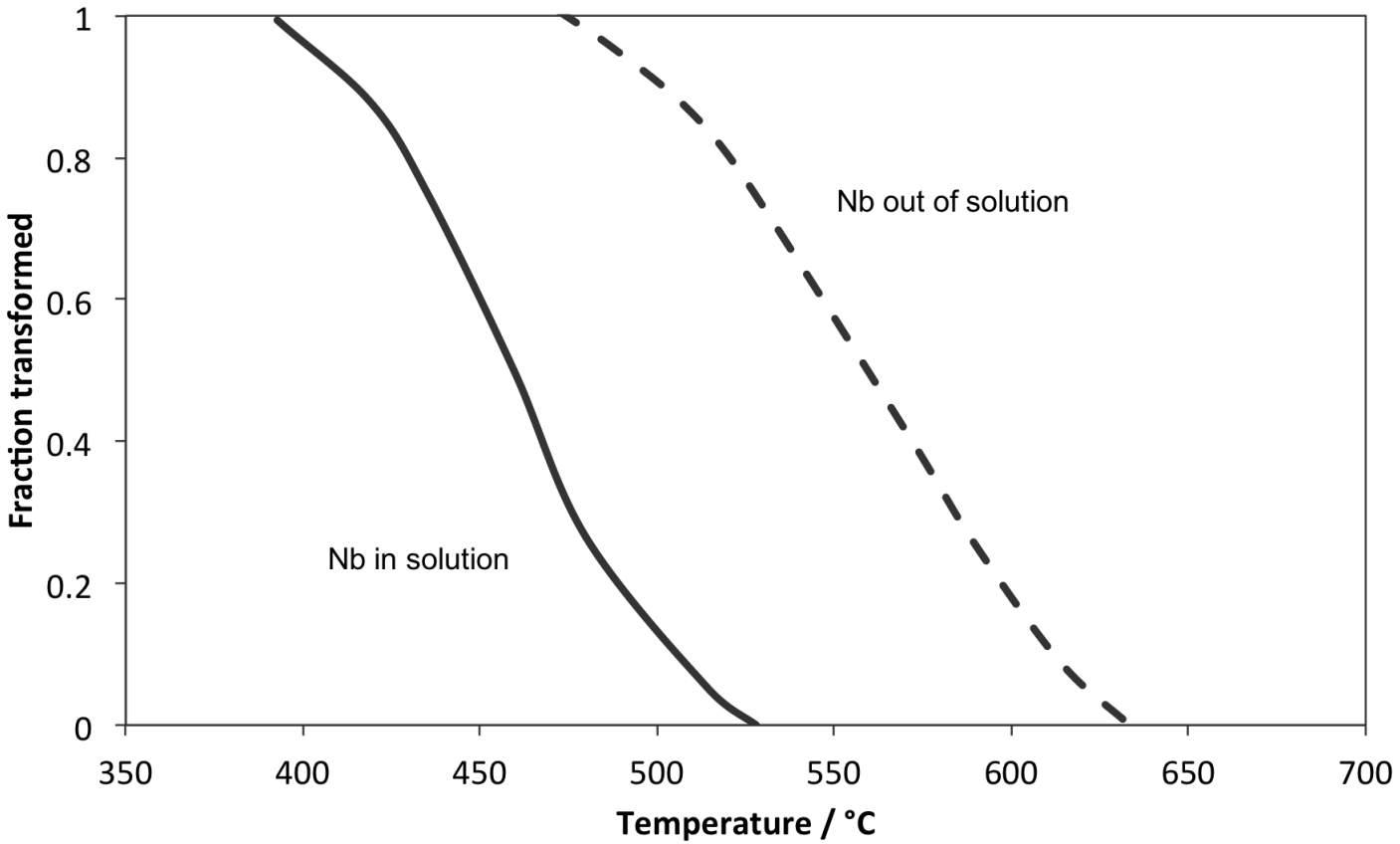

Figure 1.18: Influence of niobium on austenite decomposition and transformation in a 0.034 wt% niobium-microalloyed X80 steel cooled from 1350 °C at 30 °C s^{-}1 after [71].

The increase in hardenability due to niobium is unlikely to be related to improving the stability of austenite, based on work by Yeo which shows the reduction in M_s with increasing Nb from 0.05-0.8 wt%, but with an increase in M_s at concentrations less than the lower bound [72].

Hanazaki *et al.* refer to a solute-drag effect which occurs the solute partitions to a moving interface to reduce the interfacial free energy [73, 74]. There is, however, no established theoretical framework for this proposed phenomenon. Bhadeshia shows that in the α/γ interface, the drag effects due to the paritioning of niobium is unlikley [75] due to the much larger diffusion coefficient of niobium in austenite (as compared to that of iron) [52, 76].

Yan and Bhadeshia have most recently proposed that the retardation of allotriomorphic ferrite formation is related to the reduction in the γ/γ interfacial energy [77]. The final microstructures transformed into a mixture of bainite and martensite across most cooling conditions from 1260 ℃, where most of the niobium is in solution, as illustrated in figure 1.19, while lower temperature heat treatments, at 960 ℃ showed the formation of allotriomorphic ferrite across similar cooling rates. Figure 1.20 shows that the influence on on hardenability is revealed at a constant austenite grain size, by

comparing the relative reduction in transformation temperature for different amounts of niobium in solution for a a similar prior austenite grain size in figure 1.20 [77].

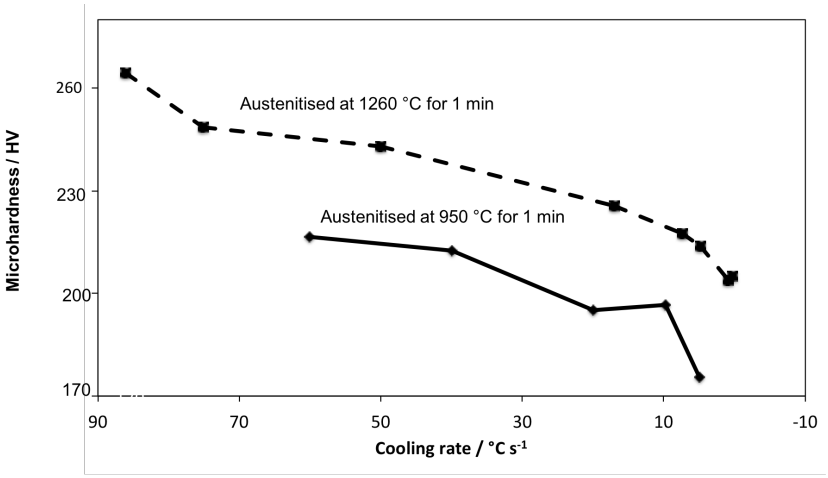

Figure 1.19: Hardness values of continously cooled samples, after Yan and Bhadeshia [77].

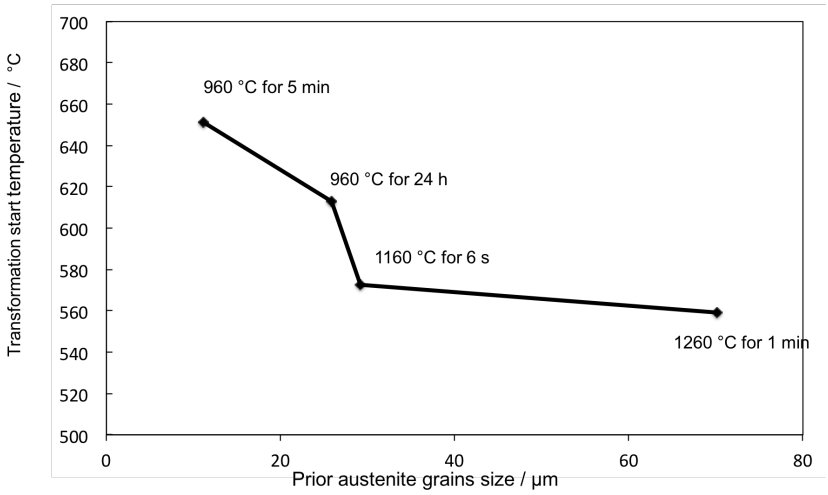

Figure 1.20: The relationship between transformation temperature and prior austenite grain size in X80 (0.095 wt% Nb - 0.05 wt% C) steel after different austenitising heat treatments, followed by cooling at 20 $^{\circ}\mathrm{C\,s^{-1}}$. The prior austenite grain size is similar for the steels heat treated at 960 °C for 24 h and 1160 °C for 6 s, with a reduction in transformation tempertaure with increasing austenite grain size, after Yan and Bhadeshia [77].

1.2.6 Microstructure of X80 steels

Due to the very low carbon content of conventional X80 steels, and the fine scale of the related microstructure, interpretation has been challengin. Work by Yan and Bhadeshia shows it to be mainly bainite, which forms between 500 °C to 600 °C [78]; thin bainitic ferrite plates separated by austenite

films,as shown in figure 1.21. In line with the theory that has been presented in this review, the kinetics of transformation are depressed following austenitisation at high temperatures where the austenite grain size is large, as is the amount of niobium in solution, figure 1.22.

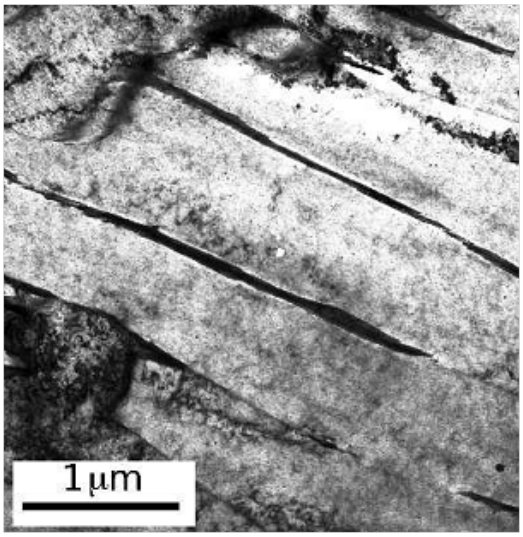

Figure 1.21: Transmission electron micrograph of X80 steel showing bainite microstructure [78].

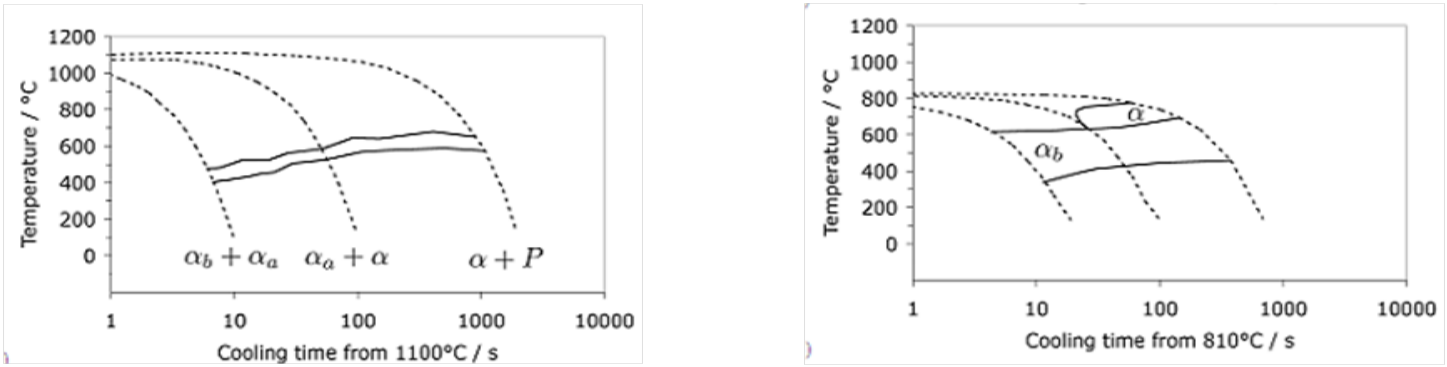

(a) **(b)**

Figure 1.22: The continuous cooling transformation diagrams for X80 steels, showing the kinetics associated with a high austenitisation temperature and (a) a lower austenitisation temperature for 40% deformed austenite prior to transformation [78].

	Pipe body / MPa	Weld / MPa
Yield strength $R_{0.5}$	555-705	-
Tensile strength $R_{0.5}$	625-825	625 min.

Table 1.2: Strength of welded X80 pipe (as per product specification in ISO3183:2007). The value for the yield strength is obtained at 0.5% total extension of the sample [78].

Composition and mechanical properties

The composition of X80 steels is defined by the American Petroleum Institute:

Grade	C	Mn	P	S	Nb+Ti+V
X80	0.22	1.85	0.025	0.015	0.15

Table 1.1: American Petroleum Institute specifications in maximum wt% for common grades of pipeline steel [78].

The typical commercial strength for these steels ranges from 700-750 MPa, with the API setting the required yield strength for this class of steels:

1.2.7 Submerged arc welding

Achieving a balance between plate strength and weldability in developing X80 steels has been a significant consideration during the alloy design [79], including the identification of metallurgically appropriate and economic welding procedures. While linepipe welding includes manufacturing and field welding, for the purposes of this work, the focus will be on fabrication by high productivity submerged arc welding (SAW). Typical welding equipment for external and internal welding of pipeline sections is illustrated in Figure 1.23.

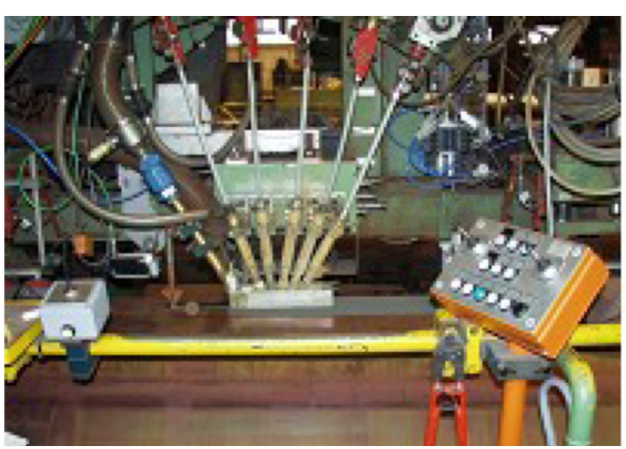

(a)

(b)

Figure 1.23: (a)Welding heads for external welding, the heads are oriented above the pipeline and (b)internal welding where the welding heads are oriented just above the lower part of the pipe interior [80]

An electric arc is used to heat and melt a metal electrode and supply the molten metal in figure 1.24. Typically, two−pass welding is used, with the initial pass along the interior of the pipe. Penetration through the thickness of the steel is achievable from a single pass for typical pipeline steel grades. The welding electrode travels along the joint line, with fusion occurring where the electrode is closest to the base material. This weld pool solidifies to create the joint. The heat-affected zone, which identifies the material that is influenced by the heat input from the welding process but not melted is shown in figure 1.24. This is a repeatable, high productivity (automated) welding solution [81].

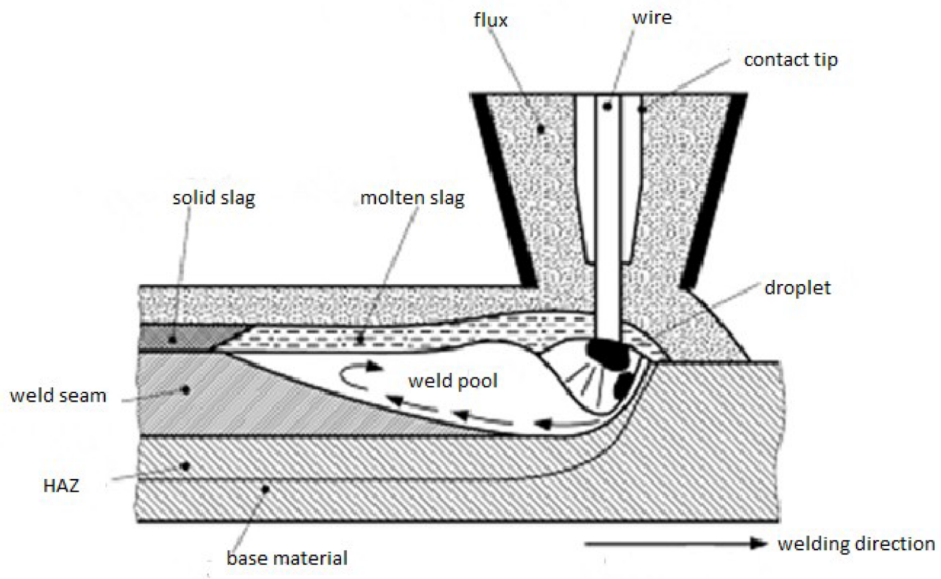

.

Figure 1.24: Illustration of submerged arc welding process [80]

Weld microstructures

A generic cross-section of a 2-pass submerged arc weld, etched to show the distinct heat-affected zone in proximity to the fused region is shown in Figure 1.25. The weld pool solidifies to form δ-ferrite which the transforms into austenite, and back into ferrite as cooling continues. The δ-ferrite has a columnar grain structure typical of solidification, which is inherited by the austenite as it grows in the solid state from the δ-ferrite parallel to the direction of heat flow. The columnar austenite grain size influences the nucleation

rate of allotriomorphic ferrite so coarse-grained weld deposits have a higher hardenability [6].

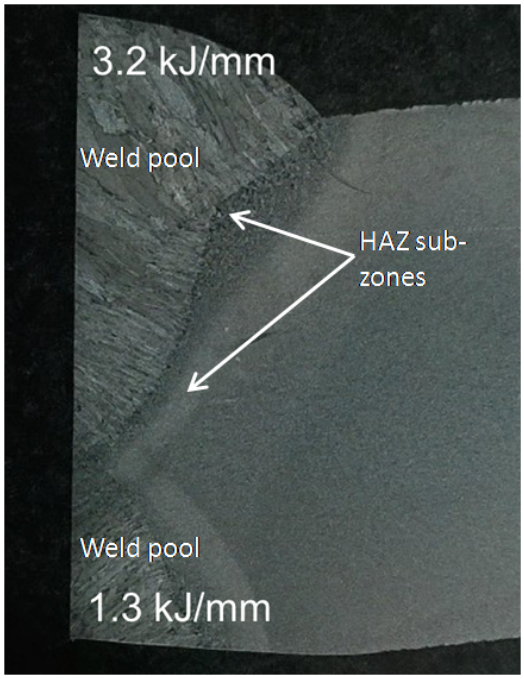

Figure 1.25: Typical weld seam with 2 passes. The first pass is along the interior of the pipeline at the lower heat input of 1.3 kJ/mm , with the second pass at a higher heat input of 3.2 kJ/mm along the external surface of the pipe, (this work).

The evolution of the microstructure in the weld and adjacent fusion zone is also affected by fluxes or gas shrouds that are used to reduce the environmental attack on the hot weld metal; this does not wholly protect the weld, leading to a high oxide content in the weld as compared to typical wrought

steels, table **??**. These oxide particles remain in the fusion zone during the solidification process, acting as heterogeneous nucleation sites and therefore have a significant influence on the subsequent evolution of microstructures. The **primary** microstructure obtained directly from solidification is composed mainly of allotriomorphic ferrite, Widmanstätten ferrite, and acicular ferrite. The manufacture of linepipe by SAW includes a second pass that results in further exposure of the underlying primary microstructure to thermal cycling generating a 'secondary' microstructure [6].

Composition / wt%	C	Mn	Si	Cu	Al	N	O
Plate	0.21	1.0	0.2	0.05	0.04	0.01	0.004
Wire	0.014	1.5	0.2	0.31	0.01	0.01	0.001
Weld	0.016	1.1	0.3	0.16	0.01	0.01	0.053

Table 1.3: Comparative chemical compositions of welded sections [6].

Microstructural evolution in the heat-affected zone

There is a gradient of affected microstructures in the heat-affected zone refelcting the variation in cooling rate due to heat depositied during welding this is illustrated in figure 1.26. The zones vary in width as a function of heat input, chemical composition of the base metal, and the cooling rate associated with the welding parameters [82].

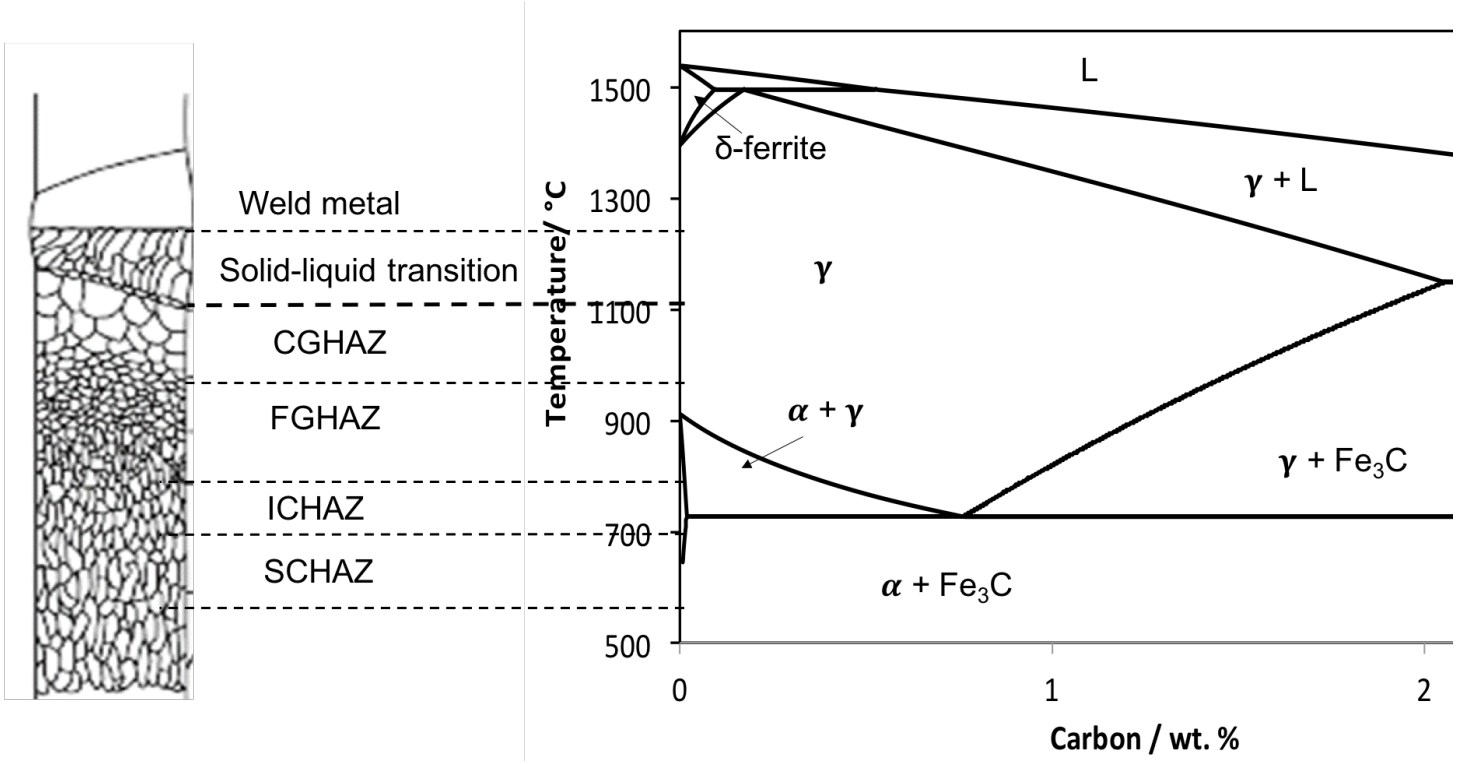

Figure 1.26: Sections of the HAZ and fusion line, with related temperature ranges in the Fe-C phase diagram after [83]

	Sub-zone
CGHAZ	Coarse-grained HAZ
FGHAZ	Fine- grained HAZ
ICHAZ	Inter-critical HAZ
SCHAZ	Sub-critical HAZ

The highest peak temperatures close to the fusion zone lie between the Ac_3 and the dissolution temperature of alloy carbides leading to reduced grain boundary pinning and related austentite grain growth [84], at the coarse-grained heat affected zone, CGHAZ. At the high cooling rates that are typical of pipeline welds, and coarse austenite grains, the promotion of low temperature products like lower bainite and martensite are an undesirable risk, which can lead to low weld toughness and increased hydrogen cracking risks [85]. This usually is mitigated by reducing the amount of carbon as shown in figure 1.27 . The fine-grained heat affected zone, FGHAZ, is above the Ac_3 temperature such that full austenitsation occurs, in the presence of alloy carbides [86]. Partial austenitisation in the inter-critical coarse grain heat- affected zone, ICHAZ, is associated with coarse bainitic microstructures with regions of carbon-enriched MA islands [87, 88]. Away from the fusion zone, peak temperatures are below the A_{c3} and no phase transforma-

tion occurs, with tempering dominating the thermal effects in the sub-critical heat affected zone (SCHAZ) [58].

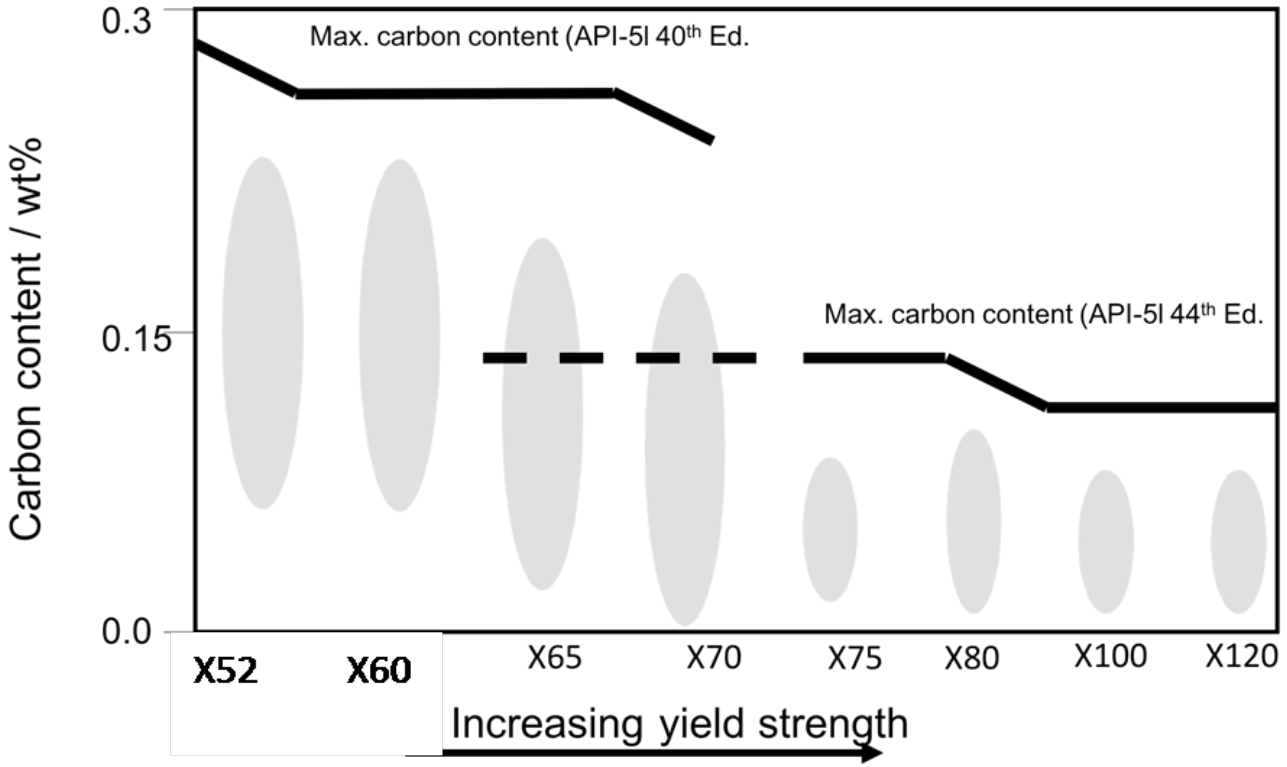

Figure 1.27: Relationship between carbon content and yield strength for different grades of commercial pipeline steels after [58].

1.2.8 Niobium in the heat-affected zone

Martensite-austenite constituent

The CGHAZ tends to be the focus of most investigations because of its coarse austenite grain structure which can be detrimental to properties [82]. In particular, martensite-austenite mixtures described earler can be egenrated leadint to low toughness. Aihara et al. show that toughness decreases as the proportion of martensite (increases in the local brittle zones increased) [89]; this data proposed a minimum in the toughness as a function of martensite fraction [90]. At the high temperatures involved in the welding process, most of the alloying elements will enter into solid solution in the region close to the fusion boundary. This can lead to hard brittle martensite after transformation, either as a major component of the microstructure or in the form of MA regions [87].

While the role MA islands remains debatable, the low carbon niobium microalloyed steels are likely to form only small amounts of brittle MA constituents [91]. However, a variation in the carbon content from 0.04 wt% C to 0.08 wt% C in a Nb-microalloyed steel (at constant niobium content) led to a higher hardness in the HAZ [92], although the increment in hardness

was moderate at around 20 HV.

Precipitates in the heat-affected zone

The multi-pass welding of Nb microalloyed steels show that the initial microstructure has not revealed effects of the repeated heat input on the HAZ microstructures [92]. Niobium decreases the size of bainitic packets, such that an increase in niobium content from 0.07 wt% to 0.10 wt%, with carbon at 0.04 wt%, leads to an improvement in yield strength [93]. These results appear to be independent of the prior austenite grain size, and localised hardenability in the HAZ [93].

An analysis of the precipitate sizes by transmission electron micrscopy, reproduced in figure 1.28 shows that a similar fraction of NbC precipitates in the steels do not completely dissolve in the HAZ and can pin the austenite grain boundaries[93].

The authors predict that during cooling after welding small and Nb-rich particles should precipitate, however this has not been shown experimentally [93].

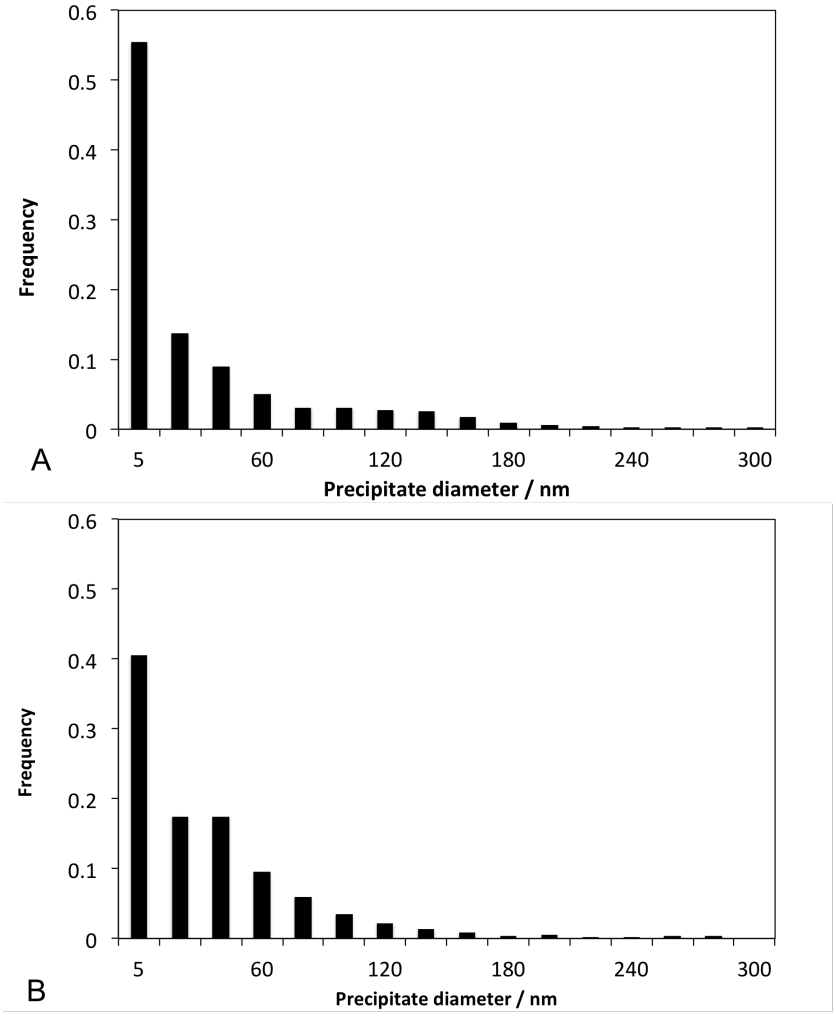

Figure 1.28: (A) NbC precipitate size distribution for 0.07 wt% niobium - X80 pipeline steel, average precipitate size is 57 nm. (B) Precipitate size distribution for 0.10 wt% niobium - X80 pipeline steel, the average precipitate size is 16 nm [93]

NbC has usually been characterised using transmission electron microscopy

[55, 93], but this necessarily limits the total amount of material that can be analysed given the magnifications involved. This limits how representative the analysed sample is of the bulk material [94].

1.3 Summary of literature review

HSLA pipelines have been subjected to considerable scrutiny, with many studies focussing on the behaviour of niobium during TMCP as well as during the production of welded pipeline sections. The influence of niobium in microalloyed steels can be summarised as follows [21, 42, 93, 95]:

1. Precipitates of titanium and niobium are used to control grain size through Zener pinning .

2. Niobium carbide also exerts an influence on the austenite grain size in the heat-affected zone through the same mechanism.

3. Solute niobium affects hardenability by retarding allotriomorphic ferrite formation.

4. Niobium carbides contribute to mechanical properties through precipitation strengthening.

There are two distinct contributions to structure-property relationships that are subject to scientific analysis; that of niobium precipitates and solute niobium to the evolution of steel microstructures in the heat-affected zone. There is an added complexity introduced during the welding process where the distribution of niobium between precipitates and solid solution will change in the vicinity of a welded joint, along with significant changes in microstructure. While there has been significant work done on characterizing the effects of solute niobium in the HAZ using simulations [4, 96, 97], there is paucity of empirical analysis of the evolution of HAZ microstructures due to the empirical impact of differing populations of alloy precipitates, and the correlated concentrations of solute niobium.

The work presented in the subsequent chapters to break new ground by utilising advanced characterization techniques to measure the evolution of structure-property relationships by varying precipitate populations and the associated concentrations of solute niobium in the HAZ sub-zones of niobium-microalloyed pipeline steels. The aim is ultimately to express the observations into quantitative modes that exploit phase transformation theory and structure−property relationships.

Chapter 2

Experimental methods

2.1 Introduction

The X80 steel, manufactured using high-temperature processing or HTP, under consideration contains an exceptionally large concentration of Nb at 0.1 wt%, table 2.1, with calculations that show about 35% of the Nb remains in solution, [98] with the rest precipitating Ṡince two concepts were to be tested, the steel plates were heat treated following practice reported elsewhere [4, 99]. The variety of heat treatments implemented different proportions of precipitated and dissolved Nb so that the influence of the proportion on structure following welding could be dissolved. The methods address the following concepts:

- The influence of niobium, whether in solution or in precipitates, on the development of gradients of structure and properties in the weld heat-affected zone.

- The specific effects of niobium in the coarse-grained heat-affected zone where mechanical properties are most likely to be compromised.

The designed heat treatments achieved both of these requirements, enabling study of the sub-zones of the HAZ through direct analysis and characterization of the heat treat plates and the development of different niobium distributions in the steel plates which could subsequently be welded to develop a HAZ for further characterization of the influence of the different niobium configurations on the formation of HAZ sub-zones.

2.1.1 Materials

The composition of the API X80 line pipe steel used in the Cheyenne Plains Pipeline, supplied by the industrial sponsor, CBMM is listed in table 2.1. The plates of steel were supplied in sections of $500\,\text{mm} \times 300\,\text{mm} \times 15\,\text{mm}$.

C	Mn	P	S	Si	Cu	Ni	Nb	Al	Cr	Ti	N	Ca
0.05	1.55	0.012	0.002	0.12	0.24	0.13	0.095	0.037	0.23	0.011	0.0033	0.0012

Table 2.1: Composition of the supplied Cheyenne Plains X80 Steel /wt%

Design of Heat Treatments

The range of heat treatments, defined by thermodynamic calculations, figure 2.1 and from literature [4, 99], were designed to alter the initial state of the steel prior to deposition of the welds is listed in table 2.2.

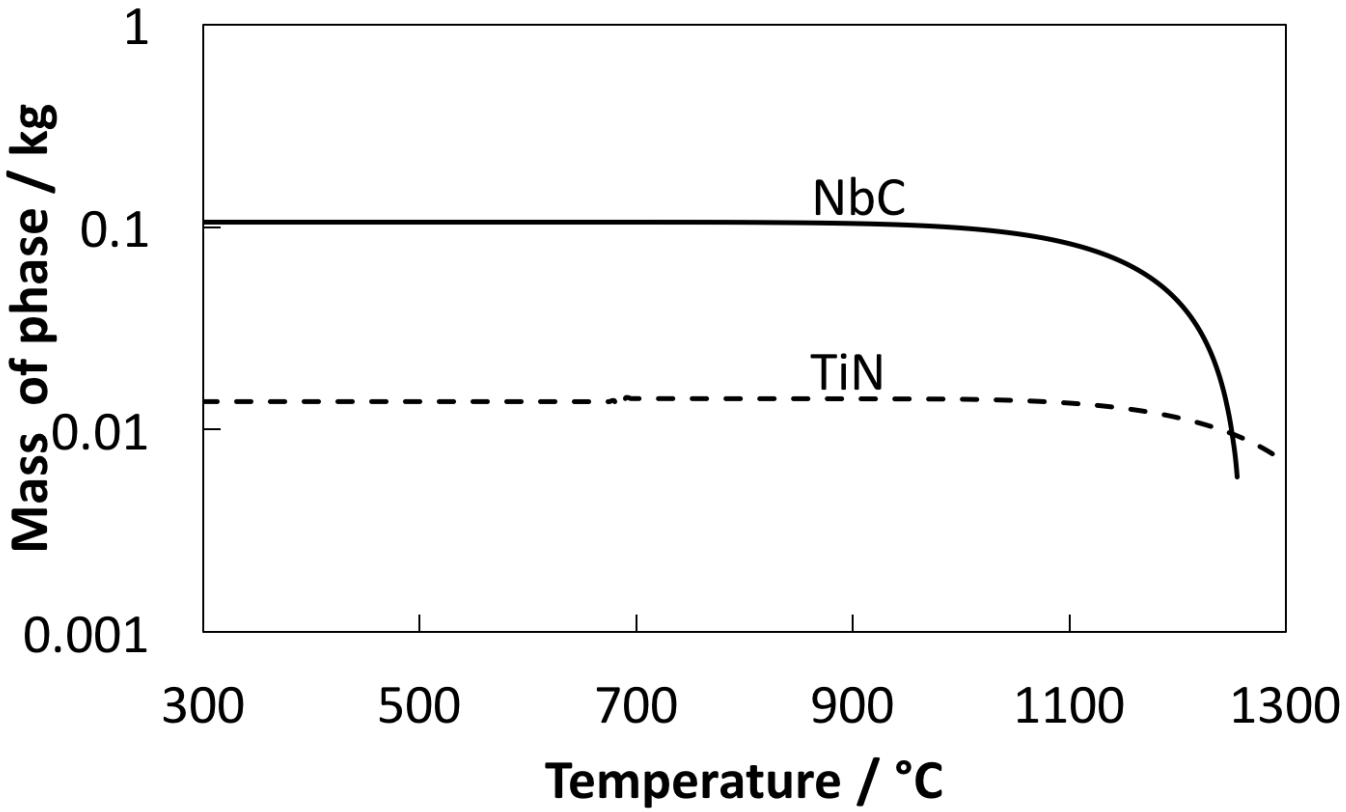

Figure 2.1: Thermodynamic modelling data from MTDATA showing dissolution temperature of TiN and NbC.

Plate identification	Heat Treatment	HAZ sub-zone
X80	As received X80	BM
X80T	Tempered at 650 ℃ for 1 h	SCHAZ
950N	Normalised from 950 ℃ for 1 h	ICHAZ
950NT	Normalised from 950 ℃ for 1 h, tempered at 650 ℃ for 1 h	ICHAZ
1100Q	Held at 1100 ℃ for 1 h and water quenched	CGHAZ
950Q	Held at 950 ℃ for 1 h and water quenched	CGCHAZ
1230Q	As received X80, held at 1230 ℃ for 1 h and water quenched	CGHAZ
1230QT	As received X80, held at 1230 ℃ for 1 h and water quenched, tempered at 650 ℃ for 1 h	CGHAZ
1100QT	As received X80, held at 1100 ℃ for 1 h and water quenched, tempered at 650 ℃ 1 h	CGHAZ

Table 2.2: Design of heat treatments.

Controlled heat treatments were carried out in commercial furnaces at Special Steels Ltd. in Sheffield, UK. Contact thermocouples were used to monitor the thermal profiles in the steel plates, reproduced in figures 2.2 to 2.5:

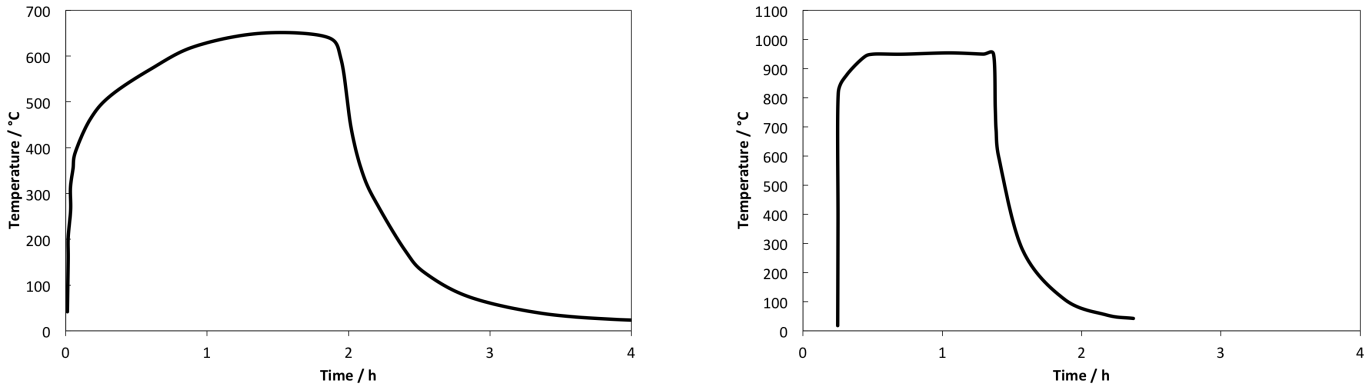

(a) **(b)**

Figure 2.2: (a)As received X80, tempered at 650℃ for 1 h. (b)As received X80, normalised from 950℃ for 1 h.

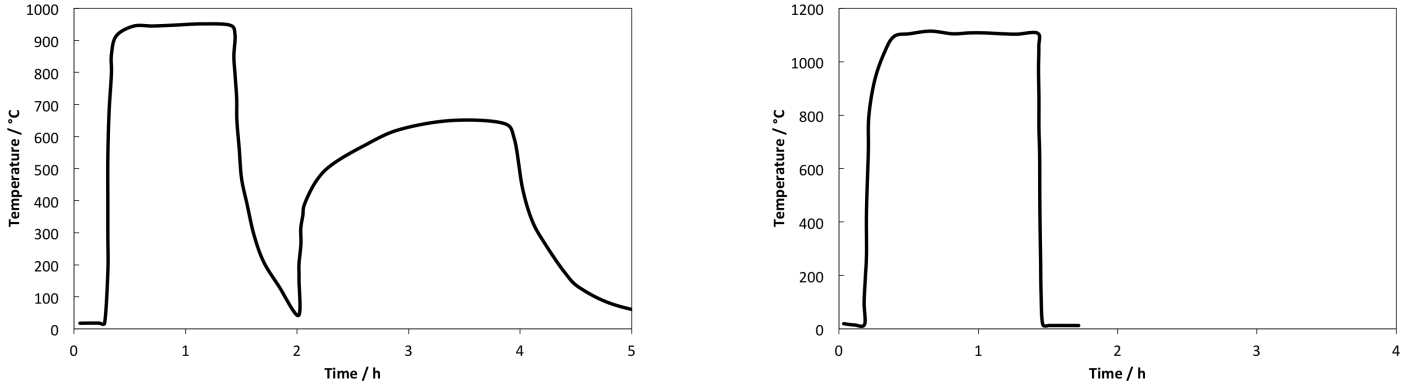

Figure 2.3: (a)As received X80, normalised from 950 ℃ for 1 h, tempered at 650 ℃ for 1 h. (b)As received X80, held at 1100 ℃ for 1 h and water quenched.

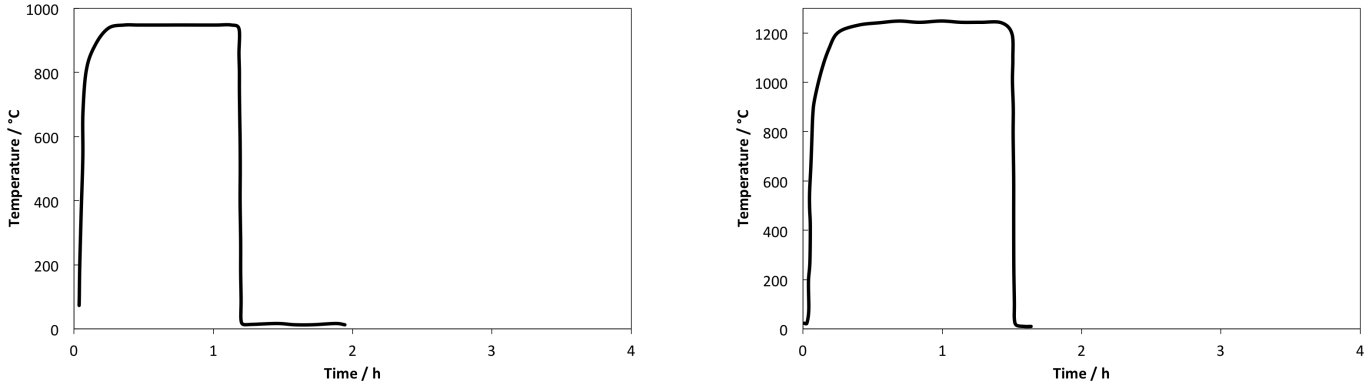

(a) **(b)**

Figure 2.4: (As received X80, held at 950 ℃ for 1 h and water quenched. (b)As received X80, held at 1230 ℃ for 1 h and water quenched.

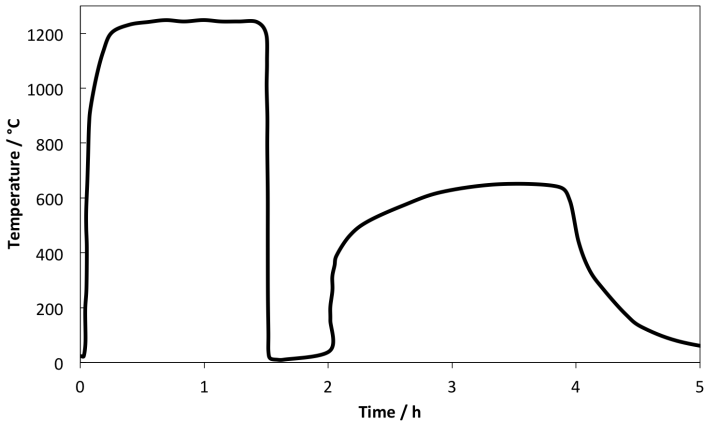

Figure 2.5: As received X80, held at 1230 ℃ for 1 h and water quenched, tempered at 650 ℃ for 1 h.

2.1.2 Submerged arc welding of plates

Sections of heat treated plates detailed in Table 2.2 were submerged arc welded at Tata Steel UK Swinden Technology Centre. The plates were tack welded in the configuration noted in Figure 2.7, such that 2 discrete tack welded panels were manufactured. Each panel was then submerged arc-welded with 2 passes, the first pass had a heat input of 1.3 kJ/mm, and the second with a heat input of 3.2 kJ/mm. There were no tack welds within 100 mm of the joint. Figure 2.6 shows the tack-welded plate assembly. An etched cross-section of a completed weld is shown in Figure 2.8.

Figure 2.6: Plate assembly on welding table with joint submerged in flux prior to second pass.

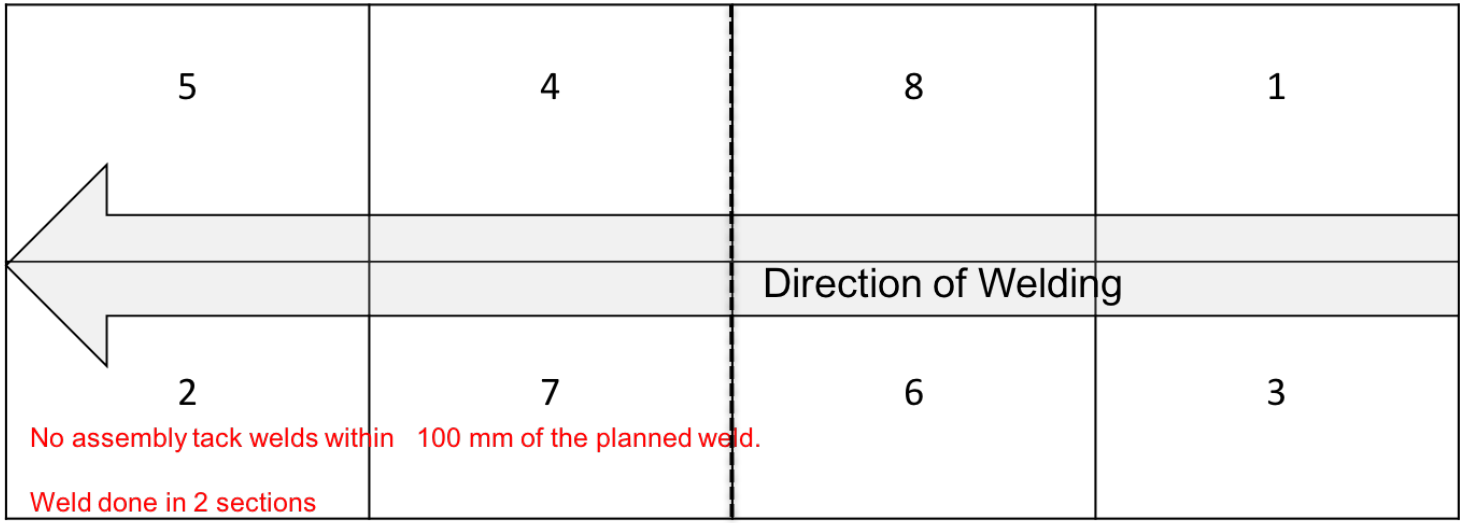

Figure 2.7: Assembled weld panel; the panel was welded in two sections.

An Oerlikon OESD3 welding wire was utilized with OP 122 agglomerated fluoride basic SAW flux. The compositions are shown in Table 2.3 and Table 2.4.

C	Mn	Si	S	P	Ni	Cr	Mo	Cu
0.117	1.71	0.266	0.005	0.009	0.016	0.024	0.002	0.05

Table 2.3: Composition of welding wire (wt%)

CaF_2	CaO+MgO	Al_2O_3	SiO_2 + TiO_2
25	40	20	15

Table 2.4: Composition of OP12 Flux (Wt%)

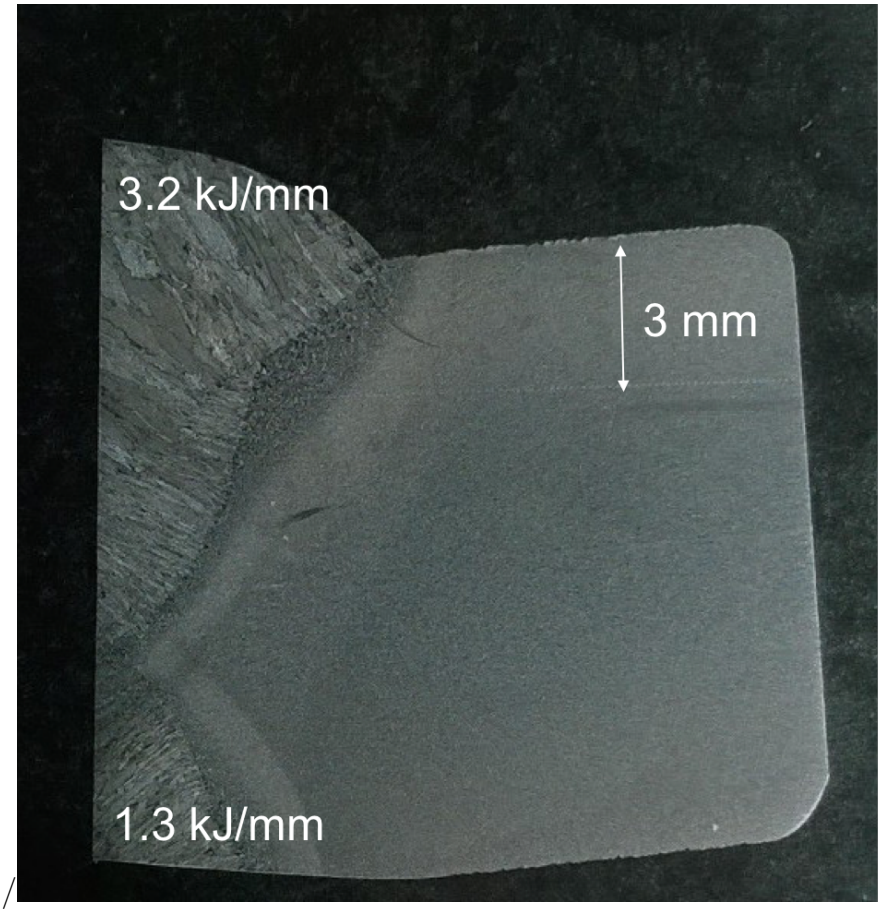

Figure 2.8: Section of welded sample showing profiles of high and low heat input passes.

2.1.3 Microstructural observations

Metallography

Sections were removed from individual plates, and mounted in conductive bakelite as in Figure 2.8, before polishing to a 1μm finish. The steel was then etched in a 2% nital solution. Optical microscopy of was conducted using a Zeiss-Axiotech optical microscope with attached QImaging MicroPublisher 3.3 RTV camera up to a maximum magnification of 500×.

Thermal etching

Cylindrical samples of 12 mm × 8 mm, as in figreure 2.9, were machined from the as-received X80 steel plate by electrical discharge machining, with a 3 mm × 12 mm flat strip ground and polished to a 1μm finish, as in figure 2.9. Thermal etching was carried out using a Thermecmastor thermomechanical simulator (Thermec), in which samples were austenitised under vacuum and quenched. The thermal etching process reveals austenite grain boundaries by the the surface tension driven grooves that form where the boundaries meet the surface [100]. Three samples of X80 steel were individually held at 950 ℃, 1100 ℃ and 1230 ℃ for 1 h prior to quenching using helium gas.

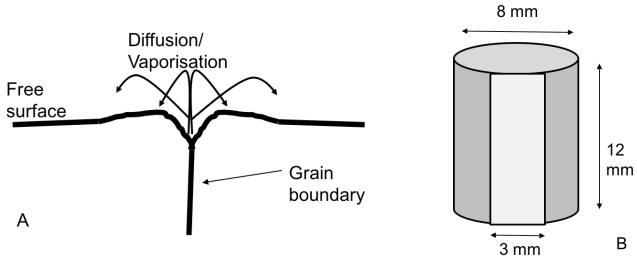

Figure 2.9: (A) Grooves form at the intersection of a free surface and a grain boundary [100]. (B) Schematic of a Thermecmaster sample prepared for thermal etching.

Grain size measurements

The ImageJ image analysis software was used to characterise the grain intercept distributions [101] after thermal grooving. The software computes the area in pixels of enclosed areas (determined by image contrast). ImageJ allows measurement of grain sizes by a user-defined scale. For statistically meaningful results, sufficient counts were collected until the maximum error became 5% [102].

2.1.4 Mechanical testing

Tensile testing

Tensile testing was carried out on an Instron LCF machine with a 100 kN load range. Samples were machined to comply with ASTM E8Mthe 0.2% proof stress , the ultimate tensile strength and the elongation were measured. Testing was done at room temperature, with a cross-head speed of 0.1 mm/min.

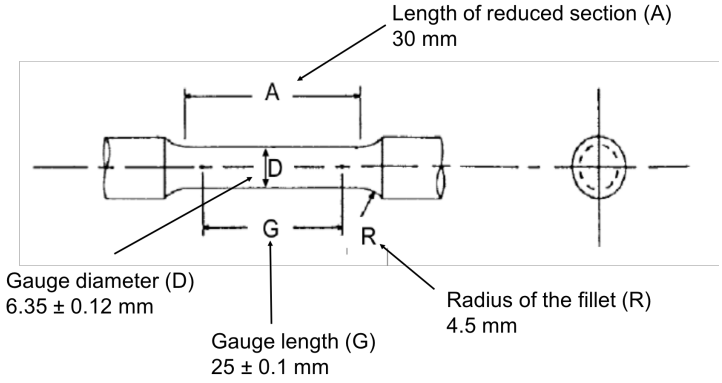

Figure 2.10: Dimensions of the ASTM E8M tensile specimen.

Hardness measurements

Hardness testing was carried out using an Qness Q10 Automatic testing machine in Vickers testing mode. The base metal was tested using a 10 kg

load, with a minimum of 3 measurements. The average of the measurements, quoted as a mean and its deviation.

Hardness measurements across the heat-affected zone were taken 3 mm below the plate surface for the second pass as in Figure 2.8, and 2 mm below the plate surface for the first welding pass. A series of measurements was taken across the heat-affected zone as shown in figure 2.11.

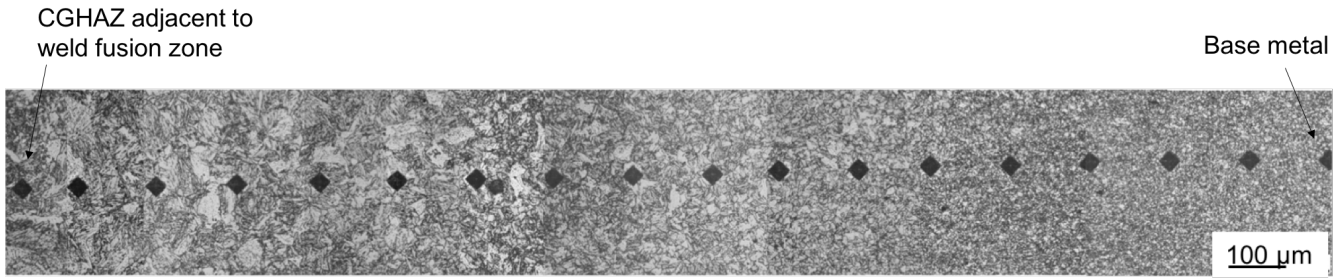

Figure 2.11: A composite image of vickers hardness indentations using a 0.3 kg weight, taken across the heat-affected zone and into the base metal of as-received X80 plate.

Hardness entropy

A method has been developed by Sugden and Bhadeshia to represent the heterogeneity of microstructure, so that it can be related to to the degree of scatter in toughness [103]. Scatter should be at a minimum for a homogeneous microstructure. This method was applied to the hardness measurements taken across the heat-affected zone with the combined data divided into 12 groups or bins of consistent size. The number of bins and their size is user defined in line with the amount of data that is available for analysis.

The number of bins, 12, was defined by the hardness values ranging from <180 HV to >280 HV, in 10 HV steps. The microstructural heterogenity is expressed as an 'entropy' because the equation follows the same as a configurational entropy, but it is expressed here that the analogy is purely coincidental, the term implying non-uniformity in the micrsotructural informaion:

$$entropy = \sum_{i=1}^{12} = -x_i \ln x_i \tag{2.1}$$

where x is the fraction of hardness values in a particular bin and i is the bin number.

2.1.5 Heat treatments

Tempering

Tempering heat treatments were carried out in a Carbolite rapid heating RHF 16/3 box furnace. Samples measuring 3 mm × 3 mm × 10 mm were extracted from the heat-treated plates, 1100Q, 950Q and 1230Q as summarised in Table 2.2. The tempering treatments are summarised in Table 2.5.

Tempering temperatures	Time / min
450 ℃	15
500 ℃	15
650 ℃	15
800 ℃	15

Table 2.5: Tempering heat treatments.

Dilatometry

Dilatometry measures the dimensional changes during the course of phase transformations in samples undergoing heat treatments [104]. The offset method is used [105] to define transformation temperatures,from dilatometric data, consistent also with the analysis by Yan [78].An applied example is shown in figure 2.12.

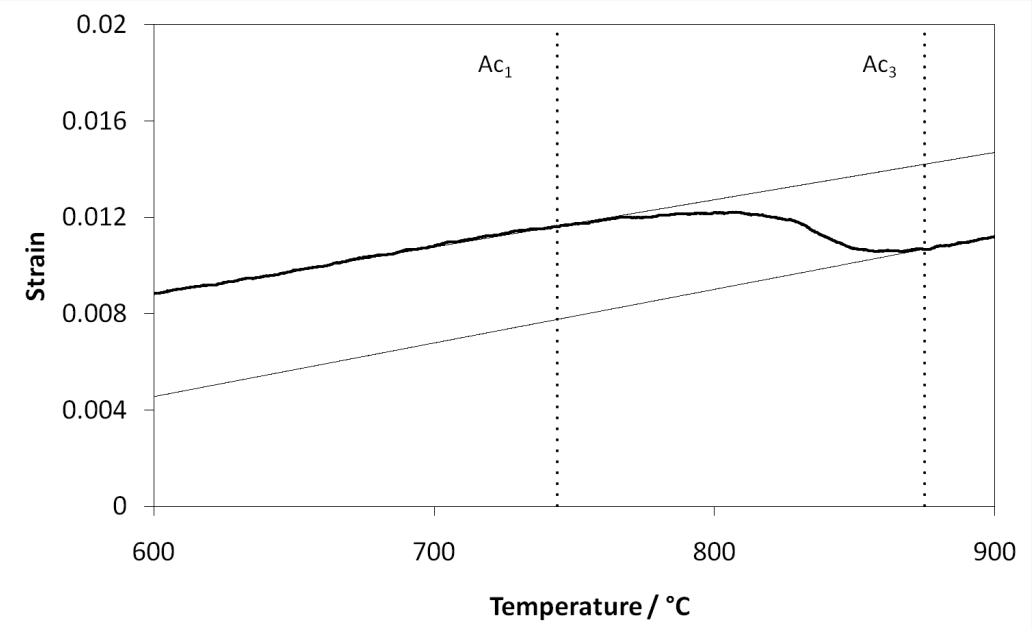

Figure 2.12: An application of the offset method used to calculate the transformation start and finish temperatures during an austenitisation experiment in this work.

Dilatometric measurements were carried out using, a TA Instruments DIL805A/D dilatometer (figure 3.6) and a Thermecmaster thermomechanical simulator, both with high purity compressed helium utilised as the cooling medium during quenching. In the former the samples DIL805A were 3 mm × 10 mm rods, while the simulated samples are as shown in figure 2.9B.

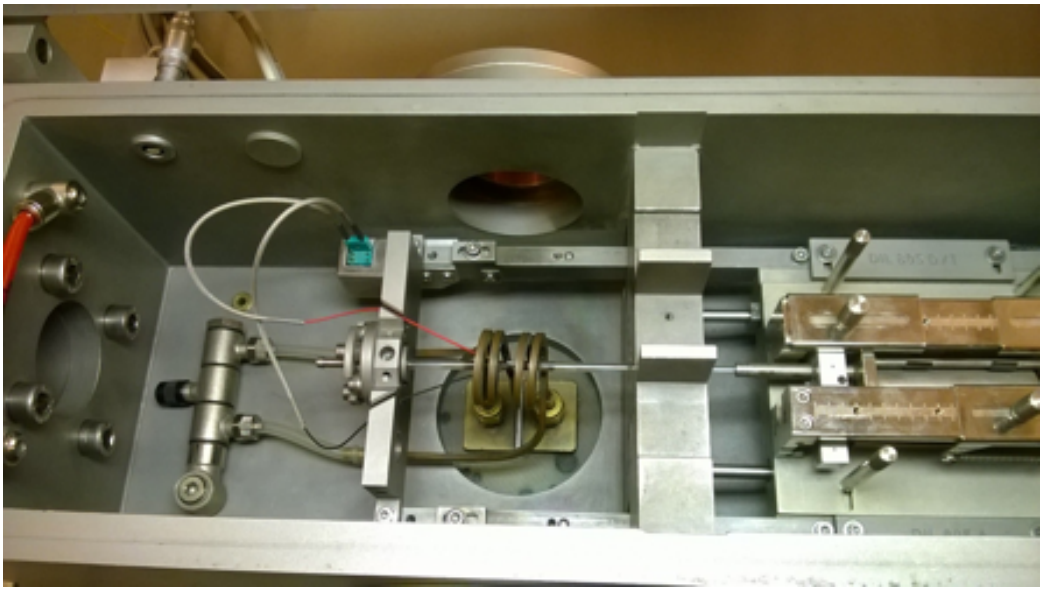

Figure 2.13: DIL805A/D internal configuration. The sample, a 10 mm long rod, with a 3 mm diameter, is held between push bars in the heating coil.

2.1.6 Thermodynamic modelling

Thermodynamic calculations were carried out to estimate the phase equilibria during heating using the National Physical Laboratory's Metallurgical and Thermodynamic Data Bank (MTDATA) software. By analysing the Gibbs free energy of a user-specified system, a calculation can done to estimate the composition and equilibrium fractions of any phases present from the variety available in the database. The quality of the results is dependent on the

available data for the subsystem databases used in the calculation [106]. For this work MTDATA version 4.73 with the SGTE, PLUS and TCFE databases were used.

2.1.7 Transmission electron microscopy

Samples were cut into thin slices of 150 µm using a diamond cutting wheel and then ground to 40 µm using 1200 µm grit grinding paper. The discs were electro-polished using a twin jet polishing machine with a solution 80% ethanol, 15% glycerol, and 5% perchloric acid at 24 V. Samples were observed in a FEI Tecnai Osiris transmission electron microscope in scanning mode (STEM) at accelerating voltage of 200 kV using high angle annular dark field imaging. Energy-dispersive X-ray spectroscopy (EDX) was used to gather chemical composition information.

High angle annular dark field imaging (HAADF)

Annular dark-field imaging is used for mapping samples in STEM based on collecting scattered electrons with an annular dark-field detector. This allows for the sampling of many more scattered electrons that can typically pass through an objective aperture. Contrast in HAADF images formed

by high-angle, incoherently scatted electrons is sensitive to variations in the atomic number in the sample, as well as variations in density and thickness. Hence in Figure 2.14, the alloy precipitates can be distinguished from the ferrite matrix and EDX mapping then can be used for element identification.

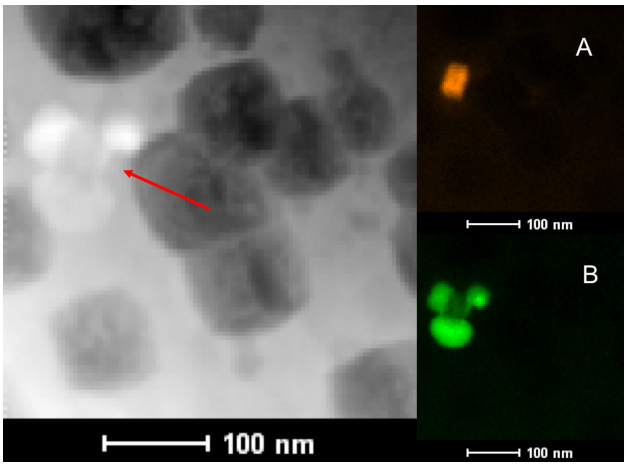

Figure 2.14: The main HAADF image showing the light-coloured precipitates, indicated by the arrow. EDX images show (A) TiN and (B) NbC, based on the identification of the metallic components of the precipitates. This image is taken from this work, and shows X80 steel.

2.1.8 Inductively coupled plasma mass spectrometry

Inductively coupled plasma mass spectrometry (ICP-MS) is used for detecting metals in low concentrations, up to one part per 10^{15}. The steel sample is dissolved in strong acid and ionized, the mass spectrometer is used to sep-

arate and quantify these ions. The ICP-MS measurements were carried out at the CBMM analytical laboratory in Araxa, Brazil using the Perkin-Elmer NexION 300S apparatus, measure the amount of niobium in solution in a variety of samples.

Chapter 3

Advanced experimental method

3.1 Advanced characterization

An X-ray scattering technique was used for measuring the precipitate size distributions in the steel samples, so that cubic millimetres of material can be studied in contrast to transmission electron microscopy, where orders of magnitude smaller smaples are examined. TEM was nonetheless used as a complementary technique for direct observations and limited validation of the X-ray method.

The amount of niobium in solution was also determined using advanced mass spectroscopy enables full characterization of the distribution of niobium in the steel as precipitate and solute.

These key, advanced techniques are summarised in this chapter.

3.1.1 Overview of small-angle scattering

Small-angle scattering (SAS) is a technique that utilises deflected collimated radiation for measuring structures from a few Angstrom in size to millimeters [107, 108]. Small deflections away from the original beam trajectory after interaction with structures are interpreted to yield size data.

X-ray scattering intensity, during SAXS, is determined as a function of the scattering vector q, defined in Equation 3.1:

$$q = \frac{4\pi}{\lambda} \sin 2\theta \tag{3.1}$$

where λ is the wavelength of the X-ray, and 2θ is the scattering angle, figure 3.1.

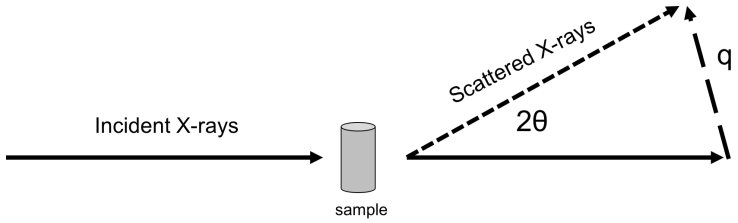

Figure 3.1: Geometry of X-ray scattering.

Small angle X-ray scattering

SAXS can be used to determine the size distribution of particles of a defined shape. The scattered X-rays are collected on a flat 2-dimensional plate detector, producing an image as the output; an example of this 2-dimensional data is shown in Figure 3.2.

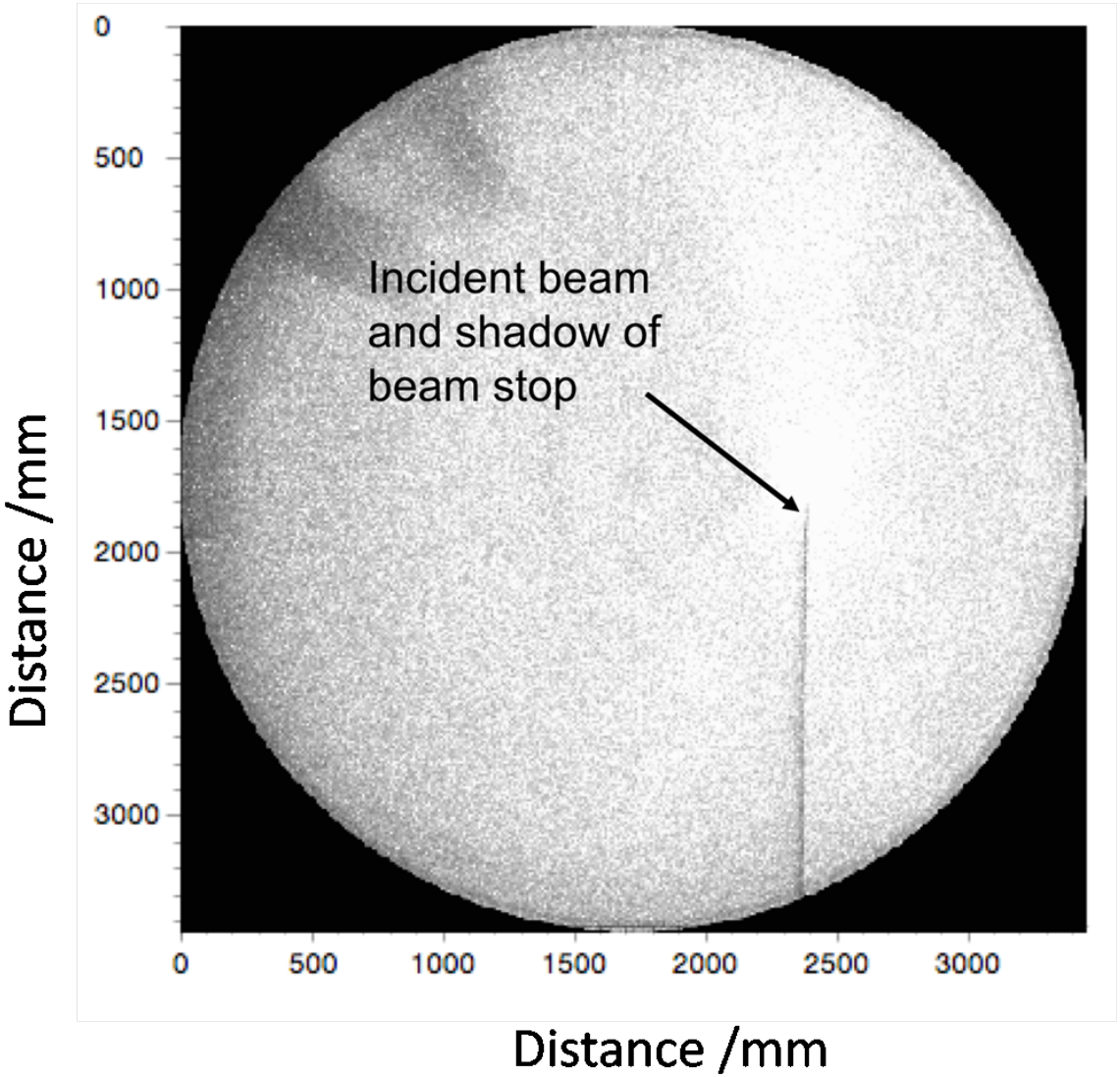

Figure 3.2: MAR345 detector showing the results of a SAXS experiment. The bright region identifies the point where the unscattered, collimated beam is incident on the detector, the other bright regions correlate to scattered electrons.

This image is then converted into a spectrum i.e. 1-dimensional information. This requires fitting the SAXS intensities to those derived from to models based on a known shape e.g. spherical precipitates.

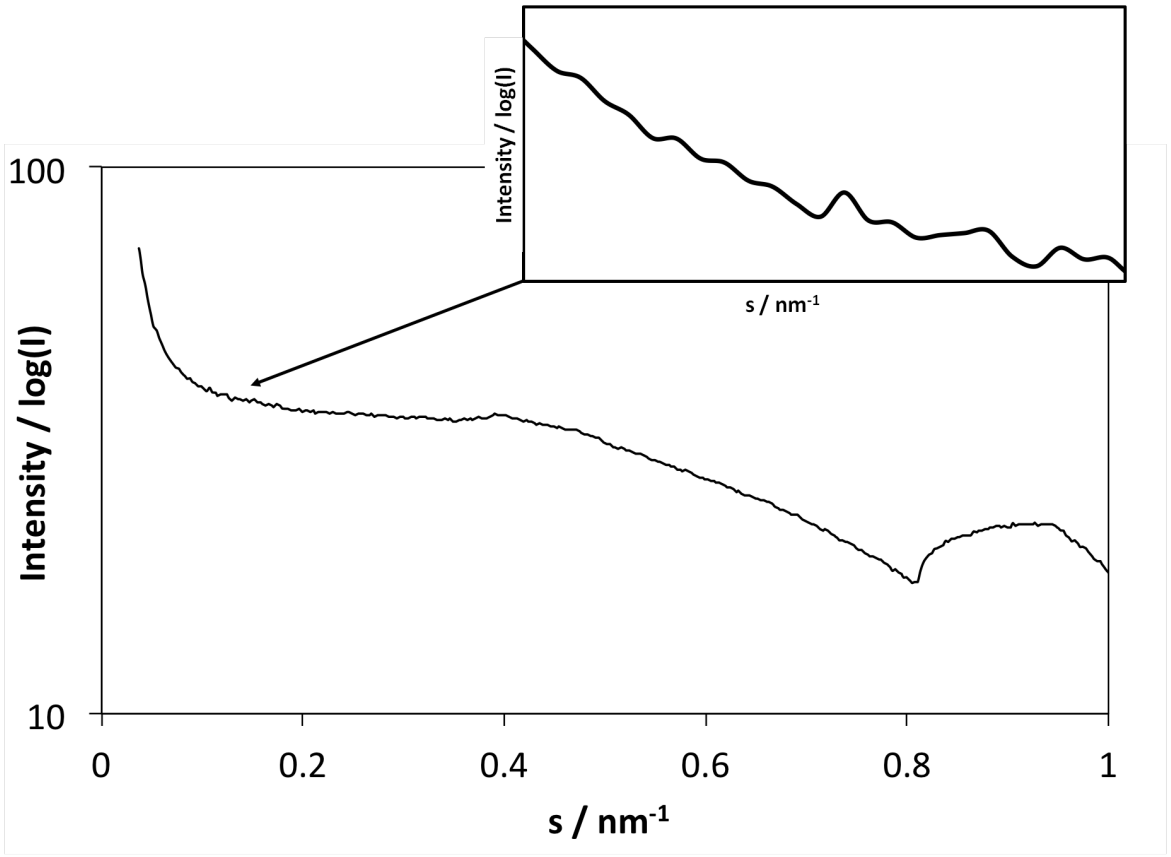

Figure 3.3: 1-dimensional data generated using DAWN [109]. Each deviation from a straight line, or 'bump', must be assessed as a scattering structure in further analysis.

A number of analytical tools exist for the conversion of the 2-dimensional SAXS data, in Figure 3.2 to 1-dimensional spectra, as in Figure 3.7.

SAXS experimental methodology

The SAXS experiments were carried out at the High Energy Materials Science (HEMS) beamline at Deutsches Elektronen-Synchrotron (DESY) [110], at the P07 beamline, figure 3.4 is used for high energy X-ray diffraction and other imaging techniques [111].

Figure 3.4: DESY P07 beam line showing beam collimator.

The beamline set-up process and data analysis has been summarised in Figure 3.5.

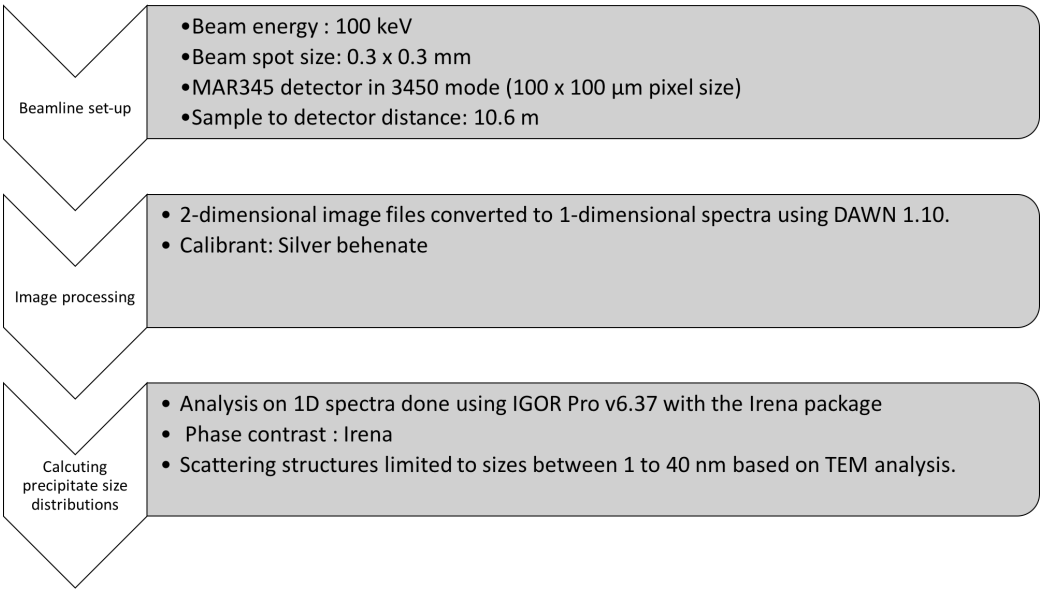

Figure 3.5: Summary of the SAXS experiment from beam-line set-up to calculating precipitate size distributions.

A beam energy of 100 keV, was utilised to ensure penetration through a $3\,\text{mm} \times 10\,\text{mm}$ rod held (figure 3.6), with a spot size of 0.3 mm × 0.3 mm. A Mar345 detector with a 100 µm by 100 µm pixel size, at a sample to detector distance of 10600 mm was used to cover a wide range of scattered beams. Calibration of the system was done using a silver behenate solution provided by the beamline facility. The phase contrast was calculated using the full alloy composition with the Irena phase contract calculator [112]. 1D spectra

were derived from the SAXS 2D images using Dawn 1.10 [109], and IGOR Pro v6.37 with the Irena package was then used to calculate the precipitate size distributions [112].

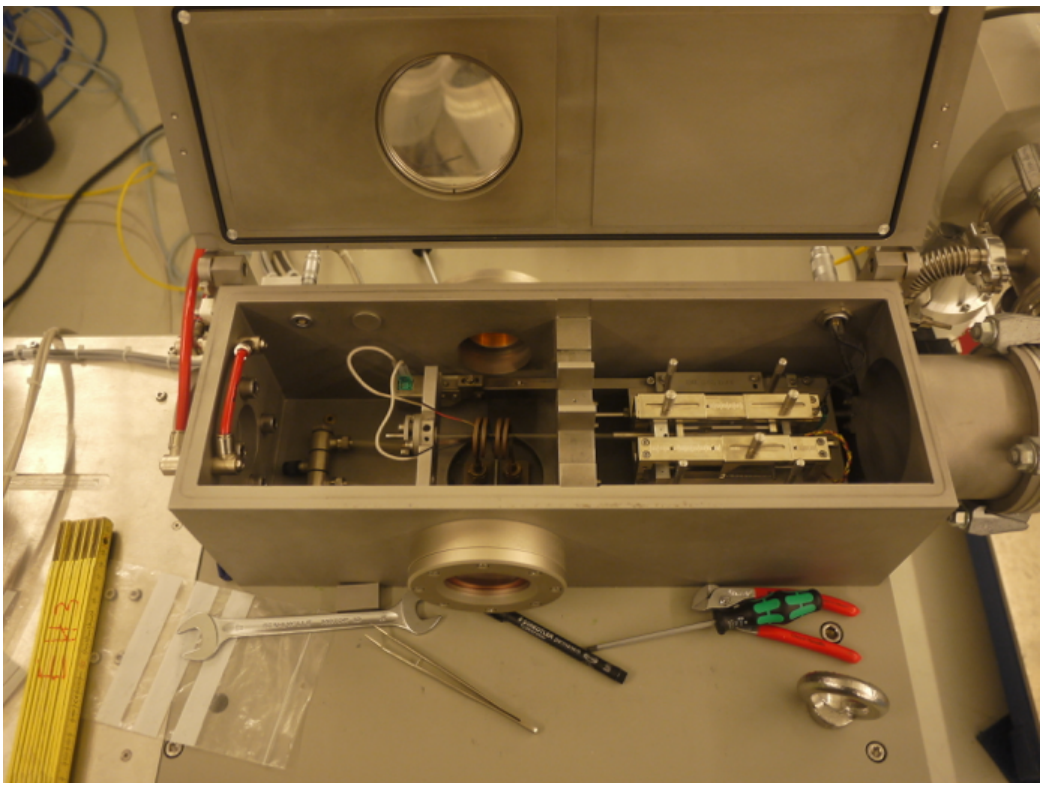

Figure 3.6: The samples were a 3 mm × 10 mm rods, held in a DIL805A dilatometer, with windows to allow access for the beam.

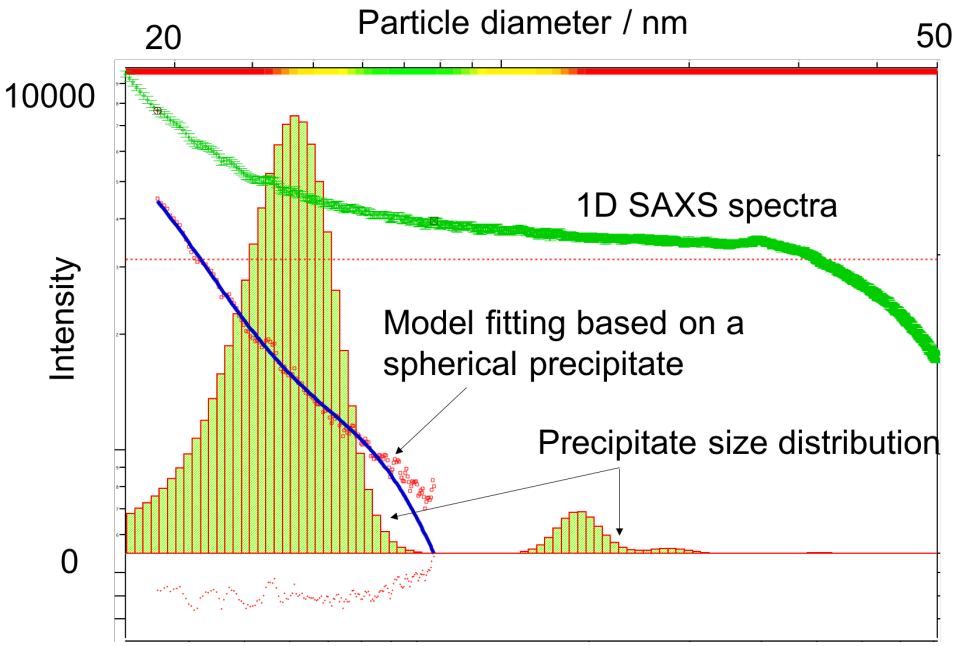

Figure 3.7: Analysis of precipitate sizes using Irena SAS analysis for precipitate size distributions. The intensity correlates to the populations of specific precipitate sizes. The data presented here were collected at DESY.

Assumptions and sources of error

Precipitate size distributions from the small-angle scattering data were obtained using the maximum entropy (MaxEnt) method developed by Potton *et al.* and adapted by Jemian *et al.* for Irena macros [112]. This method describes the data as histogram-based size distributions over a range of precipitate sizes in defined diameter bins. Scattering calculated from trial dis-

tributions is fitted to the measured data, and used to solve the histogram size distribution [112].

The MaxEnt methodology imposes a high standard for errors (typically 1 standard deviation of the true intesity), by closely matching the data with the calculated data such that the goodness of fit criteria (based on the sum of squared standardised residuals) are close to the population of data points used in the analysis [112].

However, errors can be scaled or specifically defined within the Irena system to account for the influence of polycrystallinity and phase variations in the material. Very fine microstructural phases can contribute to scattering, as can phase changes which are not wholly accounted for in the relatively smaller contrast between allotropic phases in steel.

Chapter 4

Characterization of precipitates

4.1 Introduction

Two effective strategies are well established in controlling the development of microstructures in Nb-microalloyed steels. The pinning of austenite grain boundaries by precipitates and the segregation of dissolved niobium to austenite grain boundaries which may lead to a reduction in their mobility [113, 114]. These phenomena exert control over the recrystallization processes during the hot deformation of steel by limiting the austenite grain size, and are used widely in the controlled rolling of steels. However, they will also influence transformations during welding, where large transient thermal cycles are imposed across the heat-affected zone.

It is therefore critical that Nb, in solution and as an alloy carbide, is fully characterized in order to enable the interpretation of structure-property relationships in the HAZ.

4.2 Measurements of niobium in solution

Table 4.1 shows values of Nb in solution, measured from sections of the heat treated plates using inductively coupled plasma mass spectroscopy (ICP-MS), the process of which has been described in the experimental sections of this work, and in more detailed elsewhere [55]. The results range from 688 ppmw following quenching from 1230℃, in 1230Q, to under 50 ppmw following normalising from 950℃ and tempering at 650℃, in 950QT. These figures relate to the amount of dissolved niobium that is present in the matrix, the remainder being assumed to be precipitated.

Plate ID	Heat Treatment	Nb in solution / ppmw
X80	As received X80	336
X80T	Tempered at 650 ℃ for 1 h	344
950N	Normalised from 950 ℃	56
950NT	Normalised from 950 ℃, tempered at 650 ℃	48
1100Q	1100 ℃ for 1 h, quenched	438
950Q	950 ℃ for 1 h, quenched	86
1230Q	1230 ℃ for 1 h, quenched	688
1230QT	1230 ℃ for 1h, tempered at 650 ℃ ,1h	658
1100QT	1100 ℃ for 1h, tempered at 650 ℃ ,1h	400*

Table 4.1: Measurements of niobium in solution from ICP-MS experiments conducted at Araxa, Brazil. The datum * indicates an estimated value.

The data from table 4.1 are consistent with the thermodynamic modelling using MTDATA discussed in earlier chapters of this work. The amount of dissolved Nb increases in line with the austenitising temperature, T_γ. Heat treatment at 950 ℃ (950Q, 950N, 950NT) shows significantly greater precipitation, as compared to the tempering of the as-received X80 steel at 650 ℃, X80T. The heat treatments of the quenched plates 1230Q and 1100Q show a noticeable reduction in the dissolved Nb after tempering (1230QT and 1100QT).

4.3 Volume fraction of NbC precipitates

Empirical measurements of Nb in solution enabled calculations using a mass balance to derive the volume fraction of NbC. NbC and α-iron were assumed to have approximately equivalent densities (7.8 $\mathrm{g\,cm^{-3}}$ and 7.5 $\mathrm{g\,cm^{-3}}$ respectively), hence equating the weight fraction to volume fraction, f_{NbC}, in each heat treated condition, where f_{NbC} is given by:

$$\frac{\text{Total niobium in X80 steel , wt \%} - \text{ Niobium in solution, wt \%}}{\text{Mass of niobium} \big/ \text{Mass of niobium carbide}} \tag{4.1}$$

Plate ID	Niobium in solution /wt%	f_{NbC}
X80	0.00336	7.0×10^{-4}
X80T	0.00344	6.9×10^{-4}
X80N	0.0056	1.0×10^{-3}
X80NT	0.0048	1.0×10^{-3}
1100Q	0.00438	5.8×10^{-4}
950Q	0.0086	9.8×10^{-4}
1230Q	0.0262	3.0×10^{-4}
1230QT	0.0292	3.3×10^{-4}
1100QT	0.04	6.3×10^{-4}

Table 4.2: Calculated volume fractions from the measured niobium in solution using ICP-MS. Total wt % niobium in the X80 steel under analysis is 0.095 wt%, and the ratio of the mass of niobium to the mass of niobium carbide is 0.88.

4.4 Characterization of precipitates

Grain boundary pinning by precipitates exerts Zener pressure, that opposes the motion of the grain boundary, and is proportional to $\gamma \cdot {}^{f_{ppt}}/_{r}$, where γ is the grain boundary energy, f_{ppt} is the precipitate volume fraction, and r is the mean size of a sperhical precipitate [115]. Martin *et al.* have reviewed the influence of inter-particle spacing and particle diameters in the influence

of pinning particles on the process [46], and have shown the influence inter-particle distances in the context of the Orowan equation:

$$\Delta\tau = \frac{2T_l}{\lambda\, b} \tag{4.2}$$

where, $\Delta\tau$ is the change in shear stress over the value for a precipitate free metal, T_l line tension between particles of spacing, λ. The Orowan equation establishes a relationship between λ and the strength of an alloy, where an increment in the inter-particle spacing will reduce strength in a heat-treated alloy. This effect, along with the strengthening influence of fine precipitates in grain refinerment and precipitation strengething [**?**], highlights the importance of precipitate sizes and their distribution in determining the structures and properties in the steel.

Most work has focussed on the utilisation of high resolution electron microscopy techniques [55, 93] to define precipitate sizes. However, this necessarily limits the total amount of material that can be analysed due to the very small sections that can are subjected to the transmission electron microscopy analysis that is required to identify nano-scale particles.

In order to successfully analyse bulk sections of heat treated materials

to identify the precipitate size distributions, an X-ray scattering technique was selected. Small-angle X-ray scattering (SAXS) is a technique that can be utilised for quantifying size distributions in systems with nanometre scale aggregates. The experimental procedure has been covered in earlier chapters of this work, and a very detailed analysis of the process is described by Jemian et al. [116, 117].

4.4.1 Verification of the SAXS data

The use of the SAXS technique to characterize the precipitate size distribution in X80 steels provides the first quantitative data on NbC distribution in this important class of steels. X80 steel contains several components that are capable of 'scattering' X-rays, including a range of various precipitated artefacts such as alloy carbides (e.g TiN and AlN) and cementite. These can affect the quality of the data, so data processing techniques first help minimise such errors, including limiting the sizes and shapes of assessed precipitates, were utilized in the data analysis used in this work.

However, it is useful to conduct an independent verification of the SAXS data to ensure that the data analysis has been appropriate and that results are valid. In this work, the existing literature has been utilised in order

to compare the relative contributions of precipitation strengthening as determined by precipitation characterisation using electron microscopy with precipitation strengthening contributions determined by analysis of the precipitate size distribution from SAXS.

Validation against precipitation strengthening data

Lu et al. have considered the relative contributions of strengthening mechanisms to the yield strength of microalloyed steels [55]. A range of Nb-microalloyed steels were assessed, covering a number of steels that fall within the X80 designation . The composition of X80-A4B used by Lu et al. had a similar compositionto the steel utilised in this work. This is shown in Table 4.3.

C	Mn	Si	Al	N	Cu+Ni+Cr	Mo	Nb	Ti	V
0.035	1.7	0.283	0.044	0.0058	0.66	0.305	0.091	0.017	0.003

Table 4.3: Composition of X80-A4B steel / wt. % [55]

In order to validate the SAXS experimental procedure and the related data the relative contribution of precipitate strengthening to the yield strength can be used as a proxy for determining the size distribution of precipitates, where a large dispersion of fine precipitates are expected to correlate to higher

relative contributions to the yield strength. These were calculated using a discrete precipitation strengthening formula, and compared with the result for X80-A4B published by Lu et al.

Precipitation strengthening contributions to yield strength

Marouplos et al. have calculated the individual strengthening contributions of microstructural features in steels to the overall yield strength, where precipitation strenthening was calculated using the Hirsch and Humphreys equation (equation 4.3) [94]. The inputs into this equation rely on the experimental data listed in Table 4.4 which were derived from the SAXS and plasma mass spectrometry experiments conducted in this work.

$$\sigma_p = \left(\frac{6.26}{L}\right) \ln\left(\frac{D}{2.48 \times 10^{-4}}\right), \tag{4.3}$$

where D is the mean precipitate diameter in μm, L is the carbide spacing in μm, and defined as:

$$L = D\left[(\frac{\pi}{4f})^{1/2} - 1\right] \tag{4.4}$$

where f is the volume fraction of NbC in table 4.4 and D is the mean precipitate diameter in μm, defined as:

$$D = \left[\frac{2}{3}(\bar{x}_V^{-2} + \sigma_V^2)\right]^{1/2} \tag{4.5}$$

where $\bar{x}_V$ is the mean diameter of NbC precipitates, σ_V is the volume of the NbC precipitates σ_s of the precipitate size data from SAXS analysis (Appendix 2).

Lu et al. use mass spectrometry analysis to define precipitate sizes, and use the following equation, based on Orowan looping to calculate the precipitation strengthening contribution to the yield strength:

$$\sigma_{ppt} = \left(\frac{10.8 f_v^{1/2}}{D}\right) \ln\left(\frac{D}{6.125 \times 10^{-4}}\right) \tag{4.6}$$

where $D$is the size of precipitates in micrometers, f_v is the volume fraction of the average precipitate size and σ_{ppt} is the precipitation strengthening. These data are taken from from table 4.4.

Plate ID	L /µm	D /µm	Volume fraction of NbC	σ_{ppt} /MPa	$\sigma_{ppt}{}^{*}$ /MPa	Yield strength/MPa
X80	0.1205	0.0037	7.0×10^{-4}	140	162	530
X80T	0.1065	0.0032	6.9×10^{-4}	151	183	556
950N	0.0842	0.0031	1.0×10^{-3}	189	231	357
950NT	0.0814	0.0031	1.0×10^{-3}	193	239	323
1100Q	0.1135	0.0032	5.8×10^{-4}	141	172	440
950Q	0.1135	0.0025	9.8×10^{-4}	210	279	420
1230Q	0.1305	0.0026	3.0×10^{-4}	113	152	446
1230QT	0.1184	0.0025	3.3×10^{-4}	122	166	550
1100QT	0.1020	0.0030	6.3×10^{-4}	152	192	630

Table 4.4: Contributions of precipitation strengthening to yield strength. $\sigma_{ppt}{}^{*}$ is caclulated using the equation from equation 4.6 [55]

The σ_{ppt} calculated from data using SAXS and ICP-MS in this work, when used with equation 4.3 is very close to the value calculated by Lu et al. 140 MPa as compared to 146.1 MPa [55]. The Orowan equation used by Lu et al, equation 4.6, gives a slightly higher value, but within about 20 MPa of the value from the literature. The two methods do show a close correlation in Figure 4.1, and either can be used to show that the SAXS data analysis is valid.

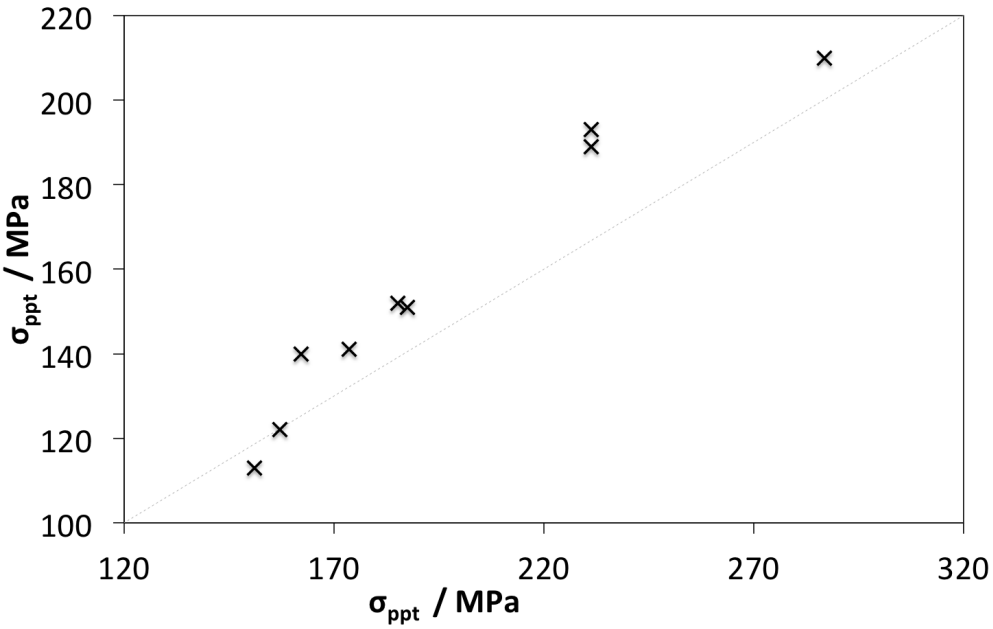

Figure 4.1: A comparison of σ_{ppt} calculated by equation 4.3 (Hirsch and Humphreys) versus equation 4.6 (from Orowan looping).

Precipitation and σ_{ppt}

As the volume fraction of precipitates increases for a specific precipitate size, the contribution to the yield strength from precipitation strengthening increases as noted in figure 4.2. This figure also indicates the increasing contribution of precipitation strengthening with smaller precipitate sizes to the yield strength of the material. Hence for a constant microstructure, strength will increase with an increase in volume fraction of precipitates of

a constant or smaller size i.e. for a given microstructures, with an average precipitate size of 3 nm, mechanical properties will increase if tempering leads to the formation of a greater volume fraction of precipitates in the 1-3 nm size range.

However, where microstructures vary, with heat treatments, factors other than precipitation strengthening contributions will dominate. Figure 4.3 shows a relationship between the overall yield strength and the proportion of strength contributed by precipitation, as the yield strength reduces due to the heat treatment conditions, the contribution of precipitation strengthening (as a proportion of the total yield strength) increases dramatically as in table 4.5, as the yield strength decreases in figure 4.3.

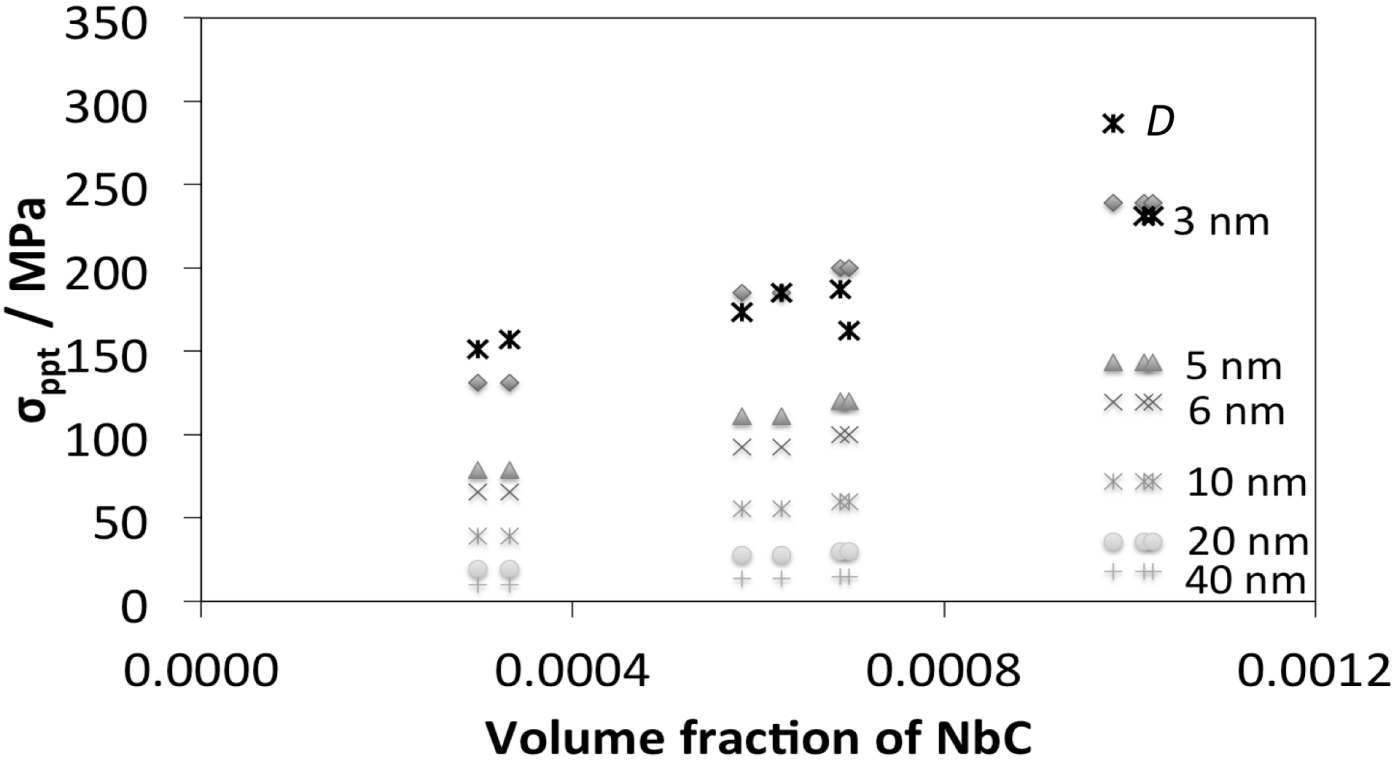

Figure 4.2: σ_{ppt} calculated for a range of precipitate sizes and precipitate volume fractions using Equation 4.6. D is the precipitate size from Table 4.4

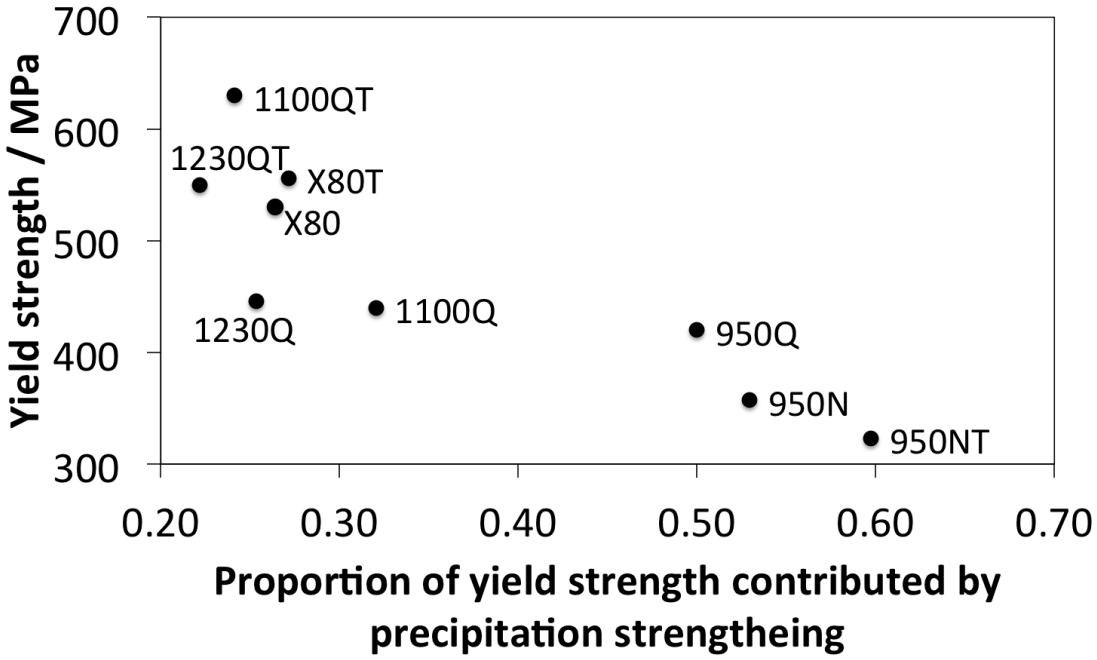

Figure 4.3: Yield strength versus proportion of strength contributed by σ_{ppt}.

This trend of the increasing contribution of precipitation strengthening to the yield strength is noted in figure 4.4 which shows the highest volume fraction of NbC correlated to the the highest contribution, as a proportion, of precipitation strengthening to the yield strength. However, as has been noted, the yield strength for the highest volume fraction NbC correlates to the lowest overall yield strength values in table 4.5. Therefore in order to assess the contributions of the effect of precipitation to the strength, figure

4.5 considers the change in yield strength with regard to the change in volume fraction on tempering of the heat treated plates. A clear trend can be observed showing the increment in yield strength with increased volume fraction of NbC for a constant microstructure.

In order to fully analyse the effects of tempering however, beyond the identification of trends in yield strength, it is apparent that quantitative analysis of the precipitate sizes is useful in offering a greater amount of reliable information as to the effects of precipitate coarsening and precipitation on the bulk properties of the steel.

Plate identification	σ_{ppt} /MPa	Yield strength/MPa	Contribution of σ_{ppt} to yield strength
X80	140	530	0.26
X80T	151	556	0.27
950N	189	357	0.53
950NT	193	323	0.60
1100Q	141	440	0.32
950Q	210	420	0.50
1230Q	113	446	0.25
1230QT	122	550	0.22
1100QT	152	630	0.24

Table 4.5: Proportion of yield strength contributed by σ_{ppt}.

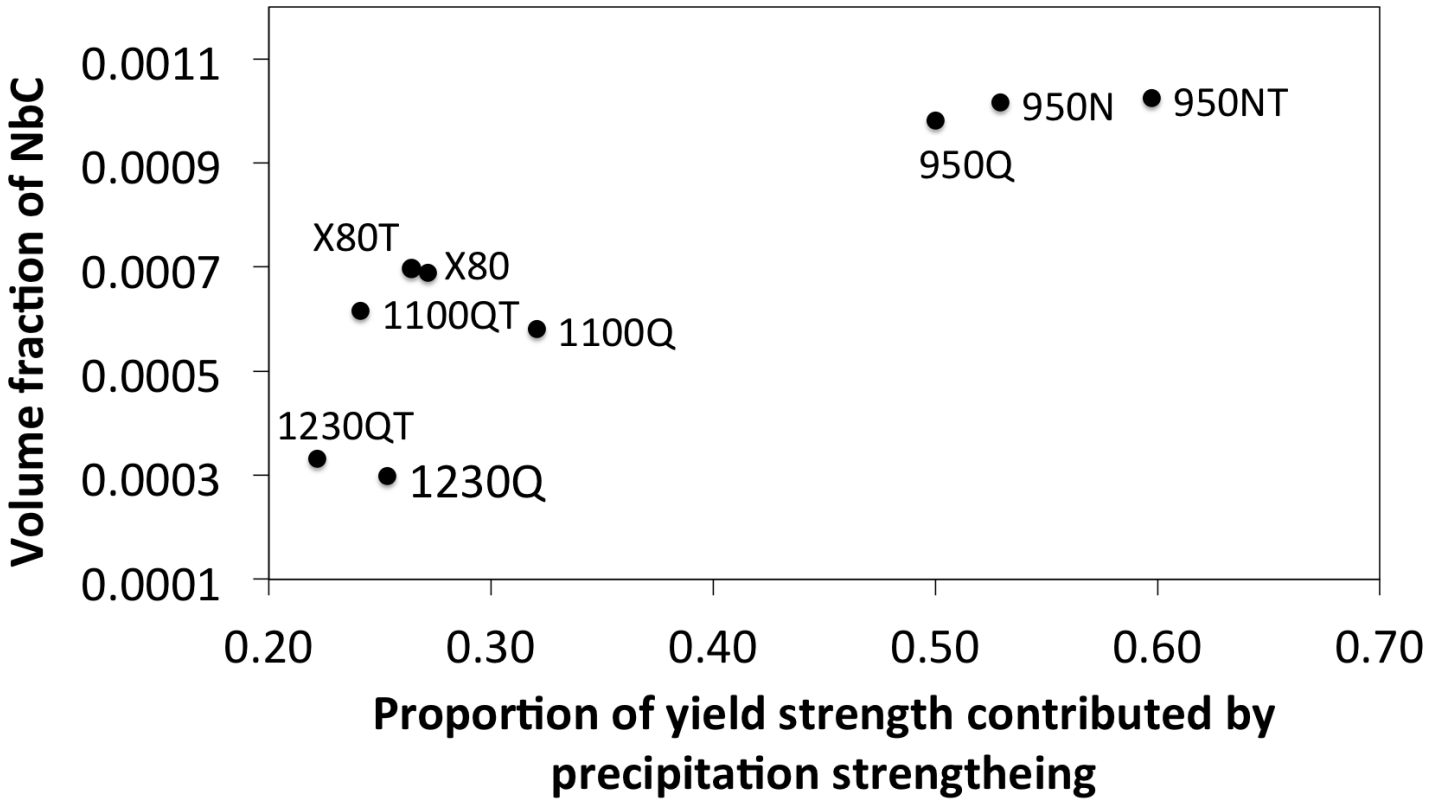

Figure 4.4: The influence of heat treatments on the change in yield strength and volume fraction of NbC .

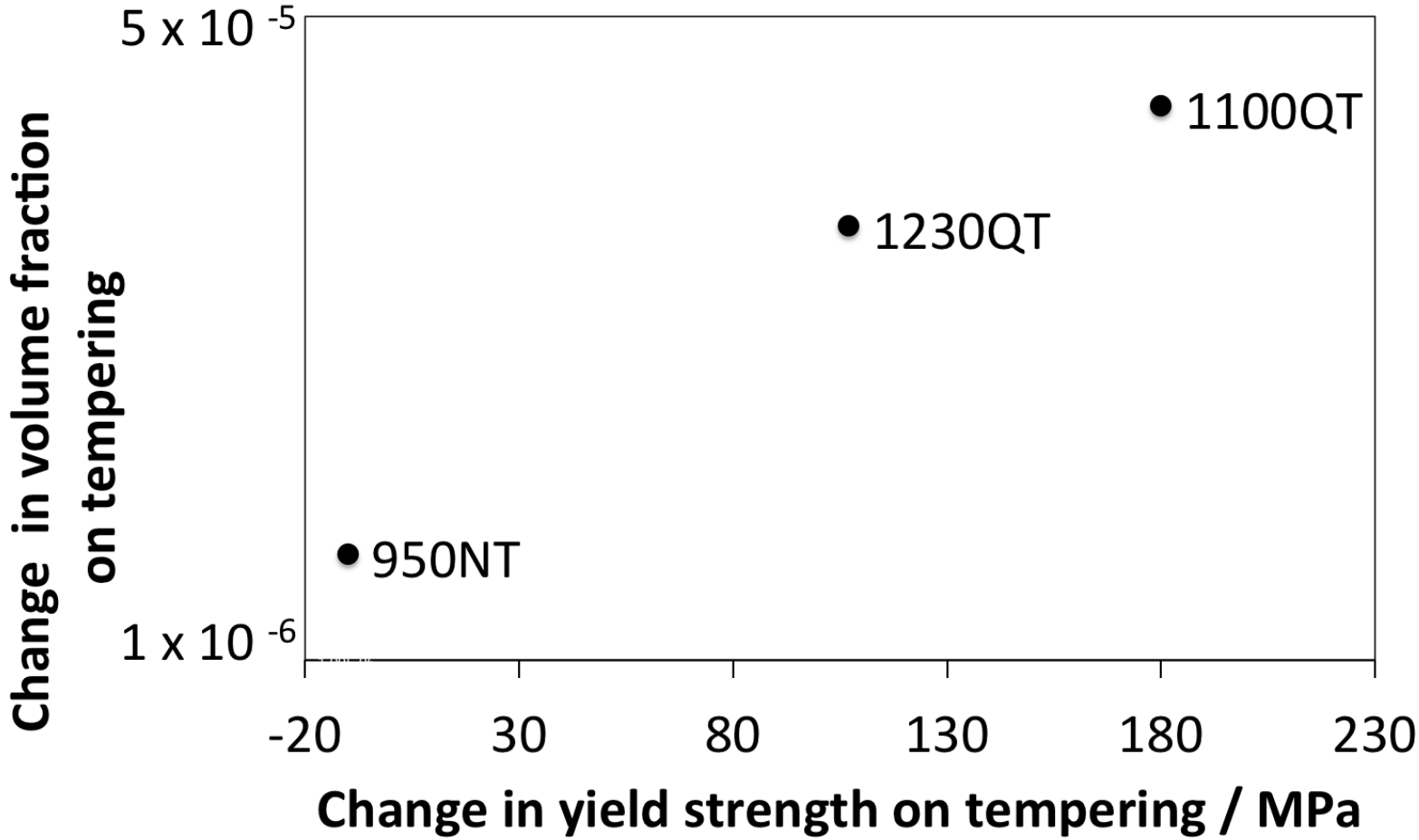

Figure 4.5: The influence of tempering treatments on the change in yield strength and volume fraction of NbC for a constant microstructure.

4.4.2 Precipitate size entropy

A technique is proposed based on work by Sugden and Bhadeshia [103] on quantifying the microstructural heterogeneity across welds. In principle, the equation quantifies the entropy i.e. the number of variations, in a system. Equation 4.7 utilises the fraction of precipitates in a given size range to develop an entropy value, therefore it is proposed that some predictions can be made on the state of the precipitate sizes across the heat treated plates using the data in Table 4.6 and other information that has been discussed in this chapter. The entropy is defined as:

$$entropy = \sum_{i=1}^{13} = -x\, ln\, x \tag{4.7}$$

where x is the number of precipitates in a size bin divided by the total number of precipitates, i is the bin number. A total of 13 bins were used in this calculation, taken from the size ranges allocated to the measured precipitate size distributions noted in figure 4.6 which is representative of the precipitate size distribution data that was measured from the SAXS experiment.

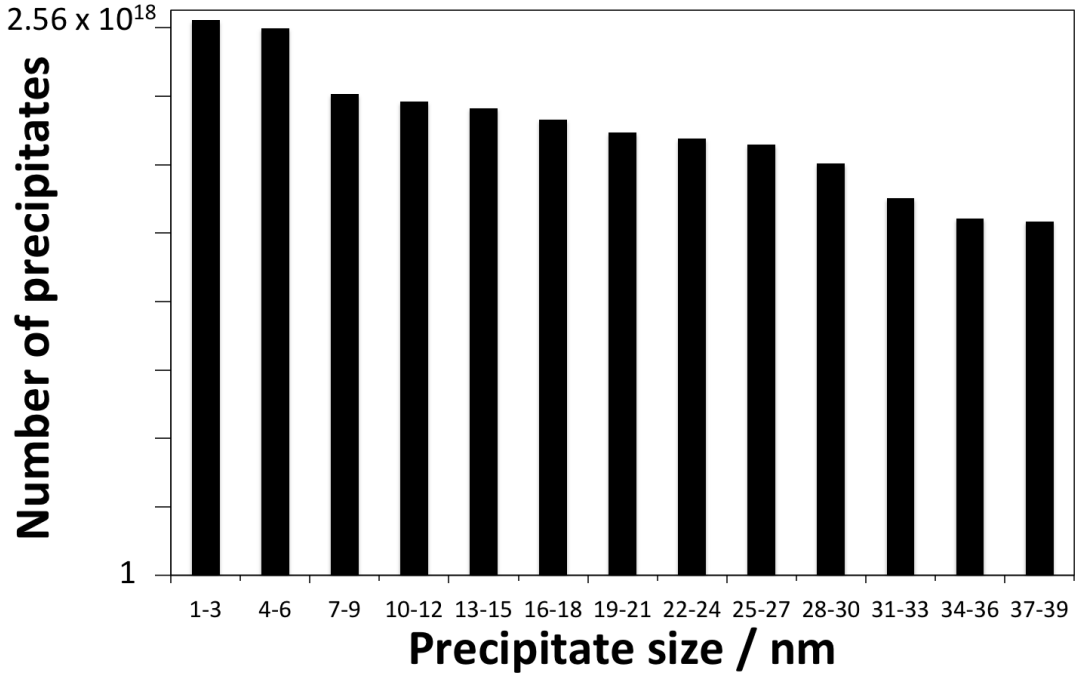

Figure 4.6: Precipitate size distribution for 1100Q.

The relative proportions (frequency) of the precipitate sizes is noted in figure 4.8 and shows the relative dominance of the finer precipitates. The use of the entropy values calculated for the precipitate size distribution for each heat treated plate allows for a useful metric for comparing the relative size distributions for the precipitates in each plate condition.

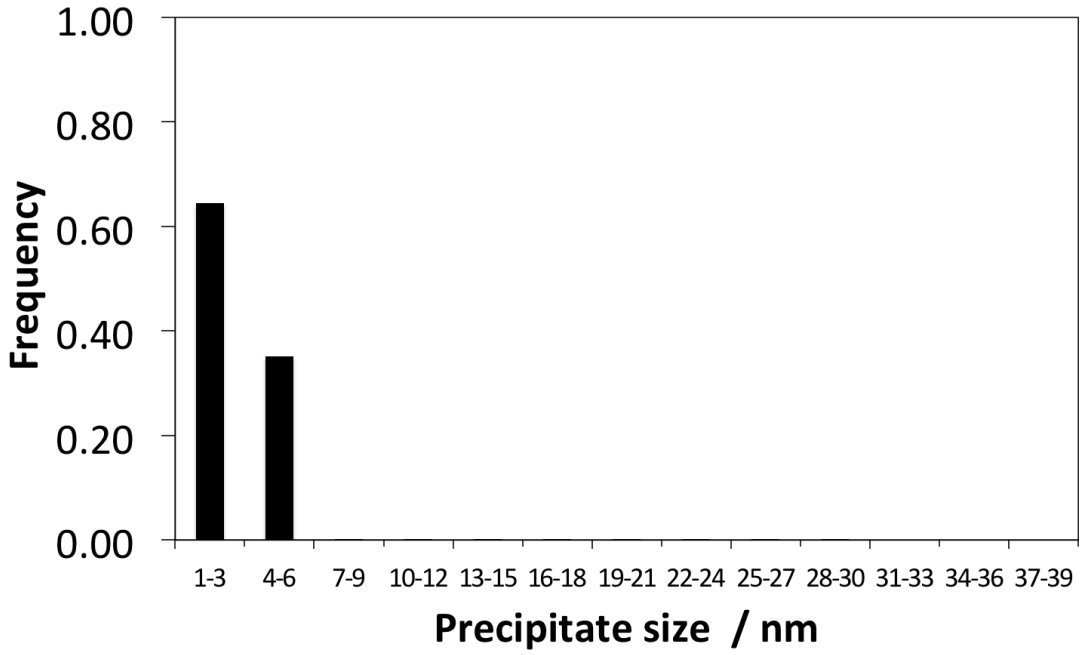

Figure 4.7: Relative proportions of precipitate size distribution for 1100Q.

Table 4.6 shows the associated precipitate entropy for each heat treated condition. The highest entropy value is 0.91, and is related to the highest heterogeneity in precipitate sizes i.e. that distribution with the widest range of precipitates of an appreciable number, as opposed to 0.08, the lowest value, related to a distribution dominated by a single size i.e. the lowest entropy or precipitate size heterogeneity. A comparison of the the two distributions is shown in figure 4.8, with 1230QT dominated by precipitates in a single size

bin, and X80 with a range of precipitate sizes represented in the distribution i.e. the distribution is less uniform.

Plate	Calculated entropy	Dissolved Nb / ppmw
X80	0.91	336
X80T	0.71	344
950N	0.68	56
950NT	0.63	48
1100Q	0.68	438
950Q	0.23	86
1230Q	0.19	688
1230QT	0.08	658
1100QT	0.57	400

Table 4.6: Precipitate heterogeneity in heat treated X80 steels. The maximum entropy is 0.91, and ranges down to a minimum at 0.08

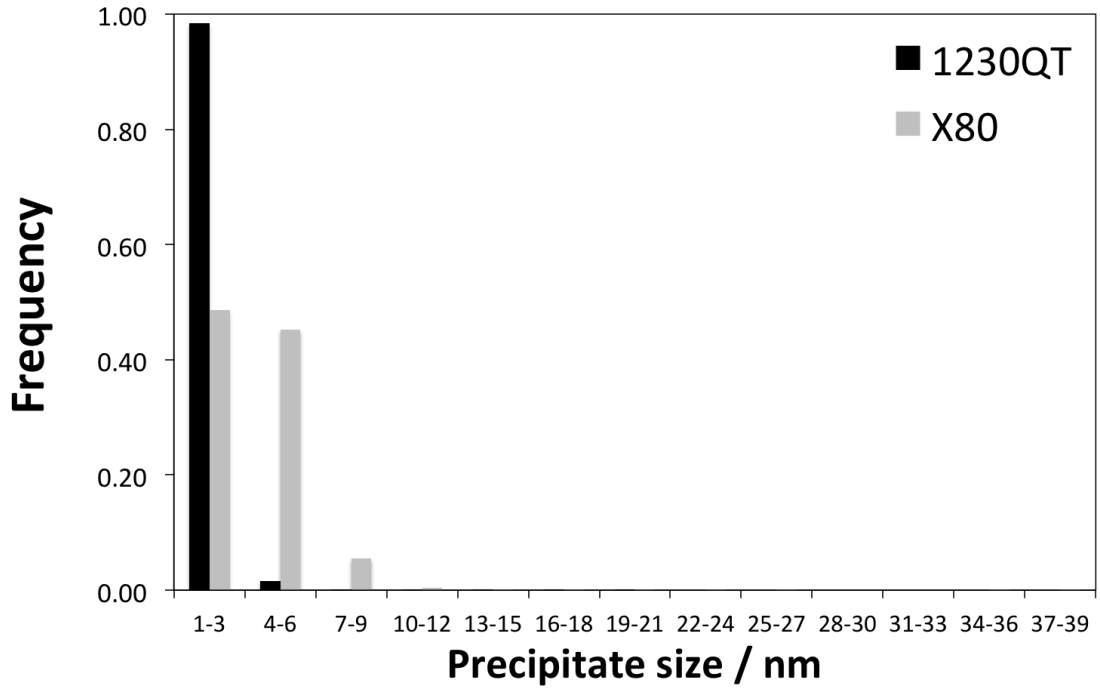

Figure 4.8: Difference between the lowest and highest entropy values for 1230QT (0.08) and X80 (0.91).

X80

X80 is the as-rolled plate, and is expected to show the highest entropy value consistent with a wide range of precipitate sizes. Indeed a wide range of precipitate sizes in thermomechanically processed X80 steels has been reported in the literature [55].

The tempering of X80 steel has a limited impact the calculated volume fraction of the precipitated NbC and a comparatively modest increment on

mechanical properties (30 MPa for X80T, as compared to in excess of 100 MPa for 1230QT), however a degree of precipitation hardening does occur; this is confirmed by the relative reduction in precipitate entropy as the number of fine precipitates in the size distribution increases, resulting in lower uniformity in the distribution.

Heat treatments at 950 ℃

A significant amount of NbC has precipitated in 950Q as indicated in table 4.6. This is likely dominated by the precipitation of fine precipitates during heating of the original X80 structure since the lower entropy value calculated for 950Q suggests that a narrow size range in the distribution, and along with the high relative contribution by precipitation strengthening noted in the data in Table 4.4 indicates that fine precipitates dominate the distribution.

In contrast, the sample normalised from 950 ℃, 950N, has an entropy value of 0.68, closer to that of X80, although a smaller amount of dissolved Nb indicates that most of the Nb has precipitated under the effects of the relatively slower cooling rate associated with normalising, which leads to precipitation over a range of temperatures.

On tempering to form 950NT, further precipitate ripening occurs, with

coarser precipitates and resulting in a lower entropy value in 4.6.

Heat treated at 1100 ℃

The solubility of NbC in equilibrium with austenite is considerably greater at 1100 ℃ when compared with 950 ℃, so a significant amount of Nb is in the dissolved state (table 4.6). Any precipitates that will survive at this temperature are likely to be coarse, as fine precipitates dissolve more readily due to the higher surface area to volume ratio. Dissolution occurs until equilibrium is established when the number density and volume fraction of particles will be small, indicated by the significant amount of dissolved Nb at 1100 ℃in table 4.6, but with a range of precipitate sizes reflecting the original distribution but with different proportions for each size bin. hence such a distribution exhibits a relatively large entropy value.

On tempering the quenched microstructure to give 1100QT, further fine precipitation is expected to occur, these are likely to dominate the distribution, and this is reflected in the lower entropy value.

Heat treated at 1230 ℃

The entropy of the distribution of precipitates in 1230Q is expected to be lower that that of 1100Q, where the bulk of the precipitates at this temperature will have dissolved, as indicated in table 4.6.

1230QT shows a the lowest entropy value of 0.08, consistent with the precipitation of very fine precipitates that dominate the distribution on tempering.

It is important to point out that the entropy values as used here are for different heat treatments, but the bin definitions are identical for all heat treatments. This is necessary to compare gross changes. Thus uniformly fine precipitates can in principle fall into a single size bin and hence give a low relative entropy.

4.5 Precipitate size distributions in the heat treated plates

A number of predictions have been using the precipitate size entropy, in this section the quantitative data gathered by SAXS, which has been used to derive entropy values, will be analysed.

The precipitate size data measured using SAXS represent the first size distributions determined quantitatively in the heat treated plates. Such data helps the rigorous interpolation of grain boundary pinning phenomenon that are critical to the evolution of structures and properties in thermomechanically processed Nb-microalloyed steels. Furthermore, the particle distributions as defined by the transient thermal gradients during welding are expected to determine the evolution of the microstructures in the hAZ of welds.

It is noted at the outset that the interpretation of SAXS data is not straightforward but confidence can be boosted assessing the data against metallurgical trends.

The population of precipitates in a particular size range is obtained by dividing the number in that size range by the total number of precipitates. In

order to account for the amount of NbC present in each size range, a further step has been introduced to include the volume distribution of the NbC precipitates in order to highlight the distribution of precipitated NbC across the size range. This step is a function within the Irena software package, and uses the precipitate size (diameter) to calculate a volume based on the user-defined shape (spherical for NbC).

4.5.1 Size distributions in precipitated niobium

Figure 4.9 shows the distribution of precipitate sizes in **X80** and **X80T**. Fine precipitates, those between 1 and 5 nm which are most effective in grain boundary pinning, dominate the distributions in both plates [115]. It is known that fine precipitates have high surface area to volume ratios, hence while there may be a high population density of these fine precipitates, they may not necessarily be account for the maximum volume of available NbC. Here, figure 4.10, which utilizes the volume distribution of the precipitates offers information into the distribution of the bulk of the NbC that precipitates during thermomechanical processing of X80. The volume of each precipitate is calculated from precipitate size calculated from SAXS analysis, and shape (spherical for NbC) which is user-defined.

The coarser precipitates are present in very much smaller numbers, but each coarse precipitate compromises a comparatively significant volume as opposed to the finest precipitates.

A significant part of the volume fraction of NbC comes from coarser precipitates, with precipitates in the 4-6 nm size range dominating the distribution. Therefore the coarser precipitates, which are low in count, contain much of the NbC i.e. they are fewer, but larger. Since a proportion of the NbC is present in coarser precipitates, when dissolution of precipitates occur in the CGHAZ during welding, a distribution with a few coarse precipitates may result in a comparatively higher amount of dissolved Nb. This has broad implications for the structures and properties in the region due to the effect of dissolved Nb on limiting austenite grain growth [77].

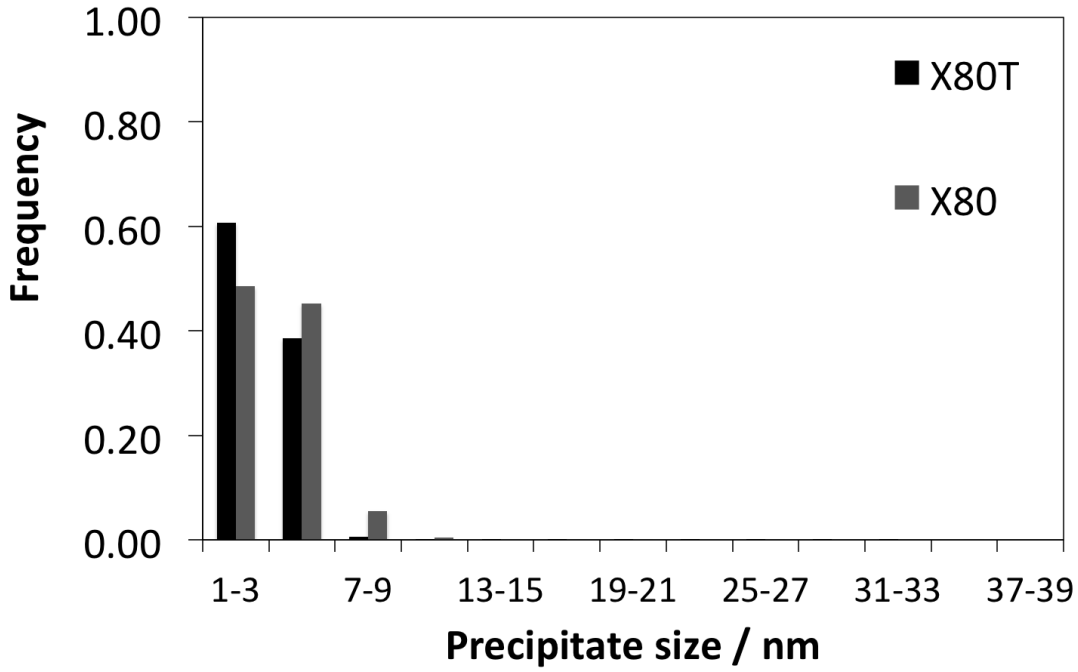

Figure 4.9: Precipitate size distribution in X80 and X80T.

On tempering of X80, fine precipitates within the first two size bins are formed as noted in the SAXS data from figure 4.10, and illustrated in figure 4.11. The increment in the volume distribution following tempering in the 4-6 nm size range suggests that some nucleation occurs on existing fine precipitates, but population of precipitates is dominated by the finest size range in figure 7.4.

The broad range of precipitate sizes observed in these plates confirms that high entropy values associated with X80T and, X80, which had the

highest entropy value. Tempering of X80 increases the number of fine precipitates, effectively reducing the peak entropy from 0.91 to 0.71 in table 4.7.

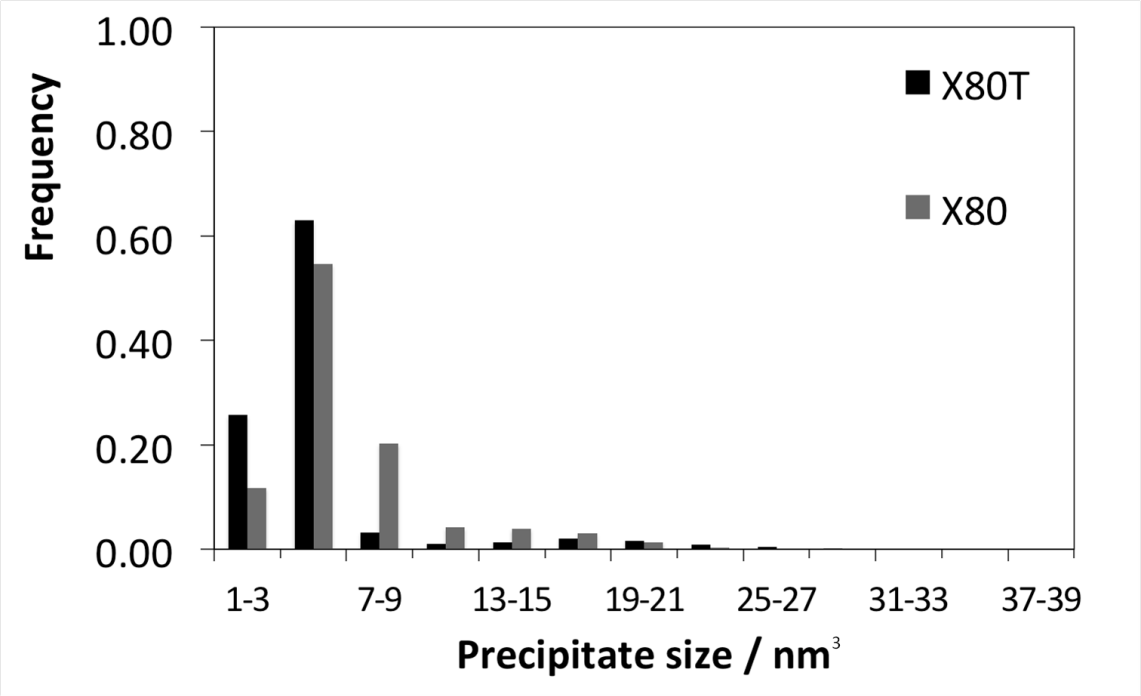

Figure 4.10: Precipitate volume distribution in X80 and X80T.

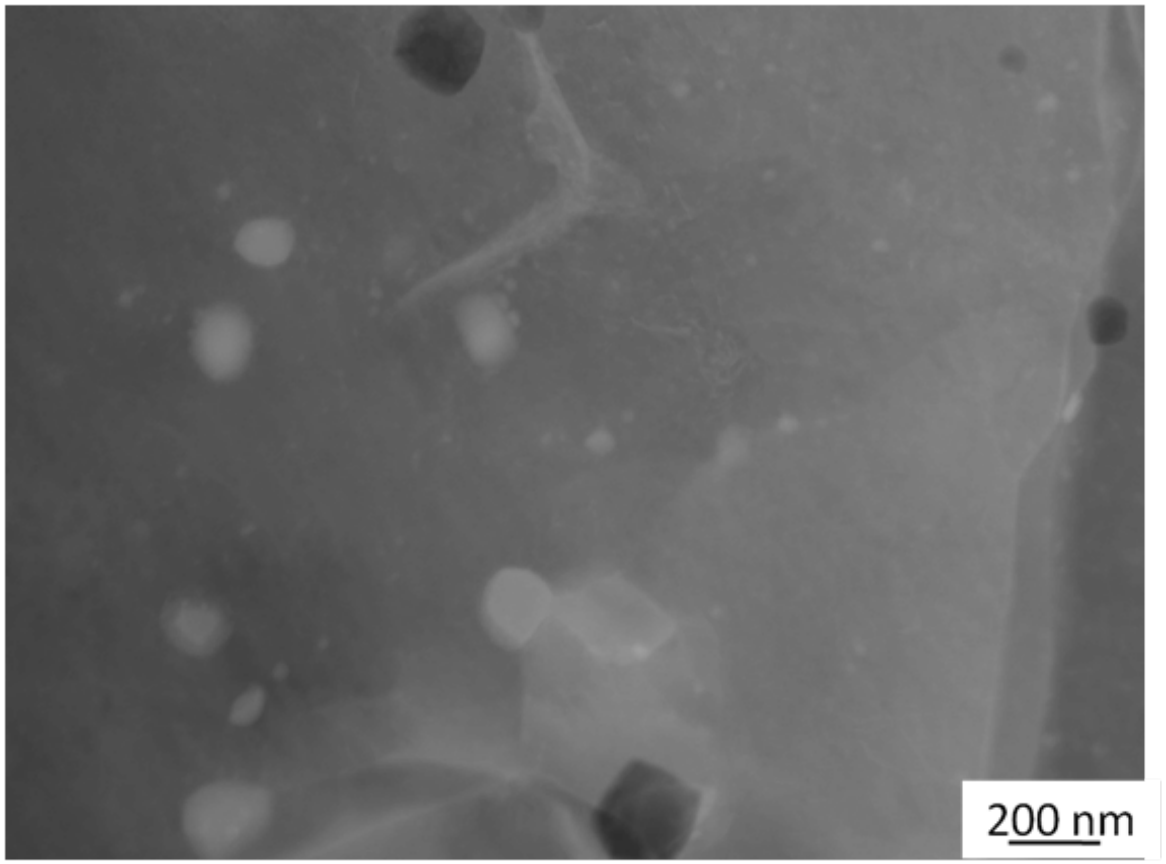

Figure 4.11: HAADF image of X80T showing the wide size distribution of (light-coloured) precipitates in X80T.

On quenching from 950℃, significant precipitation occurs, with only 86 ppmw of Nb (from the total of 950 ppmw in the steel) retained in solution. Figure 7.11 shows that the bulk of the precipitate sizes in **950Q** are within the 1-3 nm size bin. The dominance of a single size bin leads to the low entropy in the precipitate size entropy value reported in table 4.6, however the prevalence of fine precipitates in the re-austenitised microstructure (examined in Chapter 5) correlates to over half the yield strength in the plate contributed by precipitation strengthening phenomenon, noted in table 4.5. The precipitate volume distribution in figure 4.13 shows that the bulk of precipitation is related to the nucleation of fine precipitates; during heating and holding at 950℃, nucleation is the dominant effect at NbC particles form in the matrix, on quenching, the kinetics for growth by diffusion are limited hence the large volume fraction of precipitates in 950Q is related to fine precipitates.

The high proportions of yield strength contributions by σ_{ppt} are consistent across **950N** and **950NT**, with size distributions that continue to be dominated by fine precipitate sizes within a coarse matrix (discussed in Chapter 7). The presence of coarser particles in 950N and 950NT is apparent in figure 4.13, indicating that normalising from 950℃ and subsequent tem-

pering to give 950NT shows ripening of coarse precipitates on consideration of figure 4.13. This is consistent with the Ostwald ripening, i.e. the growth of coarser particles at the expense of finer particles [46], and can be observed in figure 4.14, where the larger precipitates have a limited number of finer precipitates in their periphery.

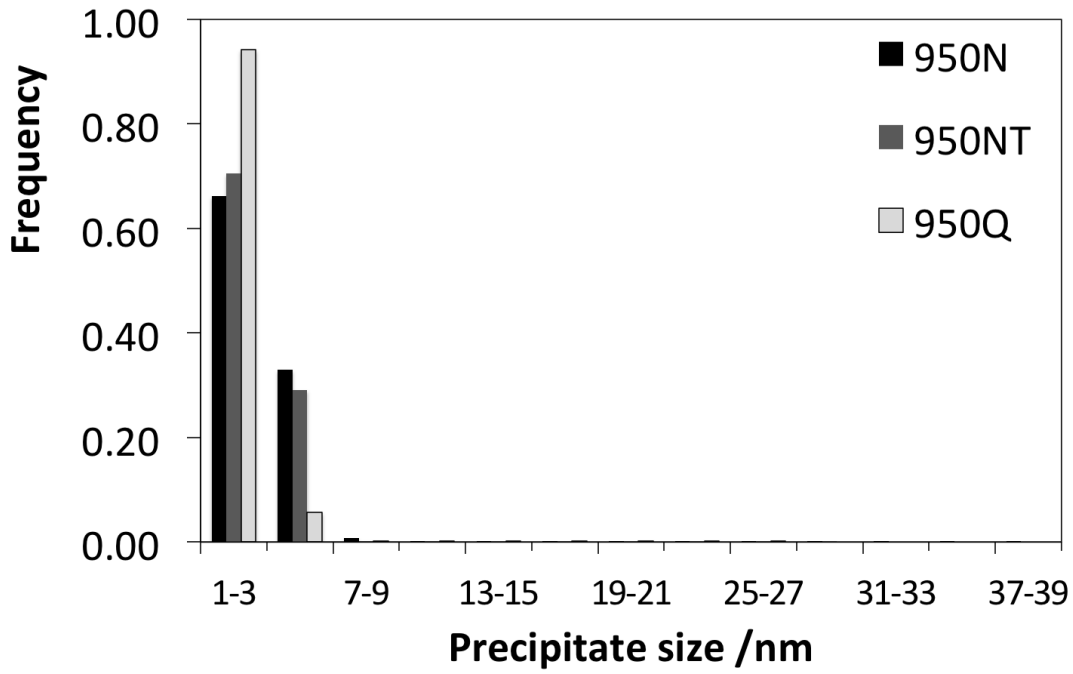

Figure 4.12: Precipitate size distribution in 950Q, 950N and 950NT.

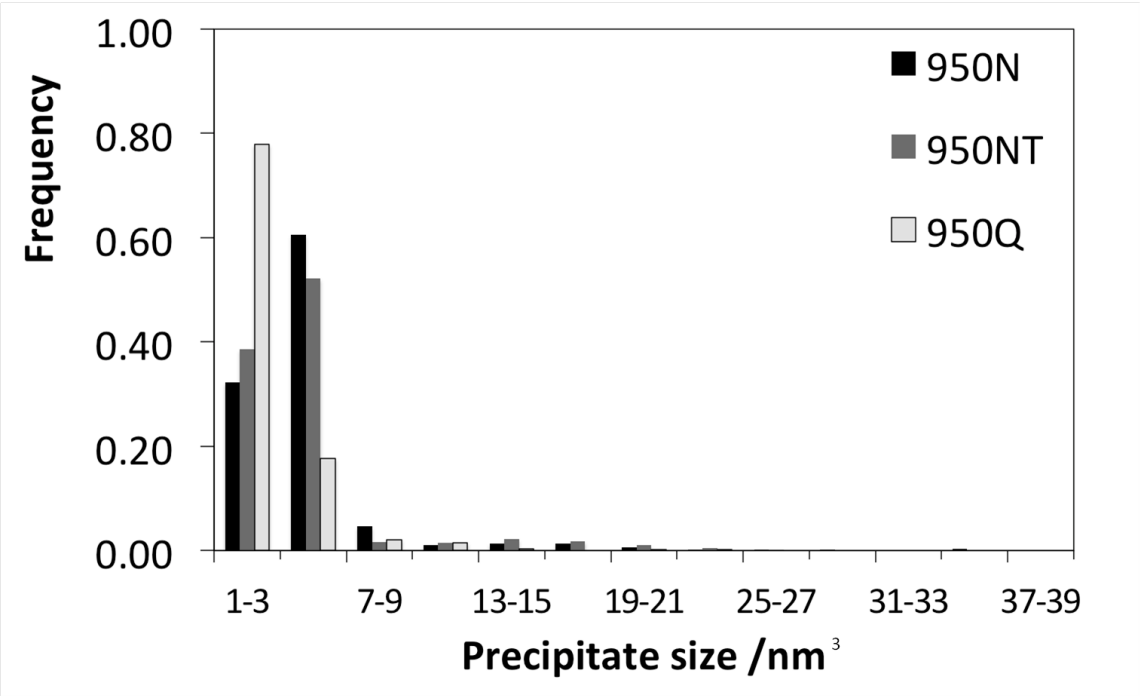

Figure 4.13: Precipitate volume distribution in 950Q, 950N and 950NT.

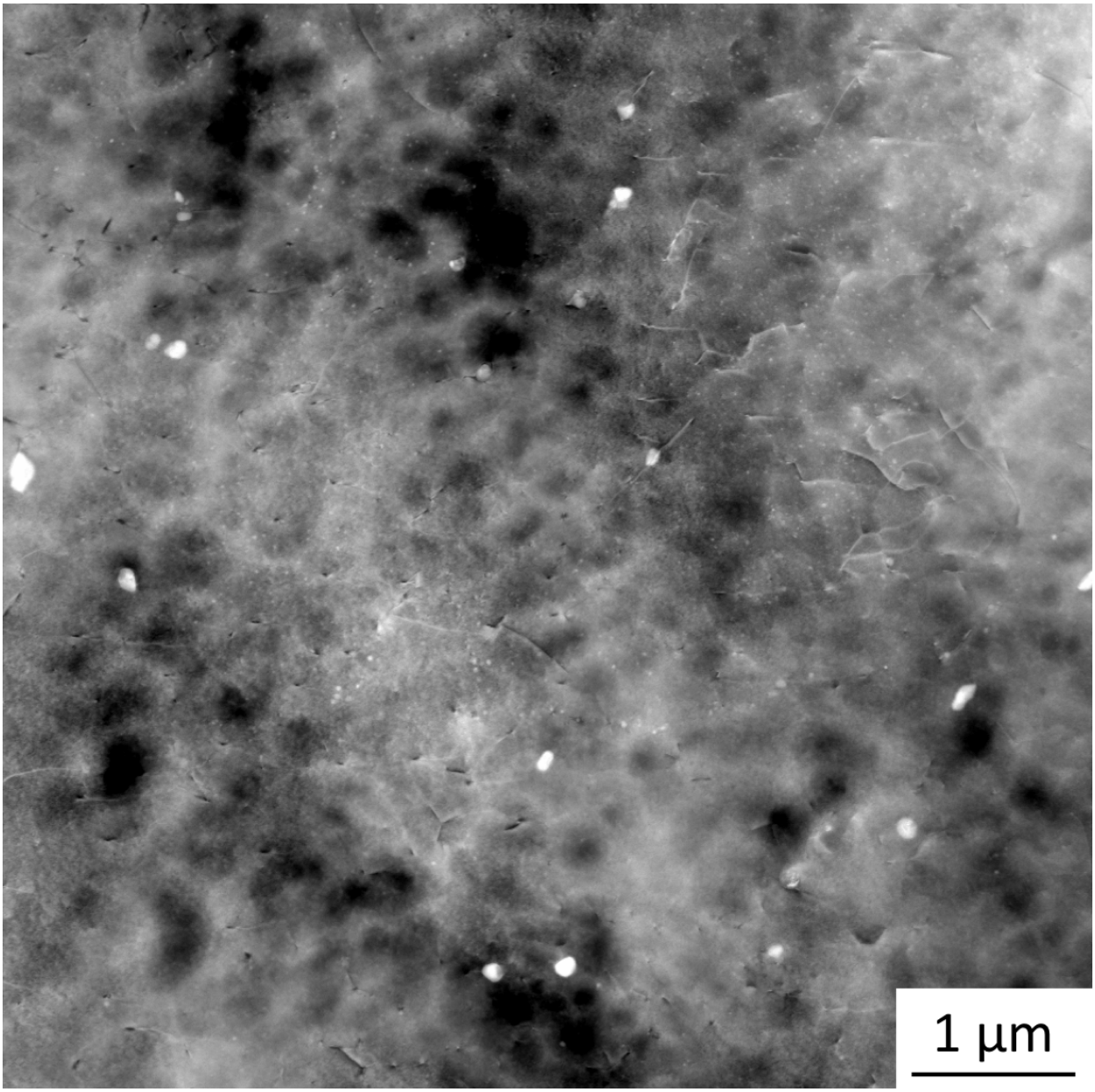

Figure 4.14: Transmission electron micrograph showing the range of precipitate sizes in 950NT.

The total number of precipitates significantly reduces on heating to 1100℃ to form **1100Q** indicated by the higher amount of dissolved Nb in table 4.7. Since finer precipitates will dissolve preferentially as has been discussed, the distribution indicated in figure 7.17 which is dominated by fine precipitates, observed in figure 4.16, is related to the shrinkage of precipitates during heating to and holding at 1100℃. Figures 4.16 and 4.14 show the dramatically different precipitate size distributions that evolve following heat treatment, with many more precipitates, both fine and coarse, in 950N. Only a few, fine precipitates are visible at the same magnification in figure 4.16. On tempering to form 1100QT, there is a notable increase in the volume fraction of NbC precipitates in table 4.4, along with an increment in the yield strength. The dispersion of fine precipitates can be observed in figure 4.17, with a number of precipitates at heterogeneous nucleation sites like grain boundaries. The relative increase in fine precipitates is reflected in the reduction of the entropy value, as a larger population of precipitates form within the smallest size bin.

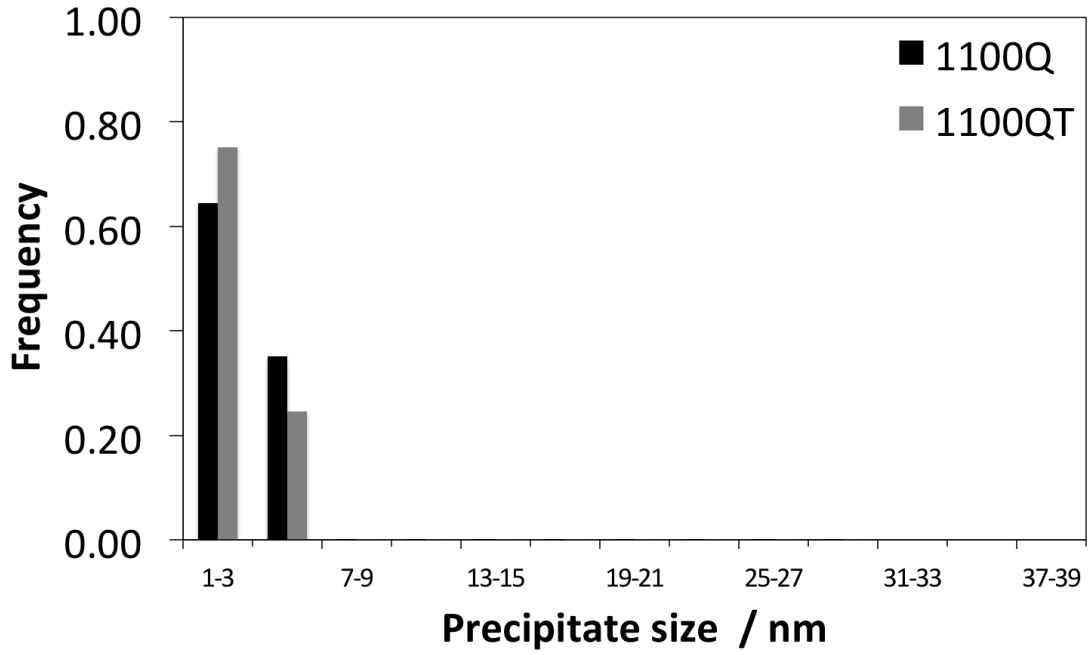

Figure 4.15: Precipitate size distribution in 1100Q and 1100QT.

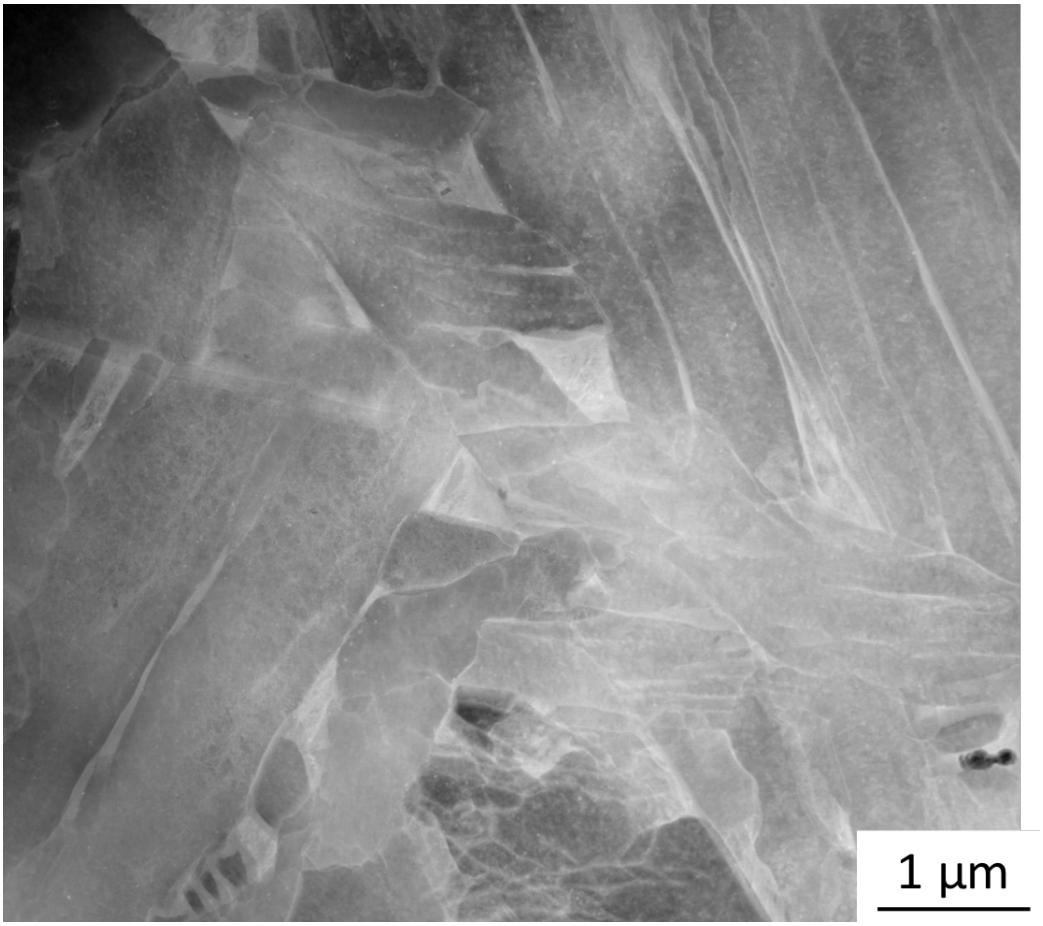

Figure 4.16: Transmission electron micrograph of 1100Q, the precipitates in the steel are very fine and not easily visible, but are noted in the SAXS data showing the precipitate size distribution.

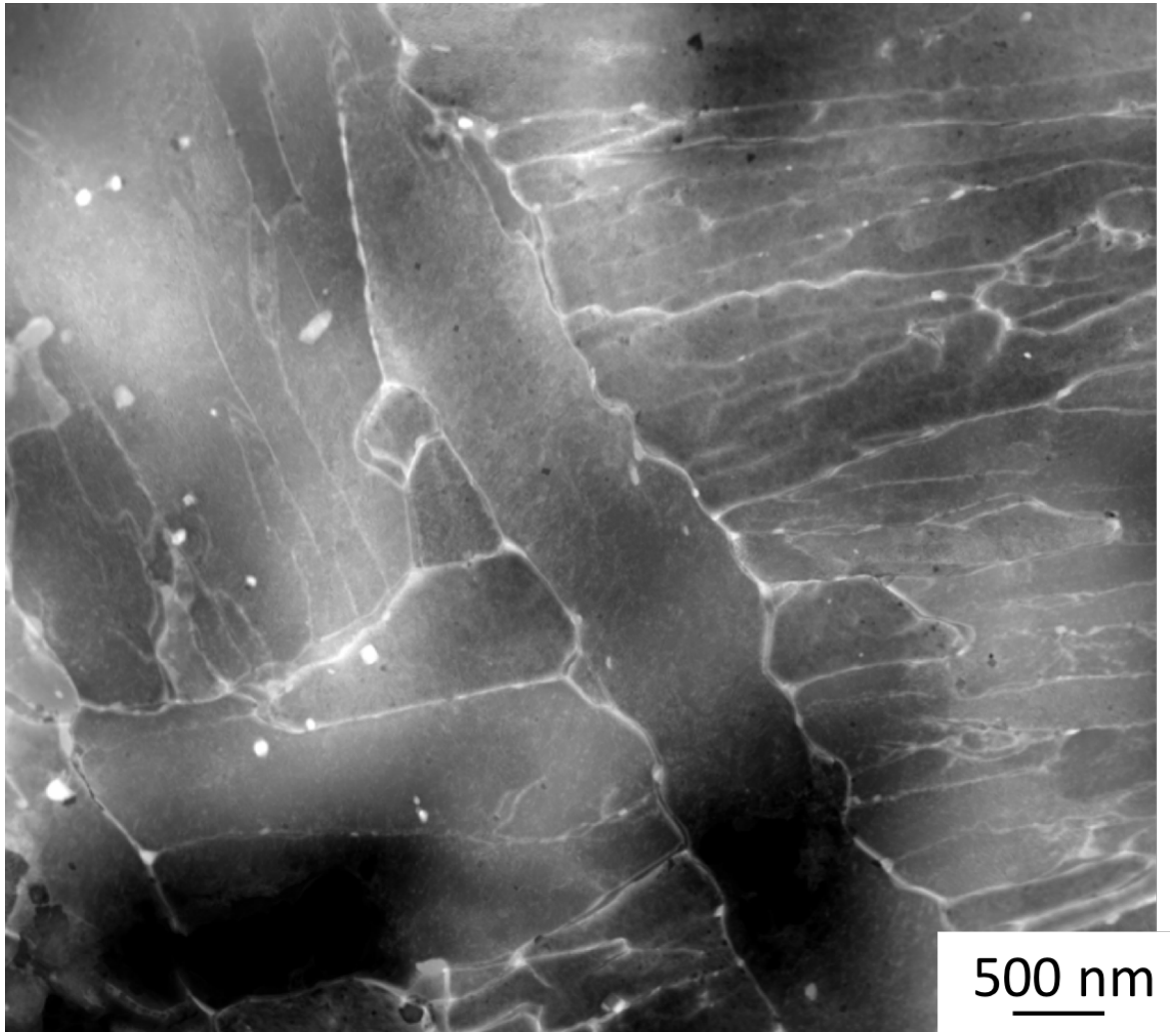

Figure 4.17: Transmission electron micrograph showing the a larger number of fine precipitates 1100QT.

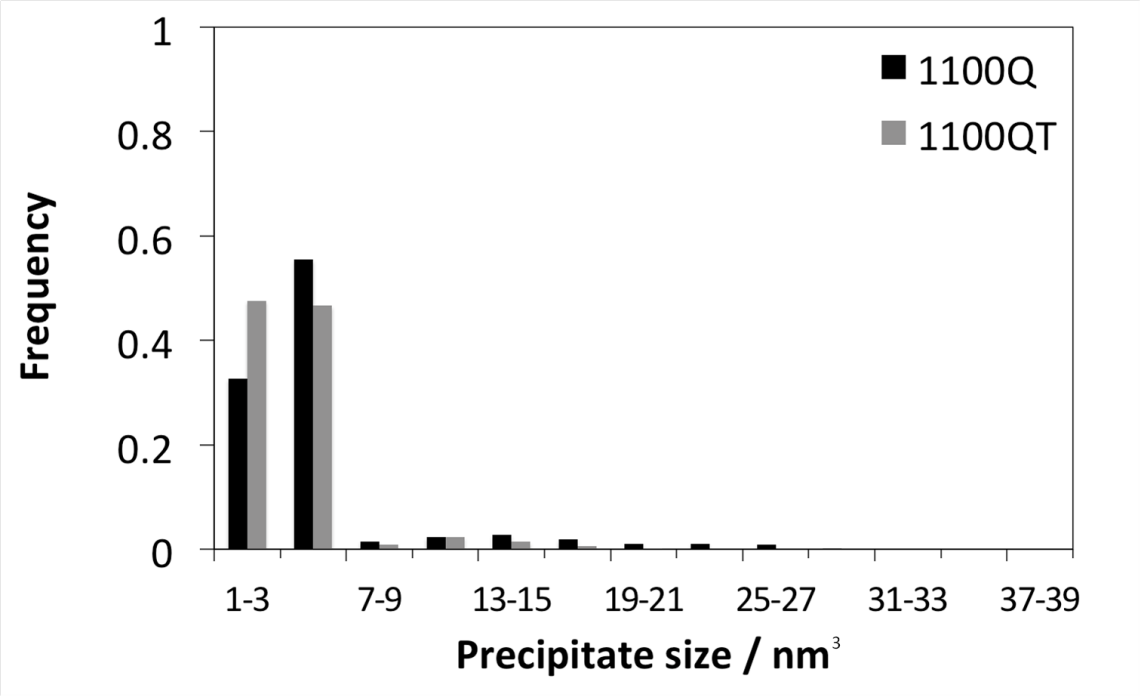

Figure 4.18: Precipitate volume distribution in 1100Q and 1100QT.

Heat treatment at 1230℃ leads to dissolution of the bulk of the NbC in **1230Q** and **1230QT** as is noted in table 4.7. The dissolution of the NbC is also noted in figure 7.24 where cuboid TiN is visible as the NbC, which nucleates heterogeneously on TiN precipitates, enters into solution. While few NbC precipitates exist following this heat treatment, the precipitates shrink into the smallest size bins. A comparison can be made of the relative amount of NbC in the volume distributions at each size bin in figure 4.20. The

relative reduction in NbC is notable following the hold at high temperature as well as the dominance of the finest precipitate sizes in the quenched plates, corroborated by the relative frequency in the precipitate size distribution in figure 7.22.

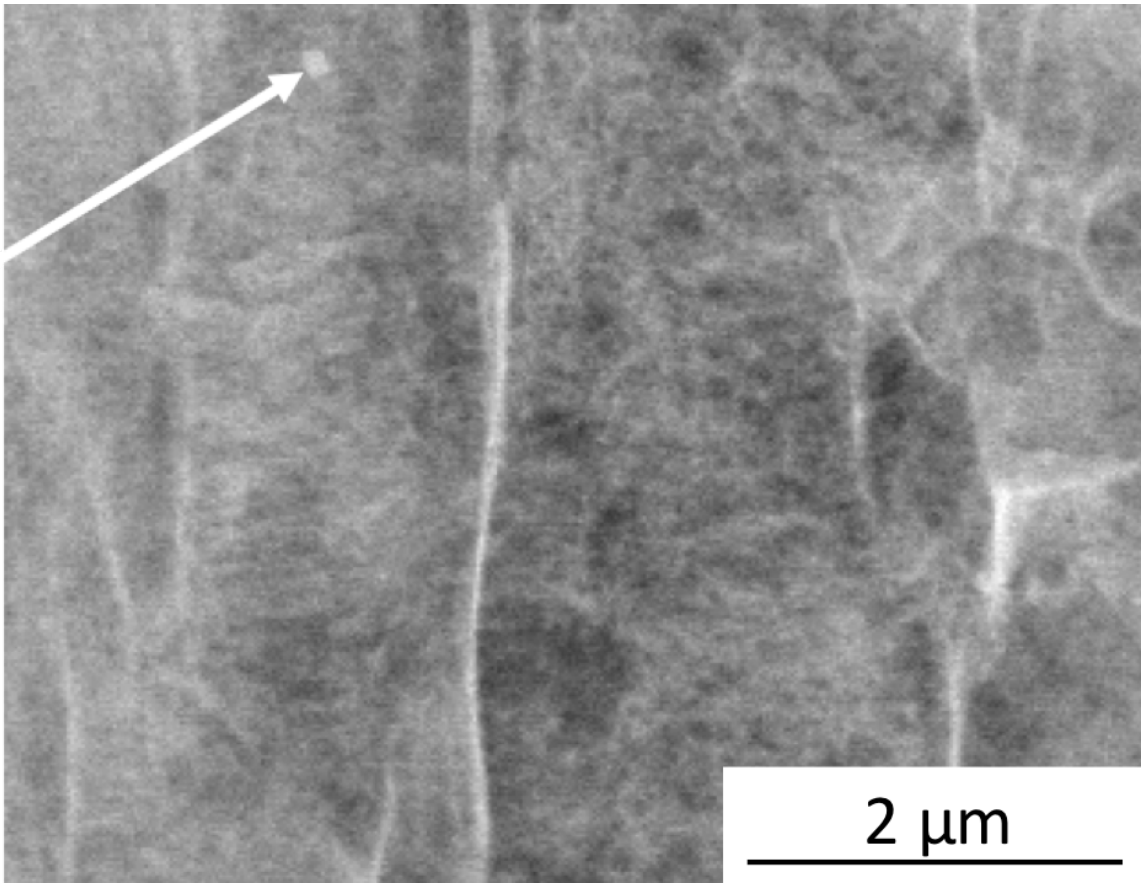

Figure 4.19: Transmission electron micrograph showing a stable TiN precipitate, visible with the bulk of the Nb in solution.

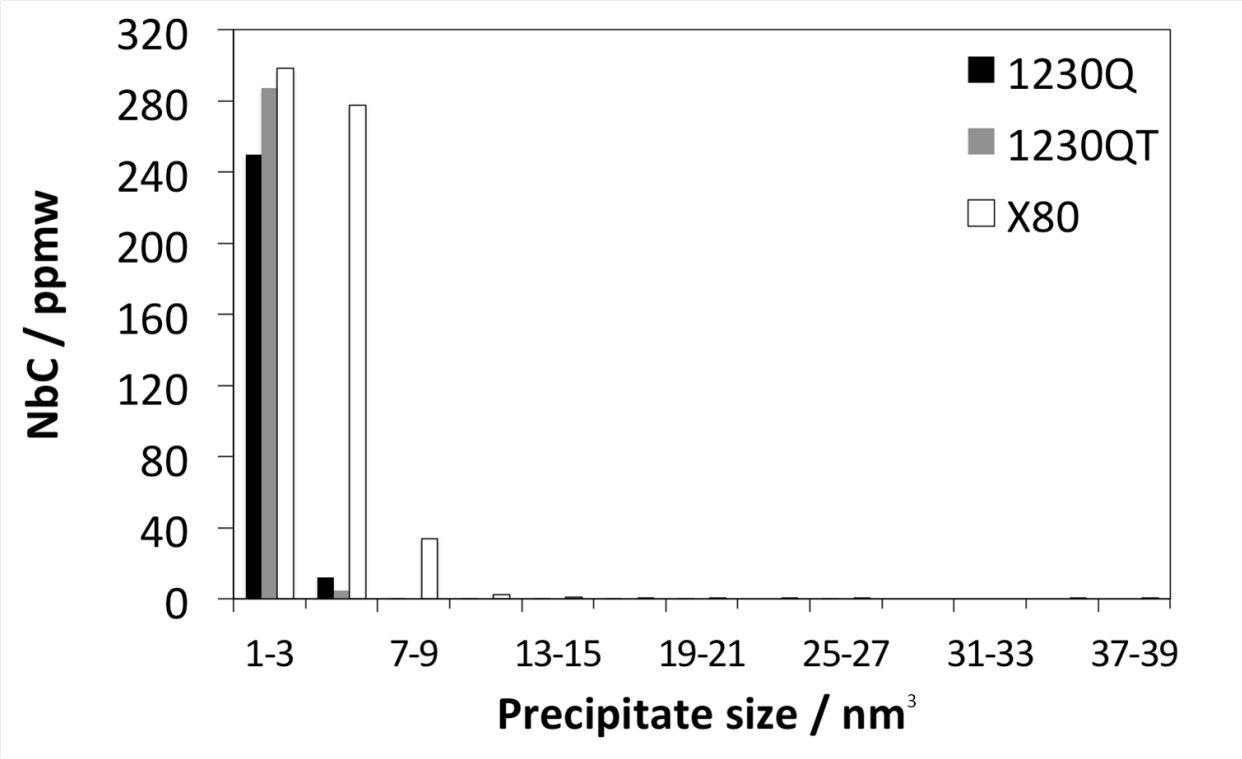

Figure 4.20: Precipitate volume distribution in X80, 1230Q and 1230QT showing the amount of NbC in each size bin.

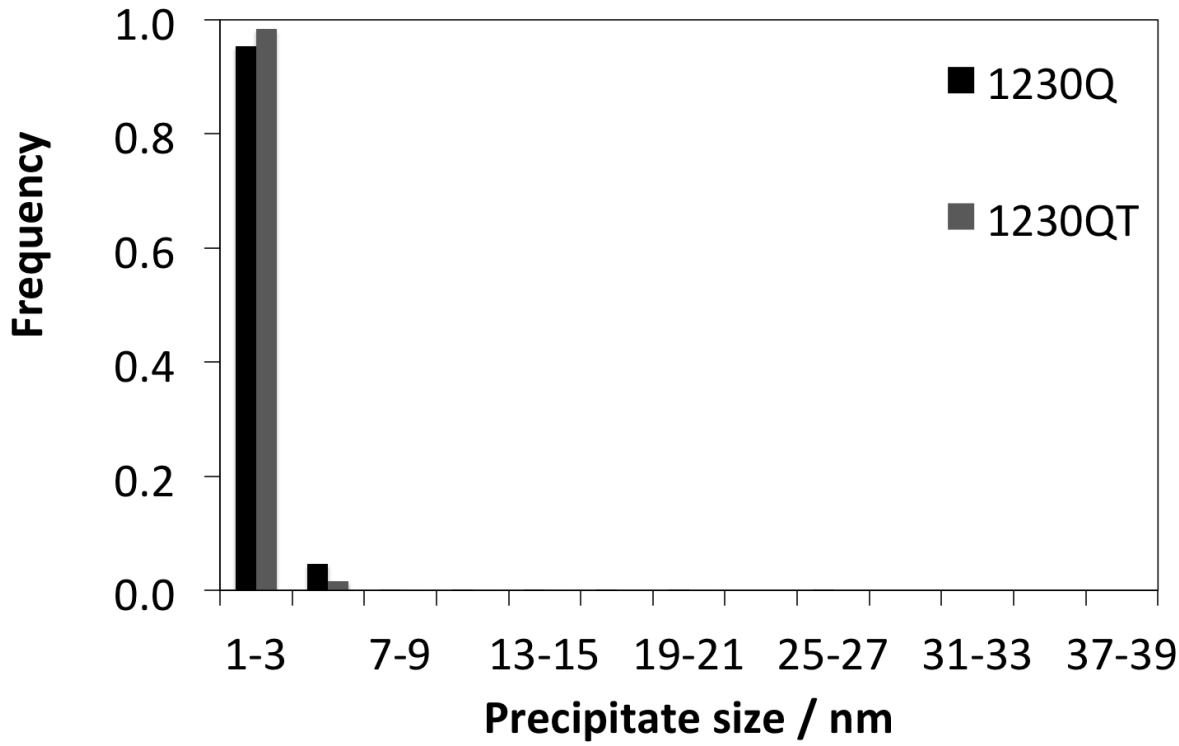

Figure 4.21: Precipitate size distribution in 1230Q and 1230QT.

4.6 Summary

This chapter has covered the measurement and evolution of varying precipitate distributions in the heat treated steel, along with some validation of the methodologies employed in characterizing the precipitates.

The volume fraction of precipitated NbC for each plate conditions has been assessed using ICP-MS, and applied in the validation of the SAXS data by calculating and comparing σ_{ppt} across the plate conditions. Higher contributions of σ_{ppt} to the yield strength were found to correlate to poor mechanical properties, while volume fractions of precipitates when correlated enhanced yield strength were inferred to be related to the nucleation of fine precipitates, where yield strength decreased, precipitation coarsening occurred.

The concept of precipitate entropy has been proposed, and a range of predictions were made using the existing data and the entropy values around the expected precipitate size distributions.

Precipitate distributions were analysed by consideration of the precipitate size and volume distribution. Dissolution at higher temperatures was confirmed with respect to the very much reduced precipitate counts associ-

ated with 1100Q and 1230Q. The nucleation of fine precipitates correlated to increments in mechanical properties, with precipitate coarsening as the dominant mechanism where a reduction in the properties was noted.

The full characterization of the precipitates will enable the analysis of the microstructural evolution of the heat treated plates, and hence, HAZ sub-zones in the following chapters.

Chapter 5

Prior austenite grain sizes in the HAZ

5.1 Introduction

The state of niobium in the heat treated X80 plates helps understand the evolution of microstructures . The influence of dissolved Nb and precipitated NbC is assessed on austenitisation as well as on subsequent transformations.

5.2 Austenitisation in the HAZ

The coarse and fine-grained regions of the HAZ result from complete austenitisation. Figure 5.1 shows that even at low magnification, these regions are

dramatically different from the parent plate microstructures illustrated in the far field.

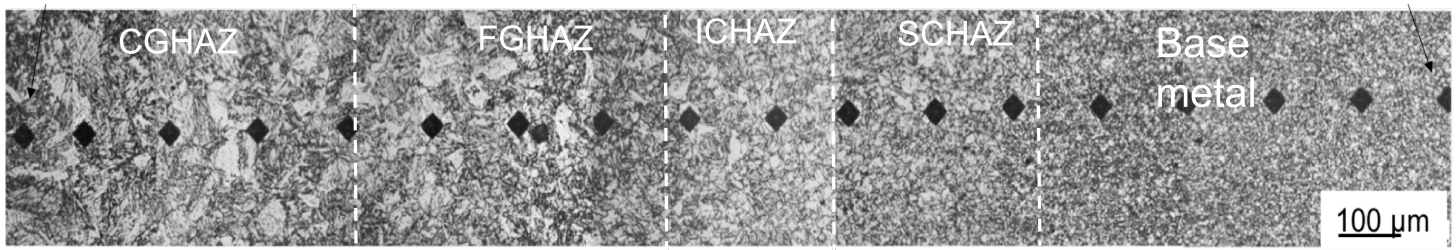

Figure 5.1: Illustration of approximate locations of the HAZ sub-zones in X80 welded with a 3.2 kJ/mm heat input. FGHAZ is the fine-grained heat-affected zone, ICHAZ is the inter-critical heat-affected zone, and SCHAZ is the sub-critical heat-affected zone.

5.2.1 Prior austentite grain sizes

The treated samples 950Q, 1100Q and 1230Q were austenitised at quite different temperatures so it is useful to characterise their austenite grain sizes. The data should reflect both the fundamental effect of temperature in accelerating kinetics and the role of niobium and its carbide. Prior austenite grain size measurements were taken following the experimental methodology described in Chapter 2.

T_γ / ℃	V_{NbC}	[Nb] / ppmw	d_γ / μm
950 ℃	9.8×10^{-4}	86	12 ± 2
1100 ℃	5.8×10^{-4}	438	28 ± 10
1230 ℃	3.0×10^{-4}	688	200 ± 20

Table 5.1: Prior austenite grain size measurements for 950Q, 1100Q and 1230Q. The samples were quenched at $80\,℃\,s^{-1}$. T_γ is the austenitising temperature, V_{NbC} is the volume fraction of NbC precipitates, [Nb] is the amount of niobium in solution and d_γ is the prior austenite grain size.

Austenitised at 950 ℃

Figure 5.2 shows that the precipitate size distribution associated with 950Q is dominated by fine particles with a majority of the Nb precipitated as NbC

(table 5.1), confirmed by microscopy as shown in figure 5.3, where a large number of fine precipitates can be identified. HAADF was used in order to enable easy identification of precipitates, the annular dark field image is formed by incoherently scattered, high angle electrons that are sensitive to variations in atomic number of elements in the sample, such that so-called Z-contrast images are formed, with elements with higher atomic numbers, such as Nb and Ti, as in figure 5.3, appearing as light coloured precipitates, in contrast to the darker iron matrix.

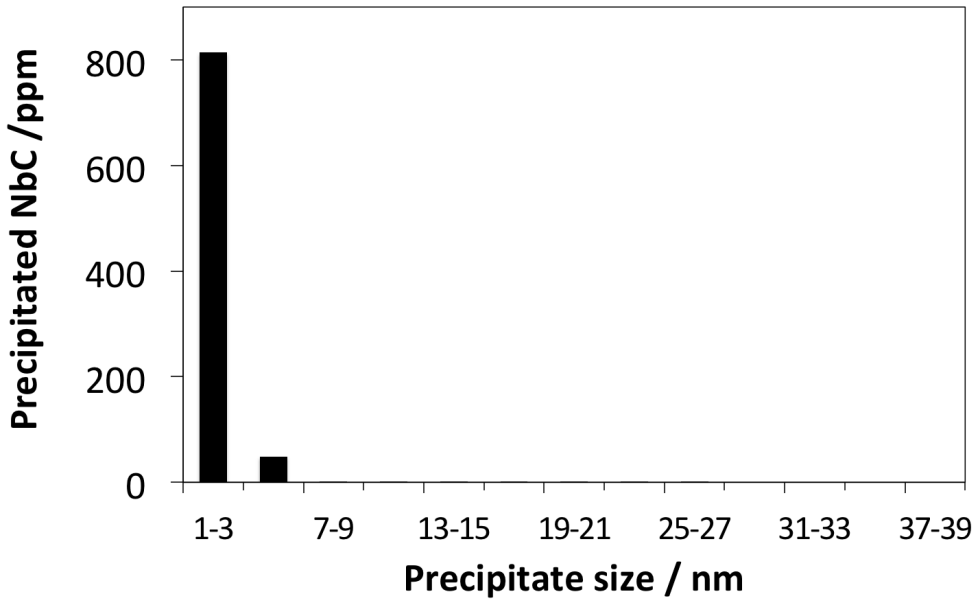

Figure 5.2: Precipitate size distribution in 950Q calculated using SAXS analysis of precipitate sizes, and the amount of Nb out of solution.

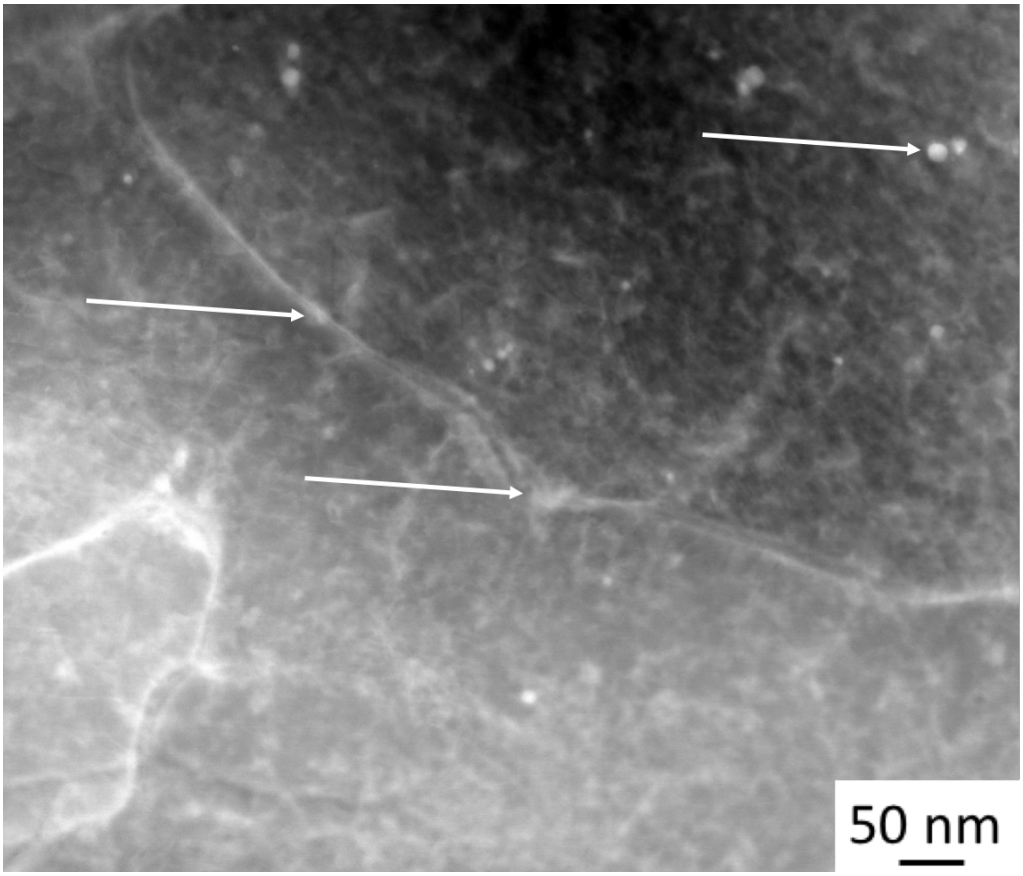

Figure 5.3: Transmission electron micrograph examination of 950Q using HAADF shows the a range of precipitates. The arrows indicate the locations of precipitates that have nucleated in the matrix and at the grain boundary. The spherical shape of the precipitates is consistent with that of NbC.

These fine precipitates resist asustenite grain boundary motion [115], as shown in Figure 5.4, therefore limiting grain size increasing beyond just 12μm (figure 5.5).

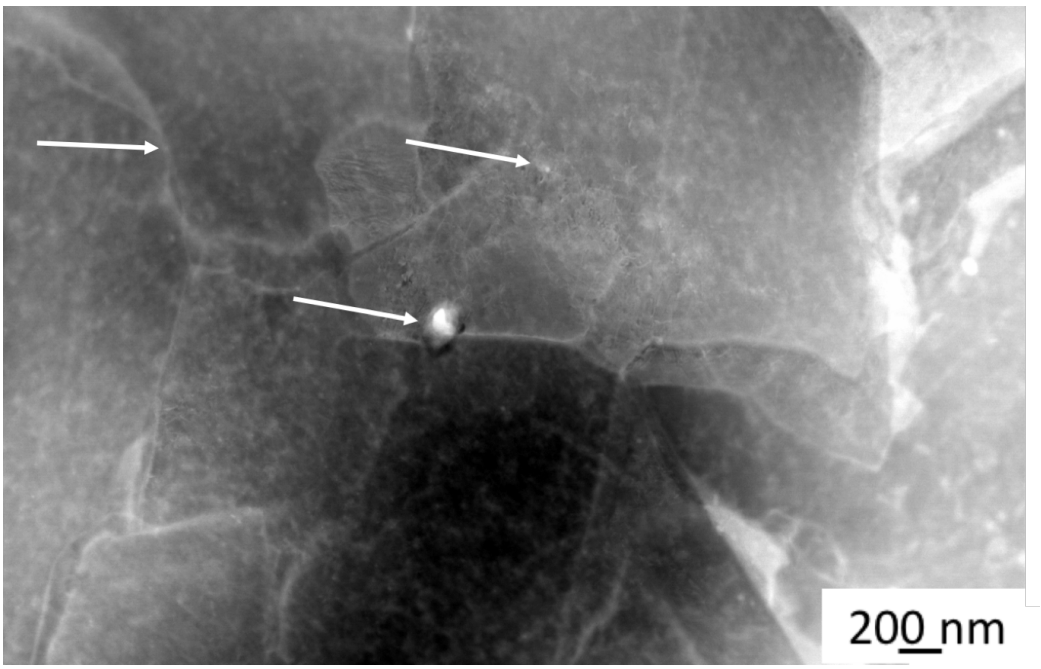

Figure 5.4: HAADF TEM micrograph taken of 950Q. The arrows indicate precipitates that have precipitated in the matrix and at a grain boundary.

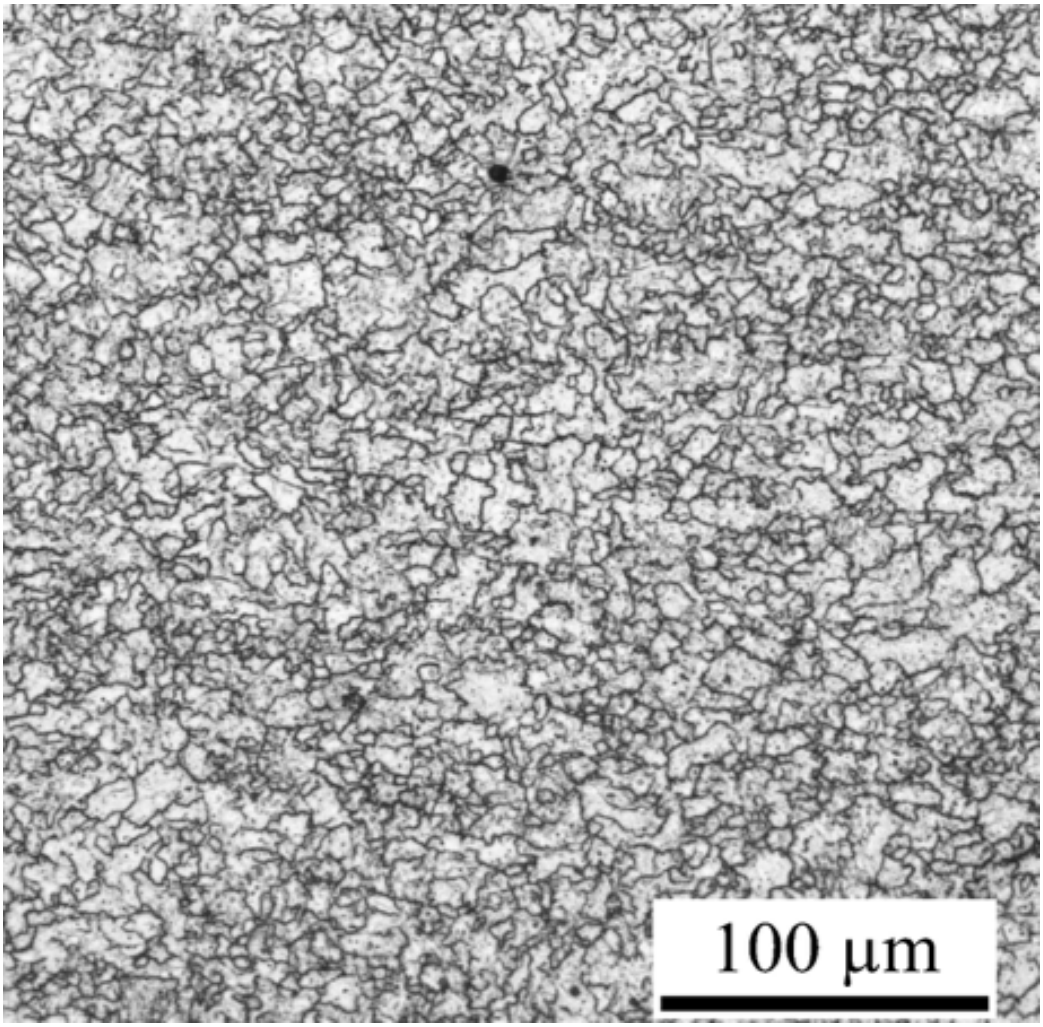

Figure 5.5: Prior austenite grain size revealed after thermally grooving at 950℃.

Austenitised at 1100℃

A larger proportion of NbC dissolves on heating to 1100℃,, with fewer of the fine variety available for pinning as illustrated in figure 5.6 with the dominant

size range at for the 950 ℃, T_γ.

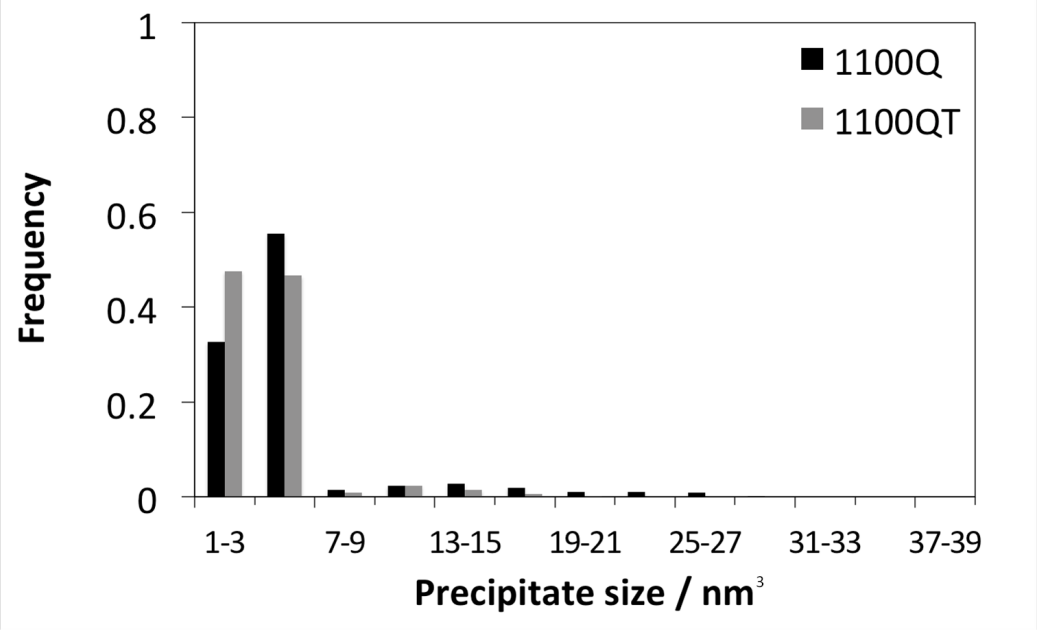

Figure 5.6: Precipitate volume distribution in 1100Q calculated using SAXS analysis of precipitate sizes.

This leads to an overall larger prior austenite grain size, at around 28 μm. However, figure 5.7, exhibits a range of grain sizes. Analysis of the grain sizes reveals a bimodal distribution in figure 5.8, where two distinct peaks are visible at 10 μm and 30 μm in the distribution of intercepts. The bimodal distribution of intercepts illustrated in figure 5.8 is typical of circumstances where the solubility of Nb increases to a point where the particles in some regions are able to dissolve before others, so that pinning forces themselves

are heterogeneously distributed.

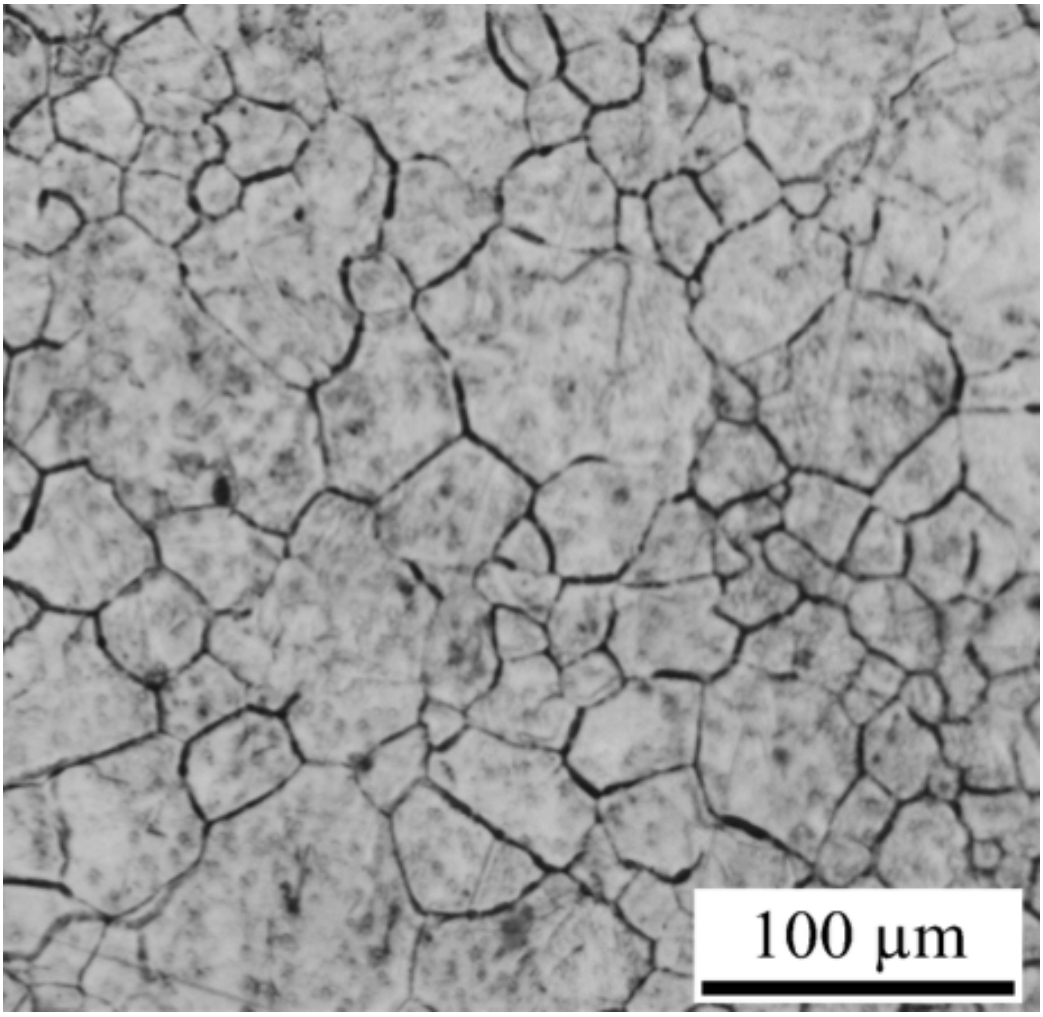

Figure 5.7: Prior austenite grain size after thermally grooving at 1100 ℃ by holding at this temperature for 1 hour under vacuum prior to quenching in helium.

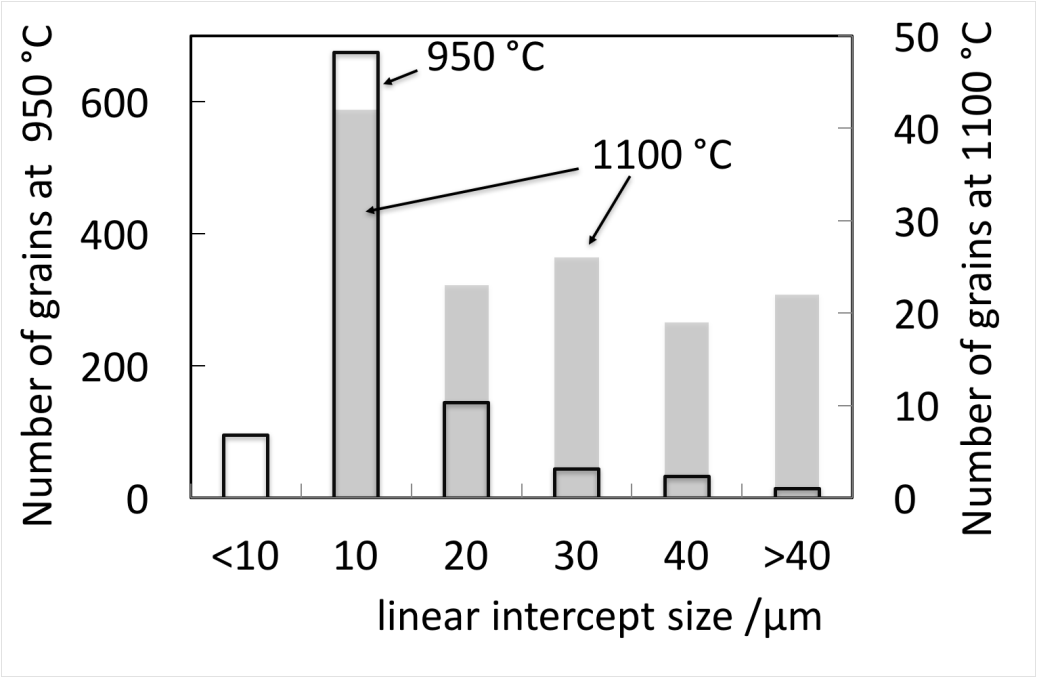

Figure 5.8: Bimodal distribution of prior austenite grain size at 1100℃ as compared to the distribution at 950℃ with a single maximum at 10µm.

Examination of 1100Q under transmission electron microscopy reveals apparently smaller grains with pinning precipitates at the grain boundaries, as well as possible evidence of larger grains in figure 5.9 if sectioning effects are ngelected. This is consistent with the findings from the thermal etching experiment, and the related bimodal intercept distribution in figure 5.8.

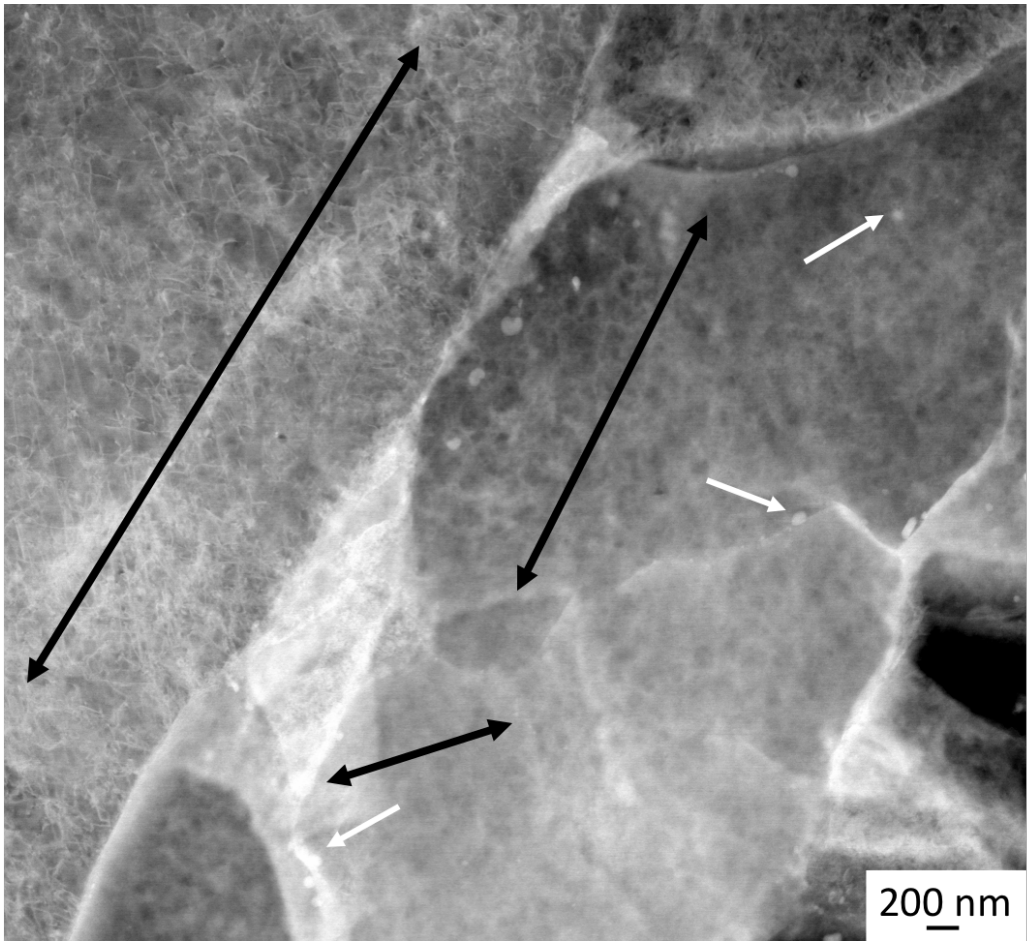

Figure 5.9: HAADF TEM micrograph of plate 1100Q. The white arrows indicate precipitates that have pinned grain boundaries. Black arrows highlight dramatically different grain sizes, assuming that the differences are large enough to not be classified as sectioning effects.

Austenitised at 1230℃

More NbC is able to dissolve at 1230℃, (figure 5.10) consistent with the large austenite grains in figure 5.11.

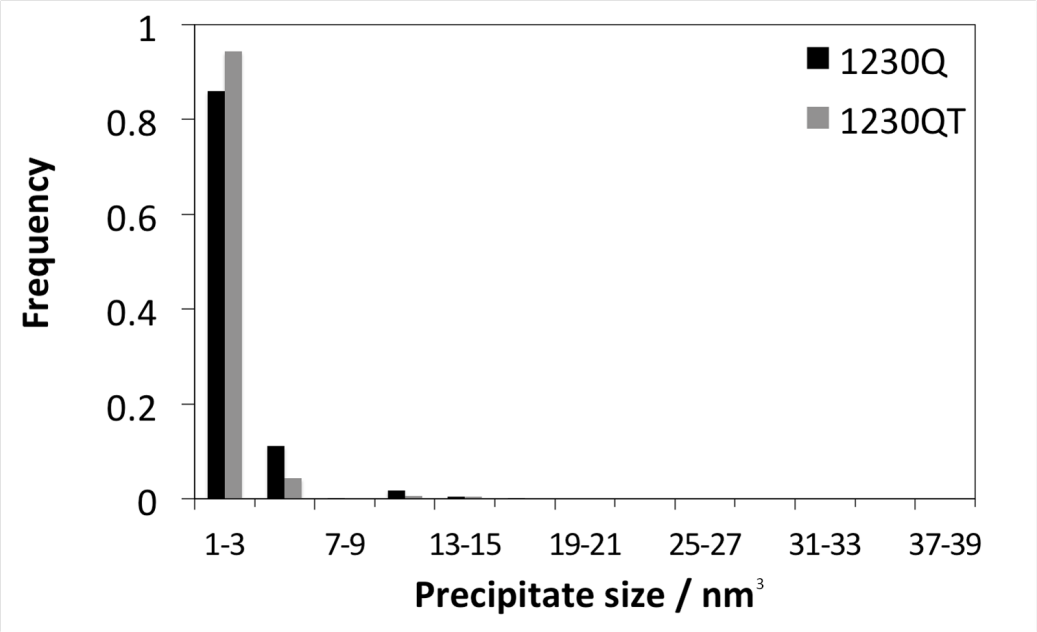

Figure 5.10: Precipitate volume distribution in 1230Q.

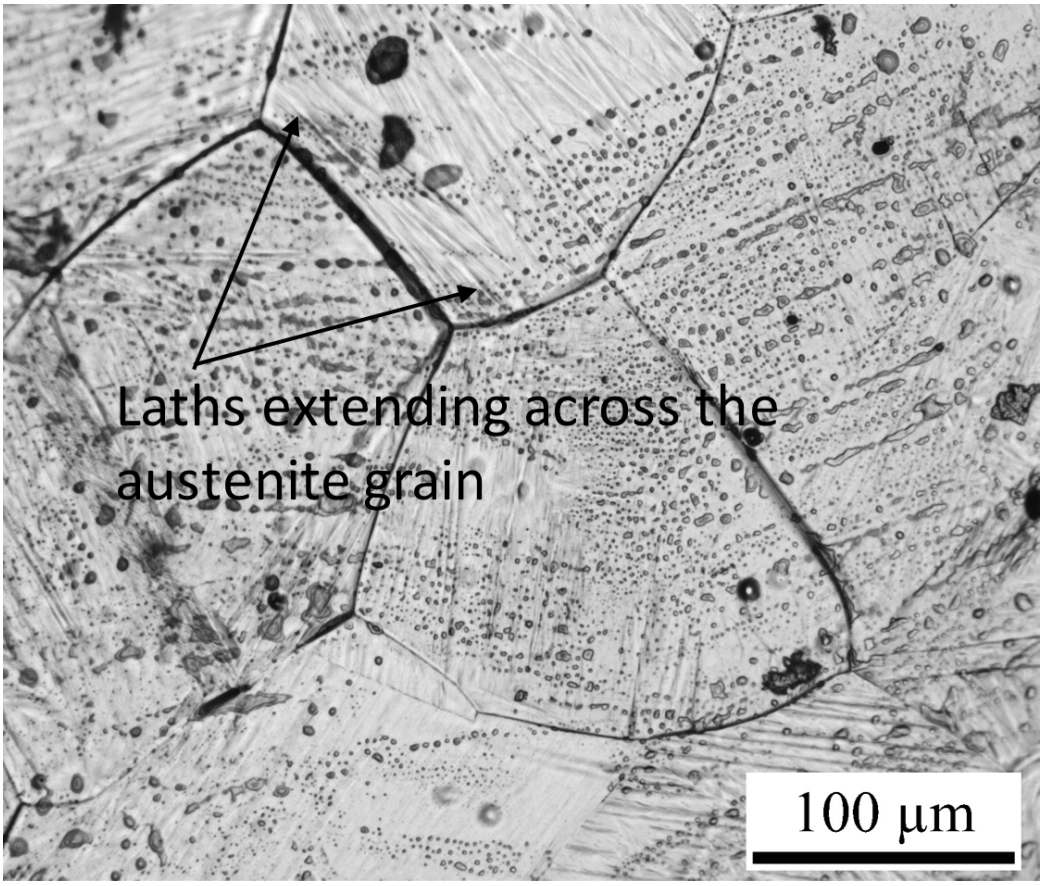

Figure 5.11: Prior austenite grain size after thermally etching at 1230℃. Laths can be observed across each individual grain. Grain size: $\overline{200} \pm 20\,\mu m$

The extent to which dissolution of NbC occurs at 1230 ℃ can be qualitatively assessed from figures 5.12 and 5.13. In figure 5.12, X80T, where only 344 ppmw on the Nb is in solution, shows a 'rabbit-ear' precipitate morphology of a niobium-titianium carbo-nitride (Nb,Ti(C,N)), where NbC nucleates on the more stable TiN. At 1230 ℃, the NbC dissolves to leave cuboid TiN precipitate which is stable up to 1300 ℃. Such a TiN precipitate can be observed in figure 5.13.

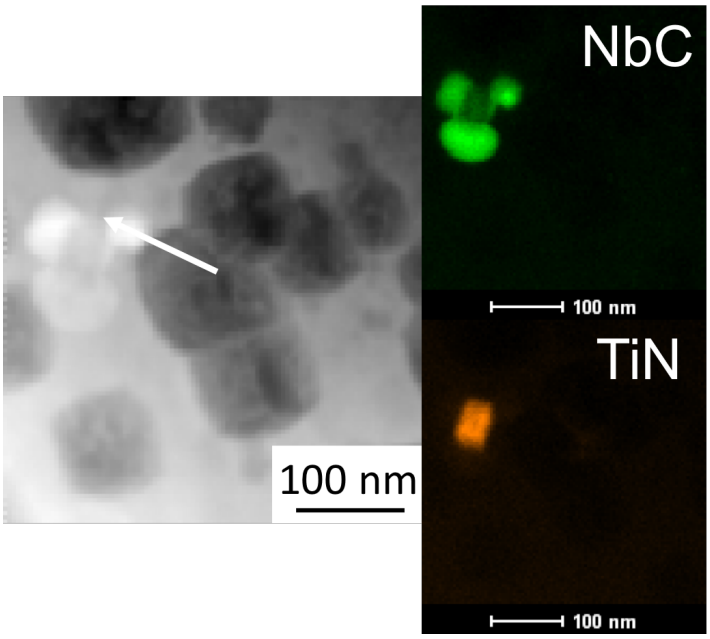

Figure 5.12: HAADF TEM micrograph of plate X80T showing the 'rabbit-ear' morphology of Nb,Ti(CN). EDX mapping with a dwell time of 300 ms, and a step-size of 2.5 nm was used to identify Nb and Ti.

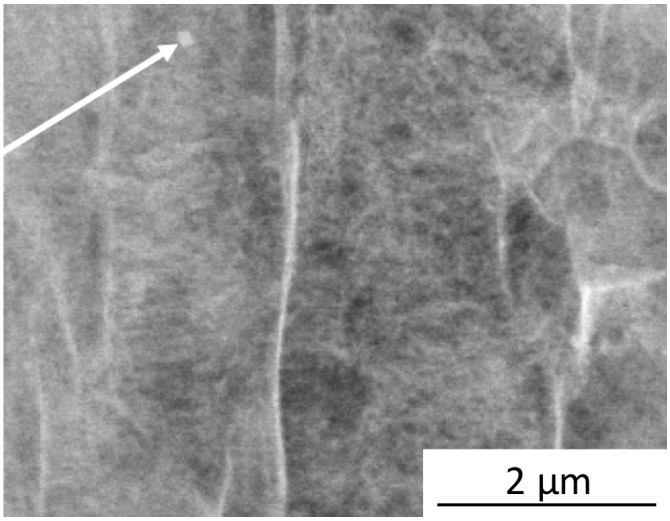

Figure 5.13: HAADF TEM micrograph of plate 1230Q. The dissolution of NbC reveals a cuboidal TiN precipitate, indicated by the arrow.

5.2.2 Summary

NbC precipitate size distribution has a dramatic effect on the evolution of the prior austenite grin size. The evidence of the martensite lath surface relief axtending across grains identified by the thermal grooving creted at high temperature corresponds to the locations of the austenite grain boundaries (figure 5.11.

It is worth considering the precipitate size entropy that has been previously proposed in this work, as it can be inferred that lower entropy values

will be consistent with unimodal distributions of the prior austenite grain sizes, while higher entropy distributions i.e those significant populations of different grain sizes will correlate to bimodal distributions. At 0.23, 950Q has a low entropy, consistent with a single, dominant precipitate size range, and from figure 5.8, results in a unimodal prior austenite grain size distribution. 1230Q also shows a low entropy, 0.19, consistent with a constant (large) prior austenite grain size. 1100Q, with a 0.68 entropy value (where the maximum value associated with the highest entropy is 0.91, and the median is 0.63), correlates to a bimodal distribution.

Chapter 6

Microstructural evolution in the heat treated steels

6.1 Introduction

Thermal etching has revealed the austenitic grains that form the precursors to the microstructures that developed following austenitisation, and hence across the HAZ of a weld. The discussion about the prior austenite grain size has necessarily focussed on the influence of NbC precipitates due to their dramatic effects on grain size control through pinning. However, the presence of Nb in solution also merits discussion as it has been shown to exert influence over phase transformations that occur during cooling [77, 78]. Dilatometery measurements were used to investigate the transformations.

6.1.1 Kinetics of phase transformations

A key feature of the HAZ is the fast heating and cooling thermal cycles that occur across the affected region. The temperature at which 50% of the microstructure has transformed to austenite, $T_{\gamma_{0.5}}$, during heating was determined.

Figure 5.11 shows evidence of surface relief on the austenite grain, consistent with martensite, it is possible that the stored strain energy due to shape deformation will enhance the kinetics of the transformation. However, although $T_{\gamma_{0.5}}$ is apparently lowest for 1230Q in figure 6.1, the differences for the three analysed plates, 1230Q, 1100Q and 950Q is around 5 ℃; within the uncertainty associated with the experimental method and analytical techniques. Therefore there is no significant variation in the kinetics of austenitisation detected on heating at $30\,℃\,s^{-1}$.

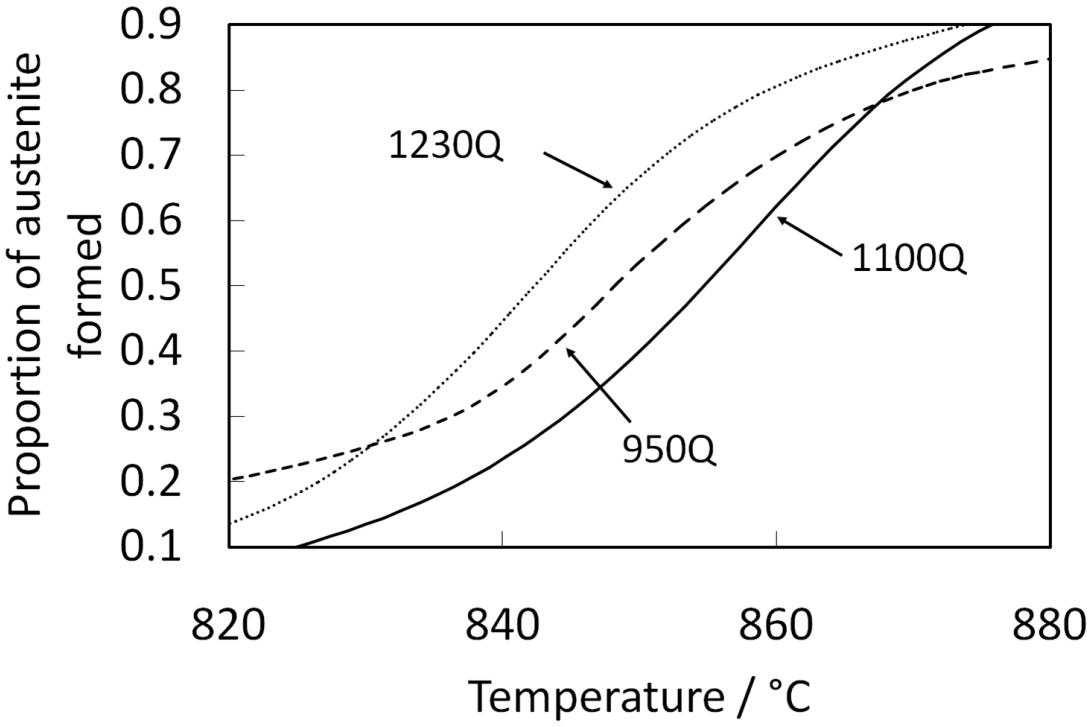

Figure 6.1: Proportion of austenite formed at a heating rate of 30℃ s^{-1}.

In the phase transformation range, an increase in Nb in solution will correlate to an increase in the transformation temperature when austenite first forms, Ac_1 [118]. Yan *et al.* show that prior austenite grain size and Nb in solution influence transformation temperatures [77]. The effect of these factors on the Ac_1 is listed in table 6.1.

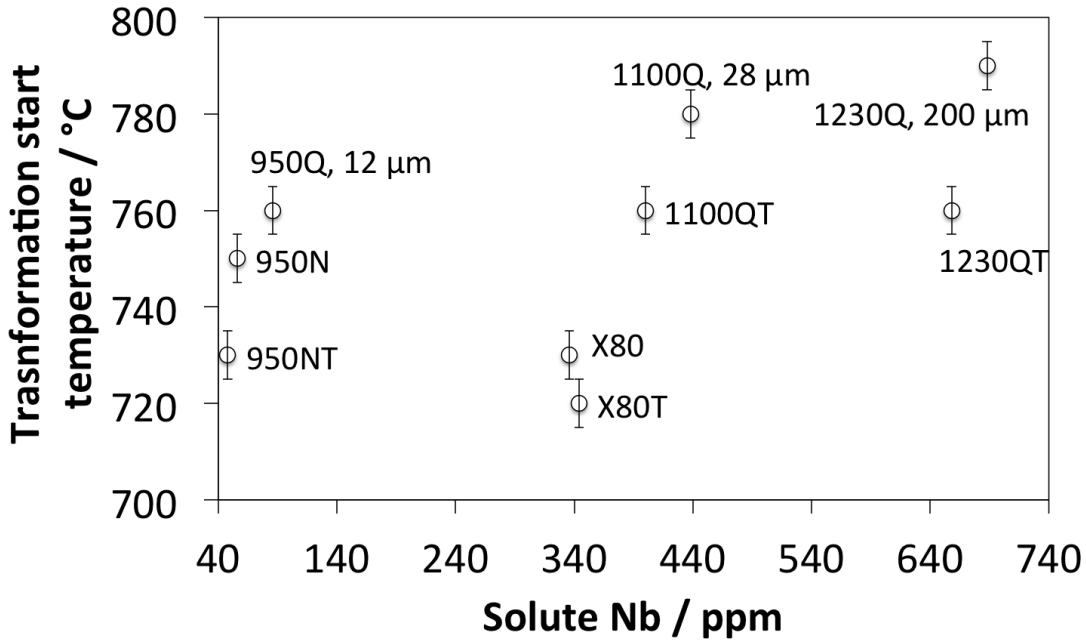

Figure 6.2: Influence of Nb on transformation start temperature on different plate conditions. The prior austenite grain size has been included for 950Q, 1100Q and 1230Q

Plate Identification	Nb in solution/ppmw	Transformation start temperature, $Ac_1/\pm 5$ ℃	Dilatometry offset
1230Q	688	790	1×10^{-5}
1230QT	658	760	1×10^{-5}
1100Q	438	780	1×10^{-5}
1100QT	400	760	1×10^{-5}
950Q	86	760	1×10^{-5}
950N	56	750	1×10^{-5}
950NT	48	730	1×10^{-5}
X80	336	720	1×10^{-5}
X80T	344	715	1×10^{-5}

Table 6.1: Summary of data from measurements using a Dil-805A dilatometer. Samples taken from the heat treated plates were heated to 1300 ℃ at a rate of 30 ℃ s^{-1}.

Figure 6.2 shows the correlation of the Ac_1 temperature, i.e. the transformation start temperature, with dissolved Nb. The prior austenite grain size data for plates 950Q, 1100Q and 1230Q, show increasing transformation temperature with the increasing austenite grain size(figure 6.2). The tempering treatment at 650 ℃ obviously has no influence on the austenite grain size so changes are related to variations in dissolved Nb annd general tempering phenomenon such as dislocation recovery. All plate conditions show an increase in the transformation start temperature with increasing Nb in solution in table6.1 and figure 6.2.

The discussion thus far has focussed on the effects of Nb on phase transformations during heating. In this section the phases that form on cooling are analysed. Samples of X80 were heated to 1300 ℃, at 30 ℃ s^{-1} held for 5 s, and quenched at 80 ℃ s^{-1}, using controlled heating and cooling rates in a dilatometer. The transformation temperatures were derived using the offset method, and presented in figure 6.5 where phases transformations that evolved across a range of cooling rates are shown.

Yan et al. calculated a range of critical tempertures for Nb-microalloyed X80 steel [78]. The martensite start temperature for X80 steel, M_s, the tempertaure at which martensite forms, is around 464 ℃ and the bainite

transformation region is between 500 ℃ and 600 ℃, the formation of allotrimorphic ferrite occurs above 600 ℃, and at cooling rates around 5 ℃ s^{-1} as reported in [113].

Figure 6.5 shows that phase transformations in the quenched plates are likely to contain bainite and martensite phases across.

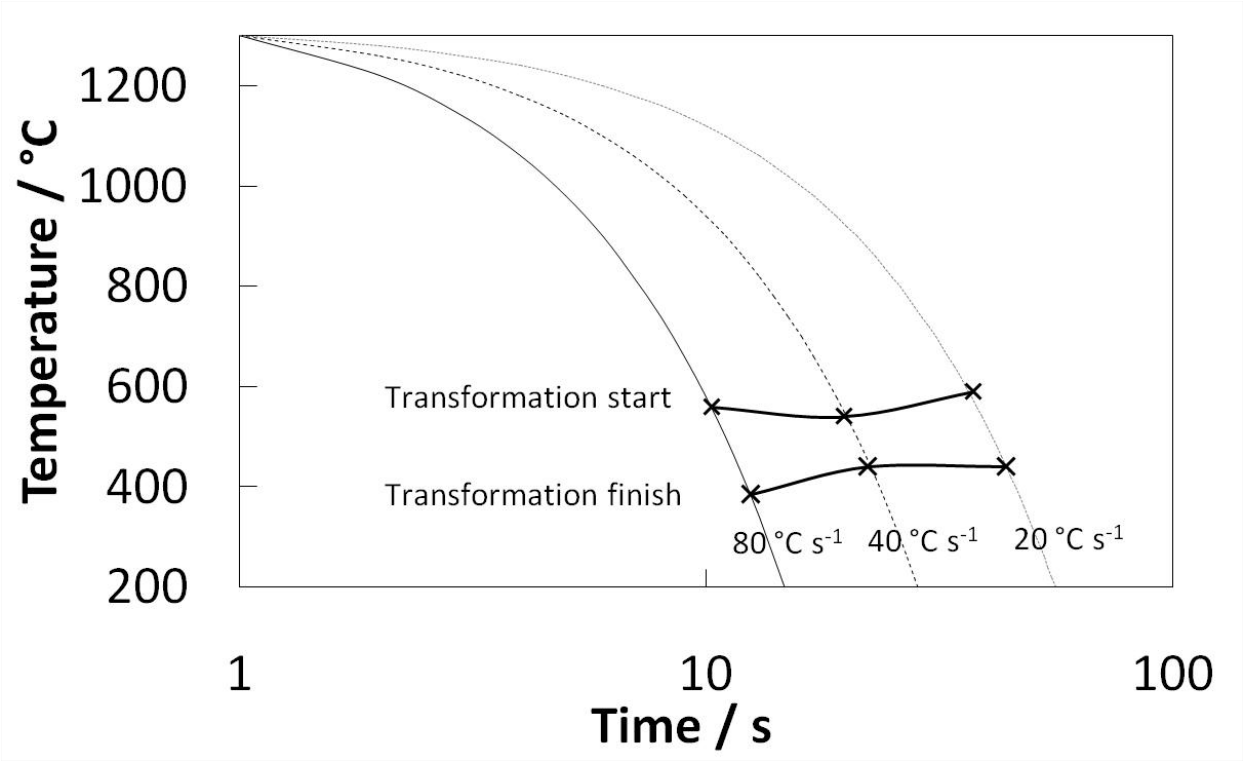

Figure 6.3: Continuous-cooling-transformation (CCT) for X80 on controlled cooling, over a range of cooling rates, from 1300 ℃.

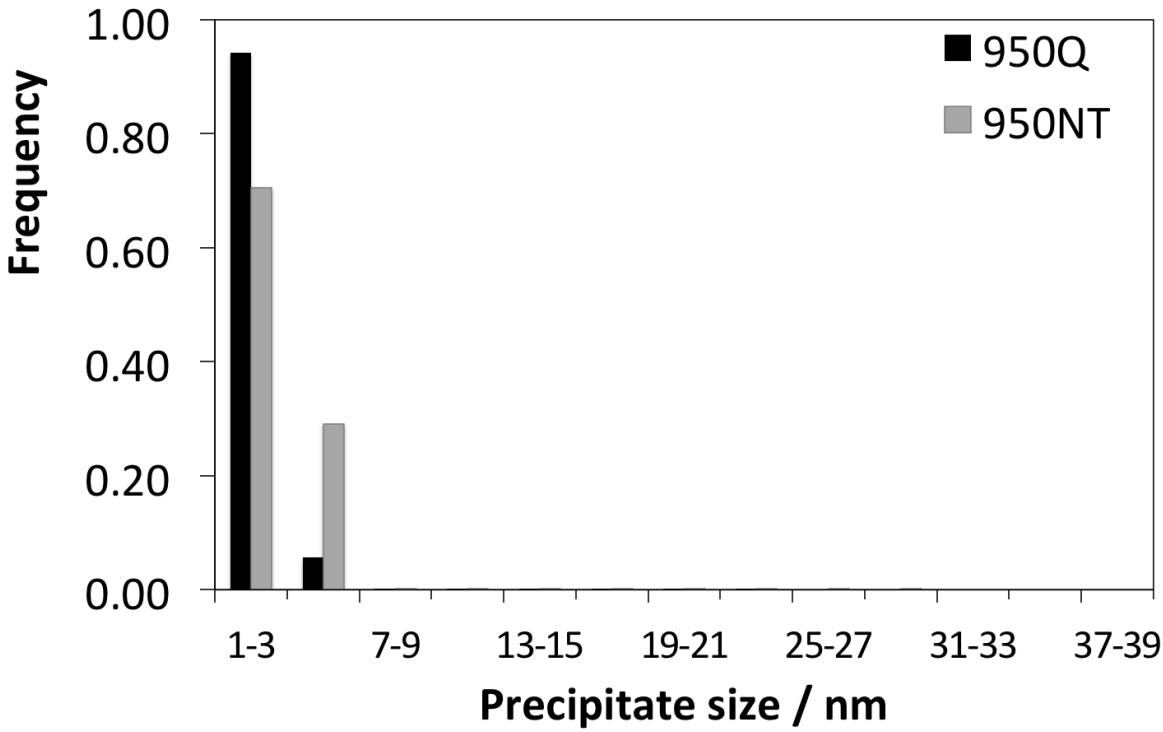

Figure 6.4: Precipitate size distribution in 950Q and 950NT.

6.1.2 Phase transformations on cooling

The transformation temperatures of the heated samples, on controlled cooling in a dilatometer are shown in figure 6.5 where phases transformations that evolved across a range of cooling rates.

Yan *et al.* calculated a range of critical tempertures for Nb-microalloyed X80 steel [78]. The martensite start temperature for X80 steel, M_s, the tempertaure at which martensite forms, is around 464 ℃ and the bainite transformation region is between 500 ℃ and 600 ℃, the formation of allotrimorphic ferrite occurs above 600 ℃, and at cooling rates around $5\,℃\,s^{-1}$ as reported in [113].

Figure 6.5 shows that phase transformations in the quenched plates are likely to contain bainite and martensite phases across the range of cooling rates studied.

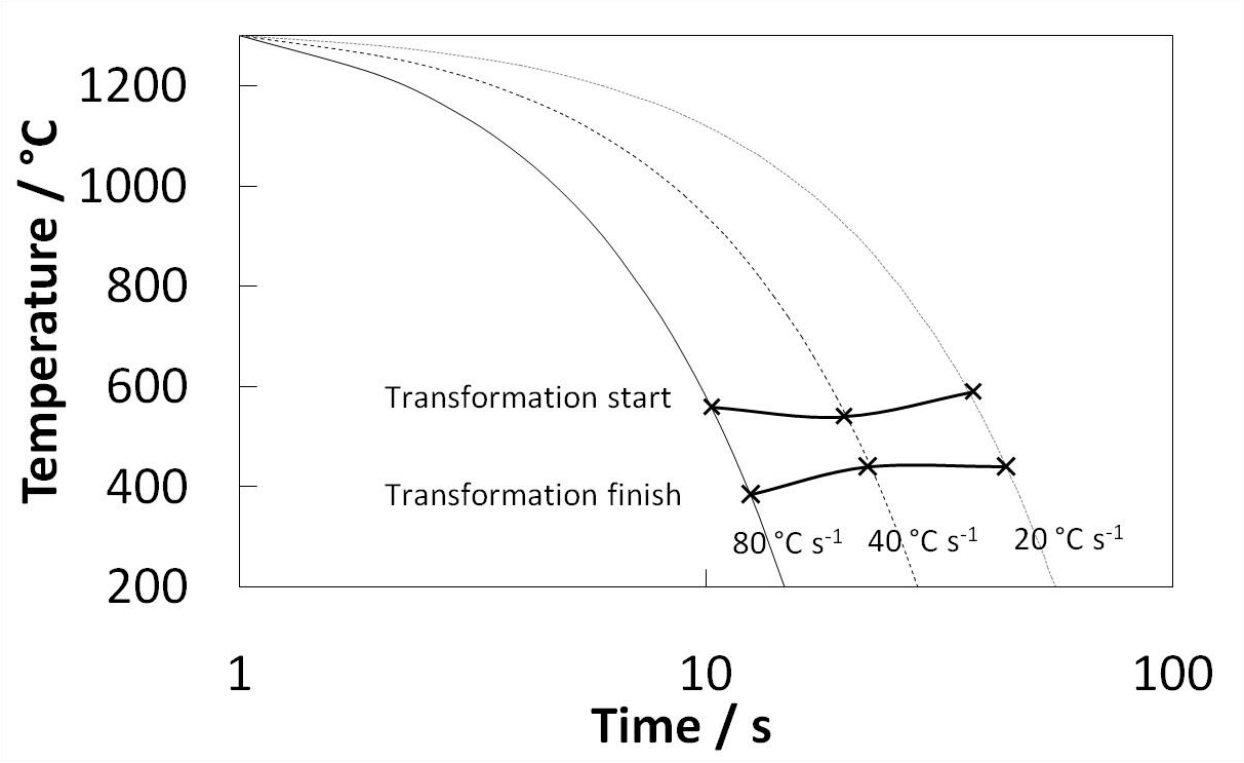

Figure 6.5: Continuous-cooling-transformation (CCT) for X80 on controlled cooling, over a range of cooling rates, from 1300 ℃.

6.1.3 Summary

Nb in solution increases the transformation temperature on heating. The high grain boundary area per unit volume and fine precipitate sizes associated with X80 and X80T correlates with the lowest transformation temperatures.

A greater hardenability is apparent when the amount of Nb that dissolves during austenitisation increases. It is not surprising therefore that

austenitisation at 950℃, where much of the Nb is precipitated shows the lowest hardenability. The data analysed in previous sections can be used to make some predictions about the microstructures that will evolve based on the heat treatments in table 2.2.

While the issue of hardenability has only been explored in the case of X80 steels, the CCT experiments form a basis for proceeding with further experiments that will enable assessment of the microstructures that develop in the CGHAZ to include the effect of solute Nb on hardenability.

Chapter 7

The effect of Nb on microstructures

7.1 Introduction

The state of niobium in the heat treated plates helps understand the evolution of microstructures. The influence of dissolved Nb and precipitated NbC is assessed on austenitisation as well as on subsequent transformations.

7.2 Mechanical testing

Initial work following production of the heat treated plates focussed on the characterisation of the plates using tensile testing and hardness measure-

ments in order to analyse variations across the heat-affected zone.

There was clear evidence of the influence of precipitation strengthening, with the quenched and tempered plates showing increments in yield strength and hardness, in table 7.1. The yield strength for the as-received plate X80 is consistent with the product specification defined in level 2 (PSL2) in ISO 3183:2007 for X80 steel at 555 MPa.

Plate number	Proof strength, $R_{p0.2}$ / MPa	Hardness / HV10
X80T	553*	208 ± 1
950N	330*	164 ± 3
950NT	320*	153 ± 2
1100Q	450	213 ± 2
950Q	380	212 ± 3
1230Q	480	227 ± 3
1230QT	587	250 ± 3
X80	546	212 ± 3
1100QT	630	220 ± 3

Table 7.1: Mechanical properties of heat treated X80 steel. For *, the lower yield stress has been reported.

7.3 Weld simulations

It has been demonstrated that Nb affects the transformation temperature during austenitisation. The influence of Nb during the cooling of austenite, specifically on delaying the transformation of austenite to allotriomorphic ferrite is an established phenomenon that is leveraged in the thermomechnical processing of microalloyed steels [6]. Yan *et al.* show that for the same prior austenite grain size, Nb in solution led to a reduction in the austenite grain boundary energy, resulting in suppression of the transformation start temperature. This is because heterogeneous nucleation on grain boundaries is more effective when the latter have a high interficial energy per unit area. Heterogeneous nucleation involves the elimination of a segment of boundary and hence a reduction of net energy that is not found during homogeneous nucleation [77].

The behaviour of the plates, heat treated in order to control the amount of Nb in solution, under examination are expected to be consistent with these phenomena:

1. The plate condition should show an increase in the γ to α transformation start temperature with a reduction of Nb in solution due to

precipitation.

2. A reduction in transformation temperature should occur with increasing prior austenite grain size, simply because of the corresponding reduction in the number density of nucleation sites. Plates heat treated at 950℃ with higher transformation temperatures as opposed to the larger prior austenite grain sizes in those heat treated at 1100℃ and 1230℃.

By using heat treatments that simulate the thermal cycle close to the weld fusion line [4, 119, 120] to include quenching; transformation temperatures were investigated using dilatometry (with the full range of resultant curves included in Appendix 2) in order to examine the total effect exerted by the variations in plate conditions. The resultant data e.g. prior austenite grain sizes should not be treated as conclusive due to the limited sample sizes used, but do offer useful insight.

The properties and transformation temperatures shown in table 7.2 are based on quenching at $80\,℃\,s^{-1}$ from 1300℃.

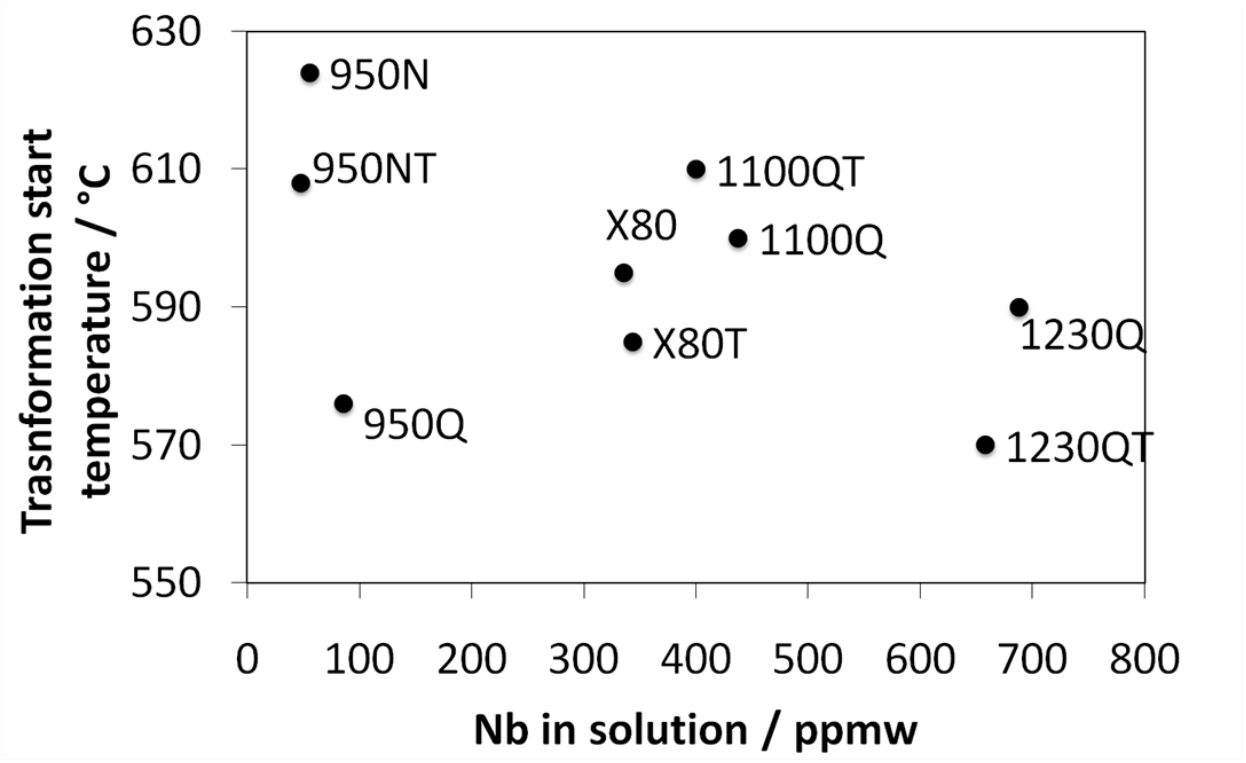

Figure 7.1: Variations in the transformation start temperature with dissolved Nb.

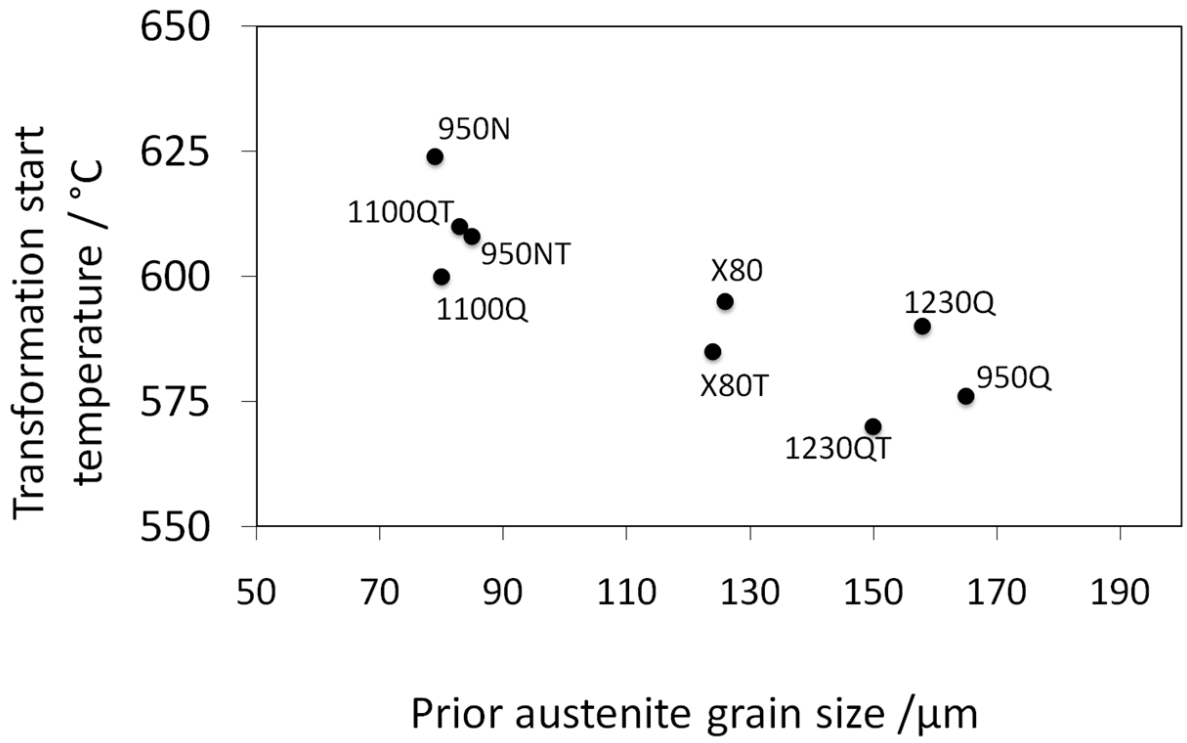

Figure 7.2: Variations in the transformation start temperature with the prior austenite grain size measured from the dilatometric samples.

Plate Number	Start temp. /℃	Finish temp. /℃	Hardness /HV10	γ grain size / μm	Precipitate heterogeneity	Dissolved Nb /ppmw
X80	510	380	246 ± 8	126 ± 17	0.91	336
X80T	534	389	234 ± 2	124 ± 13	0.71	344
950N	585	462	322 ± 2	79 ± 11	0.68	56
950NT	603	440	290 ± 2	85 ± 10	0.63	48
1100Q	538	427	241 ± 4	80 ± 18	0.68	438
1100QT	534	412	283 ± 1	83 ± 18	0.57	400
950Q	572	422	259 ± 2	165 ± 60	0.23	86
1230Q	588	400	282 ± 6	158 ± 25	0.19	688
1230QT	575	392	260 ± 1	150 ± 55	0.08	658

Table 7.2: Summary of dilatometry and hardness data collected using cooling rate of 80 ℃ s^{-1} from 1300 ℃. An offset of 1×10^{-4} was used in order to calculate the transformation temperatures .

7.4 X80

Figure 7.3 shows the conventional bainitic microstructure of X80 associated with X80 linepipe steel.

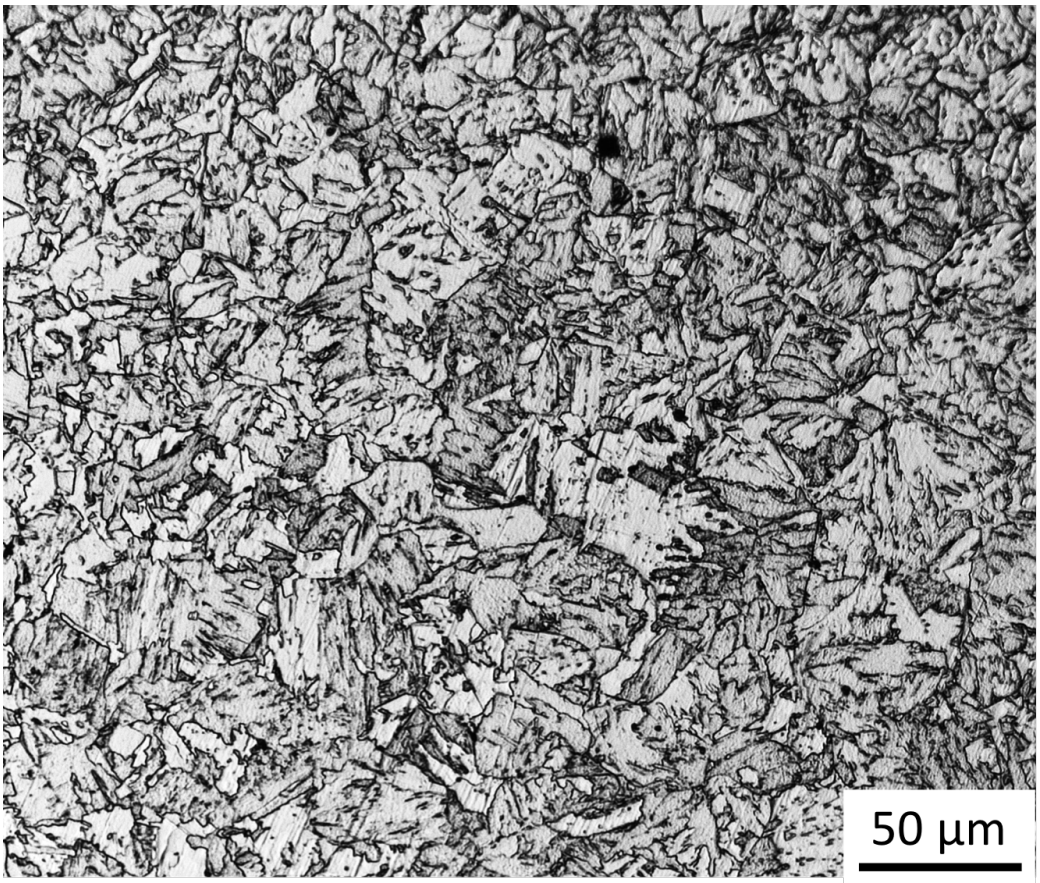

Figure 7.3: The bainitic microstructure of X80 pipeline steel.

The measured precipitate size distribution shows the fine precipitates that pin grain boundaries during TMCP and benefit the yield strength through

precipitation strengthening. Figure 7.4 shows that tempering precipitates a large number of fine precipitates such that the strength increases , as shown in figure 7.5 [63].

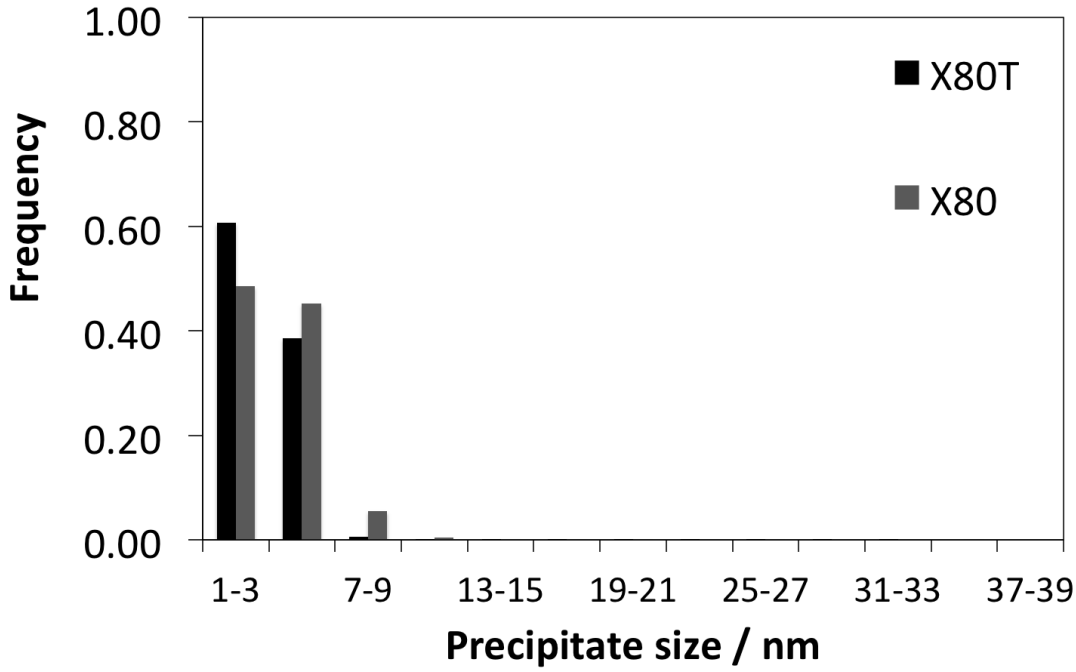

Figure 7.4: Precipitate size distribution in X80 and X80T.

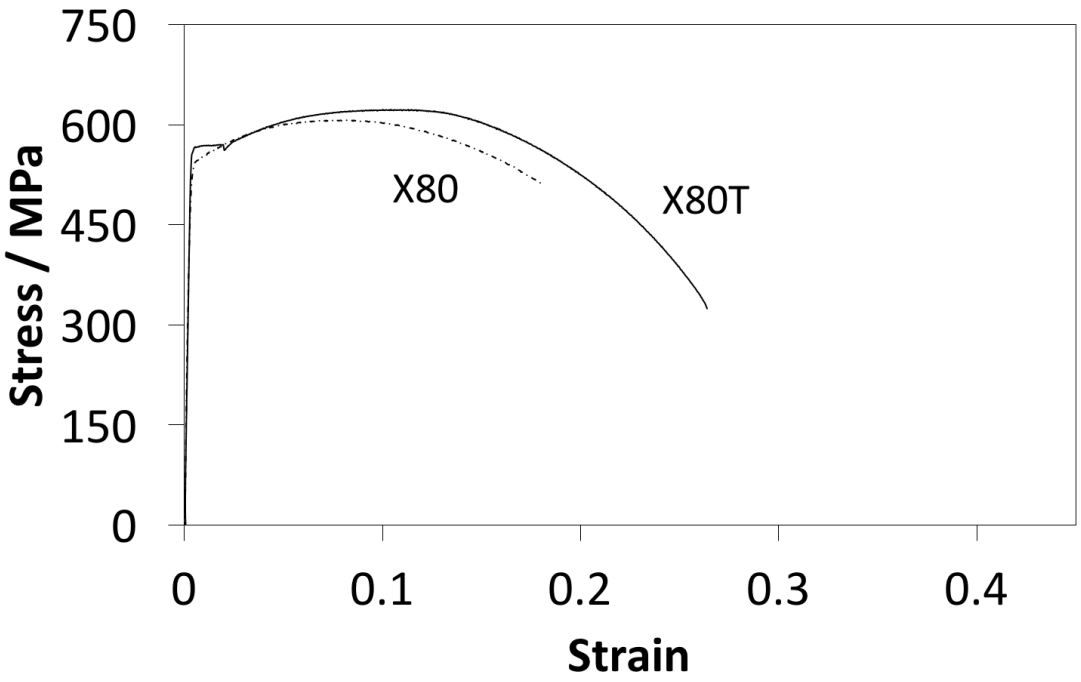

Figure 7.5: Stress-strain curves for X80 and X80T.

The X80 and X80T plates, assumed to contain relatively large number of precipitates show distinct upper yield points consistent with the unpinning of dislocations at a sufficiently large stresses. Figure 7.6 shows a similar microstructure with a range of precipitate sizes noted on observing the tempered plate under TEM.

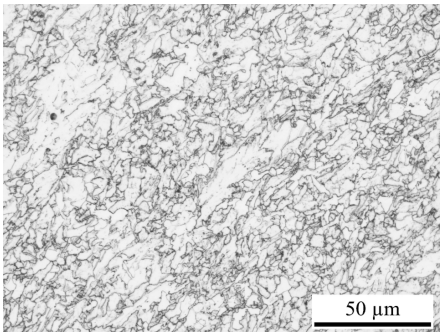

(a)

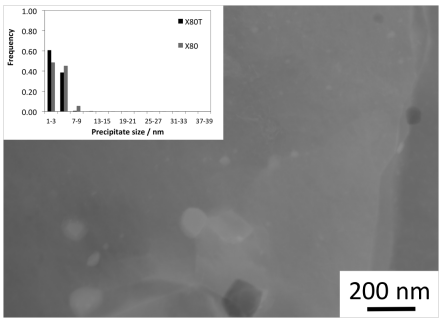

(b)

Figure 7.6: (a) Shows the microstructure of tempered X80 using optical microscopy.(b) TEM HAADF image of X80T showing the range of precipitates associated with the X80 and tempered X80 steel, which follows from the high precipitate size entropy number associated with the as-received plate.

7.4.1 Weld simulation

The transformation start and finish temperatures associated with X80 and X80T (table 7.2) show a wide range consistent with bainite and martensite formation. The austenite grain size noted in the samples exposed to thermal cycling, suggest that the wide distribution of sizes, expressed by the high precipitate size entropy, results in the availability of pinning precipitates during thermal cycling, effectively limiting the prior austenite grain size to just around 125 µm.

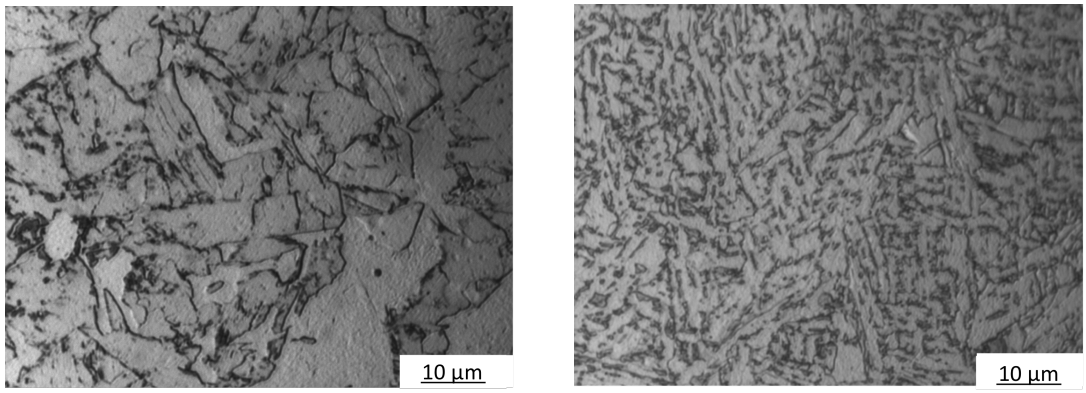

(a) **(b)**

Figure 7.7: (a)Microstructure of X80T and (b) X80 quenched from 1300 ℃, the bainitic plates are separated by regions of retained austenite

7.5 Heat treated at 950 ℃

Austenitisation leads to a softer microstructure containing allotriomorphic ferrite (figure 7.8)than the bainite and martensite obtained on cooling from 1230 ℃(figure 7.23, table 7.1). This is expected because the austenite grains are larger in the latter case as is the dissolved Nb content, both of which increase hardenability.

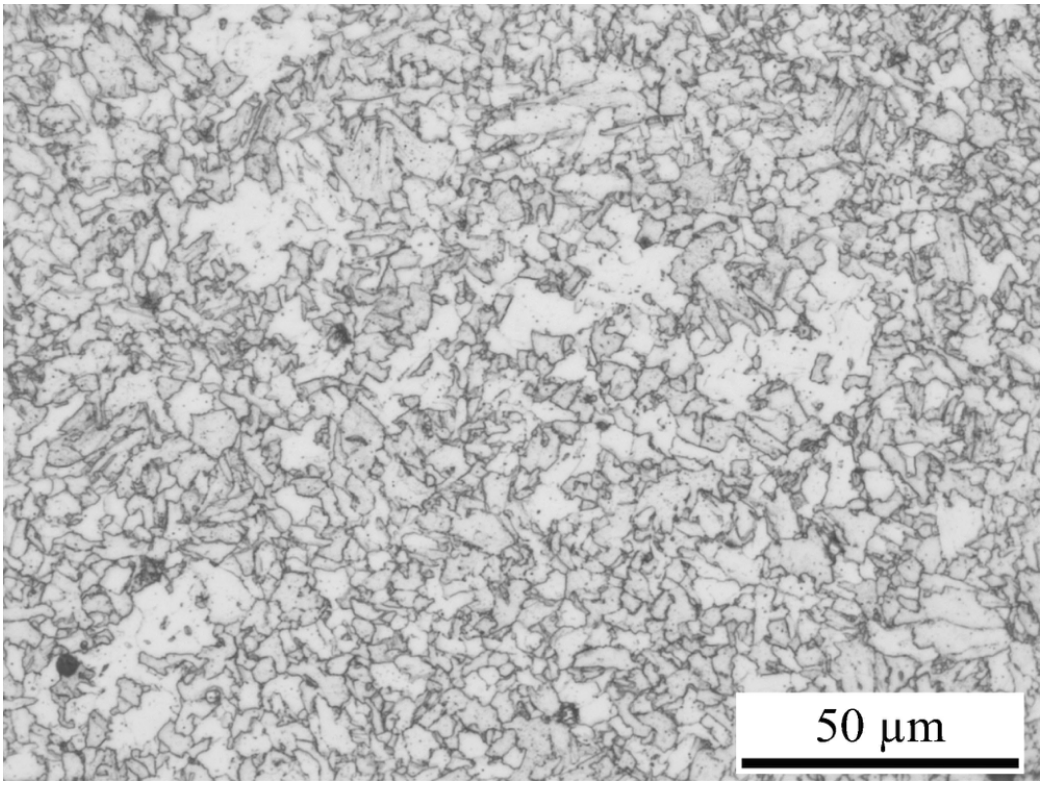

Figure 7.8: (a) Microstructure of 950Q, showing some coarsening as compared to X80.

Normalising from the austenitising temperature, 950 ℃ , leads to significantly coarser and softer microstructures as austenite grain grow without the influence of pinning precipitates due to the increased precipitate ripening that occurs during normalising. This is noted in the variation in precipitate size distributions in figure 7.11 and figure 7.10, which shows the large precipitates that form over the heat treatment.

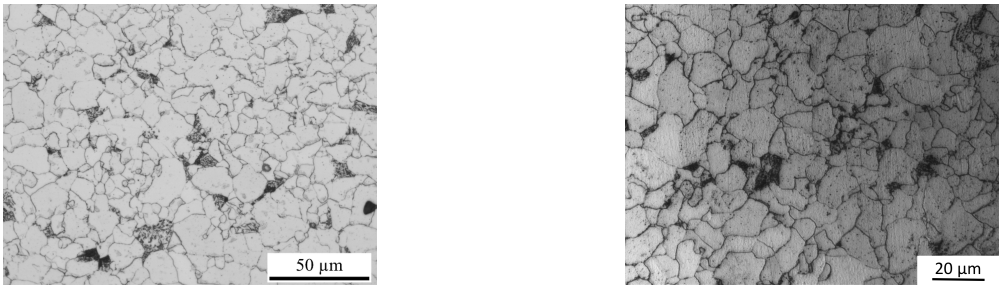

(a) **(b)**

Figure 7.9: (a) Optical micrograph of 950N. (b) Optical micrograph of 950NT. Both plate conditions show a coarse ferrite-pearlite microstructure on normalising.

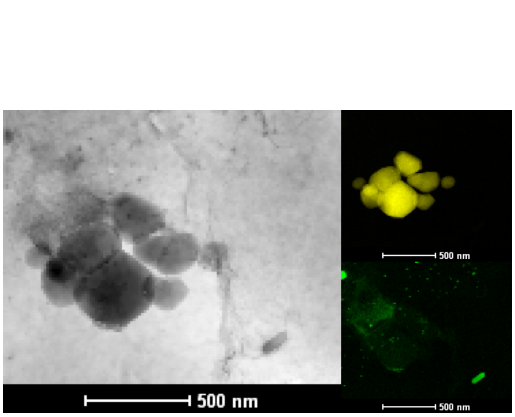

(a)

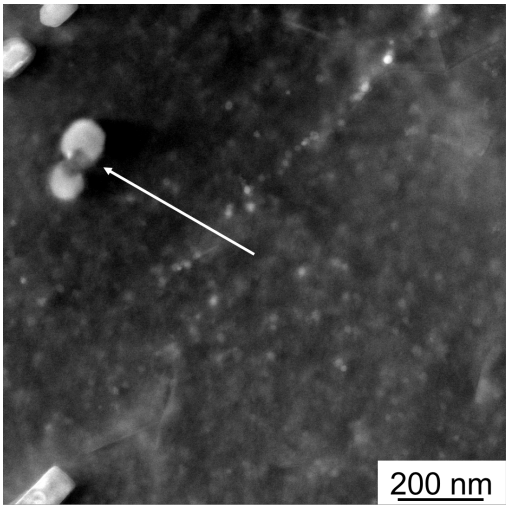

(b)

Figure 7.10: (a)Transmission electron micrograph of 950NT, showing coarse precipitates. (b)Transmission electron micrograph using HAADF of 950NT. The white arrow indicates NbC precipitated on TiN.

The relatively higher proportion of coarser precipitates, indicated in figure 7.11,means that grain boundary pinning is limited with coarser precipitates growing at the expense of smaller ones in the normalised plates, as noted in figure 7.11 , and by the relatively larger inter-precipitate distances in the 950N and 950NT, discussed in Chapter 4. The stress-strain diagram, figure 7.12, shows the loss of the defined yield point with a reduction precipitates fine enough to impede dislocation motion and require 'unpinning.

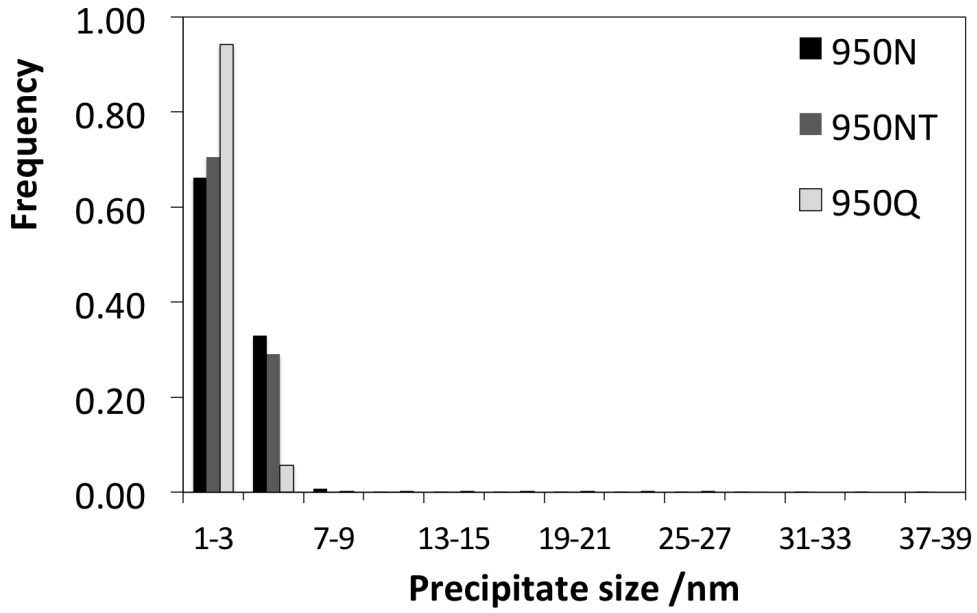

Figure 7.11: Precipitate size distribution in 950Q, 950N and 950NT.

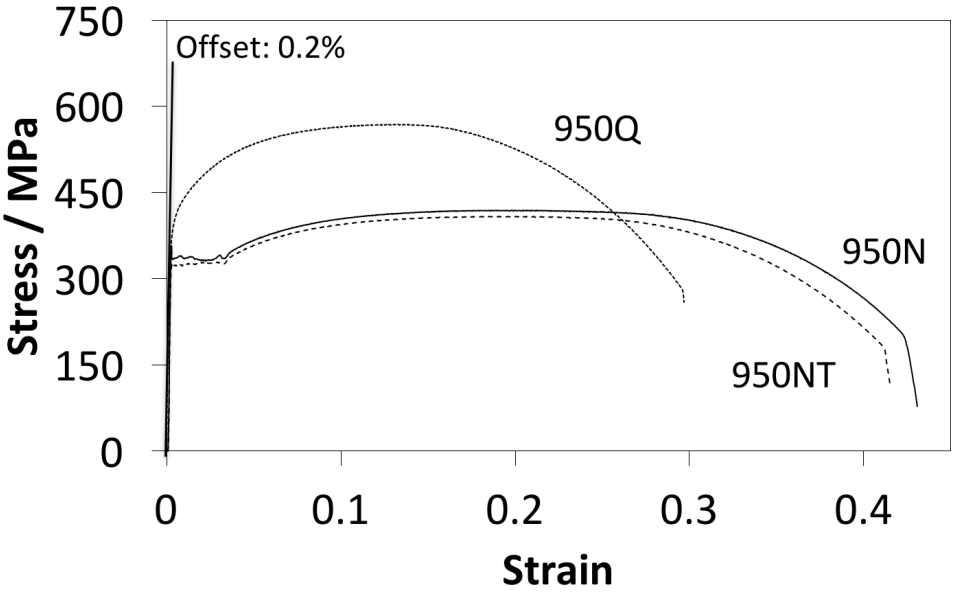

Figure 7.12: Stress-strain curves for 950N which was normalised from 950 ℃. 950NT which was normalised from 950 ℃ and tempered at 650 ℃. 950Q water quenched from 950 ℃; proof stress measurements, using a 0.2 % offset, $R_{p0.2}$, are illustrated on this plate where there is no defined yield point.

On thermal cycling during weld simulation, the smallest prior austenite grain sizes indicated in table 7.2 correlate to the presence of coarser precipitates. It is likely that a proportion of the fine precipitates will dissolve, and this is corroborated in the case of 950Q where dissolution of the fine precipitates which dominate the distribution result in large prior austenite grain sizes. The transformation start temperature on cooling is greater than that

of X80, with the bulk of the Nb precipitated out of solution, there are a larger number of sites for the nucleation of austenite even as the finest precipitates dissolve. 950Q is expected to show a different result, with few undissolved precipitates and a larger prior austenite grain, figure 7.8, the transformation temperature should be higher than that of X80, but the increased solute Nb appears to exert the retarding effect in line with earlier heating experiments conducted at rates 5 ℃ $s^{-}1$.

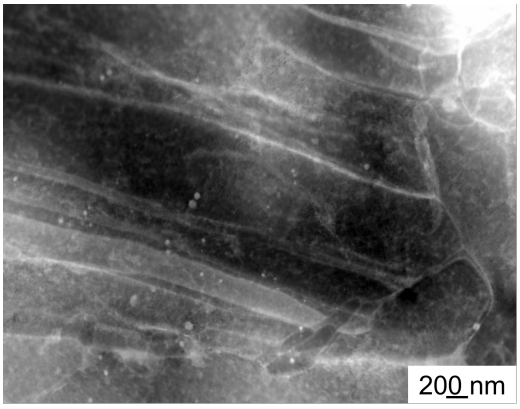

Figure 7.13: (a) Transmission electron microscopy HAADF image of 950Q showing a large number of fine precipitates.

7.5.1 Weld simulations

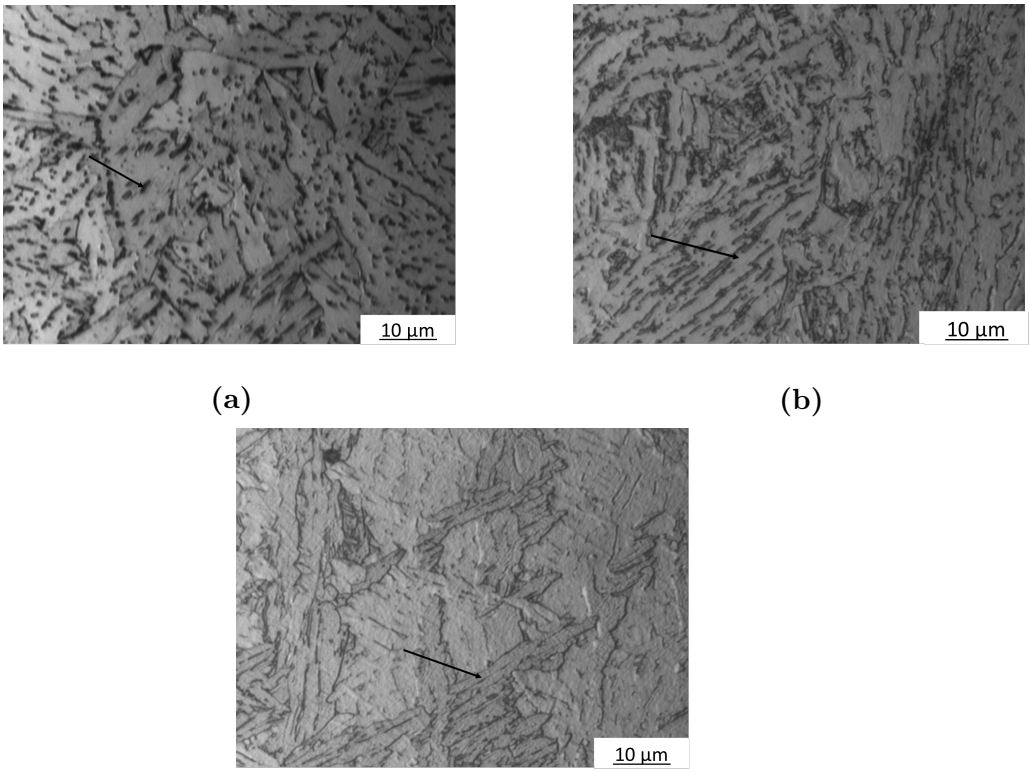

(a) **(b)**

(c)

Figure 7.14: (a) Microstructure of 950N, with an MA island indicated by the arrow. (b) 950NT shows bainitic plates separated by a larger proportion of MA islands (indicated by the arrow). (c) Microstructure of 950Q shows finer microstructure, indicated by the arrow, with dissolution of fine precipitates during thermal cycling, the microstructure appears comparatively homogeneous.

7.6 1100Q and 1100QT

Where the austenitising temperature is 1100 ℃, the bimodal intercept distribution results in the evolution of the bainitic and martensitic microstructures in figure 7.15, where a range of grain sizes are observed.

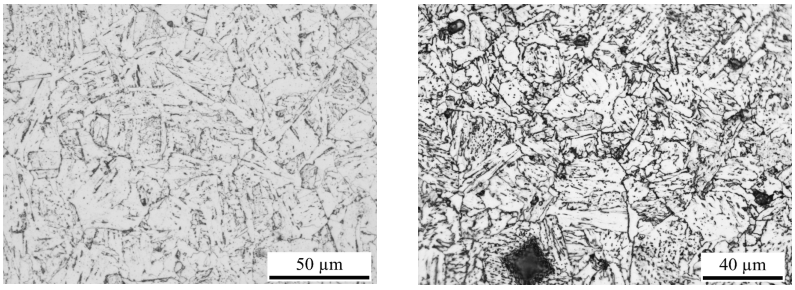

(a) **(b)**

Figure 7.15: (a)Optical micrograph of (a)1100Q and (b) 1100QT.

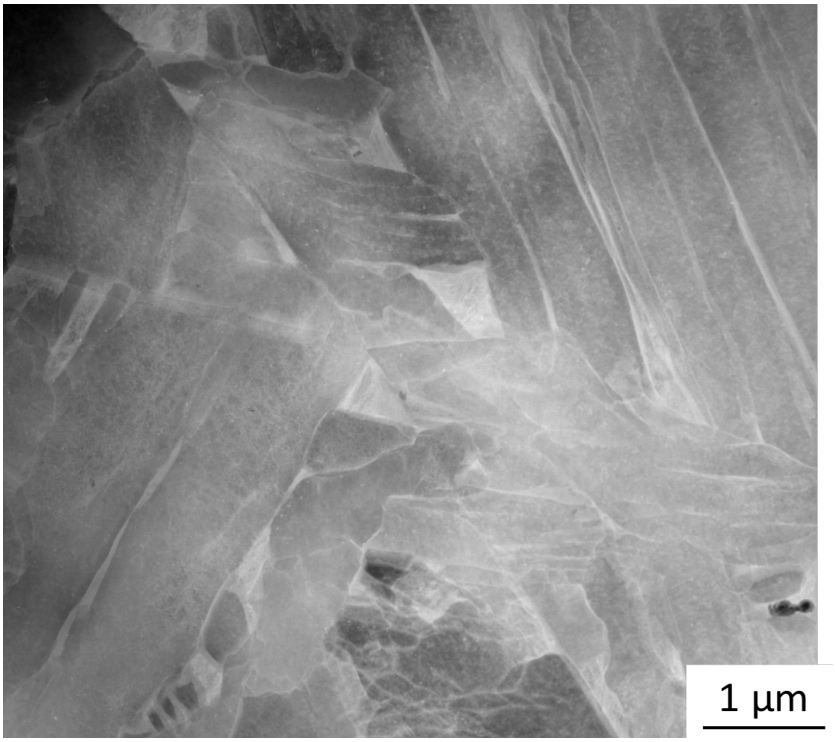

Figure 7.16: Transmission electron micrograph of 1100Q, showing fine plates of bainite and austenite films.

The effect of precipitation during tempering is apparent in figure 7.18, where the nucleation of fine precipitates, figure 7.19 and figure 7.17 results in an increment in yield strength and the evidence of dislocation pinning, with a more defined yield point in 1100QT.

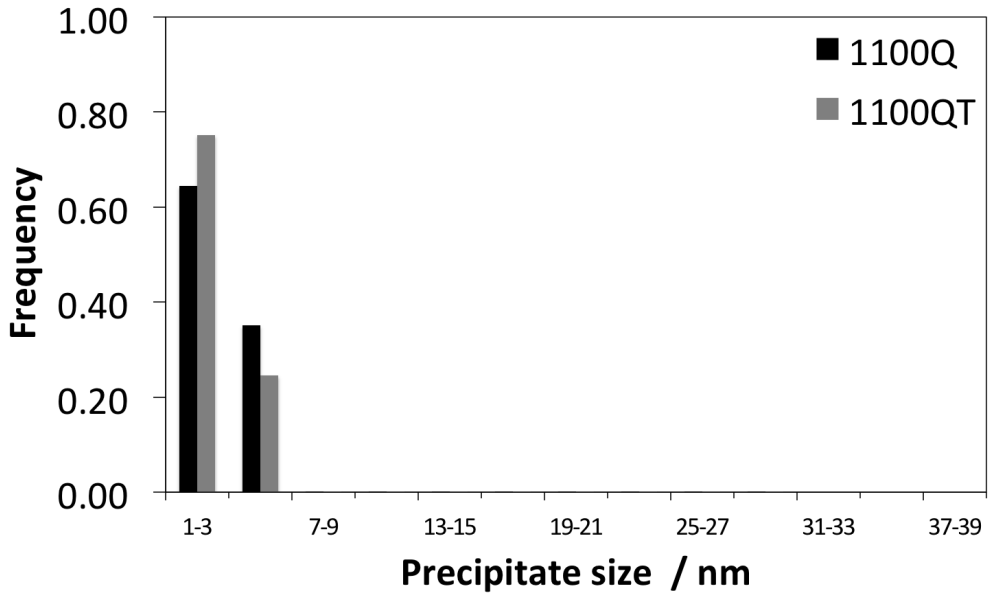

Figure 7.17: Precipitate size distribution in 1100Q and 1100QT.

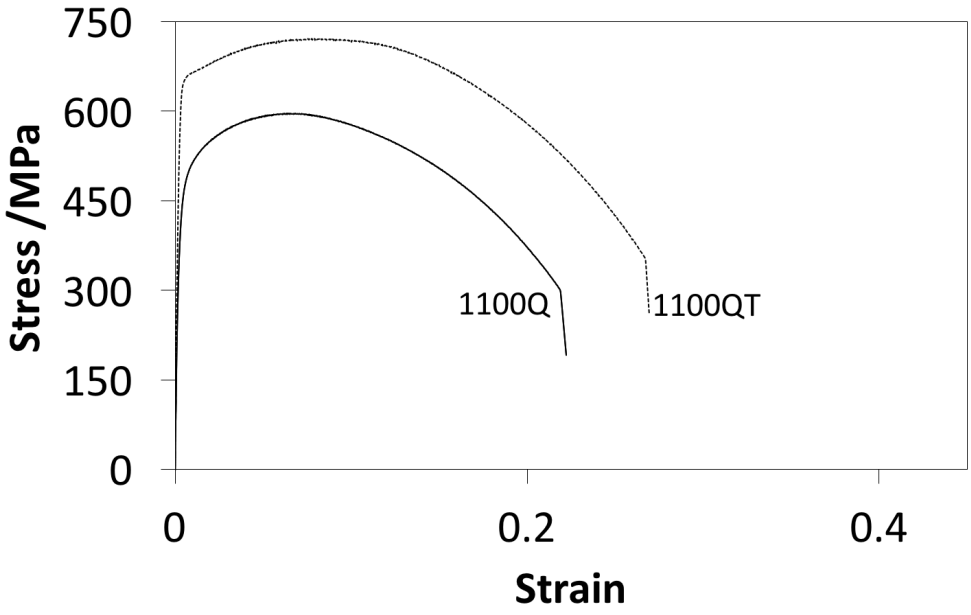

Figure 7.18: Stress-strain curves for 1100Q which was water quenched from 1100 ℃ and 1100QT which was water quenched from 1100 ℃, tempered at 650 ℃ .

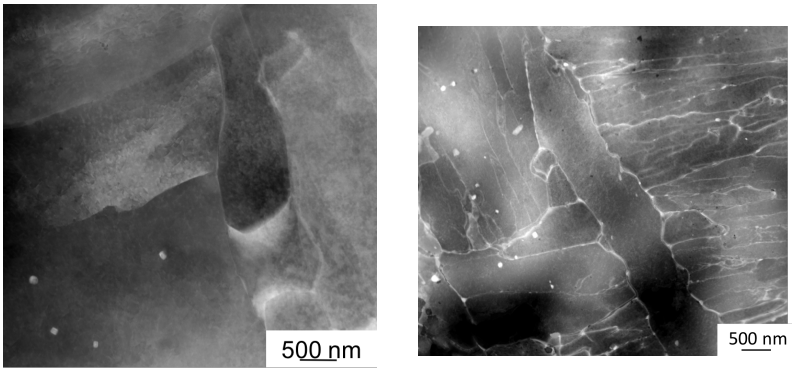

(a) **(b)**

Figure 7.19: (a)Transmission electron micrographs of (a) 1100Q and (b) 1100QT showing the increased precipitation that occurs on tempering.

7.6.1 Weld simulation

The presence of a population of persistent precipitates after thermal cycling exerts an influence on the pinning of austenite grain, with a range of grain intercepts notable in the HAZ, figure 7.20. the bimodal distribution of austenite grains, which indicates that precipitates persist during thermal cycling which pin some grain boundaries, figure 7.20. The measured transformation temperatures, table 7.2, indicate bainite and martensite in the microstructure and hardness values similar to that of X80 and X80T. However 1100Q and 1100QT do show significantly lower measured prior austenite grains fol-

lowing cycling. While it should be noted that the limited sample size does not lead to a clear conclusion, it is likely that the higher Nb content limiting grain growth as well as the presence of pinning precipitates has an effect in limiting austenite grain sizes.

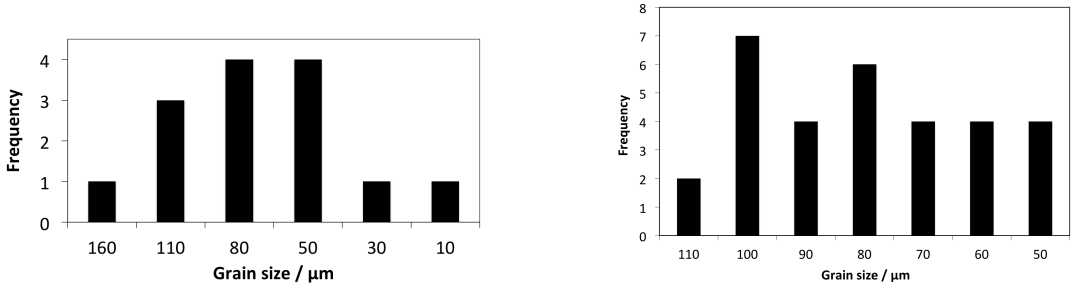

(a) **(b)**

Figure 7.20: Distribution of prior austenite grain intercepts in (a) 1100Q and (b) 1100QT following weld simulation.

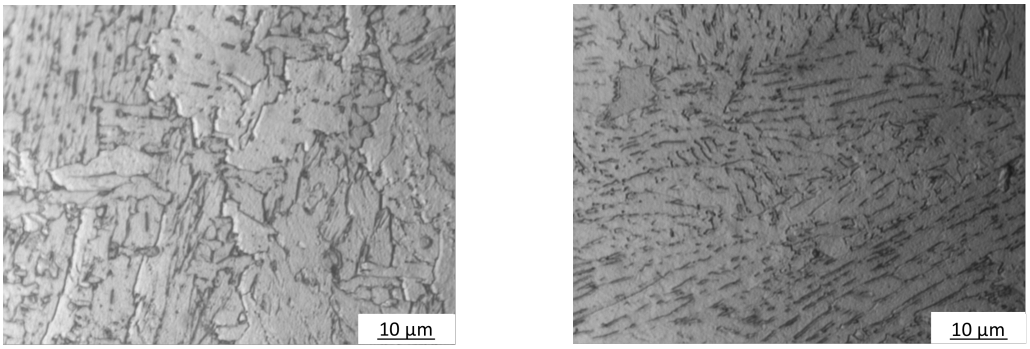

(a) **(b)**

Figure 7.21: Microstructures of (a) 1100Q and (b) 1100QT. a bainitic microstructure dominates with regions of retained austenite, martensite and bainite

7.7 1230Q and 1230QT

Austenitisation at 1230℃leads naturally to coarse austenite grains, and a high concentration of Nb leading to greater hardenability. The microstructure is composed of bainite and martensite, with laths extending between prior austenite grain boundaries. The bulk of the NbC precipitates dissolve following this heat treatment, resulting in a precipitate size distribution that is dominated by the finest precipitates, which likely re-precipitate during cooling, which is consistent across the plates which were re-austenitised.

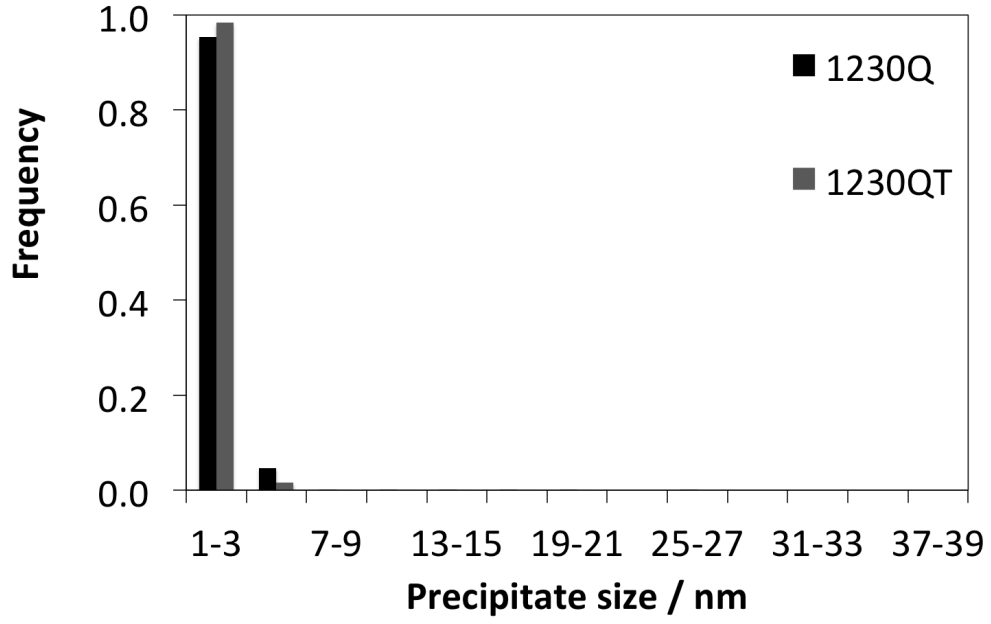

Figure 7.22: Precipitate size distribution in 1230Q and 1230QT.

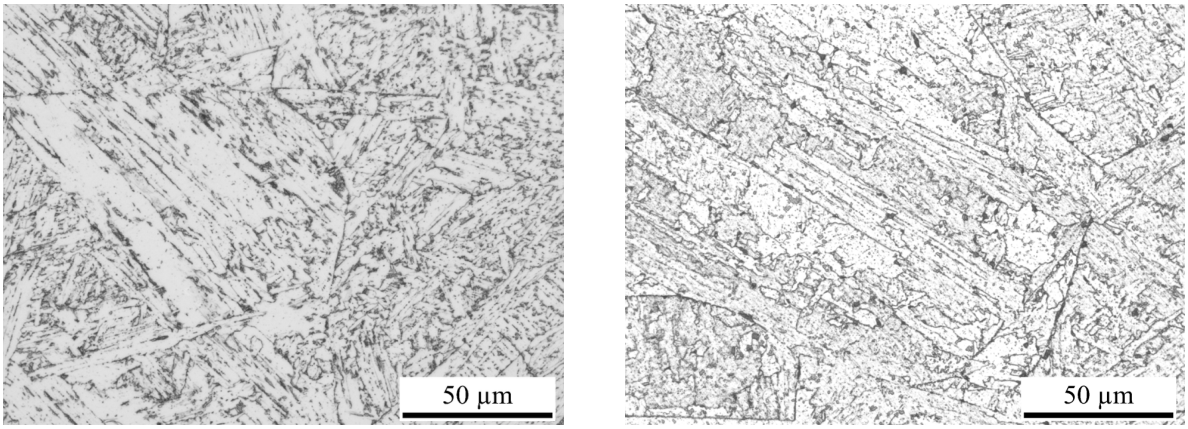

(a) **(b)**

Figure 7.23: (a) Optical micrograph of (a) 1230Q and (b) 1230QT showing large bainitic laths between the austenite grain boundaries.

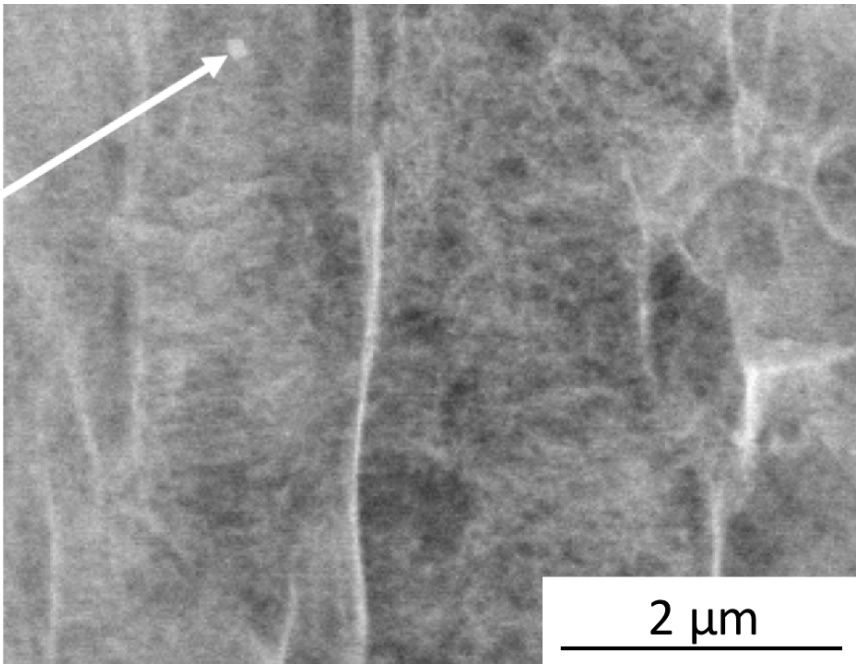

Figure 7.24: Transmission electron micrograph showing a stable TiN precipitate, visible with the bulk of the Nb in solution.

Tempering of 1230Q shows a limited increment in yield strength, figure 7.25, however a more defined yield point can be observed, consistent with the phenomenon noted in the plate austenitised at 1100 ℃.

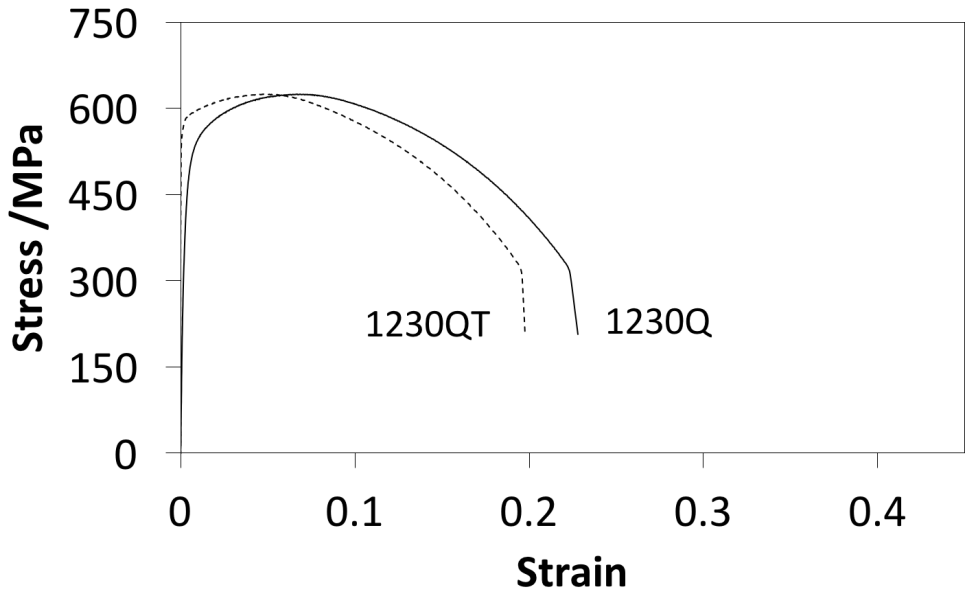

Figure 7.25: Stress-strain curves for 1230Q which was water quenched from 1230 ℃ and 1230QT which was water quenched from 1230 ℃ and tempered at 650 ℃.

7.7.1 Weld simulations

1230Q and 1230Q have the most dissolved niobium, with few precipitates. The fine precipitates which dominate the samples dissolve during thermal cycling, leading to unrestricted austenite grain growth, table 7.2 and figure **??**. The lowest transformation start temparures are consistent with a microstructure with few hetergenous nucleation sites, and also consistent with the retarding effect of Nb in solution [77].

The microstructures that evolve are similar, likely due to the higher amount of dissolved niobium and carbon in both plate conditions.

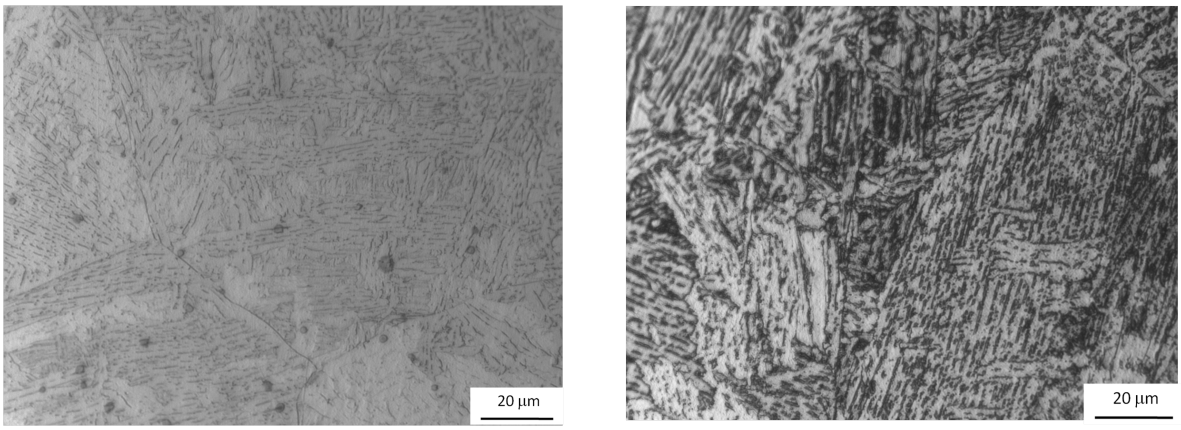

(a) **(b)**

Figure 7.26: The microstructures of (a) 1230Q and (b) 1230QT show a distribution of fine bainitic and martensitic laths.

7.7.2 Variations in the CGHAZ microstructure

It is worth noting that significant variations in the state of Nb can influence the coarseness of the lath microstructures that dominate the CGHAZ, as illustrated in figure **??**, with coarser packets in X80 as compared to 1230Q. Where the amount of Nb in solution is larger like 1100Q, the microstructure is finer, but the finest bainitic packet size is consistent with the largest Nb content on thermal cycling. This correlates to the transformation start

temperature,table 7.2.

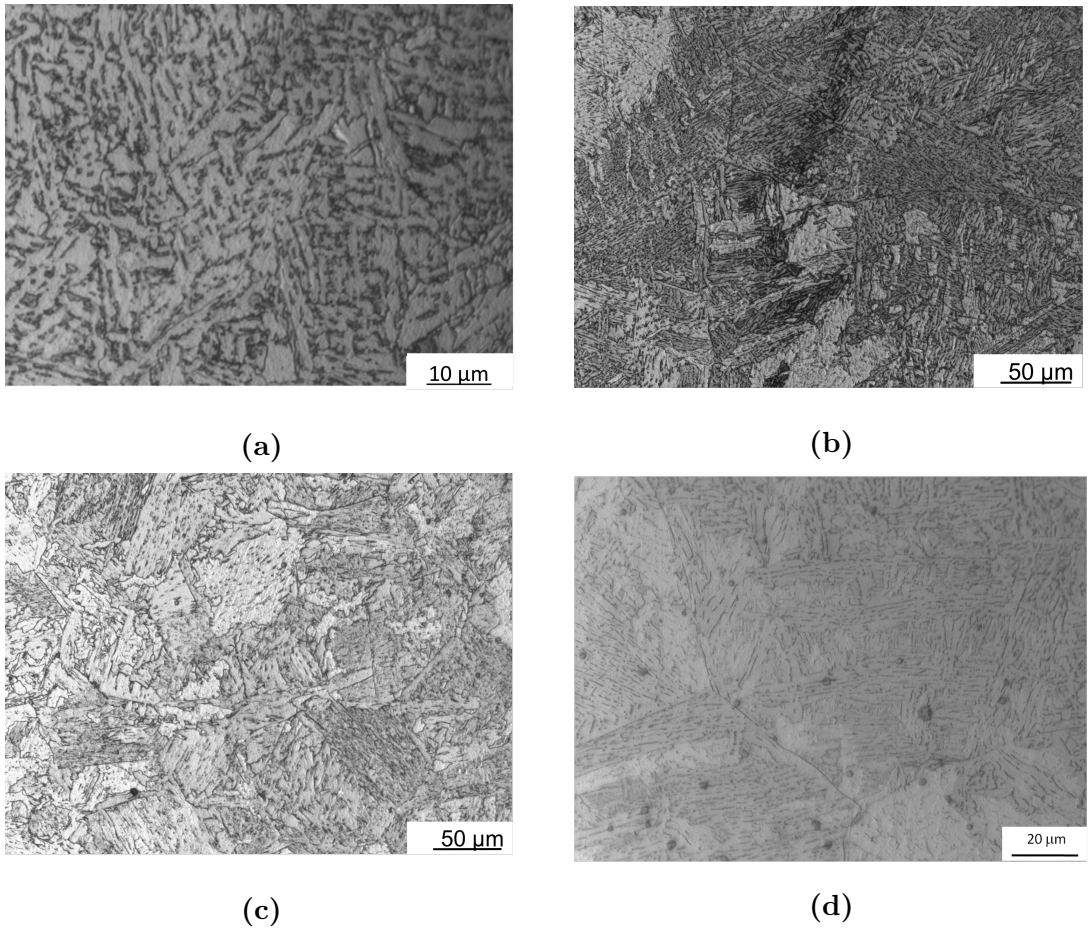

(a) **(b)**

(c) **(d)**

.

Figure 7.27: The simulated CGHAZ microstructures of (a) X80 and (b) 950Q (c) 1100Q and (d) 1230Q

7.8 Summary

The evolution of the microstructures that form in the heat treated plates is dependent on the concentration of dissolved Nb and the size of the austenite grains. Both of these increase hardenability and lead to stronger microstructures, with the trend noted in table 7.1. Control of the ratio of solute Nb and NbC will enable control of the transformation temperature. Yield strength and hardness have been utilised in assessing the microstructures that form during welding, where softer values were correlated to the presence of ferrite and consistent with the lowest transformation finish temperatures, while harder values were correlated to the presence of martensite, these have formed the basis for interpreting the microstructures that develop in the CGHAZ during welding.

Two phenomena were identified as likely to influence the transformation of the heat treated plates during quenching:

1. A reduction of Nb in solution should increase the transformation start temperature during cooling.

2. Increasing prior austenite grain size reduces the transformation tem-

perature as the number of nucleation sites decreases.

The evolution of the structures in the CGHAZ were found to be consistent with these statements. 950N and 950NT, with the with smallest austenite grain sizes and lowest dissolved niobium show the highest transformation start temperatures, with the influence of dissolved niobium and large prior austenite grain sizes most marked in 1230Q and 1230QT, with the lowest transformation start temperatures. The effect of the thermal cycle on 950Q, indicates that the precipitate size distribution is critical to the evolution of microstructures during welding, while fine precipitates can contribute to the yield strength of the plate, they are less able to resist dissolution under the high thermal gradients, and a coarse prior austenite grain can result. X80 and X80T, with high precipitate entropy values, reflecting a more uniform distribution of precipitates across a range of sizes, are able to ensure that precipitates contribute to yield strength, and coarser precipitates are available to resist dissolution such that grain size control occurs even in the HAZ.

The abnormal grain growth noted in 1100Q (and 1100QT) is indicative that the precipitate distribution that gives rise to the bimodal austenite grain sizes, persists in the CGHAZ, controlling the austenite grain across a range of sizes. This behaviour offers some evidence towards the stronger influence

of the austenite grain size, and the related availability of nucleation sites, increasing the transformation start temperature as opposed to the influence of dissolved Nb in retarding transformation during cooling. However is notable that the transformation temperatures observed in figure 7.2, show that, with similar prior austenite grain sizes, plates 1100Q and 1100QT have a lower transformation temperatures than 950N and 950NT, with a higher content of dissolved niobium.

Chapter 8

Structures and properties across the weld heat affected zone

8.1 Introduction

The purpose of work presented in this chapter is to understand, and attempt to empirically quantify the influence of niobium (in and out of solid solution)on the development of the heat-affected zone in the welded sections of plate.

8.2 Precipitation across the HAZ

To better understand the heat affected zone of a weld, the influence of a variety of thermal treatments on the as-rolled X80 plate is investigated, specifially the relationship between precipitation behaviour and the HAZ, defined here by the temperature range to which the metal is exposed during welding. Samples of 3 mm × 3 mm × 10 mm were quenched from temperatures consistent with the tempertaure ranges expected in the HAZ [4], and subsequently held for 15 minutes across a range of tempering temperatures. This follows the methodology established by Kazinczy et al. [63].

The Ae_1 and Ae_3 temperatures were identified using MTDATA calculations, and are illustrated by the dotted lines in figure 8.1.

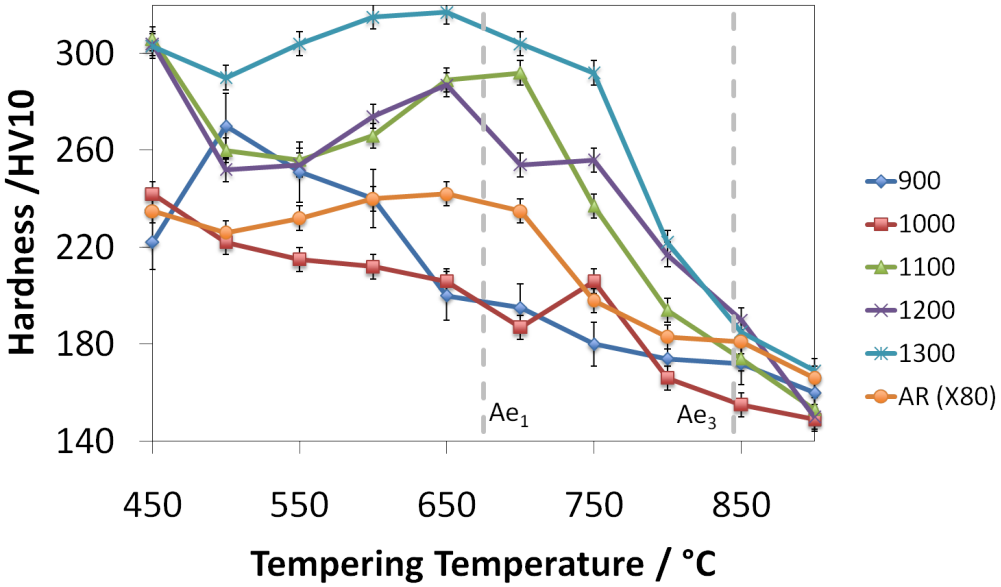

Figure 8.1: Variation in hardness by tempering the quenched plates across a range of temperatures.

It is obvious from these plots that the content of niobium that enters solution at the austenitisation temperature influences the hardening or softening response dramatically. The dominant trend is that of a higher austenitising temperature leading to a greater proportion of Nb in solution, with increased availability for precipitation during tempering. There will be an additional effect that the initial hardness of the as-quenched sample is higher when T_γ is high. This is because larger austenite grains increase hardenability.

8.2.1 Tempering plates 950Q, 1100Q and 1230Q

The bainitic microstructures associated with 950Q, 1230Q and 1100Q discussed previously, show secondary hardening on holding at 650 ℃ in figure 8.2, due to probably to NbC precipitates. Even 950Q, where little Nb is in solution, resists softening i.e. there is little difference in the samples tempered at 500 ℃and 650 ℃.

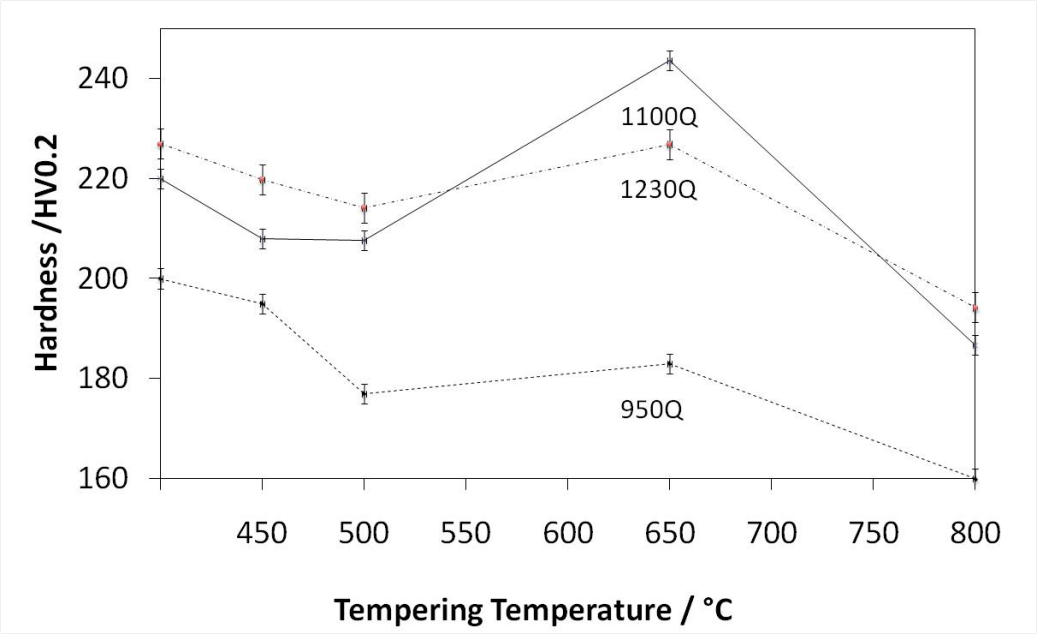

Figure 8.2: Hardness trends following tempering of heat treated plates showing an increment in hardness at around 650 ℃.

Based on the tempering experiments below, the peak hardness away from the CGHAZ and ICHAZ are likely to be related to those regions exposed to

temperatures in the vicinity of 650 ℃, at a consistent distance away from the weld fusion line.

8.3 The coarse-grained heat affected zone

In order to characterise the actual of the welding on the HAZ, samples were welded and the hardness are presented in table 8.1.The following images, figures 8.4 to 8.10 show the prior austenite grain sizes in the CGHAZ. Measurements were taken directly from the vicinity of the weld fusion line where columnar grains can be noted, and are limited to those apparent prior austenite grain that could be measured. Therefore these measurements are necessarily conclusive, but are complementary to those measured using welding simulations in the previous chapter.

Initial experimentation focussed on analysing the CGHAZ, which sees the highest temperatures in the heat-affected zone. It is clear that the prior austenite grain sizes are lower in the CGHAZ in the welds. The experimentation by dilatometry in the previous chapter showed that those samples with the largest precipitates i.e. 950N and 950NT possessed the smallest prior austenite grain sizes on thermal cycling. Hence, in the case of the welded

plates, in line with the evidence presented in table 8.1, grain-boundary pinning in the CGHAZ is influential in controlling the size of the austenite grains.

Plate identification	Austenite grain size, d_γ / μm ±3 μm	Hardness, HV0.2±10	Precipitate size entropy of the welded plate
X80T	45	200	0.71
950N	55	206	0.68
950NT	53	210	0.63
1100Q	50	221	0.68
950Q	60	184	0.23
1230Q	75	211	0.19
1230QT	70	200	0.08
X80	48	210	0.91
1100QT	55	215	0.57

Table 8.1: Prior austenite grain sizes and hardness values at the CGHAZ.

The data in table 8.1 and figures 8.4 to 8.12 are largely consistent with the trends from weld simulations in the previous chapter. 1230Q, 1230QT and 950Q have the largest prior austenite grain size in the CGHAZ, with a notable correlation to the precipitate size entropy. While fine precipitates dissolve to enable large austenite grains, the presence of coarser precipitates in steel will restrict grain growth in the vicinity of the fusion line.

The hardness values show limited variations from 200 HV across the plates, where persisting precipitates do not contribute to hardening, higher hardenability from increased Nb in solution and larger prior austenite grains is likely to contribute. This is a likely reason for the consistent yield strength noted in the HAZ of some Nb-microalloyed steels, which can remain within the X80 designation even after welding [121]. In table 8.1 the hardness varies little from X80 to 1230Q or 950N.

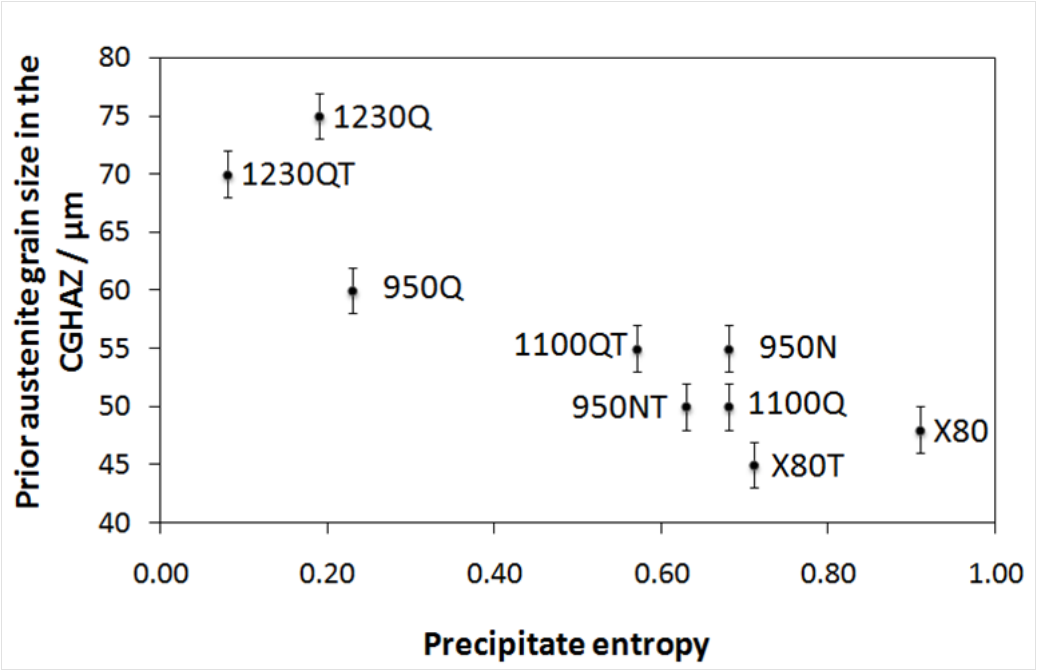

Figure 8.3: Prior austenite grain size in the CGHAZ versus precipitate size heterogeneity (entropy).

Figure 8.3 shows that the precipitate size entropy is important in determining the austenite grain size in the CGHAZ. 1230Q and 1230QT with a low volume fraction of NbC precipitates and low precipitate size entropy (mainly fine precipitates) have few pinning particles and large austenite grain evolves at the highest temperatures in the HAZ as noted in figures 8.4 and 8.5.

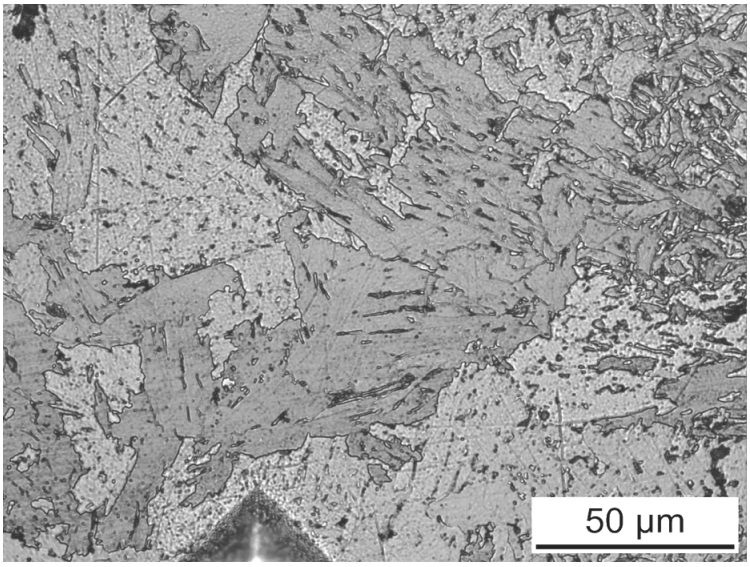

(a)

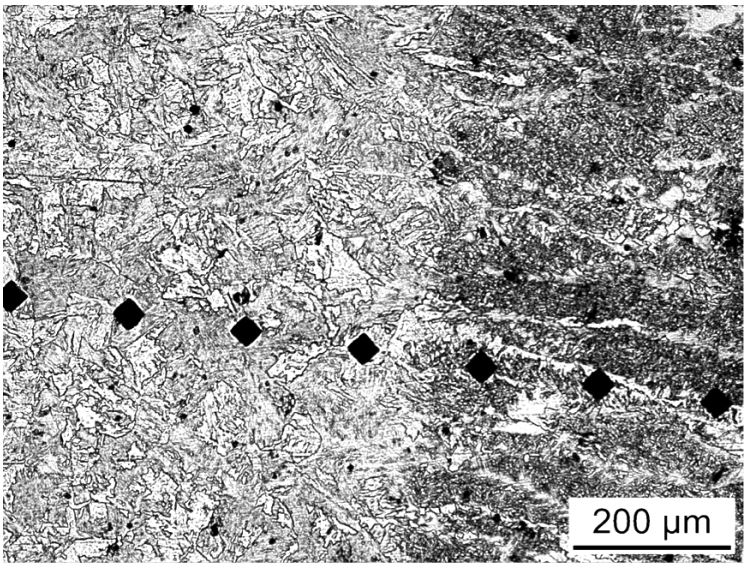

(b)

Figure 8.4: 1230Q: $d_\gamma = 75 \pm 3$ µm. These measurements are taken directly from the weld CGHAZ and show the columnar grains in the fusion zone.

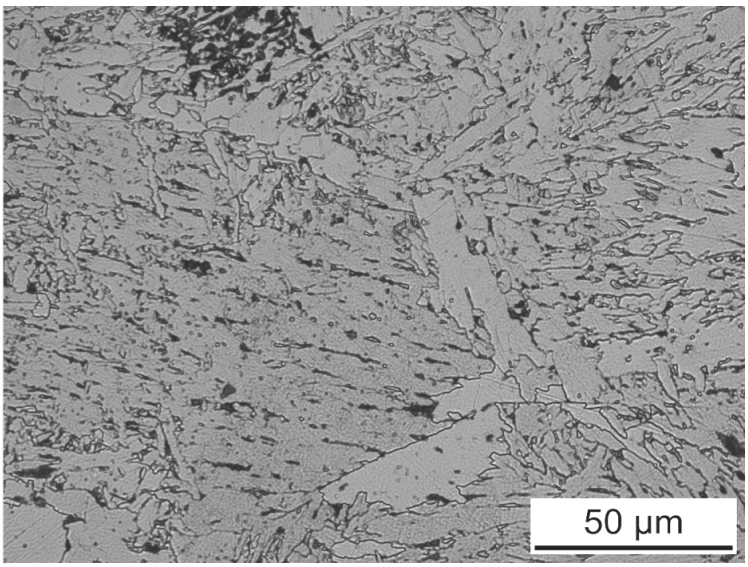

(a)

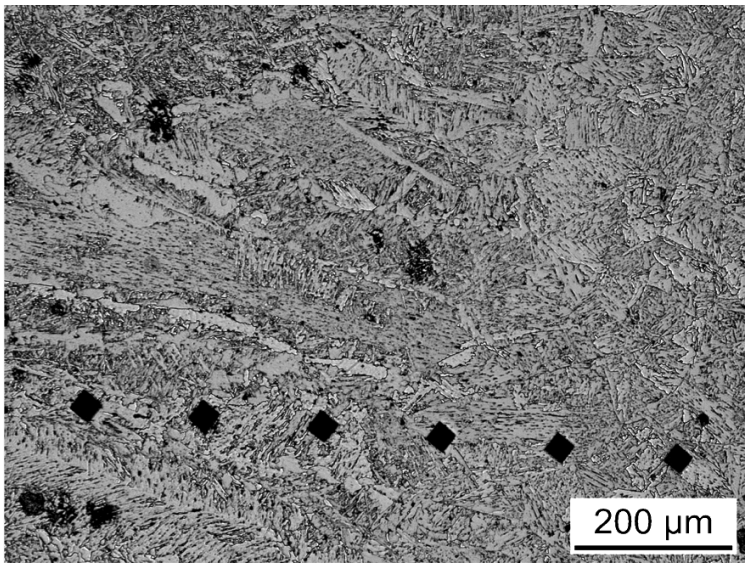

(b)

Figure 8.5: 1230QT: $d_\gamma = 70 \pm 3$ µm

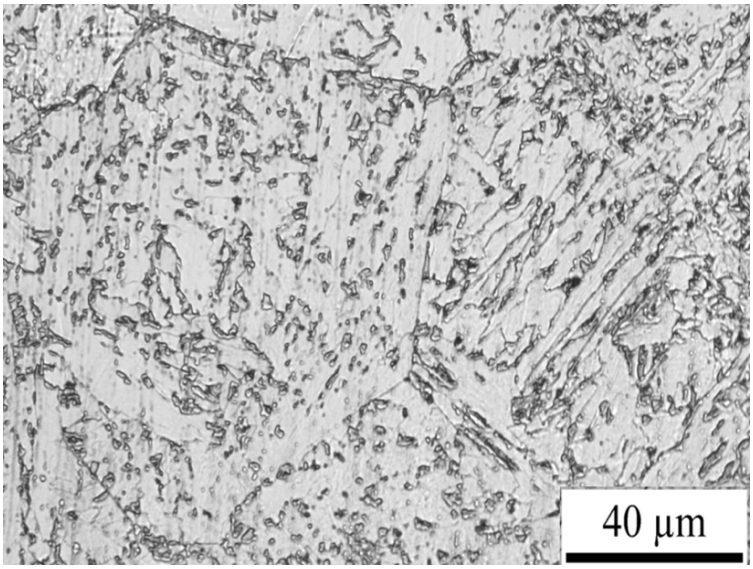

(a)

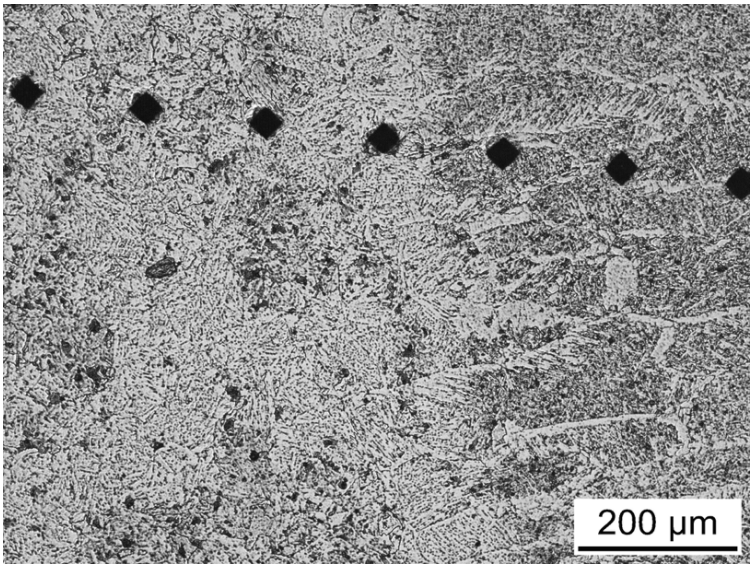

(b)

Figure 8.6: 950Q: $d_\gamma = 60 \pm 3\,\mu\text{m}$

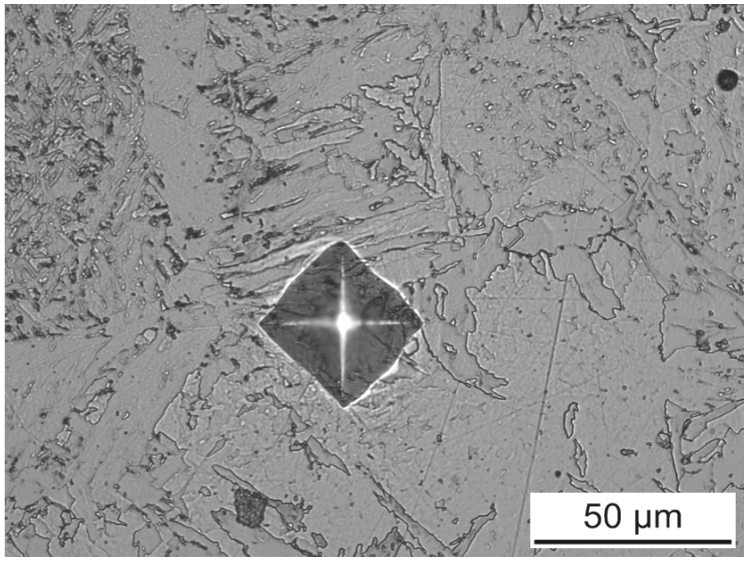

(a)

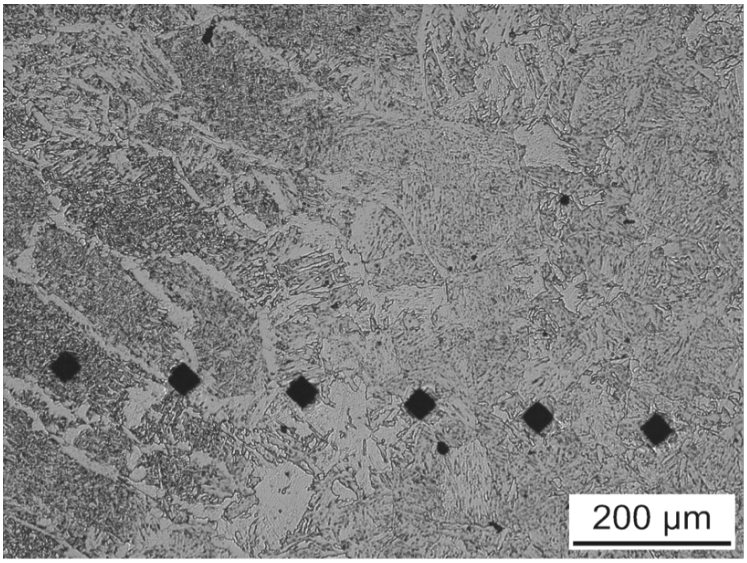

(b)

Figure 8.7: 950N: $d_\gamma = 55 \pm 3\,\mu\text{m}$

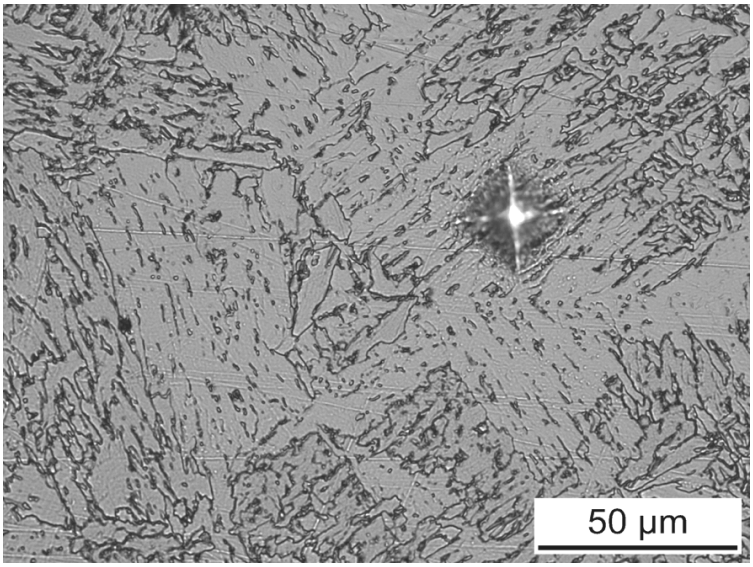

(a)

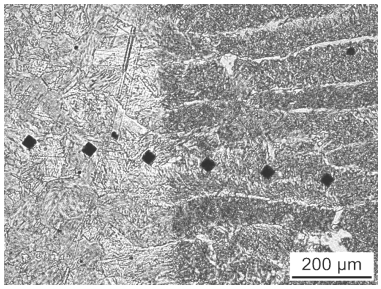

(b)

Figure 8.8: 950NT: $d_\gamma = 53 \pm 3$ µm

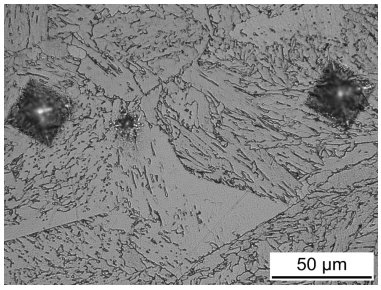

(a)

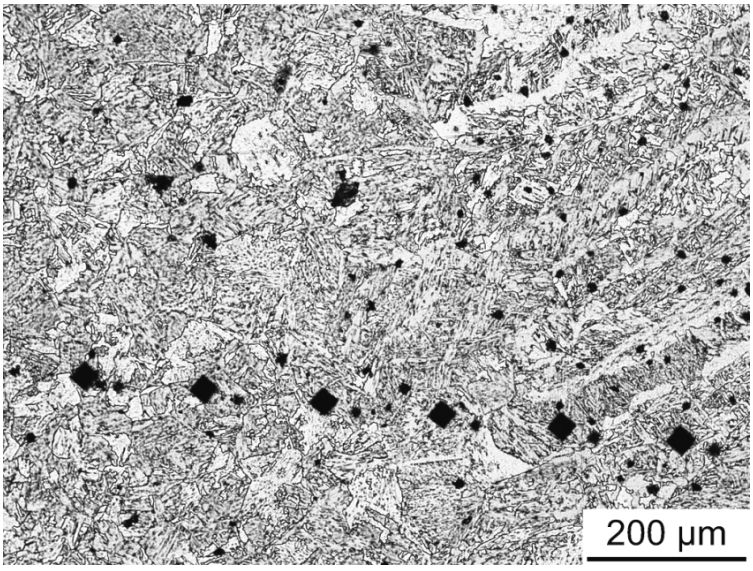

(b)

Figure 8.9: 1100Q: $d_\gamma = 50 \pm 3$ µm

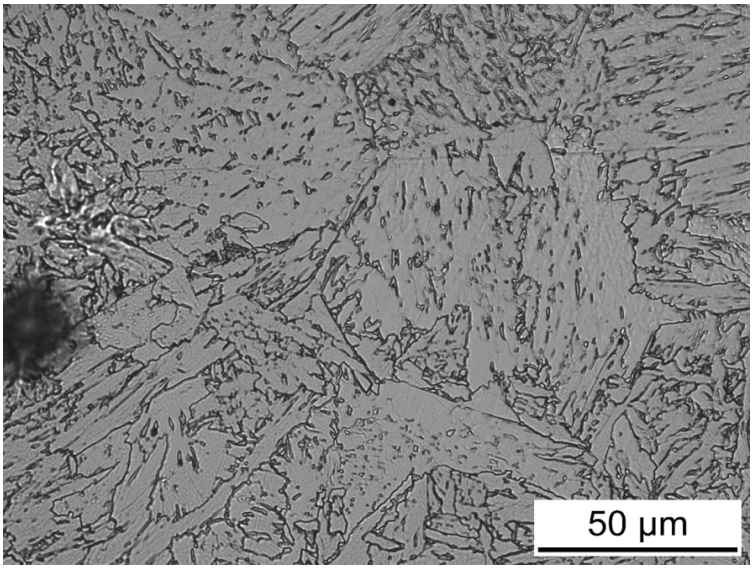

(a)

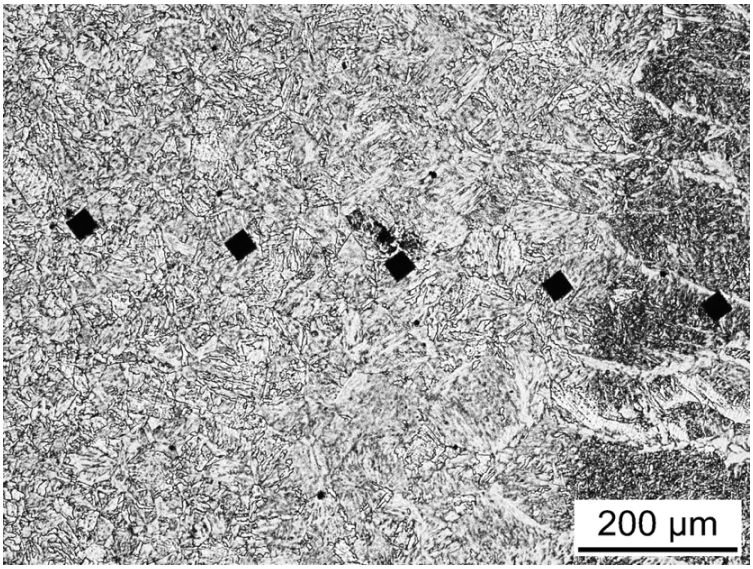

(b)

Figure 8.10: 1100QT: $d_\gamma = 65 \pm 3$ µm

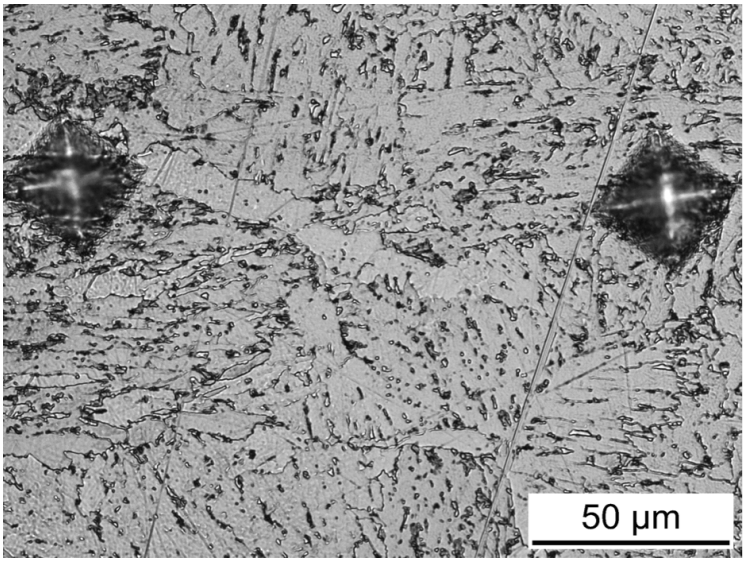

(a)

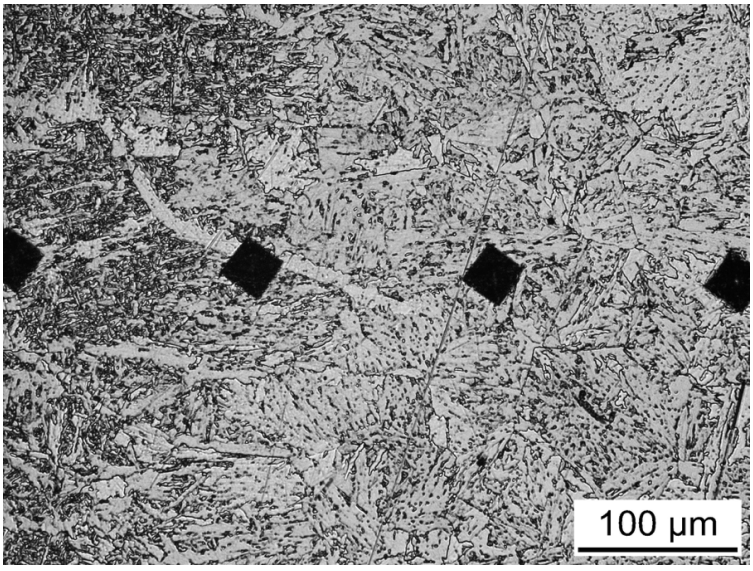

(b)

Figure 8.11: X80: $d_\gamma = 48 \pm 3$ µm

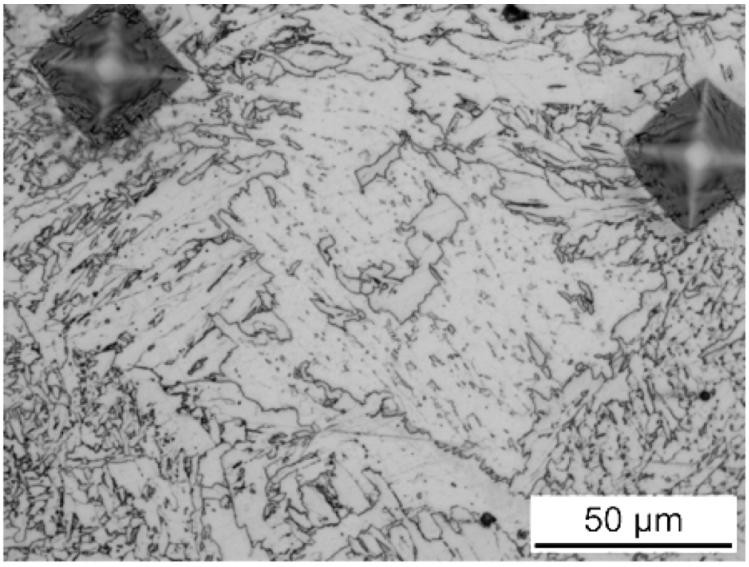

(a)

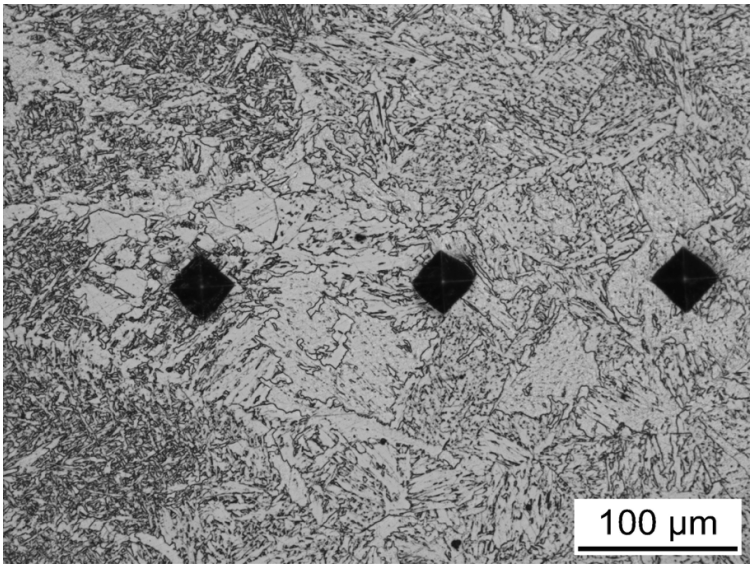

(b)

Figure 8.12: X80T: $d_\gamma = 45 \pm 3$ µm

8.3.1 Microstructural entropy across the heat-affected zone

The weld entropy values reported here reflect the heterogeneity in the microstructure across the HAZ such that, 950N at 1.07 has a relatively consistent hardness value across the HAZ, reflecting an uniform microstructure. The highest value, 1.69, associated with 1230QT, suggested significant variations in hardness across the HAZ, and hence, significant variations in microstructure. The hardness entropy or microstructural heterogeneity values are useful in indicating how dramatic the influences of Nb and temperature ranges from the welding process are across the HAZ for each plate condition.

Plate Identification	Heat treatment	Hardness entropy
X80	As received X80	1.66
X80T	Tempered at 650℃	1.58
950N	Normalised from 950℃	1.07
950NT	Normalised from 950℃ and tempered at 650℃.	1.30
950Q	Water quenched from 950℃	1.46
1100Q	Water quenched from 1100℃	1.31
1100QT	Water quenched from 1100℃ , tempered at 650℃	1.59
1230Q	Water quenched from 1230℃	1.55
1230QT	Water quenched from 1230℃ , tempered at 650℃	1.69

Table 8.2: Hardness entropy across the heat-affected zone.

An experimental plan was designed to show that the scatter in charpy toughness values increases with entropy, on the basis that uniform hardness distribution would lead to less scatter in toughness. However the resources required to conduct the experiments were not available. An attempt has been made to present and characterise hardness variations across the HAZ of the plates analysed in this work. Figure 8.13 shows the simulated HAZ based on the microstructures of the heat-treated plates. A comparison to figure 8.14 shows relatively similar trend in hardness for X80 steel, with the minimum hardness in figure 8.14 correlating to the plate normalised from 950 ℃.

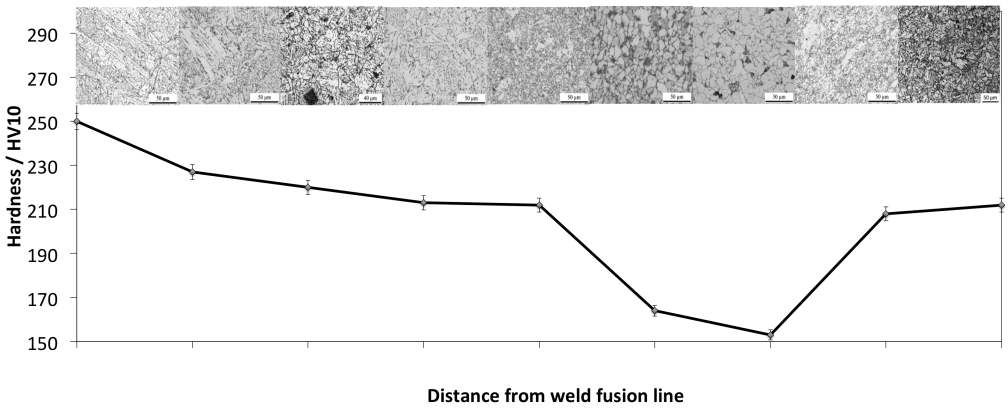

Figure 8.13: Predicted microstructures and hardness values in the HAZ of welded X80 steel.

The thermomechanically processed microstructure associated with X80 and X80T naturally shows the lowest difference in hardness entropy, with similar microstructures in both plates, it is likely that at 3 mm from the fusion line where both plates show an increment in hardness, there is cumulative value of secondary hardening in the tempered plate. This cumulative tempering effect is notable in 950N and 950NT, where the tempered plate retains a higher hardness value. These plates show a largely consistent low hardness value around 5 mm from the fusion line, where 950Q shows a dramatic increment in hardness, consistent with the tempering experiments, figure 8.2.

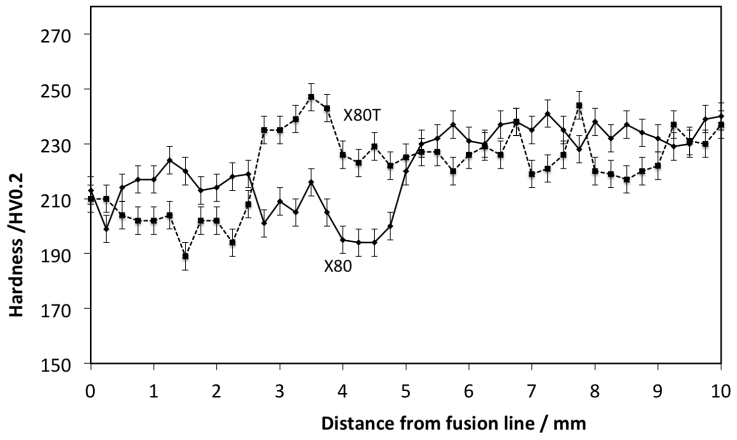

(a)

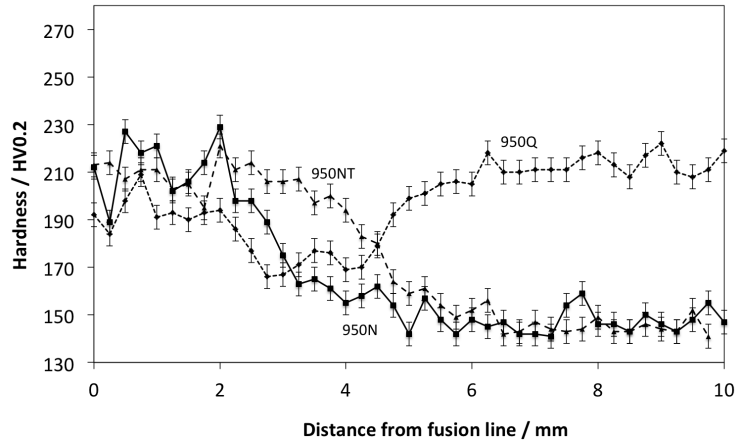

(b)

Figure 8.14: (a)Hardness profile across the heat-affected zone of X80 and X80T.(b)Hardness profile across the heat-affected zone of 950Q, 950N and 950NT.

The martensite and bainite microstructures associated with the higher austenitising temperatures are expected to show more significant increments

in hardness in regions where tempering occurs. This is apparent in 1230Q and 1100Q, the tempered plates are softer in the HAZ, increasing at around 5 to 6 mm from the fusion line, where the maximum secondary hardening appears to occur (likely at around 650 ℃). Therefore, closer to the fusion, where 'tempering' temperatures are higher, precipitate coarsening dominates as shown in figure 8.2, where the material softens at at temperatures higher that 650 ℃. This effect is limited on the quenched plates with few precipitates, which show increased hardness as nucleation occurs. Farther away from the fusion line, secondary hardening dominates.

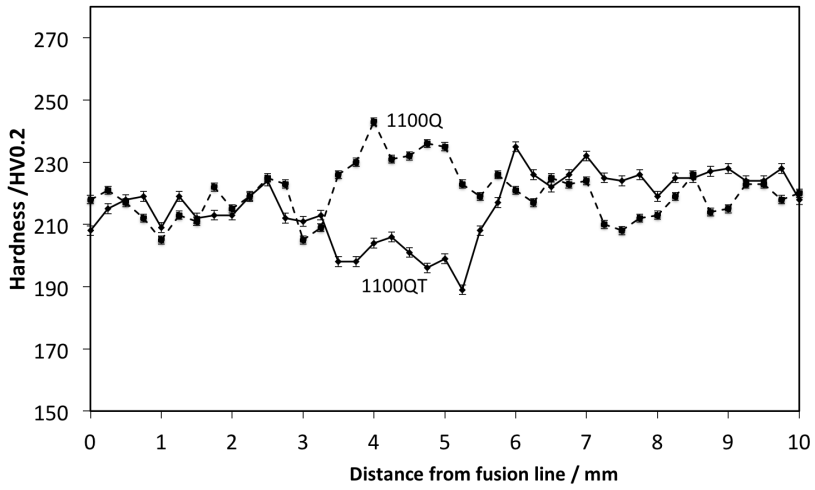

(a)

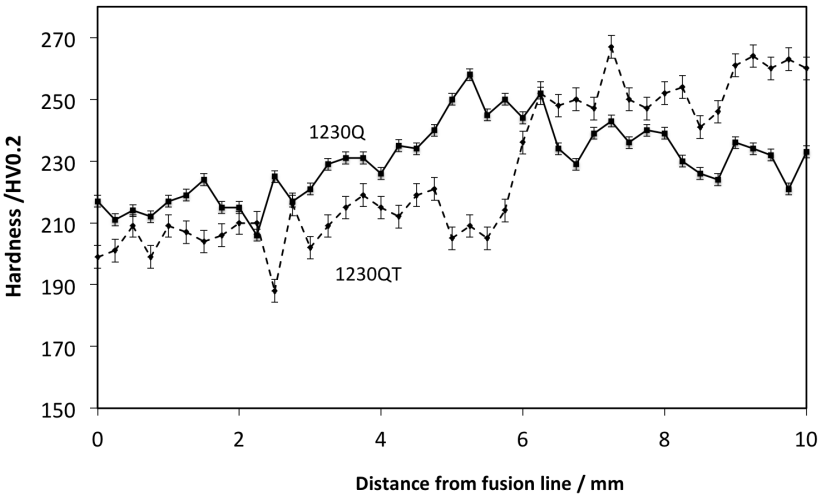

(b)

Figure 8.15: (a) Hardness profile across the heat-affected zone of 1100Q and 1100QT.(b) Hardness profile across the heat-affected zone of 1230Q and 1230QT.

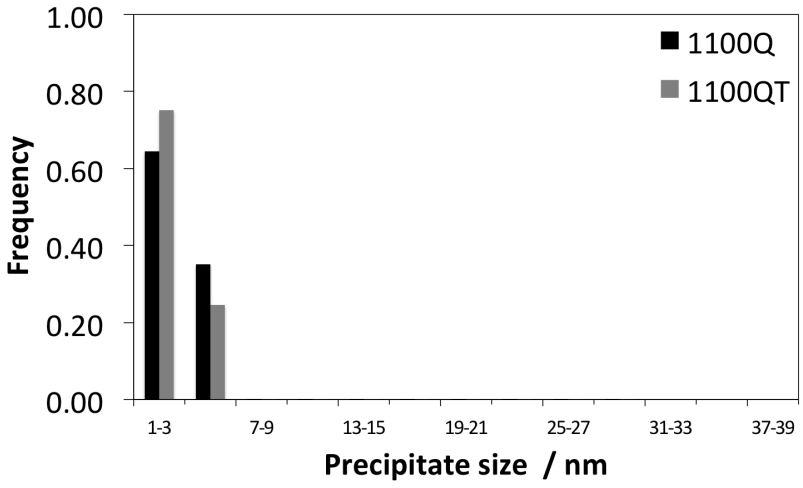

(a)

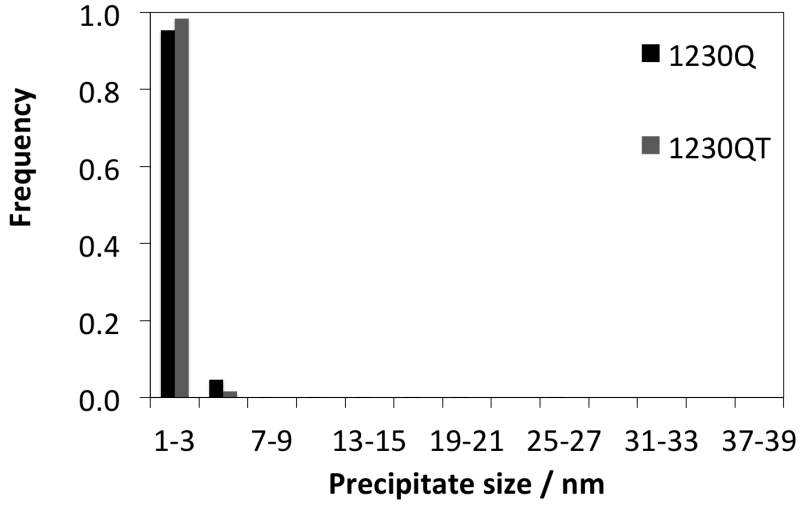

(b)

Figure 8.16: (a)precipitate size distribution for 1100Q and 1100QT.(b)precipitate size distribution for 1230Q and 1230QT

8.4 Summary

The evolution of austenite grains in the CGHAZ correlates to the entropy of the precipitates, with the availability of a population of coarse precipitates prior to thermal cycling during welding, limiting the growth of austenite grain boundaries. However this does not necessarily correlate to the hardness of the microstructure, where the drivers for higher hardenability have an effect, figure 8.17.

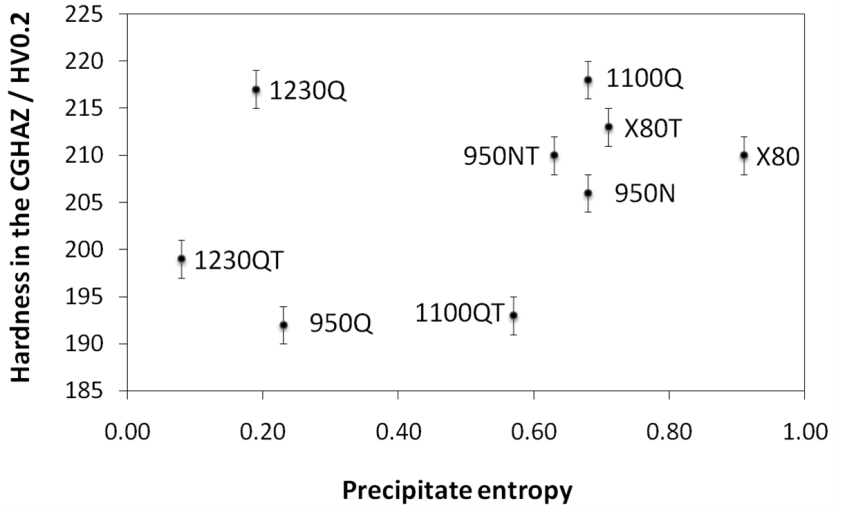

(a)

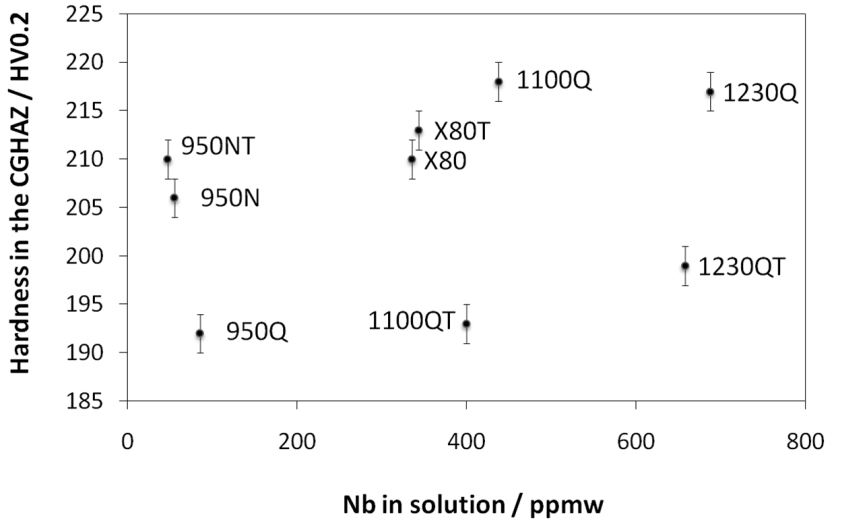

(b)

Figure 8.17: The effect of (a) precipitate entropy and (b) Nb in solution, on the hardness of the CGHAZ microstructure.

Chapter 9

Conclusions and future work

9.1 Conclusions

The aim of this project was to examine the influence of niobium on the heat-affected zone of thermomechanically processed niobium-microalloyed X80 linepipe steels welded using the submerged arc welding process. The established influence of Nb from the thermomechanical processing of high strength low alloy steels indicates that solute niobium as well as precipitated niobium carbides will:

- Control the austenite grain size by pinning the grain boundaries.
- Retard the kinetics of transformation during rolling.

Previous work based on the effects of niobium during welding of the as-rolled X80 steels have focussed on the structures and properties that develop in the HAZ for grades of X80 steel alloyed with different amounts of niobium. This has limited the examination of the specific influences of niobium carbides and Nb in solution for varying amounts of niobium in the steel composition. In order to fulfil the aim of the current project a range on experiments were undertaken that, for the first time, enabled characterisation on the HAZ sub-zones, and the contributions of the different states of Nb to the evolution of the HAZ, for a constant niobium content. The conclusions drawn from this work are summarised below:

1. A small-angle X-ray analysis technique has been utilised for the first time to measure the precipitate sizes and their distribution in bulk samples of Nb-micro-alloyed HSLA steels. The results were verified against existing a range of existing techniques such as transmission electron microscopy and mass spectroscopy. The complementary use of plasma mass spectroscopy was utilised in determine the volume fraction occupied by niobium carbides following heat treatments that simulated the sub-zones of the heat-affected zone, each with unique states of niobium.

2. The precipitate size distribution has been expressed in terms precipitate entropy, a method which easily quantifies the total population of sizes across the examined plate heat treatments for comparison.

3. The precipitate size distribution data showed that a bimodal size distribution developed on austenitisation at 1100 ℃ such that the austenite grain sizes in the plate condition showed an abnormal, bimodal distribution due to the dissolution of fine NbC precipitates, but grain boundary pinning by persisting, coarser precipitates.

4. The influence of niobium in the coarse-grained heat-affected zone was found to be similar to that reported for thermomechanical processing, dissolved Nb reduces the transformation temperature for a constant prior austenite grain size. However, the influence of the prior austenite grain as offering sites for the heterogeneous nucleation appears to strongly correlate to the transformation temperatures in the heat-affected zone, and this is related to the precipitate size distribution in the starting microstructure. Hence the original bimodal precipitate size distribution delivers a bimodal prior austenite grain size distribution in the coarse-grained heat affected zone. While characterisation of

the coarse-grained heat-affected zone following welding substantiated findings from weld simulations, it is clear that a range of precipitate sizes are required in the base steel in order to assure the benefits of precipitation strengthening in the unaffected steel away from the weld fusion zone and heat-affected areas, while a population of coarser precipitates are available to persist close to the fusion line after welding in order to control the austenite grain size.

5. Coarser precipitates that do dissolve due to the thermal gradients result in regions of high concentrations of martensite and retained austenite (the so-called 'MA-islands', the presence of dissolved Nb, or fine precipitates that readily dissolve, correlates to a homogenised distribution and a finer microstructure with fewer such islands in the coarse-grained heat-affected zone.

The findings discussed here address the prime objective of this work of studying the effects of niobium in the coarse-grained heat-affected zone, and provides a novel analytical technique and quantification method for characterising alloy carbides in steels.

9.1.1 Suggestions for future work

A number of areas worthy of further investigation are prompted by findings in this project:

1. The evolution of the precipitate size distribution during simulation of the coarse-grained heat affected zone close to the fusion line, and across a range of simulated thermal cycles consistent with different parts of the weld will enable characterisation of all parts the entire heat-affected zone. The use of small-angle X-ray scattering along with dilatometry will enable measurements of the changes to the population of precipitates during the simulation.

2. In order to further characterise the influence of niobium on the weld heat-affected zone, a range of X80 steels of varying compositions should be exposed to the thermal simulations and precipitate size measurements described in the previous item. This will account the dramatic changes in dissolved niobium that occurs close to the fusion line.

3. The use of Nb-microalloyed steels in sub-sea conditions for oil and gas transport exposes the steel to degradation by hydrogen-induced cracking, which affects high-strength materials. The use of SAXS to measure

precipitate size distributions in bulk samples can be used to compare different configurations of precipitate sizes to assess the effectiveness of different processing routes in developing a appropriate size distribution such that hydrogen is trapped effectively without reducing the exceptional mechanical properties of the steel.

Appendix 1

List of dilatometry curves from weld simulations

Dilatometry measures the dimensional changes during the course of phase transformations in samples undergoing heat treatments [104]. The offset method is used [105] to define transformation temperatures,from dilatometric data, consistent also with the analysis by Yan [78].

Dilatometric measurements were carried out using, a TA Instruments DIL805A/D dilatometer (figure 3.6) and a Thermecmaster thermomechanical simulator, both with high purity compressed helium utilised as the cooling medium during quenching. In the former the samples DIL805A were 3 mm × 10 mm rods, while the simulated samples are as shown in figure 2.9B.

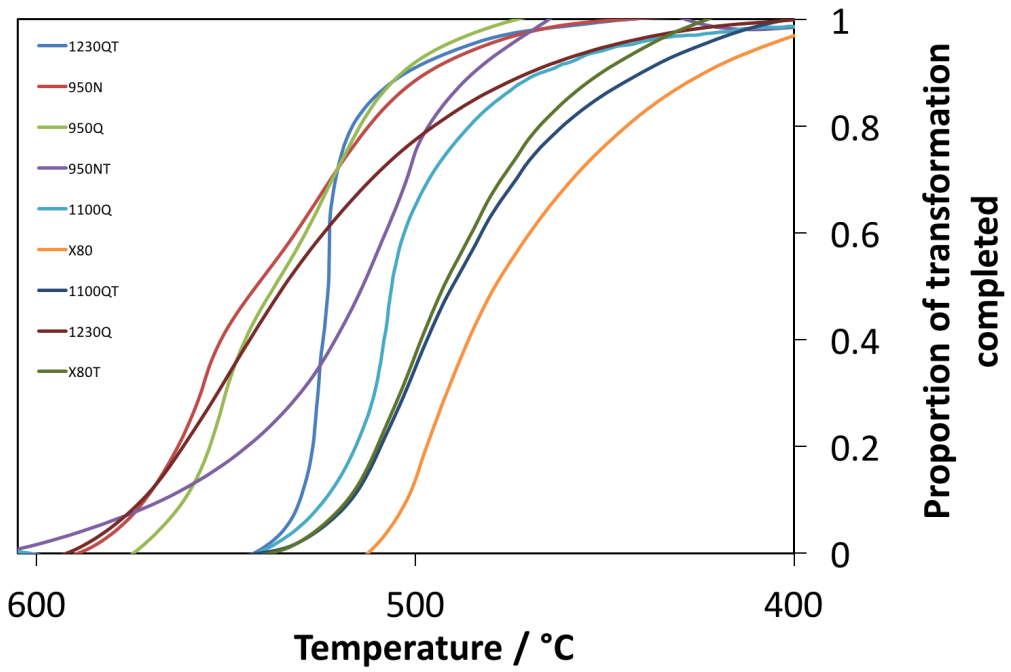

Figure 1: An interpretation of the dilatometric data across the samples of X80 steel on quenching from 1300 ℃.

Figure **??** is an example of the output of data from the dilatometric experiemntation expressed in the following curves. The phase transformation tempertaures and the rate of phase transformations have been used in this work to interpret the influence of microstructure and the Nb component on the transformations that occur during welding.

.1 Heating curves

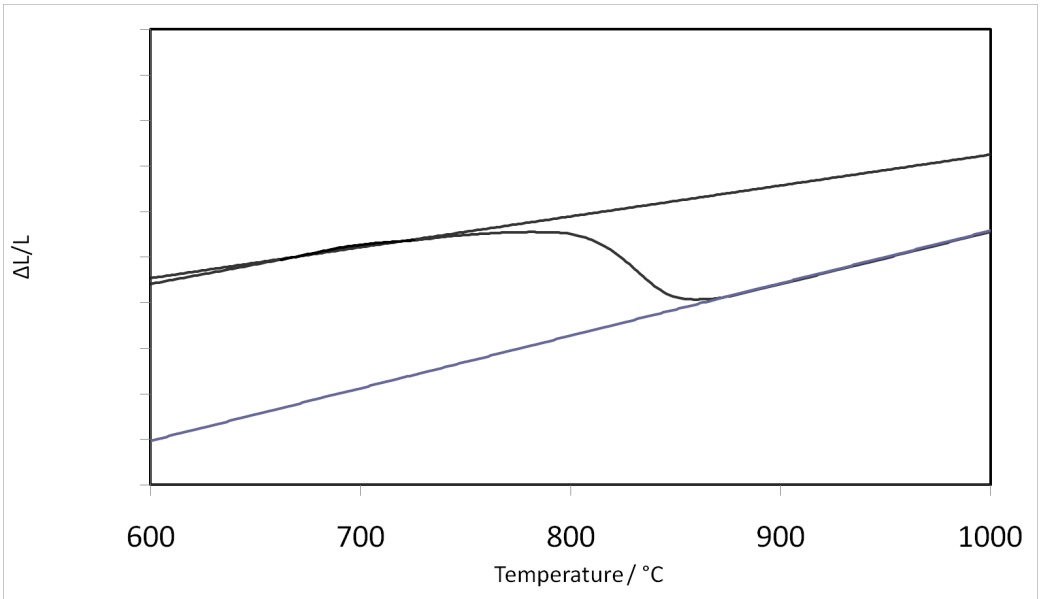

Figure 2: Dilatometry curve for heating X80 at 80 °C s^{-}1.

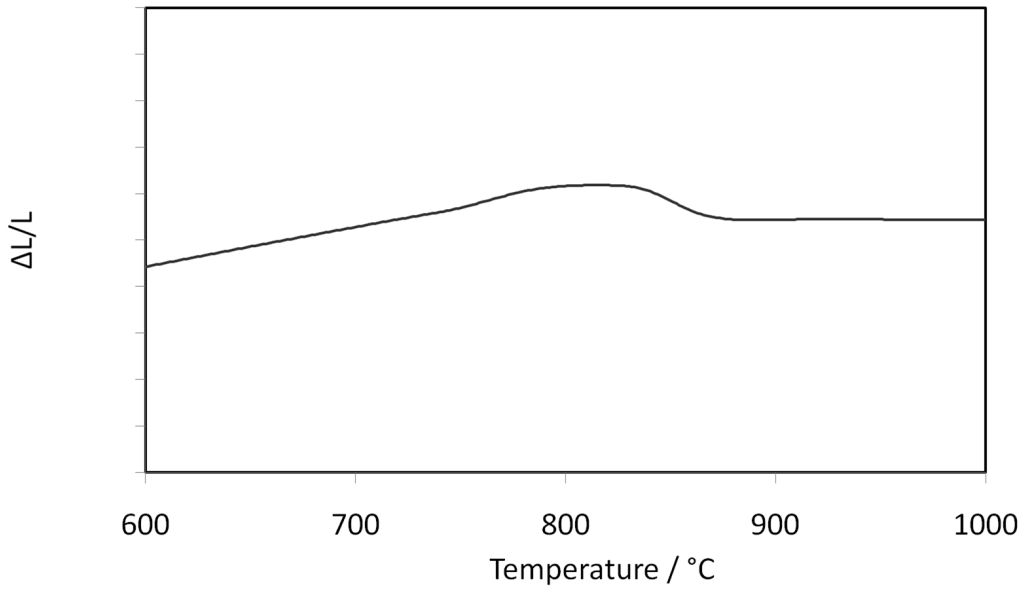

Figure 3: Dilatometry curve for heating X80T at 80 °C s⁻1.

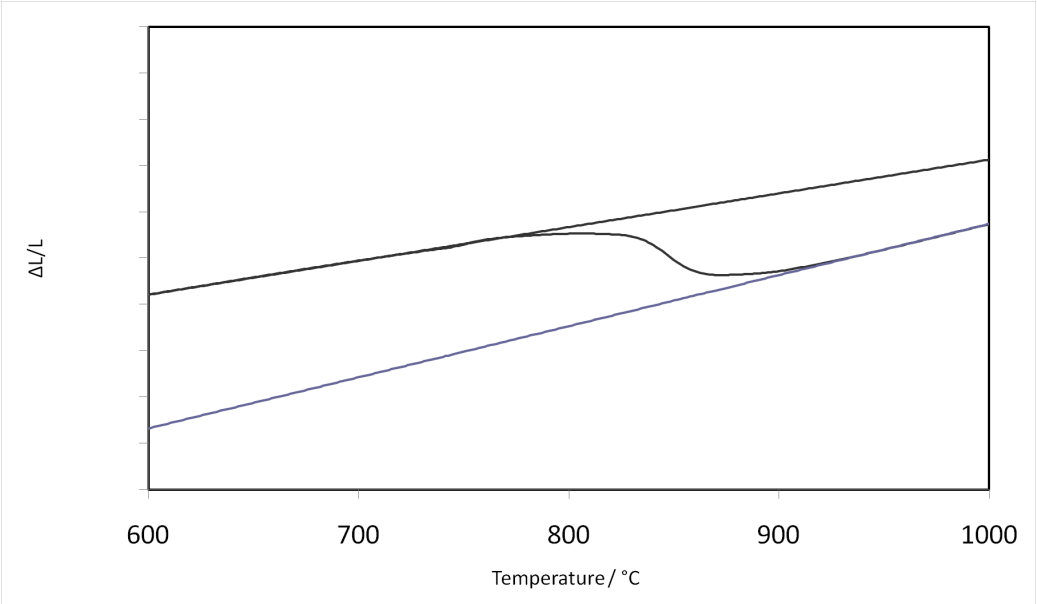

Figure 4: Dilatometry curve for heating 950N at 80 °C s⁻1.

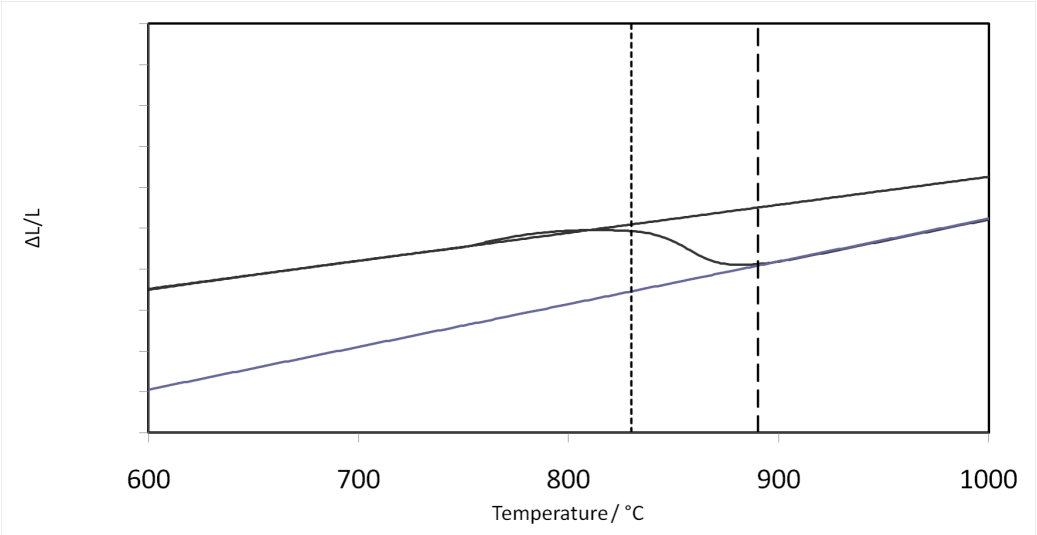

Figure 5: Dilatometry curve for heating 950NT at 80 °C s⁻1.

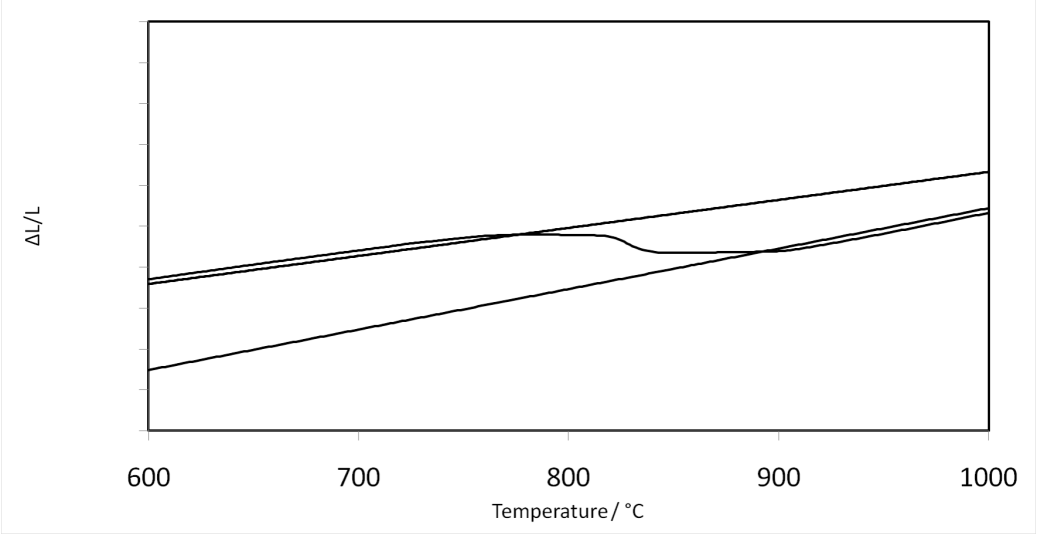

Figure 6: Dilatometry curve for heating 950Q at 80 °C s⁻1.

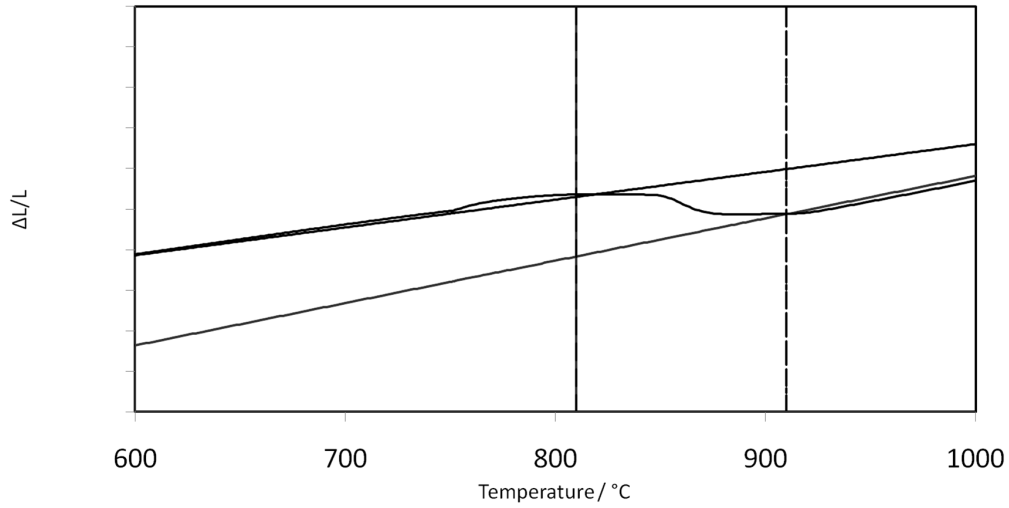

Figure 7: Dilatometry curve for heating 1100Q at 80 °C s^{-}1.

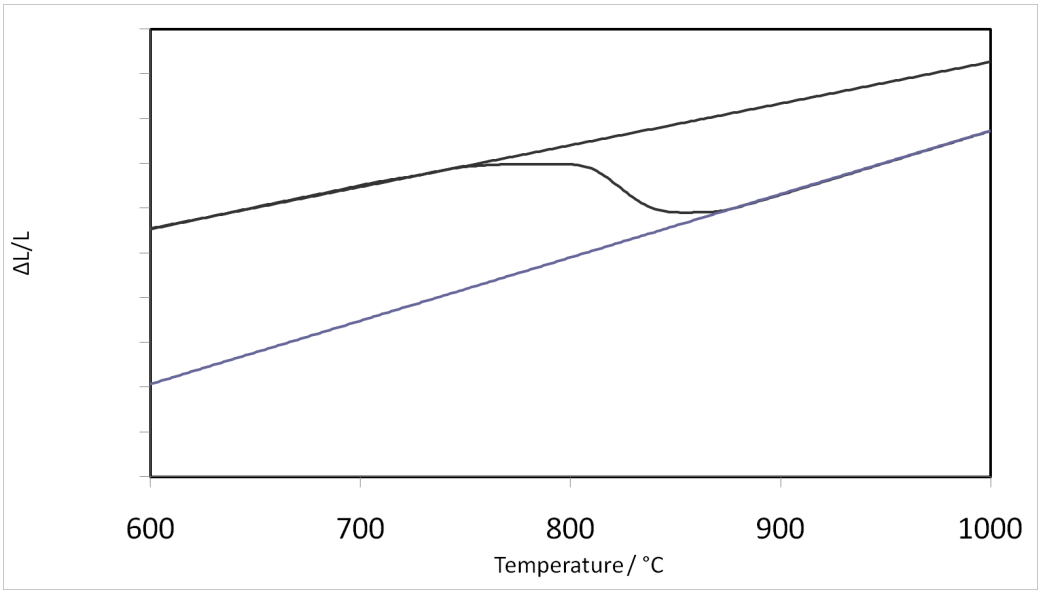

Figure 8: Dilatometry curve for heating 1100QT at 80 °C s^{-}1.

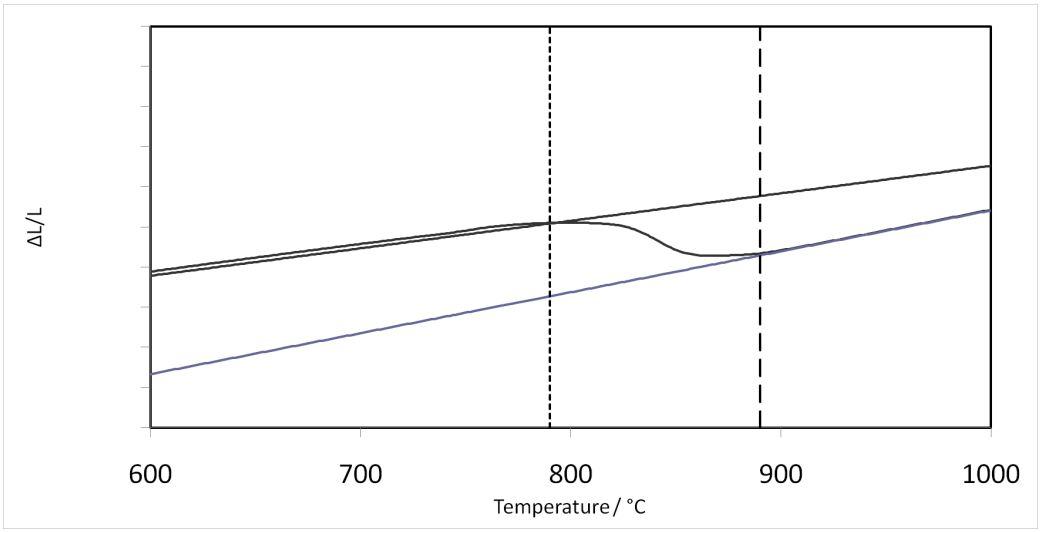

Figure 9: Dilatometry curve for heating 1230Q at 80 °C s−1.

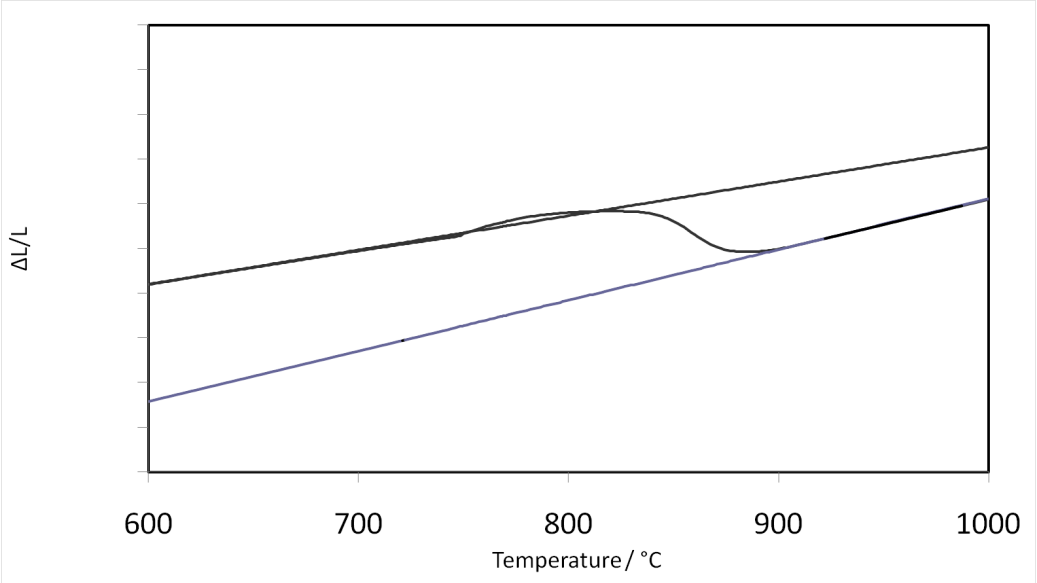

Figure 10: Dilatometry curve for heating 1230QT at 80 °C s−1.

.2 Quenching curves

List of dilatometry curves from weld simulations:

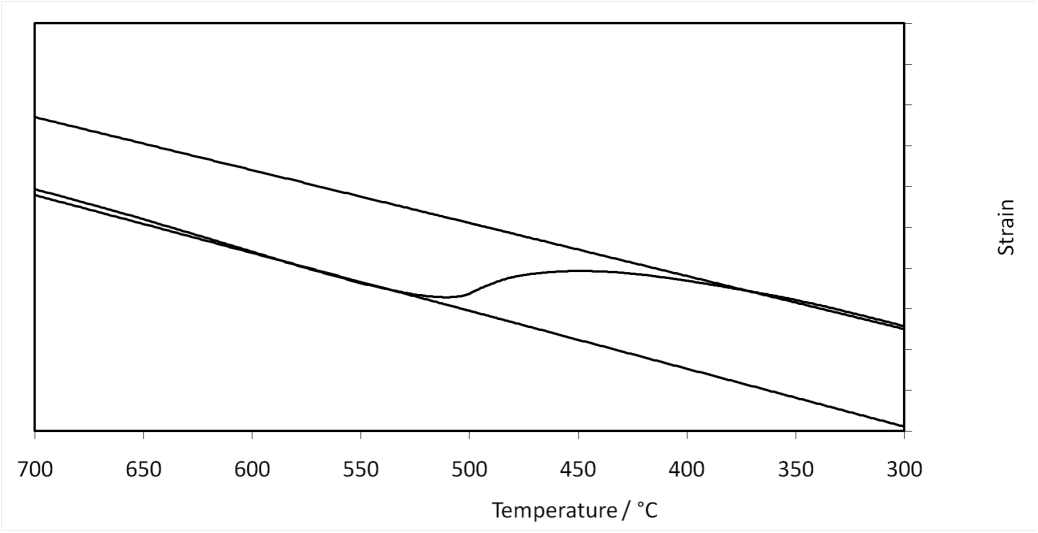

Figure 11: Dilatometry curve for cooling X80 at 80 °C s⁻1.

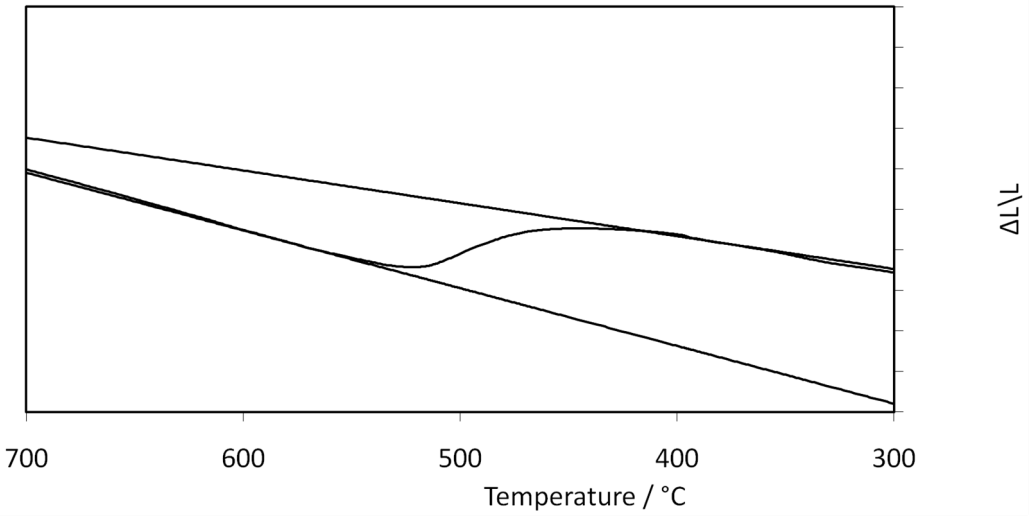

Figure 12: Dilatometry curve for cooling X80T at 80 ℃ s^{-}1.

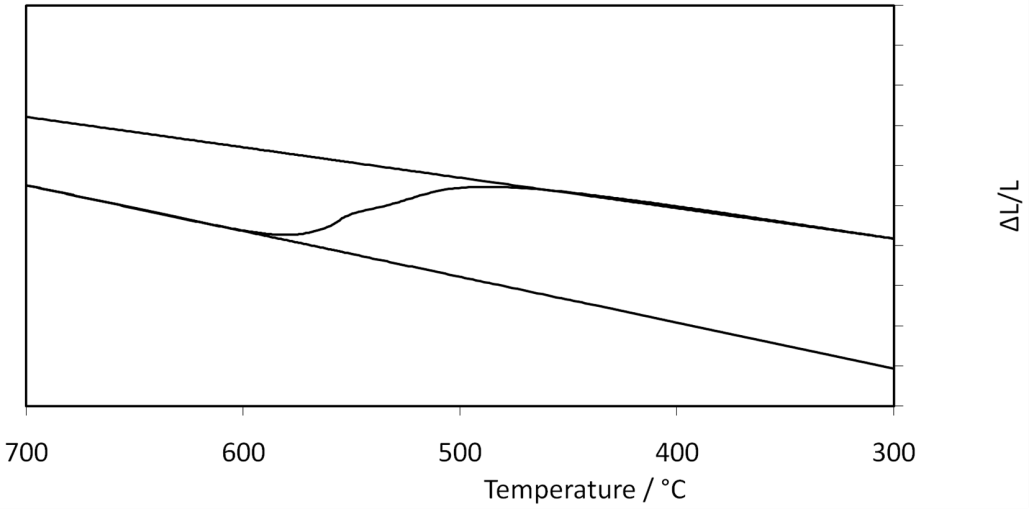

Figure 13: Dilatometry curve for cooling 950N at 80 ℃ s^{-}1.

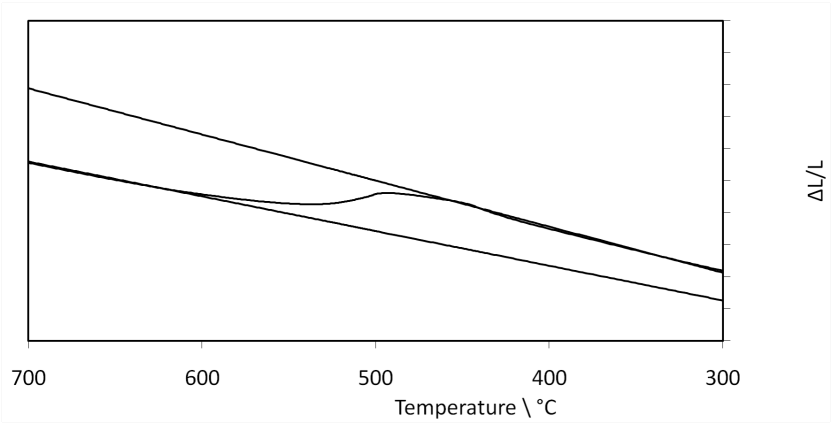

Figure 14: Dilatometry curve for cooling 950NT at 80 °C s−1.

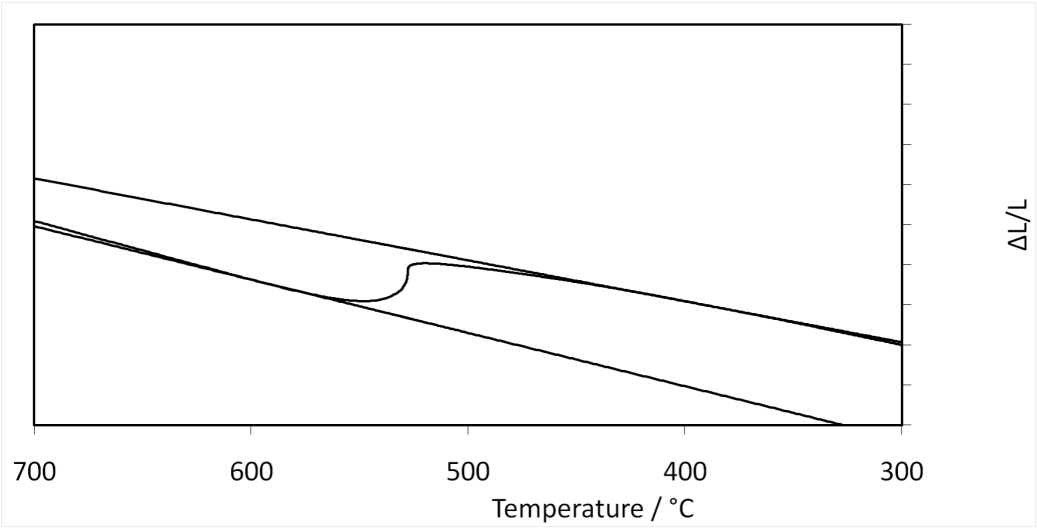

Figure 15: Dilatometry curve for cooling 950Q at 80 °C s−1.

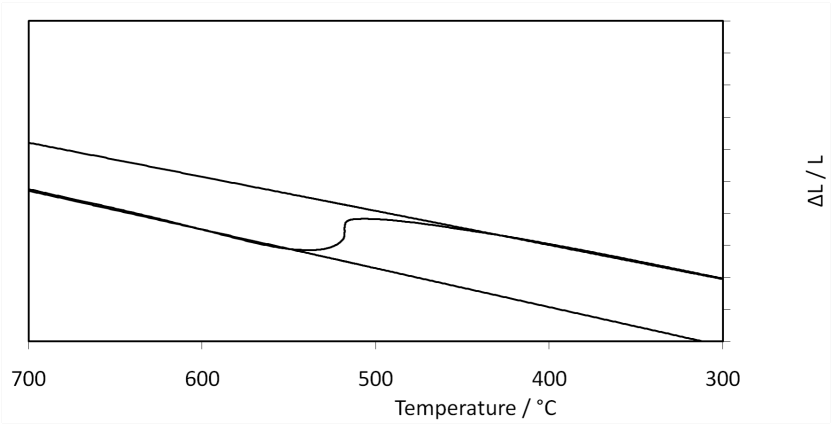

Figure 16: Dilatometry curve for cooling 1100Q at 80 ℃ s⁻1.

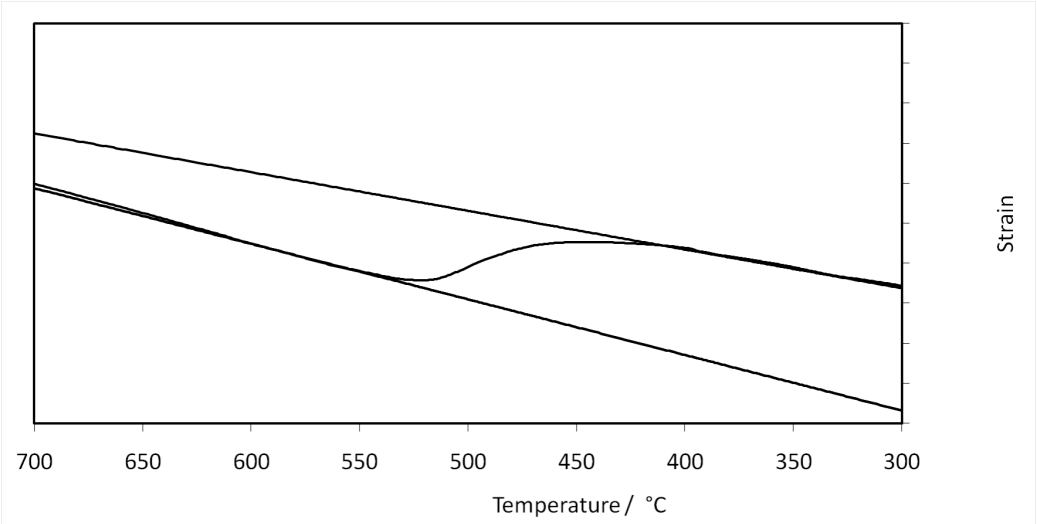

Figure 17: Dilatometry curve for cooling 1100QT at 80 ℃ s⁻1.

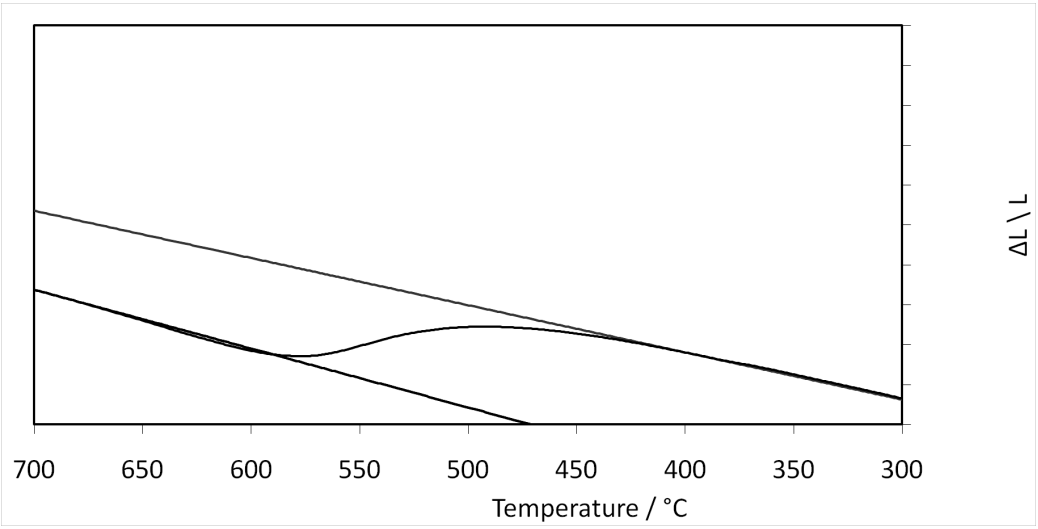

Figure 18: Dilatometry curve for cooling 1230Q at 80 °C s⁻1.

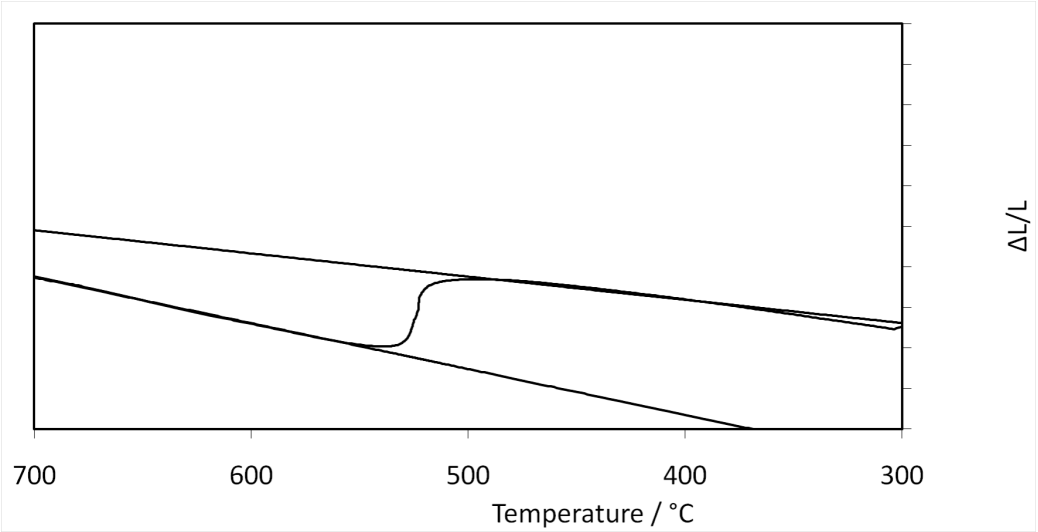

Figure 19: Dilatometry curve for cooling 1230QT at 80 °C s⁻1.

Bibliography

[1] CBMM. *Welding of Niobium Microalloyed Linepipe Steels: 50 years of History and Experience. in International Seminar on Welding of High Strength Pipeline Steels*. TMS, 2013.

[2] CBMM. *Effects of Microalloying and Hot Rolling on Toughness and Yield Strength on API X80 Grade Steel Strips. in Fundamentals and Applications of Mo and Nb Alloying In High Performance Steels.* TMS, 2014.

[3] H. Kawano. Tmcp steel plate with excellent haz toughness for high-rise buildings. pages 110–113, 2004.

[4] I. I. Frantov, A. A. Velichko, A. N. Bortsov, and I. Y. Utkin. Weldability of niobium-containing high-strength steel for pipelines. *Welding Journal, Research Supplement*, 93:23s–29s, 2014.

[5] A. Johnson and R. Storey. Effect of carbon on the charpy v-notch ductile-brittle transition curve.

[6] R. W. K. Honeycombe and H. K. D. H. Bhadeshia. *Steels: Microstructure and Properties, 2nd edition.* Butterworths–Hienemann, London, 1995.

[7] D. Bombac, M. Fazarinc, A. Saha Podder, and G. Kugler. Study of carbide evolution during thermo-mechanical processing of aisi d2 tool steel. 2013.

[8] K. J. Irvine, F. B. Pickering, and T. Gladman. Grain refined C–Mn steels. *Journal of the Iron and Steel Institute*, 205:161–182, 1967.

[9] A. Fatehi, J. Calvo, A.M. Elwazri, and S. Yue. Strengthening of hsla steels by cool deformation. *Mater Sci Eng A*, 527(4233-4240), 2010.

[10] T. Gladman. On the theory of the effect of precipitate particles on grain growth in metals. In *Proceedings of the Royal Scoety of London Series A, Mathemtical and Phsyical Sciences*, volume 294, pages 298–309. Royal Society, 1966.

[11] C. Fossaert, G. Rees, T. Maurickx, and H. K. D. H. Bhadeshia. The effect of niobium on the hardenability of microalloyed austenite. *Metallurgical and Materials Transactions A*, 26A:21–30, 1995.

[12] G. T. Hahn, B. L. Averbach, W. S. Owen, and M. Cohen. *Fracture*. MIT Press, Cambridge, MA, USA, 1959.

[13] T. Gladman. *Physical Metallurgy of Microalloyed Steels*. Institute of Materials, London, U.K., 1997.

[14] M. Civalero, C. Parrini, and N. Pizzimenti. Production of large-diameter high-strength low-alloy pipe in italy. In *Microalloying '75*, Washington, D. C., USA, Ocotber 1975.

[15] Assocation for Iron and Steel Tehnology. *Evaluation of Low- and Medium-Carbon Nb-Microalloyed Plate Steels for Wind Tower Applications*. 2011 International Symposium on the Recent Developments in Plate Steels, 2011.

[16] J.F. Lancaster. *Metallurgy of Welding*, page 464. Abington Publishing, 1999.

[17] W. C. Leslie. Iron and its dilute substitutional solid solutions. *Metallurgical Transactions A*, 3:5–23, 1972.

[18] A. H. Cottrell and B. A. Bilby. Dislocation theory of yielding and strain ageing of iron. *Proc. Physics Society A*, 62:49–62, 1949.

[19] E.C. Hamre and A.M. Gilroy-Scott. In *Proceeding of International Symposium Microalloying'75*, Microalloying'75, page 375, October 1975.

[20] J.M. Gray. Microalloyed hsla steels. In *World Materials Congress*, page 61, Chicago, U.S.A., September 1988.

[21] M. Hamada, Y. Fukada, and Y. Komiz. Microstructure and precipitation behaviour in the heat-affected zone of c-min microalloyed steel containing nb, v and ti. *ISIJ international*, 35(10):1196–1202, 1995.

[22] F. Wever and H. Lange. The transformation kinetics of austenite - I - magnetic investigations of the decomposition of austenite. *Mitt. Kaiser-Wilhelm-Inst. Eisenforschung*, 14:71–83, 1932.

[23] K. W. Andrews. Empirical formulae for the calculation of some transformation temperatures. *Journal of the Iron and Steel Institute*, 203:721–727, 1965.

[24] N. Gupta. Illustration of comparative strengths of alloying agents (a) austenite forming alloys (b) ferrite forming alloys after andrews. 2016.

[25] Schick. Thermodynamics of certain refractory compounds. 1966.

[26] A. H. Cottrell. Chemical bonding in transition metal carbides. London, 1995. Institute of Materials.

[27] G. Krauss and S. W. Thompson. Ferritic microstructure in continuously cooled low- and ultralow-carbon steels. *ISIJ International*, 35:937–945, 1995.

[28] M. Hillert. Thermodynamics of the massive transformation. *Metall. Mater. Trans. A*, 15:411–419, 1984.

[29] T.B. Massalski. *Phase Transformations*, page 433. ASM, Metals Park, Ohio, USA, 1970.

[30] J. Cawley, C.F. Harris, and E.A. Wilson. *New Asects of Microstructures in Modern Low Carbon High Strength Steels*, page 31. ISIJ, Tokyo 1994.

[31] E.A. Wilson. *ISIJ Int*, 34(8):615, 1994.

[32] W.C. Jeong. Microstructural aspects of quasi-polygonal and granular bainitic ferritic in an ultra-low carbon interstitial-free high strength steels. *Metall Trans A*, 34A:2016–2025, 2003.

[33] H. K. D. H. Bhadeshia. The bainite transformation: Unresolved issues. *Materials Science & Engineering A*, 273–275:58–66, 1999.

[34] H I Aaronson, W. T. Reynolds, G.J. Shiflet, and G. Spanos. Bainite viewed three different ways. *Metall Trans A*, 21A:1343–1380, 1990.

[35] M. Hillert. Diffusion in the growth of bainite. *Metallurgical & Materials Transactions A*, 25:1957–1966, 1994.

[36] H. K. D. H. Bhadeshia and D. V. Edmonds. The mechanism of bainite formation in steels. *Acta Metallurgica*, 28:1265–1273, 1980.

[37] E. Swallow and H. K. D. H. Bhadeshia. High resolution observations of displacements caused by bainitic transformation. *Materials Science and Technology*, 12:121–125, 1996.

[38] W. Bleck. *Werkstoffkunde Stahl Fur Studium un Praxis*. Wissenschaftsverlag Mainz GmbH, 2004.

[39] S. Wang and J.R. Yang. Effect of chemical composition, rolling and cooling conditions on the amount of martensite/austenite (m/a) constituent formation in low carbon bainitic steels. 154:43–49, 1992.

[40] C. L. Davis and J. E. King. Effect of cooling rate on intercritically reheated microstructure and toughness in high strength low alloy steel. *Materials Science and Technology*, 9:8–15, 1993.

[41] M. Gomez, P. Valles, and S. F. Medina. Evolution of microstructure and precipitation state during thermomechanical processing of a X80 microalloyed steel. *Materials Science and Engineering A*, 528:4761–4773, 2011.

[42] P. Brozzo, G. Buzzichelli, A. Mascanzoni, and M. Mirabile. Microstructure and cleavage resistance of low-C bainitic steels. *Metal science*, 11:123–130, 1977.

[43] A. Di Schino, L. Alleva, and M. Guagnelli. Microstructure evolution during quenching and tempering of marteniste in a medium carbon steel. In *4th Joint International Conference on Recrystallization and Grain Growth*, 2010.

[44] F. Fazeli, T. Jia, and M. Militzer. Critical assessment of bainite models for advanced high strength steels. *Solid State Phenomena*, 172–174:1183–1188, 2011.

[45] T. Gladman. *The Physical Metallurgy of Microalloyed Steels*. IOM Communications, London, 1996.

[46] J. W. Martin, R. D. Doherty, and B. Cantor. *Stability of microstructure in metallic systems*. Cambridge University Press, Cambridge, U. K., 2 edition, 1997.

[47] J. W. Christian. *Theory of Transformations in Metals and Alloys*. Pergamon Press, Oxford, U. K., 1965.

[48] S.Polat M.A. Dvorack and Hayden Chen. The early stage of gamma prime precipitation in a nickel silicon alloy. (18):1395–1399, 1984.

[49] M. Volmer and A. Weber. *Z. Phys. Chem*, (119):277, 1925.

[50] R. Becker and W. Doring. *Annalen der Physik*, 24:719, 1935.

[51] R.M. Brito and H.J. Kestenbach. *J Mater Sci*, 16:1257–1263, 1981.

[52] A. J. Deardo, J. M. Gray, and L. Meyer. Fundamental metallurgy of niobium in steel. In H. Stuart, editor, *Niobium '81*, pages 685–759, Warrendale, Pennsylvania, USA, 1981. TMS-AIME.

[53] C.S. Smith. *Metal Interfaces*, page 65. ASM International, Ohio, USA, 1952.

[54] A. Kelly and R. B. Nicholson. *Strengthening Mechanisms in Crystals*. Elsevier, Amsterdam, Holland, 1971.

[55] J. Lu, O. Omotoso, J. B. Wiskel, D. G. Ivey, and H. Nenein. Strengthening mechanisms and their relative contributions to the yield strength of microalloyed steels. *Metallurgical & Materials Transactions A*, 43:3043–3061, 2012.

[56] Y. Z. Wang and A. G. Khachaturyan. Multi–scale phase field approach to martensitic transformations. *Materials Science & Engineering A*, 438–440:55–63, 2006.

[57] S. Akhlaghi and D.G Ivey. *Canadian Metallurgical Quarterly*, 41(1):111–119, 2002.

[58] R.C. Cochrane. Haz microstructure and properties of pipeline steels. *Proceedings of the INternational Seminar on Welding of High Strength Pipeline Steels*, pages 153–188, 2013.

[59] S. Okaguchi, T. Hashimoto, and H. Ohtani. Effect of niobium, vanadium and titanium on transformation behavior of hsla steel in accelerated cooling. In *Physical Metallurgy of Thermomechanical Processing of Steels and Other Metals*, volume 1, pages 330–336, Tokyo, Japan, 1988. Iron and Steel Institute of Japan.

[60] J. M. Gray, W. W. Wilkening, and L. G. Russell. Transformation characteristics of very-low-carbon steels. Technical report, U. S. Steel, USA, 1969.

[61] K. Hulka and J. M. Gray. High-temperature processing of line-pipe steels. In *Niobium 2001*, pages 587–612, Warrendale, Pennsylvania, USA, 2001. TMS–AIME.

[62] L. Rönn. Niobs inverkan på TTT-diagrammet av ett mjukt stål, 1963.

[63] F. de Kazinczy, A. Axn´as, and P. Pachleitner. Some properties of niobium-treated mild steel. *Jernkontorets Annaler*, 147:408–433, 1963.

[64] H.K.D.H. Bhadeshia. Steels: Microstructure and properties, fourth edition. 2017.

[65] R. K. Amin and F. B. Pickering. Ferrite formation from thermo-mechanically processed austenite. In A. J. DeArdo, G. A. Ratz, and P. J. Wray, editors, *Thermomechanical processing of microalloyed austenite*, pages 377–403, Pittsburgh, USA, 1981. TMS–AIME.

[66] G. I. Rees, J. Perdrix, T. Maurickx, and H. K. D. H. Bhadeshia. The effect of niobium in solid solution on the transformation kinetics of bainite. *Materials Science and Engineering A*, 194:179–186, 1995.

[67] C. Ouchi, T. Sampei, and I. Kozasu. The effect of hot rolling condition and chemical composition on the onset temperature of γ/α transformation after hot rolling. *Transactions of the Iron and Steel Institute of Japan*, 22:214–222, 1982.

[68] M. Enomoto, N. Nojiri, and Y. Sato. Effects of vanadium and niobium on the nucleation kinetics of proeutectoid ferrite at austenite grain boundaries in Fe-C and Fe-C-Mn alloys. *Materials Transactions, JIM*, 35:859–867, 1994.

[69] P. J. Felfer, C. R. Killmore, J. G. Williams, K. R. Carpenter, S. P. Ringer, and J. M. Cairney. A quantitative atom probe study of the nb excess at prior austenite grain boundaries in a Nb microalloyed strip-cast steel. *Acta Materialia*, 60:5049–5055, 2012.

[70] M. Wang. Analysis of improvement of anti-contact fatigue for bearing steel by ion implantation. In *3rd Internatonal Conference on Measuring Technology and Mechatronics Automation*, number 5720821 in 1, pages 467–470, Washington, D. C., USA, 2011. IEEE Computer Society.

[71] W.J. Poole et al. Microstructure evolution in the haz of girth welds in linepipe steels for the arctic. In *Proceedings of the 8th international pipeline conference*, Calgary, Alberta, Canada, 2010.

[72] R. B. G. Yeo. Effects of some alloying elements on the transformation of Fe-22.5Ni wt% alloys. *Trans. Metall. Soc. AIME*, 227:884–890, 1963.

[73] J. W. Cahn and W. C. Hagel. Theory of pearlite reaction. In V. F. Zackay and H. I. Aaronson, editors, *Decomposition of Austenite by Diffusional Processes*, pages 131–192, New York, 1962. Intersciences.

[74] M. Hillert and L. I. Staffansson. The regular solution model for stoichiometric phases and ionic melt. *Acta Chimica Scandinavica*, 24:3616–3626, 1970.

[75] H. K. D. H. Bhadeshia. Considerations of solute drag in relation to transformations in steels. *Journal of Material Science*, 18:1473–1481, 1983.

[76] H. K. D. H. Bhadeshia. Critical assessment: Diffusion–controlled growth of ferrite plates in plain carbon steels. *Materials Science and Technology*, 1:497–504, 1985.

[77] Pei Yan and H. K. D. H. Bhadeshia. The austenite–ferrite transformation in enhanced-niobium, low-carbon steel. *Mater. Sci. Technol.*, (31):1066–1076, 2015.

[78] Pei Yan and H. K. D. H. Bhadeshia. Mechanism and kinetics of solid-state transformation in high-temperature processed linepipe steel. *Metall. Mater. Trans. A*, 44A:5468–5477, 2013.

[79] C. Liu and S. D. Bhole. Challenges and developments in pipeline weldability and mechanical properties. *Science and Technology of Welding and Joining*, 18:169–181, 2013.

[80] A. Liessem. Essential welding aspects for high strength linepipe. In TMS, editor, *International Seminar on Welding Of High Strength Pipeline Steels*, Araxa, Brazil, 2013. CBMM.

[81] J.C. Coiffer. Combination of laser beam and submerged arc process for the longitudinal welding of large-diameter welded pipe. In *Proc. Int. Symp.*

on 'Safety in application of high strength steel, Trondheim, Norway, 1997. Statoil Research Center.

[82] P. Kirkwood. Weldability - the role of niobium in the heat affected zone of microalloyed high strength line pipe steels. In *Niobium*, 2013.

[83] K. E. Easterling. *Introduction to the Physical Metallurgy of Welding*, page 133. Butterworth–Heinemann, 2nd edition, 1992.

[84] L.J. Cuddy and J.C. Raley. Austenite grain coarsening in microalloyed steels. *Metall. Trans. A*, 14:1989–1995, 1983.

[85] S. Moeinifar, A. H. Kokabi, and H. R. Madaah Hosseini. Influence of peak temperature during simulation and real thermal cycles on microstructure and fracture properties of the reheated zones. *Materials and Design*, 31(6):2948–2955, June 2010.

[86] J.L. Andia, L.F.G. de Souza, and I.S.Bott. Microtrcutiral and mechanical properties of the intercritically reheated coarse grained heat affected zone (iccghaz) of an api 5l x80 pipeline steel. *Mater. Sci Forum*, 783-786:657–662, 2014.

[87] C. L. Davis. *Cleavage initiation in the intercritically reheated coarse grained heat affected zone of steels*. PhD thesis, University of Cambridge, Cambridge, U. K., 1994.

[88] B.C. Kim. Microstructure and local brittle zone phenomenon in high strength low alloy steel welds. *Metallurgical & Materials Transactions A*, 22A:139–149, 1991.

[89] S. Aihara and K. Okamoto. Influence of LBZon HAZ toughness of TMCP steel. In D. G. Howden J. T. Hickey and M. D. Randall, editors, *Metallurgy,*

Welding and Qualification of Microalloyed Steel Weldments, pages 402–427, Florida, USA, 1990. American Welding Society.

[90] S. Suzuki, G. Rees, and H. K. D. H. Bhadeshia. Modelling of brittle zones in the HAZ of steel welds. In T. Zacharia, editor, *Modelling and Control of Joining Processes,*, pages 186–193, Florida, USA, 1993. American Welding Society.

[91] H. K. D. H. Bhadeshia. About calculating the characteristics of the martensite-austenite constituent. In *Welding of High Strength Pipeline Steels*, pages 99–106, Materials Park, Ohio, USA, 2013. TMS.

[92] T. Lolla, S.S. babu, S. Lalam, and M. Manohar. Comparison of simulated heat affected zone microstroctures of niobium microalloyed steels subjected to multi-pass weld thermal cycles. In TMS, editor, *Proceedings of the International Seminar on Welding of High Strength Pipeline Steels*, pages 281–297. CBMM, TMS, 2013.

[93] M. Guagnelli, A. Di Schino, M.C. Cesile, and M. Pontremoli. Effect of nb microalloying on the heat affected zone microstructure of x80 large diameter pipeline after in-field girth welding. In TMS, editor, *Proceedings of the International Seminar on Welding of High Strength Pipeline Steels*, pages 333–339. CBMM, TMS, 2013.

[94] S. Maropoulos, J.D.H Paul, and N. Ridley. Micrsotructure-property relationships in tempered low alloy cr-mo-3.5ni-v steel. *Materials Science and Technology*, (9):1014–1019, 1993.

[95] M. Goméz and S. F. Medina. Role of microalloying elements in the mi-

crostructure of hot rolled steels. *International Journal of Materials Research*, 102:1197–1207, 2011.

[96] Y. Li, D. N. Crowther, M. J. W. Green, P. S. Mitchell, and T. N. Baker. The effect of vanadium and niobium on the properties and microstructure of the intercritically reheated coarse grained heat affected zone in low carbon microalloyed steels. *ISIJ International*, 41:46–55, 2001.

[97] Zhixiong Zhu, Jian Han, Huijun Li, and Cheng Lu. High tempertaure processed high nb x80 steel with excellent heat-affected zone toughness. *Materials Letters*, 163:171–174, 2016.

[98] H. K. D. H. Bhadeshia and R. W. K. Honeycombe. *Steels: Microstructure and Properties, 3rd edition.* Butterworth–Heinemann, London, 2006.

[99] T. Garcin, M. Militzer, W.J. Poole, and L. Collins. Microstructure model for the heat-affected zone of x80 linepipe steel. *Materials Science and Technology*, 2016.

[100] C. Garcia de Andrés, M. J. Bartolomé, C. Capdevila, D. San Martín, F. G Caballero, and V. Lopez. Metallographic techniques for the determination of the austenite grain size in medium-carbon microalloyed steel. *Materials Characterization*, 46:389–398, 2001.

[101] W. S. ; Eliceiri K. W. Schneider, C. A.; Rasband. Nih image to imagej: 25 years of image analysis. (7):671–675, 2012.

[102] H. Pous-Romero, I. Lonardelli, D. Cogswell, and H. K. D. H. Bhadeshia. Austenite grain growth in a nuclear pressure vessel steel. *Materials Science & Engineering A*, 567:72–79, 2013.

[103] A. A. B. Sugden and H. K. D. H. Bhadeshia. Microstructural entropy and the scatter in toughness. In S. A. David and J. M. Vitek, editors, *Recent Trends in Welding Science and Technology (TWR'89)*, pages 745–748, Metals Park, Ohio, USA, 1989. ASM International.

[104] M. Takahashi and H. K. D. H. Bhadeshia. Interpretation of dilatometric data for transformations in steels. *Journal of Materials Science Letters*, 8:477–478, 1989.

[105] H.-S. Yang and H. K. D. H. Bhadeshia. Uncertainties in the dilatometric determination of the martensite–start temperature. *Materials Science and Technology*, 23:556–560, 2007.

[106] NPL. MTDATA. Software, National Physical Laboratory, Teddington, U.K., 2006.

[107] A. Guinier and G. Fournet. *Small-Angle Scattering of X-rays*. Wiley, New York, 1955.

[108] O. Glatter and). Kratky. *Small Angle X-ray Scattering*. Academic Press, New York, 1982.

[109] Filik J. Wharmby M.T. Chang P.C.Y. El Kassaby B. Gerring M. Aishima J. Levik K. Pulford B.C.A. Sikharulidze I. et al. Basham, M. Data analysis workbench (dawn). *Journal of Synchrotron Radiation*, 22, 2015.

[110] N. Schell et al. *Materials Science Forum*, 772:57–61, 2014.

[111] Peter Staron, Torben Fischer, Thomas Lippman, Andreas Stark, Shahrok Daneshpur, Dirk Schnubel, Gerstenberger RObert Uhlmann, Eckart, Bettina Camin, Walter Reimers, Elisabeth Eidenberger, Helmut Clemens, Norbert

Huber, and ANdreas. Schreyer. In situ experiments with synchrotron high energy x-rays and neutrons. *Advanced Engineering Materials*, 13(8), 2011.

[112] J. Ilavsky and P.R. Jemian. Irena: tool suite for modeling and analysis of small-angle scattering. *Journal of Applied Crystallography*, 42(2):347–353, 2009.

[113] C. Yan, W. Li, L. Feng, Z. Xue, S. Bai, and F. Liu. Review of X100 pipeline steel and its field weldability. *Transactions of the China Welding Institution*, 28:105–108, 2007.

[114] C.S. Smith. *Transactions of the American Institute of Mining Engineers*, 15(175), 1948.

[115] C.R. Hutchinson, H.S. Zurob, C.W.Sinclair, and Y.J.M Brechet. The comparative effectiveness of nb solute and nbc precipitates at impeding grain-boundary motion in nb steels. *Scripta Mater*, (59):635–637, 2008.

[116] Peter Rene Jemian. Characterization of steels by anomalous small-angle x-ray scattering. 1990.

[117] Pete R. Jemian, Julia R. Weertman, Gabrielle G. Long, and Richard D. Spal. Characterisation of (cr-1movnb steel by anomalous small-angle x-ray scattering. *Acta Metall Mater*, 39:2477–2487, 1991.

[118] L.J. Swartzendruber and E. Paul. The fe-ta (iron-tantalum) system. *Bull Alloy Phase Diagrams*, pages 254–259, 1986.

[119] M. Maalekian, R. Radis, M. Militzer, A. Moreau, and W. J. Poole. In situ measurement and modelling of austenite grain growth in a Ti/Nb microalloyed steel. *Acta Materialia*, 60:1015–1026, 2012.

[120] M. Militzer, M. Maalekian, T. Garcin, and W.J. Poole. Microstructure evolution model for the haz in girth welds in x80 linepipe steels. In TMS, editor, *Welding of High Strength Pipeline Steels*, pages 261–279. CBMM Brazil, 2013.

[121] P. R. Kirkwood. Niobium and heat–affected zone mythology. Technical report, http://www.apia.net.au/, U. K., 2011.